Development of HTS Trapped Field Magnets Using 2G HTS Coated Conductors

Hengpei Liao

Department of Electronic and Electrical Engineering

University of Strathclyde

A thesis submitted for the degree of

Doctor of Philosophy

October 2023

Supervisor: Prof. Min Zhang, Prof. Weijia Yuan

Declaration

This thesis is the result of the author's original research. It has been composed by the author and has not been previously submitted for the examination which has led to the award of a degree.

The copyright of this thesis belongs to the author under the terms of the United Kingdom Copyright Acts as qualified by University of Strathclyde Regulation 3.50. Due acknowledgement must always be made of the use of any material contained in, or derived from, this thesis.

Signed:

Date: 12/02/2024

Acknowledgements

Abstract

Compact High-Temperature Superconducting (HTS) trapped field magnets stand at the frontier of breakthroughs for advanced industrial equipment, medical devices, and transportation electrification, offering capabilities that conventional permanent magnets and electromagnets cannot achieve. While superconductors capitalize on zero resistance to uphold high currents, thus generating substantial fields, traditional HTS bulks and stacks have been limited by constraints such as geometry size and mechanical robustness. As second-generation (2G) commercial HTS coated conductors advance, there's a growing emphasis on utilizing these tapes to attain expansive and stable trapped field profiles. This thesis explores the innovative magnetization mechanisms and design optimizations of HTS trapped field magnets fabricated with 2G HTS tapes through a comprehensive analysis of HTS-stacked ring magnets, hybrid HTS-stacked ring design, their mechanical stress responses, and trapped field closed-loop HTS coil under field cooling magnetization. The research primarily investigated a novel hybrid HTS trapped field magnet, integrating HTS-stacked ring magnets with HTS bulks to surpass traditional size limitations and achieve a significant trapped field of 7.35 T. It further predicted their capability to generate a trapped field exceeding the applied field due to unique induced current distributions and flux redistribution. Additionally, the study addressed the mechanical challenges posed by Lorentz forces during magnetization, presenting 3D numerical models to analyze stress and strain in HTS-stacked ring magnets. A 90 % stress reduction was seen by proper impregnation and fixation methods. Lastly, a novel closed-loop HTS coil approach was introduced, achieving a compact high-field superconducting magnet that trapped a central field 4.59 T which was higher than the 4.5 T applied field, showcasing potential for diverse high-field applications. Above the inner edge of the HTS coil, the trapped field exceeded the applied field by 1.5 T. This thesis combines experimental findings and numerical modelling to advance the understanding of HTS magnetization processes, offering insights into designing more efficient and durable compact and portable HTS magnets for applications in nuclear magnetic resonance, Maglev transportation, and HTS machinery.

Contents

List of Figures

List of Symbols

B_c	Critical field
T_c	Critical temperature
J_c	Critical current
n	Power-law exponent
T	Temperature
B	Magnetic flux density
H	Magnetic field strength
H^*	Penetration field
F_L	Lorentz force
J	Current density
F_p	Pinning force
B_{trap}	Trapped field
A	Geometrical constant of HTS bulk
μ_0	Permeability of vacuum
r	Radius of a single-grain HTS bulk
ε	Electromotive force
Φ	Magnetic flux
E	Electric field
μ_r	Relative permeability
ρ	Nonlinear resistivity of HTS materials
E_0	Critical current criterion
$J_c\,(\theta,B)$	Field-dependent critical current density
a	Diameter of the bulk superconductor
t	Thickness of the bulk superconductor
σ_S	Cauchy stress tensor
g	Mass density
u	Displacement
σ_v	Von Mises stress

τ	Shear stress
Φz	Total magnetic flux
E_m	Magnetic energy
v	Space for the magnetic field
R	Resistance
L	Inductance
F_c	Central trapped field of the HTS coil
A_0	Initial field during field decay
i_0	Initial current
i	Current

List of Acronyms

AC	Alternating current
AP	Advanced pinning
BSCCO	Bismuth-Strontium-Calcium-Copper-Oxide
DC	Direct current
FC	Field cooling
FEM	Finite element method
GdBCO	Gadolinium-Barium-Copper-Oxide
HTS	High temperature superconducting
LCR	inductance-capacitance-resistance
LNCMI	Laboratoire National des Champs Magnétiques Intenses
LTS	Low temperature superconducting
MEMEP	Minimum electromagnetic entropy production
MRI	Magnetic resonance imaging
NMR	Nuclear magnetic resonance
PCB	Printed circuit board
PDE	Partial differential equation
PFM	Pulse field magnetization
ReBCO	Rare-earth-Barium-Copper-Oxide
RL	resistor–inductor
SQUID	Superconducting quantum interference device
TSMG	Top-seeded melt growth
YBCO	Yittrium-Barium-Copper-Oxide
ZFC	Zero field cooling

Chapter 1. Introduction

1.1 Research Context

Compact high-field magnets play a crucial role in many modern technologies. They are essential in medical devices such as magnetic resonance imaging (MRI) [1], [2], [3], nuclear magnetic resonance (NMR) [4], [5], [6], transportation systems such as magnetic levitation trains [7], [8], [9], [10], et al. As we look to the future, the demand for these magnets also extends to developing advanced electrical machines [11], [12], [13], [14], [15], [16], [17], particularly for the emerging electric aviation sector [18], [19], [20], [21]. Traditionally, permanent magnets such as NdFeB have been the most common choice due to their high remanence. However, their limitations become evident when faced with the increasing demands of the above advanced technologies. This led to the exploration of low-temperature superconducting (LTS) materials, which can provide high magnetic fields without overheating issues due to their zero electrical resistance at very low temperatures [22], [23], [24], [25].

While LTS materials marked a significant step forward, HTS materials have gained attention since they were discovered [26], [27]. These materials operate at higher temperatures compared to LTS materials and have shown promising superconducting properties. HTS bulk materials especially ReBCO (Re: rare earth elements) have demonstrated unparallel capability in achieving high trapped fields in the past decade [28], [29], [30]. However, HTS bulk materials presented challenges, especially when it came to their size, mechanical strength and manufacturing for larger applications [28], [31], [32]. Besides, with the progress of second-generation (2G) HTS coated conductors or HTS tapes, HTS stacks fabricated by stacking HTS tapes also demonstrated its capability of trapping high field even though their sizes are also very limited [33], [34], [35], [36], [37].

In recent years, HTS-stacked ring magnets, based on 2G HTS tapes, have emerged as promising candidates in the realm of trapped field magnets [38], [39], [40]. This novel

magnet, constructed by stacking separated HTS tapes that have been cut and stretched, was first demonstrated by Lee et al [41]. It presents a potential resolution to the size and mechanical durability limitations associated with HTS bulk and stack materials, paving the way for flexible trapped field magnet design and utilization. It Although preliminary studies have illuminated the field-trapping capability of these HTS tape-based magnets, many of their fundamental characteristics remain underexplored [41]. Furthermore, the field-trapping capability of closed-loop HTS coils, characterized by their more refined shape and quality, remains unconfirmed. The salient challenges stemming from these ambiguities are outlined as follows:

- The magnetization mechanism of the HTS-stacked ring magnet remains unclear. While traditional HTS bulk materials are penetrated from the exterior to the interior during field cooling (FC) or zero field cooling (ZFC) magnetization, the HTS-stacked ring magnet is constructed from parallelly stacked, discrete HTS tapes. These tapes induce separate currents post-magnetization, suggesting that the penetration sequence and current distribution in the HTS-stacked ring magnet could differ significantly from that of HTS bulk materials.

- The field penetration sequence and resultant current distribution in the HTS-stacked ring magnet are ambiguous but crucial, influencing trapped field characteristics. The trapped field by the magnet is determined by the magnitude and distribution of this induced current. Owing to its distinct current layout, the HTS-stacked ring magnet's trapped field may display unique behaviours, impacting the magnet's design and optimization.

- The HTS-stacked ring magnet features a central void. Introducing HTS bulks or stacks within this space to create hybrid HTS-stacked ring magnets could optimize the HTS material volume usage and boost trapped field capabilities. Additionally, the magnetization process specific to these hybrid HTS-stacked ring magnets remains unexamined.

- The (hybrid) HTS-stacked ring magnet, during and post-magnetization, experiences substantial Lorentz forces, which could cause mechanical damage to the magnet. Understanding the mechanical behaviours, especially the force

dynamics and stress-strain relationships, is pivotal for designing and implementing this innovative HTS trapped field magnet. Yet, such analytical work remains unexplored.

- With advances in HTS tape manufacturing and performance, creating low-resistance soldered joints to connect two HTS tapes has become less challenging. HTS tapes can now be readily formed into double-pancake coils with a consistent round shape and guaranteed quality. Theoretically, an HTS double-pancake coil with soldered joints can achieve field trapping with manageable field decay rates. If this is actualized, it presents a significant alternative for HTS trapped field magnets. Both experimental and numerical investigations are essential to validate its feasibility and characteristics.

Therefore, while there have been significant advancements in the field of HTS tape-based trapped field magnets, substantial gaps in knowledge and application remain. These areas of inquiry are not merely theoretical in nature but have practical implications that can have a profound impact on technological and industrial applications. This thesis aims to address some of these gaps. Building upon existing literature and combining innovative design approaches with rigorous analytical methodologies, the research presented delves into the intricacies of (hybrid) HTS-stacked ring magnets and the HTS double-pancake coil, offering insights and potential solutions to the challenges currently faced in the field.

1.2 Research Contributions

This thesis provides the following contributions to knowledge:

- Observation and explanation of central field ascent during field cooling magnetization of HTS-stacked ring magnet. Based on experimental measurement, numerical simulation is utilized to investigate the magnetization mechanism of the HTS-stacked ring magnet. The field ascent during magnetization is explained through numerical analysis.

Chapter 1. Introduction

- Prediction of the possibility of achieving trapped fields higher than applied fields through proper designs of the HTS-stacked ring magnet. This unique property makes the HTS-stacked ring magnet fundamentally different from traditional HTS bulk and stack materials and indicates it can be more energy-efficient in trapped field applications.

- Design, measurement and analysis of hybrid HTS-stacked ring magnets with HTS bulk inserts and stack inserts respectively. The enhancement effect of hybridization on trapped fields has been validated. It is unveiled that the magnetization of a hybrid HTS-stacked ring magnet is divided into 2 stages and the central field ascent scenario is suppressed by HTS inserts.

- Analysis of force dynamics and stress-strain of the (hybrid) HTS-stacked ring magnet and proposing weak points and reinforcement methods for its optimization. The end of the splits of the HTS-stacked ring magnet sees the highest stress concentration and the HTS inserts are subjected to unbalanced Lorentz force during magnetization. The investigation offers a solution for the mechanical reinforcement of the HTS-stacked ring magnet.

- Fabrication, measurement and analysis of the HTS double-pancake coil with a closed loop under field cooling magnetization. The feasibility of using a closed-loop HTS coil to trap fields is validated and it demonstrates the capability of trapping higher fields than applied fields by experiments.

1.3 Thesis Overview

Chapter 2. This chapter commences with an overview of superconductivity and its associated theoretical models. It then discusses prevalent HTS materials and their roles in trapped field applications. Further discussions provide the distinct attributes and inherent challenges of these HTS trapped field magnets. This chapter sets the foundation for the deeper investigations that follow.

Chapter 3: This chapter delves into the production and fortification techniques employed for HTS-stacked ring magnets. It also discusses the simulation strategies for numerically modelling both standalone and hybrid versions of these magnets.

Chapter 1. Introduction

Techniques including H-formulation, mechanical equations, and the homogenized modelling approach, vital for subsequent analyses, are presented.

Chapter 4: This chapter focuses on the magnetization attributes of the HTS-stacked ring magnet. A distinctive central field ascent discerned during empirical tests is investigated using verified numerical models. The analyses unravel the causative factors of the field ascent and suggest the magnet's potential to trap fields exceeding the applied ones.

Chapter 5: The chapter begins with an exploration of the enhanced field-trapping capability realized by integrating HTS inserts into the ring magnets. Subsequent inquiry brings to light a two-phase magnetization procedure and the suppressive influence of the HTS inserts on the central field ascent.

Chapter 6: In this chapter, the mechanical behaviours of the hybrid HTS-stacked ring magnet, under two-sides fixation and wax impregnation scenarios, are analysed. Zones of stress concentration are pinpointed, prompting the proposal of mitigation techniques. The chapter also unveils and clarifies the uneven forces acting on the HTS inserts.

Chapter 7: This chapter introduces the design of the HTS double-pancake coil, highlighting its soldered joints, and probes its potential as a trapped field magnet. Experimental outcomes attest to its ability to trap fields surpassing the applied ones, while subsequent tests underscore the pivotal role of joint quality in coil stability.

Chapter 8: This concluding chapter recaps the contributions of the thesis and points out good spots for more research in the future. Recommendations are proffered, setting a direction for forthcoming research in the domain of tape-based HTS trapped field magnets.

1.4 Publications

- **Hengpei Liao**, Weijia Yuan, Zhiwei Zhang and Min Zhang, Magnetization mechanism of a hybrid high temperature superconducting trapped field magnet, J. Appl. Phys. 133 023902. 2023

- **Hengpei Liao**, Anthony R. Dennis, Weijia Yuan and Min Zhang, Magnetization characteristics of HTS stacked ring magnets with and without HTS stack inserts, J. Appl Phys. 134 083902. 2023

- **Hengpei Liao**, Weijia Yuan and Min Zhang. Mechanical Analysis of Trapped Field HTS-stacked Ring Magnets with and without HTS Stack Inserts, Acta Mech. Sin. 40, 723281 (2024)

- **Hengpei Liao**, Xavier Chuad, Jung-Bin Song, Aleksandr Shchukin, Weijia Yuan and Min Zhang. A novel trapped field magnet enabled by a quasi-operational HTS coil. Submitted to SUST. (2024)

- Tian Lan, **Hengpei Liao**, Muhammad Haseeb Iftikhar, Weijia Yuan, Alexandre Cole, Reda Abdouh and Min Zhang, Multifilament HTS Cables to Reduce AC Loss Proof of Concept Experiments and Simulation, IEEE Trans. Appl. Supercond. 20. 5901512 (2023)

Chapter 2. Superconductivity and Trapped Field HTS Magnets

2.1 Introduction

Superconductivity, a phenomenon where materials exhibit complete absence of electrical resistance and perfect diamagnetism below a specific temperature, has fascinated condensed matter physicists since its discovery in 1911 by Heike Kamerlingh Onnes [42]. This seminal observation, made in mercury chilled to near absolute zero, propelled quantum mechanics and materials science into novel territories. While mercury was the initial material to reveal its superconducting nature, further research identified a rich array of superconductors, each possessing unique properties and potential uses. The superconductors were classified into two main types: LTS materials operating near liquid helium temperatures, and HTS materials functioning closer to the boiling point of liquid nitrogen.

For years, LTS held sway, marking their presence in medical imaging, particle accelerators, and magnetic field generation [4], [6], [22], [23], [43], [44], [45], [46]. However, their dependence on extreme cold introduced challenges and inflated operational costs.

The 1986 discovery of copper-oxide-based HTS, superconducting at temperatures significantly higher than LTS, changed the game [47], [48]. These superconductors not only minimized cooling demands but also exhibited unparalleled magnetic properties, particularly in magnetic field trapping [49]. From this HTS innovation, trapped field magnets emerged. These power-efficient magnets, maintaining strong magnetic fields without ongoing energy input, promise a revolution in fields from NMR devices to emission-free electric aviation [43], [50], [51], [52]. The intricate science behind trapped field magnets, especially when using HTS, is a fusion of

theoretical and applied research. The magnetization techniques, designs, and applications reflect the synergy of these two domains.

This chapter offers a comprehensive overview of the development of superconductivity and its integration with trapped field magnets. Beginning with the foundational discoveries and classifications based on temperature benchmarks and magnetic characteristics, this chapter progresses to discuss the mathematical models underpinning superconducting behaviours. Subsequent sections detail the specificities of HTS materials, elucidating their distinct properties and their significance in trapped field magnet technology.

2.2 Superconductivity and Superconductors

When cooled below their critical temperatures, materials known as superconductors undergo a transition into superconducting states. These states are characterized by two distinctive properties: zero electrical resistance and the Meissner effect (or diamagnetic effect) [53]. As indicated, numerous materials exhibit superconductivity when they are brought below their respective critical temperatures. Notably, under specific extreme conditions, some of these materials can transition to superconducting states even near room temperature. Superconductors can be broadly categorized based on their transition temperature into low-temperature superconductors and high-temperature superconductors. Another classification criterion is their underlying superconducting states, where they are divided into Type-I and Type-II superconductors [54], [55], [56]. In the subsequent sections, the characteristics of these superconductors will be delved deeper. Given that the primary focus of this thesis is on Type-II superconductors, a detailed introduction to the relevant theoretical models will also be provided.

2.2.1 Low-Temperature Superconductors and High-Temperature Superconductors

Based on critical temperatures, superconductors can be classified as low-temperature superconductors and high-temperature superconductors. LTS require extremely cold temperatures, typically that of liquid helium, to maintain their superconducting state. LTS materials primarily fall into the category of elemental superconductors such as Lead (Pb, 7.2 K) [57], Niobium (Nb, 9.3 K) [58], Technetium (Tc, 7.8 K) [59], Mercury (Hg, 4.15 K) [60], Tin (Sn, 3.7 K) [61], Aluminium (Al, 1.2 K) [62] or simple intermetallic compounds such as Niobium-Titanium (NbTi, 10 K) [63] Niobium-Tin (Nb_3Sn, 18 K) [64]. Currently, most MRI machines and particle accelerators are using LTS materials, especially NbTi and Nb_3Sn due to their mechanical properties, ease of wire production and joint fabrication [65], [66], [67], [68]. As shown in Fig.2.1, LTS wires and cables can be manufactured in different structures and forms to meet variant requirements and applications [69]. However, except for higher cooling requirements, LTS materials have a limited critical magnetic field compared with HTS materials, meaning they can be used only up to certain magnetic field strengths before losing their superconducting state. This poses a challenge for high-field applications.

Figure 2.1: Products based on LTS materials

High-temperature superconductors manifest superconducting properties at elevated temperatures compared to low-temperature superconductors. Although termed "high temperature", these temperatures, while still within the cryogenic range, often exceed the boiling point of liquid nitrogen (77 K). This distinction significantly influences the economics and practicality of cooling mechanisms.

Chapter 2. Superconductivity and Trapped Field HTS Magnets

The inception of this category began in 1986 with the ground-breaking discovery of copper-oxide superconductors by Georg Bednorz and K. Alex Müller [26], marking the dawn of the high-temperature superconductors era. By 1987, Yttrium Barium Copper Oxide (YBa2Cu3O7 or YBCO) emerged as a leading HTS material, showing superconducting capabilities at temperatures above the boiling point of liquid nitrogen [48]. This critical discovery marked a significant turning point in the field of superconductivity, enabling the use of cost-effective and readily available liquid nitrogen for cooling, amplifying superconductivity's potential in technological applications. Current research distinguishes two primary categories of HTS materials: cuprate superconductors [70], [71], [72], [73], [74], [75] and iron-based superconductors [76], [77], [78], [79]. The cuprate family encompasses ReBCO (where "Re" denotes rare earth elements such as Yttrium (Y) [80], Gadolinium (Gd) [81], Samarium (Sm) [82], and Neodymium (Nd) [83]) and BSCCO variants [84], [85], [86], [87]. The focus of this thesis centres on cuprate HTS materials, as exemplified by the prototypes depicted in Fig.2.2.[88]

Figure 2.2: HTS ReBCO bulk materials (left) and HTS Bi-2333 tube (right)

Iron-based superconductors, a more recent discovery from 2006 [89], have gathered attention owing to their novel properties and appreciable critical temperatures, some reaching 56 K [90]. Defined by their stratified structure featuring iron-arsenide or iron-chalcogenide layers, these superconductors exhibit pronounced sensitivity to impurities and defects, occasionally introducing hurdles in their application [91]. Nevertheless, the intricacies and potential applications of iron-based superconductors

pave the way for fresh insights into unconventional superconductivity and foretell a promising horizon in their practical utility [92].

2.2.2 Type-I and Type-II Superconductors

According to the behaviours in the presence of external magnetic fields, superconductors can be classified into two types: Type-I and Type-II [93]. Generally, Type-I superconductors are perfect diamagnets. They show a complete expulsion of magnetic fields when transitioning to the superconducting state. This phenomenon is the Meissner effect [53]. Once the applied field exceeds the critical field (B_c), the superconductivity of Type-I superconductors will disappear and the material transitions back to its normal state. As shown in Fig.2.3, Type-I superconductors have a clear one B_c. The majority of Type-I superconductors are elemental metals, such as mercury (Hg) [60], lead (Pb) [57], and tin (Sn) [61].
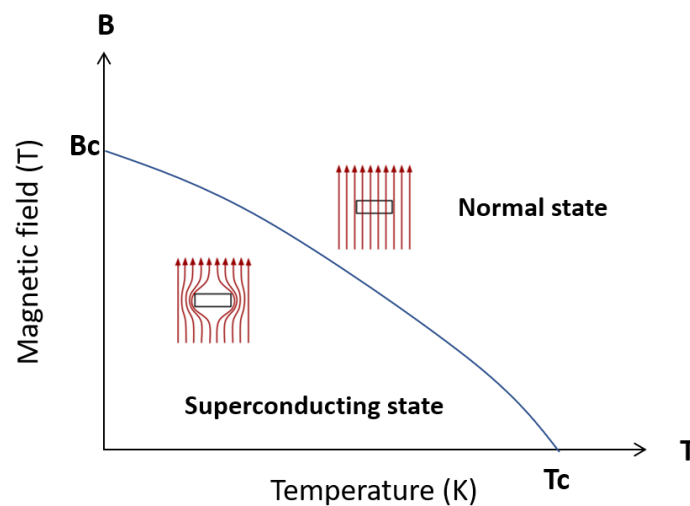
Figure 2.3: State transition of type-I superconductors

Type-II superconductors, on the other hand, exhibit similar behaviour by completely excluding a magnetic field below a lower critical field value and becoming normal again at an upper critical field. However, when the magnetic field is between these lower and upper critical fields, the superconductor enters a "mixed state" where there is partial penetration of flux as shown in Fig.2.4 [94], [95]. This partial penetration occurs in the form of "vortices" - tiny magnetic flux tubes [96]. In this situation, the

material as a whole continues to have zero resistance as current flows by the easiest path and as there are superconducting regions, and current can still flow without energy loss. It must be noted, however, that if the vortices move, they will dissipate energy. So, to create high critical current superconductors, the resistive motion of flux vortices should be pinned more rigidly [96], [97], [98]. Type-II superconductors include many alloys and complex materials. Famous examples are the high-temperature superconductors including previously mentioned ReBCO, and the family of iron-based superconductors.
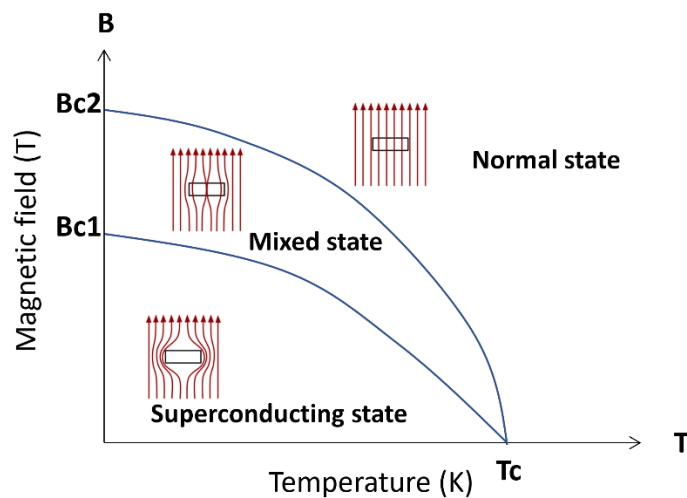
Figure 2.4: State transition of type-II superconductors

2.2.3 Theoretical Models of Type-II Superconductors

Understanding the behaviours of Type-II superconductors, especially in the presence of magnetic fields, is crucial for their technological applications. Over the years, several theoretical models have been proposed to explain the peculiarities of these materials. This section presents an overview of the key theoretical models that have significantly contributed to our understanding of Type-II superconductors.

Ginzburg-Landau Theory:

The Ginzburg-Landau theory is a phenomenological theory that describes the transition between the superconducting and normal states, especially near the critical temperature. A central feature of this theory is the introduction of an order parameter,

which describes the macroscopic quantum mechanical wave function of the superconducting electron pairs, commonly called Cooper pairs [99]. The theory provides a framework for describing how this order parameter varies in space and time. The Ginzburg-Landau parameter κ, which differentiates between Type-I and Type-II superconductors, is another crucial outcome of this theory. When $\kappa > 1/\sqrt{2}$, the material behaves as a type-II superconductor, and when $\kappa < 1/\sqrt{2}$, it's a Type-I superconductor [100], [101].

Abrikosov Vortices:

In the context of Type-II superconductors and based on the Ginzburg-Landau theory, Abrikosov predicted the existence of a lattice of vortices [102]. Each vortex is a tiny whirlwind of supercurrent that surrounds a core where the superconducting order parameter is suppressed and allows some magnetic flux to penetrate. The arrangement of these vortices in an ordered lattice prevents large-scale magnetic flux penetration, thus allowing the superconductor to maintain its superconducting state even in high magnetic fields as shown in Fig. 2.5 [103].
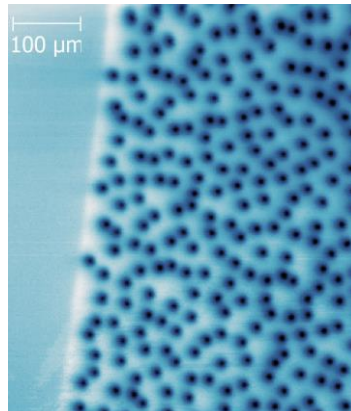
Figure 2.5: Vortices in a YBCO film imaged by scanning SQUID microscopy

Bean's Critical State Model:

Charles P. Bean proposed a model that provides an empirical description of the behaviour of magnetic flux lines within type-II superconductors exposed to varying magnetic fields [104]. Central to this model is the account for the hysteretic magnetization behaviour commonly observed in type-II superconductors. At its core, the Bean model suggests that when the external magnetic field undergoes changes, the

supercurrent within the superconductor adjusts to maintain a constant magnetic flux density. This continues until the supercurrent reaches a critical threshold. Beyond this value, the superconductor becomes resistive.

For visualization, consider Fig.2.6, where an external field H is applied to a superconducting slab. For applied fields such as 0, H*/2, H*, and 2H* parallel to the slab's surface, it's assumed that the critical current density Jc remains unaffected by these fields. When an external field H_0 is applied and subsequently removed, the superconducting slab's surface experiences an electromotive force (emf) opposite to what was felt during the field's increase. This leads to a reversal in the direction of the surface current. At a zero external field, as depicted in Fig. 2.7, each surface of the slab carries two opposing currents, resulting in a cancelling effect [104], [105].
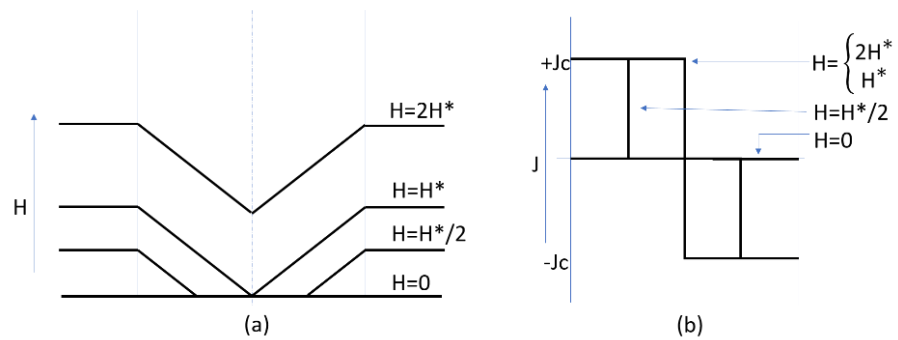
Figure 2.6: A plot of local fields and current density in an HTS slab after applying fields 0, H*/2, H*, and 2H* parallel to the slab's surface
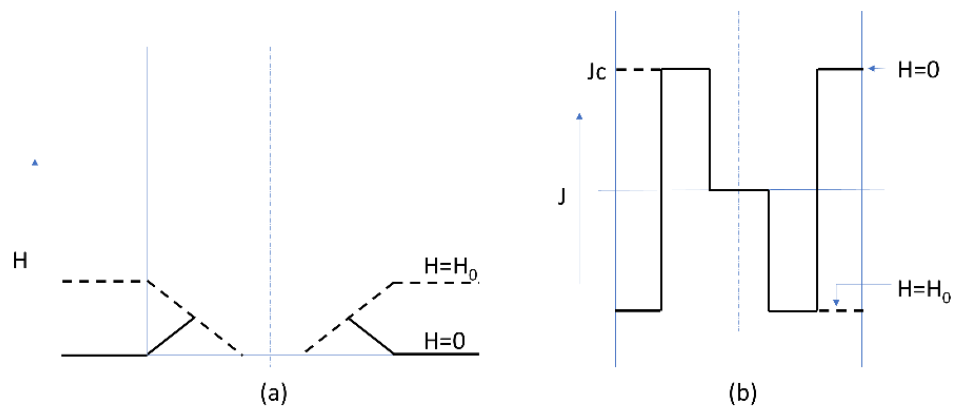
Figure 2.7: A plot of local fields and current density in an HTS slab after a field H_0 has been applied and removed

Flux Pinning:

Flux pinning, a crucial phenomenon in the domain of superconductivity, refers to the immobilization of magnetic vortices due to interactions with material defects within the superconductor. These defects, spanning from grain boundaries and point defects to various microscopic imperfections, serve as 'anchors' or 'pinning centres' that effectively 'trap' the vortices [106], [107], [108].

As introduced in the section on Abrikosov Vortices, magnetic flux lines enter the superconductor as quantized vortices when in a superconducting state. In the absence of pinning, these vortices tend to move under the influence of an external current or magnetic field, leading to energy dissipation and a subsequent loss of the superconducting state.

To understand the effectiveness of flux pinning, one can evaluate the critical current density. This represents the maximum current density a superconductor can sustain without resistance due to vortex movement:

$$-F_L = -B \times J = F_p \tag{2.1}$$

Where F_L is Lorentz driving force, B is magnetic flux, J is transport current density and F_p is the pinning force.

The efficiency of flux pinning plays a pivotal role in determining the current-carrying capacity of a superconductor, particularly in high magnetic field applications. The robustness of the superconducting state and the prevention of vortex lattice melting or rearrangement hinge upon the effectiveness of these pinning centres. Consequently, deliberate introduction and optimization of specific types of pinning centres in superconducting materials have been a focus of ongoing research, aiming to enhance their performance in practical applications [109], [110].

Flux Creep and flux jump:

Even when vortices within a superconductor are pinned, thermal activation can cause them to move slowly. This subtle motion of vortices is termed "flux creep." The movement induces a minor resistive voltage, making the superconductor less than perfectly superconducting [111]. This effect intensifies with increasing temperature

and becomes less pronounced as the material approaches absolute zero. It poses challenges to the practical performance of superconducting devices, particularly at higher temperatures.

Flux jumps are abrupt and uncontrolled movements of magnetic flux lines within a superconductor. They are often caused by thermomagnetic instabilities when a certain critical current or temperature threshold is exceeded [112]. This sudden change can lead to a noticeable resistive voltage, momentarily disturbing the superconducting state. Flux jumps are often characterized by their unpredictable nature and can lead to detrimental effects on superconducting device performance, requiring careful management and design considerations.

2.3 HTS Materials for Trapped Field Magnets

Within the sphere of trapped field applications, both HTS bulk materials and HTS stacks, crafted using HTS tapes, have been extensively researched and recognized. This section elucidates the foundational attributes and intrinsic properties of ReBCO HTS bulk materials, as well as commonly used commercial HTS tapes.

2.3.1 HTS Bulk Materials

Among previously introduced HTS materials, YBCO is a paramount development in the realm of bulk superconducting materials. Its fabrication, especially when high-quality large single grains are desired, often employs the top-seeded melt growth (TSMG) method [113], [114], [115]. This technique utilizes a seed crystal to promote controlled growth and texture in the melting process, resulting in bulk superconductors with exceptional magnetic properties. The precise control of parameters during the TSMG process, such as cooling rates and seeding orientation, plays a critical role in determining the final quality of the YBCO material [116]. To enlarge the size of the YBCO bulks, multi-seed TSMG can be used as shown in Fig. 2.8 [117], [118].
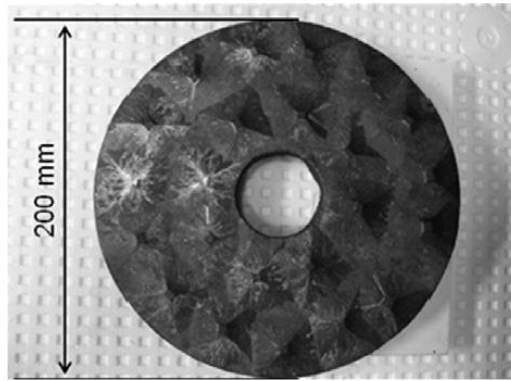
Figure 2.8: A large muti-seeded YBCO bulk superconductor

YBCO is featured for its notable transition temperature of approximately 92 K, which facilitates its operation in liquid nitrogen cooling. Furthermore, its remarkable ability to trap magnetic fields has situated it as a foundational element for advanced magnet systems. However, intricacies accompany its usage; the inherent brittleness of YBCO can be a concern, especially in applications demanding mechanical resilience [119]. Yet, its prominent role in the technological arena is undeniable, with widespread applications ranging from magnetic levitation systems to advanced HTS machines [114], [120], [121], [122], [123], [124], [125], [126].

While other HTS materials such as Bi-2223, Bi-2212 and MgB2 can also be processed as bulk materials, their superconducting performance tends to lag that of ReBCO materials [127], [128], [129], [130], [131]. Hence, they are not elaborated upon extensively in this context.

2.3.2 HTS Tape Materials

In the progressive landscape of superconducting technology, coated conductors, commonly termed as second-generation (2G) high-temperature superconducting tapes, have garnered substantial attention [132], [133], [134], [135]. These tapes employ a multi-layered structure, generally consisting of a metallic substrate, a buffer layer to accommodate lattice mismatches and prevent diffusion, and an outer layer of the superconducting material. Fig.2.9 demonstrates a typical structure of Fujikura 2G HTS tapes [136], [137].

Stabilizer [Cu plating] 20 µm
Protection layer [Ag] 2 µm
Superconducting layer [ReBCO] 2 µm
Buffer layer [MgO, etc.] 0.7 µm
Substrate
[Hastelloy]
75/50 µm
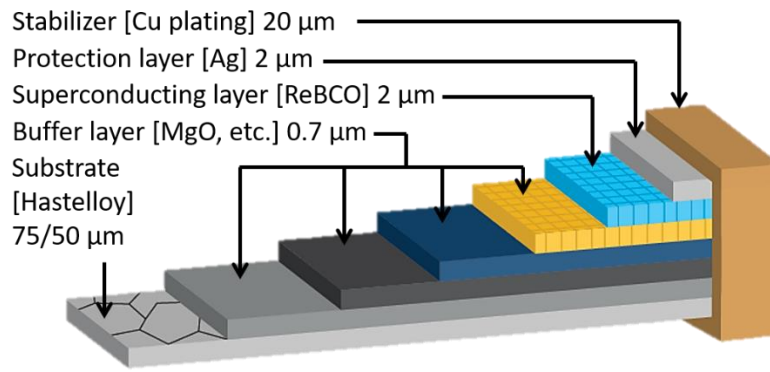
Figure 2.9: A typical structure of Fujikura HTS tapes

The layered structure of these tapes is designed to ensure optimal performance. For instance, the buffer layers mitigate detrimental interactions between the superconductor and the substrate, preserving the superconducting properties. Meanwhile, the superconducting layer itself, often YBCO or similar material, provides the tape with the desired high-temperature superconducting attributes.

Despite their many advantages, challenges persist in the domain of coated conductors. Their production requires precision and can be more costly than other methods. Moreover, the interface quality between layers is crucial and can significantly impact the overall performance of the tape. Nevertheless, with their applications in modern electronics, energy, and transportation sectors, 2G HTS tapes symbolize the promising horizon of superconducting technology [138], [139], [140], [141], [142], [143].

Building on HTS coated conductor technologies, an array of HTS cables has been conceptualized. Notable examples include the Coaxial HTS Cable [144], [145], Roebel cable [146], [147], Conductor on Round Core (CORC) cable et al [148], [149]. These innovations have been extensively explored and harnessed for both high current transmission and high-field applications.

2.4 Magnetization Approaches and Traditional Trapped Field HTS Magnets

2.4.1 Magnetisations of Trapped Field Magnets

Field Cooling and Zero Field Cooling Magnetization

Field cooling (FC) and zero field cooling (ZFC) magnetization techniques are fundamental approaches to inducing magnetization in superconductors [150]. The difference between the two methods hinges on the external magnetic field's state when the sample is cooled.

In the FC process as shown in Fig. 2.10, a superconductor is first cooled down to its operating temperature while an external magnetic field is applied. Once the superconductor reaches below its critical temperature, the magnetic field is then removed. The magnetic flux lines, now trapped within the superconductor, result in the desired magnetization [113]. Notably, during the external field's withdraw, occurrences of flux jumps and temperature spikes can happen if the removal rate is overly rapid or if there's insufficient cooling power.
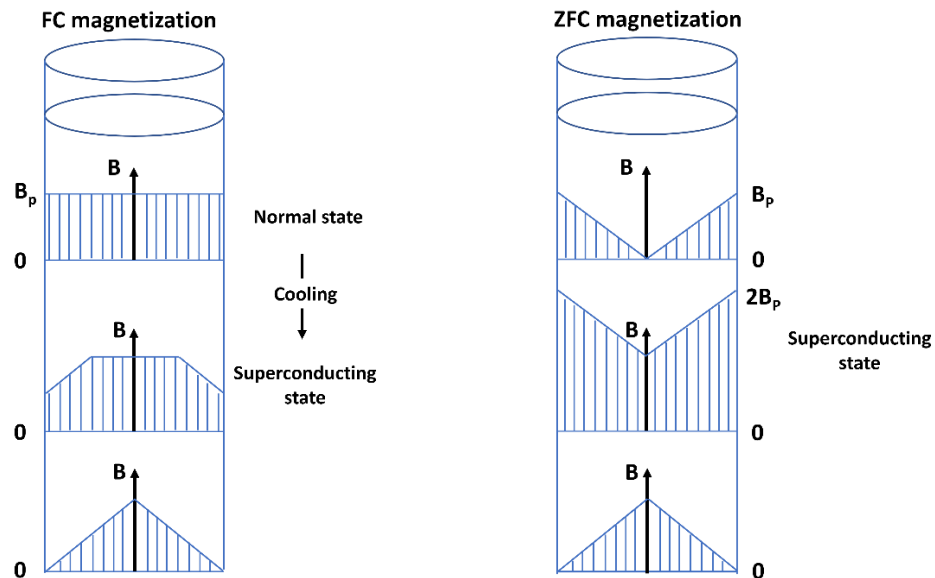
Figure 2.10: FC and ZFC bulk superconductor magnetisation techniques

using the Bean model approximation

On the contrary, in the ZFC process, the superconductor is cooled in the absence of an external magnetic field as illustrated in Fig. 2.10. Once the desired temperature is reached, an external magnetic field is applied. This method relies on the superconductor's intrinsic ability to expel magnetic fields (due to the Meissner effect) and then introduce flux lines when the field exceeds a certain threshold. This behaviour, characteristic of Type-II superconductors, is often elucidated using the Bean model.

Both procedures present distinct advantages and challenges. ZFC typically provides a deeper understanding of the superconductor's innate characteristics and its interplay with external fields. Conversely, FC usually results in a superior trapped field, explaining why most trapped field milestones have been achieved using FC magnetization techniques.

Pulsed Field Magnetization (PFM)

PFM stands out as a distinct method for magnetizing superconductors, particularly when swift magnetization is necessitated. Contrary to the continuous magnetic field application in FC and ZFC, PFM introduces a brief, intense pulse of a magnetic field. This strategic pulsing ensures deep penetration of magnetic flux lines into the superconductor. Upon cessation of the pulse, the superconductor preserves a notable portion of the introduced magnetic field, resulting in its magnetization [151], [152], [153]. Nevertheless, the magnetic field trapped through PFM typically falls short of the magnitudes attained by ZFC or FC, especially at lower operational temperatures. This discrepancy arises predominantly from the pronounced temperature elevation, attributed to the rapid flux vortex dynamics within the superconductor during the PFM process. Interestingly, at elevated operational temperatures, specifically around 77 K, the fields trapped through PFM closely rival those of the FC method.

2.4.2 Trapped Field HTS Bulk Magnets

Trapped field stands as the principal application and focus of study for HTS bulk materials. Given that these materials exhibit no resistance in their superconducting state, any magnetic field trapped within the HTS bulk remains stable, contingent on

the temperature being sustained. Owing to this enduring retention of magnetic field, it's occasionally referred to as a "permanent HTS trapped field magnet." As mentioned previously, ReBCO materials are most used in field trapping applications. Bulk YBCO disks can trap a large field due to flux pinning or induced supercurrents flowing persistently in the pellet. The trapped field (B_{trap}) is given by [115]:

$$B_{trap}=A\mu_0 J_c r \qquad (2.2)$$

Where A is a geometrical constant, μ_0 is the permeability of the vacuum, and r is the radius of a single-grain HTS bulk. Consequently, there is a direct correlation between the grain size and the trapped field: as the grain size escalates, so does the trapped field. However, with an augmented trapped field, the disk is subjected to intensified electromagnetic forces, which can occasionally result in fractures. Notably, the mechanical characteristics of YBCO display anisotropy, albeit with minimal temperature dependence. The axial tensile strength ranges between 5–10 MPa, while the strength perpendicular to the axis lies in the ballpark of 20–30 MPa [154].

Enhancing the mechanical strength to achieve higher trapped fields has been a key point of numerous studies. For large-grain samples, the fracture strength has been noted to increase from around 1 MPa to nearly 10 MPa with the inclusion of Ag [155]. However, this augmentation through silver is insufficient to guarantee consistent mechanical stability or elevated trapped fields. Besides, metal ring encapsulation has been adopted to bolster the mechanical attributes [156].

Impregnation with resin also proves efficacious in enhancing the mechanical resilience of HTS bulks [157]. When bulk discs undergo vacuum impregnation with epoxy, the resin seeps into the bulk via surface fissures and fills internal gaps, as depicted in Fig. 2.11 [157]. Moreover, the introduction of a thin-wall design — where the HTS bulk undergoes melt-processing with deliberate holes that are subsequently filled with epoxy resin — significantly enhances tensile strength, as illustrated in Fig.2.12 [32]. Leveraging these reinforcement strategies, the trapped field achieved by HTS bulk materials can surpass 17 T [115]. Presently, the record for the highest trapped field by HTS bulk materials stands at 17.6 T at 25 K, achieved using two 24.15 mm diameter GdBCO bulks, as showcased in Fig.2.13 [158].
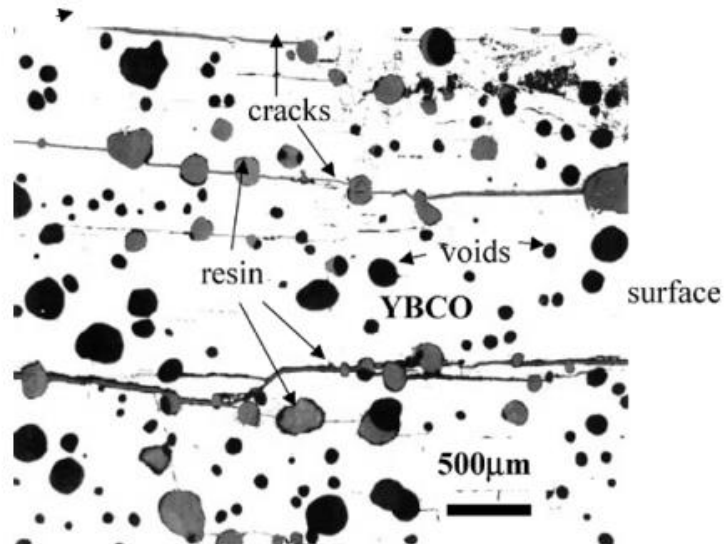
Figure 2.11: Optical micrographs for cross-section of bulk superconductor after resin impregnation
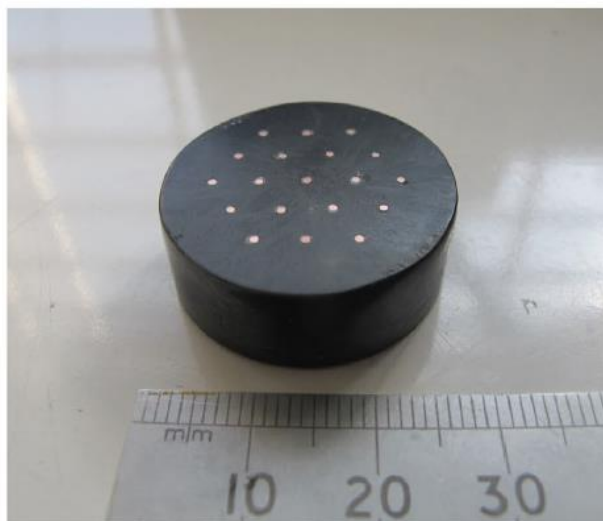
Figure 2.12: Single grain thin- wall YBCO sample with artificial holes filled with copper wires and solder to minimize stress concentration
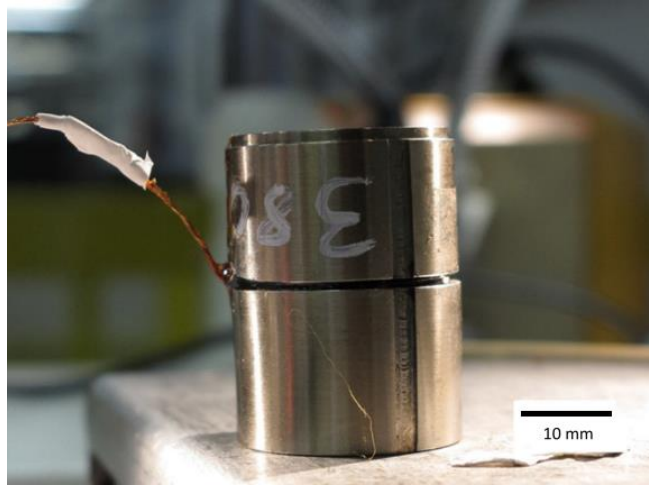
Figure 2.13: Two GdBCO bulk samples reinforced with stainless steel rings

2.4.2 Trapped Field HTS Stack Magnets

As mentioned previously, progress in HTS tape manufacture has remarkably enhanced the performance of commercial HTS tapes in both electromagnetic and mechanical aspects. Generally, HTS stacks are fabricated by cutting and stacking HTS tapes. To improve the thermal conductivity, some studies introduce soldering layers into HTS stacks [33]. Compared to HTS bulk materials, HTS tapes have superalloy substrates, which account for more than 85% of the volume fraction, and have a very high tensile strength, which means no external mechanical reinforcement is needed to counter Lorentz forces at high trapped fields [159]. Besides, the superconducting properties are generally consistent throughout the volume of the stack and defects in individual layers are smoothed out in the trapped field profiles. The silver stabilizer layer on top of the HTS layer provides thermal stability which helps dissipate heat generated inside the stack and suppresses flux jumps [160]. However, due to the restrictions on the width of commercial HTS tapes, the size of HTS stacks is limited. By far, the largest diameter of HTS stacks is 34.4 mm using 46 mm wide AMSC tapes as shown in Fig.2.14 [159]. This design employed a hybrid configuration combined with 12 mm wide SuperPower HTS tapes. It successfully trapped 17.7 T at 8 K. The present highest trapped field by HTS stacks is 17.89 T at 6.5 K with 200 sheets of $EuBa_2Cu_3O_7$ tapes with $BaHfO_3$ nanorods as shown in Fig.2.15 [33].
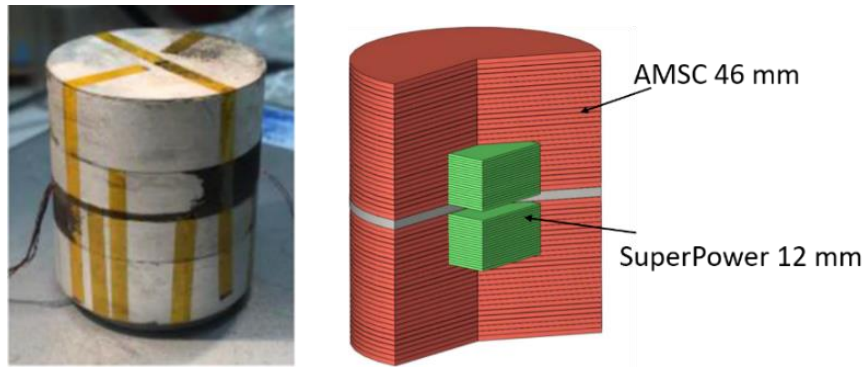
Figure 2.14: Hybrid HTS stacks with 34.4 mm diameter

Figure 2.15: HTS stacks that trapped 17.89 T at 6.5 K

2.5 Conclusion

This chapter provides a foundational overview of superconducting materials, with particular emphasis on theoretical models related to Type-II superconductors. It delves deeply into prevalent HTS materials and their pivotal roles in trapped field applications, encompassing aspects of their fabrication techniques and magnetization strategies. A selection of representative examples of trapped field HTS magnets is showcased, elucidating their distinctive attributes and associated challenges. In essence, this chapter establishes a critical backdrop for the subsequent discussions and explorations.

Chapter 3. HTS-Stacked Ring Magnet and Simulation Methodology

3.1 Introduction

As mentioned previously HTS bulk materials excel in magnetic field trapping but face challenges. Large ReBCO HTS bulks are difficult to produce due to slow growth and stringent controls. Their mechanical strength, often just tens of MPa, is another concern. Even though there are ways to fix these issues, it's still hard to use them in real-world situations. Similarly, traditional HTS stacks, limited to a 46 mm width from commercial tapes, have restricted engineering applications. To meet the requirements for large-scale applications such as HTS machines and NMR, it is necessary to develop HTS trapped field magnets with larger dimensions and a strong, stable magnetic field.

Given these challenges and the development of 2G HTS tapes, new concepts for tape-based HTS trapped field magnets are continually being explored. HTS coils with soldered joints can form a closed loop which theoretically has the potential to be utilized as HTS trapped field magnets. The width of the tapes and turns of the coil can decide the size of the magnet, which offers flexibility in the dimension. However, due to the physical properties of HTS wires or tapes, it is challengeable to fabricate perfect superconducting joints as achieved in low temperature superconductors [161]. In 2014, Yeonjoo Park et al demonstrated the first HTS joint with a resistance as low as $10^{-17}\Omega$ which was regarded as the world's first high temperature superconducting joint [162]. However, the critical current of the joint can only achieve 84 A in liquid nitrogen. Besides, the process of fabricating this joint is very complicated and time-consuming. It involves laser-drilling, stabilizer removing as well as oxygenation annealing process that lasts up to 350 hours. More recently, advancements have been made in the technology for 2G HTS tape joints. Higher critical currents and quicker soldering processes with mechanical pressure and heating have been demonstrated, and the

resistance of a ReBCO joint can be controlled at $5.3 \times 10^{-13} \, \Omega$ under a self-field at 30 K [163], [164], [165]. Other innovative HTS joint technologies including bridge-type joints [166], demountable joints [167], lap-type joints [168], joints with bulk superconductors [169], ultrasonic welding technique [170], BSCCO joints [171] et al have all demonstrated the possibility of fabricating joints connecting HTS tapes or wires with very low resistance. However, for the HTS trapped field, resistance in the circuit means the trapped field will inevitably diminish over time and Joule heat can appear during the magnetization process, while lower critical current at the joint area can further constrain the magnitude of the trapped field. These issues are considerable for the application of HTS trapped field magnets.

To fabricate HTS tape-based magnets without losses on the joints, the concept of the "wind-and-flip" method was proposed in which the HTS tape was cut through the middle and the two ends were intact [172]. Therefore, a current loop can be formed within a single tape without any additional joints. After the "wind-and-flip" process, more turns can be realized to form a pancake coil. However, the flip process and long ends of this design made the coil mechanically weak, and the coil was destroyed after the first critical current. Except for the "wind-and-flip" process, there is another way to achieve a persistent current in an HTS tape without joints by cutting and stretching an HTS tape through the centre as shown in Fig.3.1 [173]. Predicated on this approach, it is theoretically feasible to fabricate an HTS closed circuit with an exceedingly large radius, provided that the individual superconducting tape is of sufficient length. Since the original HTS tape is cut through the centre which causes some damage on the edge of the incision, the critical current of each closed loop is slightly less than half of the critical current of the original tape [39].
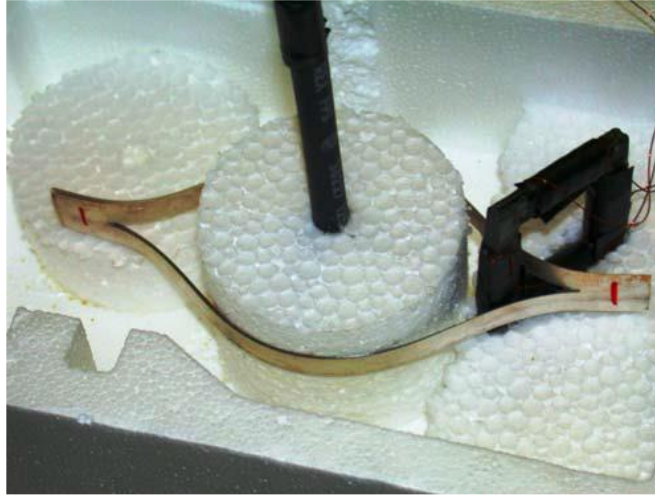
Figure 3.1: An HTS tape after cutting and stretching

To increase the circular current, many single closed circuits can be stacked together in parallel and normally called HTS ring-shape magnets or HTS-stacked ring magnets [38]. As illustrated in Fig.3.2, the HTS magnets formed by stacking cut HTS tapes are more robust and compact since each HTS tape is independently stacked together and the flip process is not required. Unlike traditional electromagnets which need external power supplies for excitation, HTS-stacked ring magnets are normally magnetized by field cooling processes due to their superconducting characteristics. In contrast to HTS bulks and stacks, HTS-stacked ring magnets produced with long commercial 2G HTS tapes can be made in various sizes which is its distinct advantage. The length of the tapes and central incision determine the size, while the number of stacked tapes can affect the thickness of HTS-stacked ring magnets. The shape of the HTS-stacked ring is adjustable due to the flexibility of HTS tapes and the external sample holders for the magnets play an important role in the shapes.
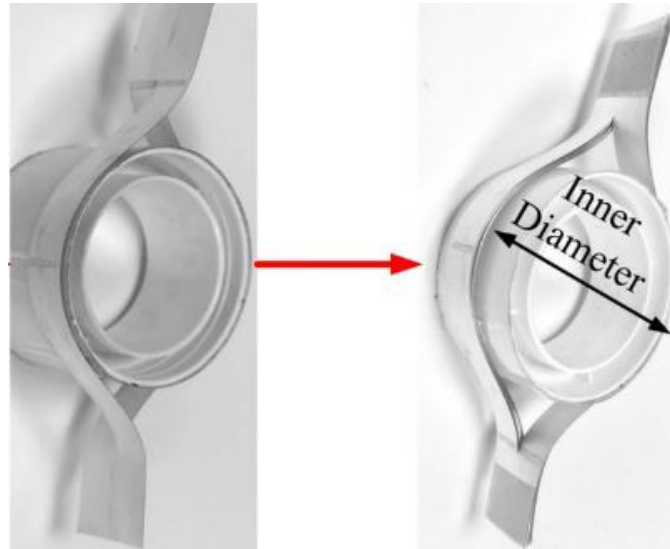
Figure 3.2: Stacking cut HTS tapes to form a HTS magnet

In 2017, our group fabricated a simple HTS-stacked ring magnet sample by stacking 9 HTS tapes, each 15 cm in length. The magnetization and demagnetization mechanisms were investigated at 77 K regarding different magnetization methods including field cooling, zero field cooling and multiple pulse field cooling [38]. The results showed that the field cooling method can achieve a larger trapped field more effectively while zero field cooling study revealed the different magnetization zones in the sample. Although the trapped field by multiple pulse field cooling is very small, it verified the feasibility of applying multiple pulse field cooling for the magnetization of HTS-stacked ring magnets. For the demagnetization, significant demagnetization was observed in the first cycle and the field decay rate was then slowed down due to the shielding effect of the independent outermost HTS layers.

Inspired by the outcomes of this study, we further investigated the trapped field performance of HTS-stacked ring magnets under lower temperatures (25 K). To achieve a higher trapped field, 200 HTS tapes with 12 mm in width were cut and stacked firmly in a brass sample holder. The sample is composed of two layers, top and bottom, with each layer formed by stacking 100 HTS tapes. In the centre of the brass holder, a hollow cylinder supports the middle of the magnet, thereby forming a ring shape. Paraffin wax mixed with aluminium nitride powder was first applied to impregnate the HTS-stacked ring magnet for better thermal conductivity and

mechanical stability. This HTS-stacked ring magnet achieved a trapped field of 4.6 T through field cooling process with a 5 T applied field [39].

For the HTS-stacked ring magnets, there are two issues that affect the trapped field performance. One is the inefficient spatial utilization because of the hollow centre area, and another is the tilted trapped field distribution due to the asymmetric geometry of the HTS-stacked ring magnets. For the tilted trapped field distribution, J. Shi et al. tried to insert a hollow Bi-2223 tube in the centre of an HTS-stacked ring magnet replacing the central supporting cylinder [174]. The two Bi-2223 tubes were cut at angles of 15 and 20 degrees respectively and two different placement strategies were implied for comparison of the compensation effect for the tilted trapped field as shown in Fig. 3.3. The results demonstrated that inserting the HTS tubes can compensate the field declination to some extent.
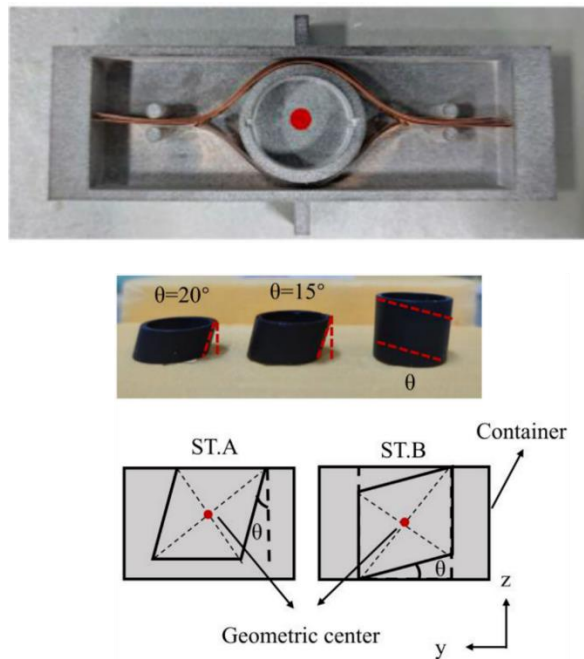
Figure 3.3 ring-shape HTS magnet with Bi-2223 tubes

To further enhance the field trapping capability, the idea of filling the central space with additional HTS materials came naturally. J Sheng et. al proposed hybridizing round HTS stacks with HTS-stacked rings and "wind-and-flip" coils respectively to increase the overall magnet size and magnetic field strength [175]. The results showed

that the inserted HTS stacks can enhance the maximum trapped field and improve its uniformity. However, studies about hybrid HTS-stacked ring magnets are still constrained to liquid nitrogen temperatures and further studies with in-depth investigations towards the magnetisation mechanism of this emerging HTS trapped field magnet design.

Overall, it is evident that for the HTS-stacked ring magnets and heir improved hybrid counterparts, despite some pertinent research having been conducted and a level of understanding attained, there remains a substantial need for further exploration and in-depth investigation, especially the special magnetization mechanism, trapped field performance at lower temperature and the mechanical behaviour due to unique fabrication process.

This chapter consists of two parts. The first part is about a new HTS-stacked ring magnet design with enhanced mechanical support and thermal conductivity. The design allocates a central space for the HTS inserts, thereby facilitating the transformation into a hybrid HTS-stacked ring magnet. The second part of this chapter concentrates on the methodology involved in the numerical calculation of the HTS-stacked ring magnet. Electromagnetic simulation and mechanical analysis computations are introduced in this chapter. Another tape-based HTS trapped field magnet, HTS coils with soldered joints, will be introduced in Chapter 7.

3.2 HTS-Stacked Ring Magnet Fabrication

An HTS-stacked ring magnet normally consists of two parts: prepared HTS tapes and a well-designed sample holder. In studies with a smaller number of HTS tapes, the samples are simply fixed by clamping two ends of tapes after cutting and a cylinder in the centre is used to create the central ring-shaped area [174]. Since the magnitude of trapped fields in the studies is low (less than 1 T), samples can be fine during tests. However, when the applied magnetization field or trapped field is increased and the temperature is lower than 77 K, the deformation and stress of the sample caused by Lorentz force need to be considered.

In the study of this thesis, each of the HTS-stacked ring magnet samples comprises more than 160 tapes. They are magnetized at the temperature of 25 K with applied fields exceeding 3T. This implies that the samples will be subject to significant forces during and after magnetization. Additionally, research concerning the hybrid HTS-stacked ring magnet is also a requirement for this thesis. Therefore, a specific design for the sample was devised in this thesis.

3.2.1 Design of HTS Ring Magnet with Enhanced Reinforcement

This thesis emphasizes two-layer HTS-stacked ring magnets. Fig. 3.4 depicts two prevalent arrangements: on the left, the two HTS-stacked ring layers are layered in the same direction; on the right, they are oriented in opposite directions. As mentioned above, HTS-stacked ring magnets suffer from tilted trapped fields due to one side of the ring being higher than the other. In the first arrangement, the trapped field inclination issue can be worsened since the unbalance is enhanced. In the second configuration, the opposite stacking can reduce the unbalanced field distribution to some extent, especially in the centre of the ring magnet. Therefore, this one is chosen for the HTS-stacked ring magnet study in this thesis. As shown in Fig. 3.4, the two sides of the ring magnet are named as closed side and open side according to the distance between the two layers.
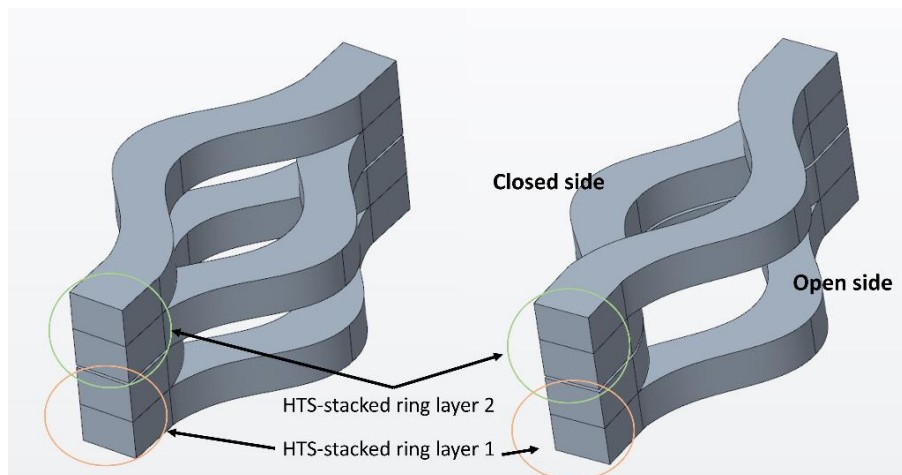
Figure 3.4: Two different configurations of HTS-stacked ring magnets

The HTS tapes used for this sample are 12 mm FESC-SCH tapes from Fujikura. The length of each of the tapes is 90 mm and each of them has a 70 mm cut in the middle, in which there are 10 mm connecting edges at the two sides of each tape. Given that the width of the tape is 12 mm, edges of 10 mm are sufficient to enable the current to flow through the ring. The cutting process is executed using a specialized laser cutting machine. Each layer of stacked rings is composed of 90 pieces of HTS tapes which leads to around 12 mm in the thickness of the HTS-stacked ring magnet. Due to the limitation of the bore size of the magnet for magnetization, the outer length/diameter of the sample has a length of 90 mm and a width of 60 mm.
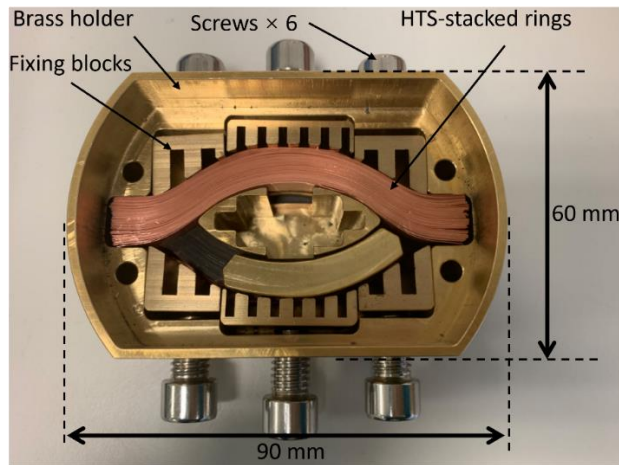
Figure 3.5: Finished HTS -stacked ring magnet sample without impregnation

To fix the HTS-stacked ring magnet for experiments, a bespoke brass holder with additional brass blocks that adapt to the shape of the ring magnet's outer edges is designed and machined, as shown in Fig. 3.5. Those blocks are called "fixing blocks", which can be pushed by six brass crews from the two sides of the holder. The hollow ring-shaped cylinder in the centre of the holder is used to create the central space of the ring magnet and it is also used for the placement of the sensors and later HTS stacks. The assembly of the HTS tapes and brass parts can be done in the following steps. First, the prepared tapes are inserted into the holder with the central cylinder inserted into the middle cuts of the tapes. Then, the adjustable fixing blocks on both sides are pushed towards the middle, fitting along the outer edges of the tapes. Hall sensors and HTS inserts (for hybrid design) are then inserted into the centre space.

Figure 3.6: Finished HTS -stacked ring magnet sample with impregnation (without cover)

To protect those HTS materials from air and moisture as well as to enhance thermal conductivity, melted wax mixed with aluminium nitride powder is then poured into the brass holder to impregnate the HTS-stacked rings and HTS inserts (hybrid design) as shown in Fig. 3.6. Finally, a brass cover is placed on the sample and secured with bolts. The holes on the brass cover are used to connect the sample to the supporters of the external magnet which is for the applied field. The wires for hall sensors and temperature sensors go through the hole at the bottom of the brass holder.

To monitor the temperature change during and after the magnetization of the HTS-stacked ring magnet, a calibrated Lakeshore Cernox SD temperature sensor is inserted into the centre area of the impregnated sample. Besides, during magnetization processes, another Cernox SD temperature sensor is attached to the top of the brass cover as shown in Fig. 3.7.
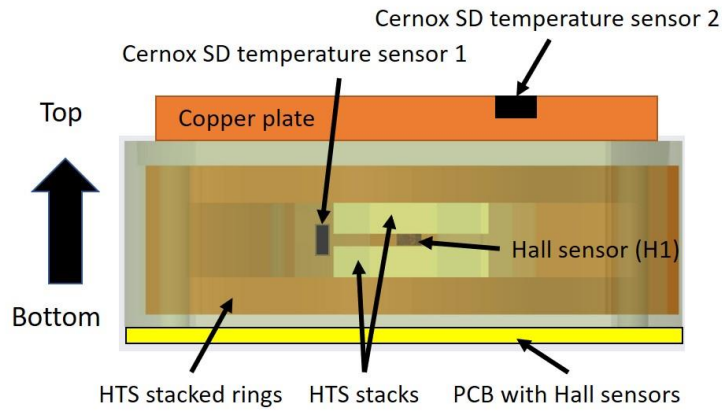
Figure 3.7: Schematic diagram of the sample structure with sensors' distribution

A Lakeshore HGT-2101 Hall sensor (H1), soldered onto a small rectangular Printed Circuit Board (PCB), is positioned at the centre. For the study involving the HTS-stacked ring magnet, two G10 blocks are employed to secure the sensor at the centre of the sample. In the case of the hybrid HTS-stacked ring magnet study, with HTS stacks inserted, this Hall sensor is situated between the two HTS stacks. To measure the trapped field at the surface of the sample, a 1 mm thick PCB with 10 Hall sensors (H2-H11) is attached at the bottom of the brass holder. The distribution of the 10 Hall sensors is shown in Fig. 3.8. Since the HTS-stacked ring magnet is symmetric, those 10 sensors are distributed only on one side. The thickness of the bottom of the sample holder is 2 mm and the Hall sensors are also 2 mm thick, so the trapped fields at 5 mm above the sample are measured.
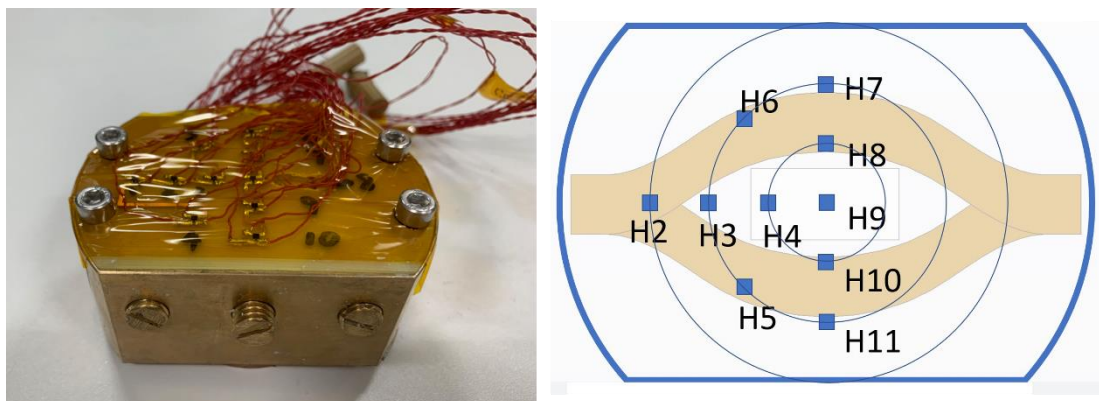
Figure 3.8: The distribution of the 10 Hall sensors at the bottom of the sample holder

3.3 Simulation Methodology

Numerical simulation is widely used in the study of HTS material. Verified and reliable numerical models can be used to help explain some phenomena observed in experiments but are hard to detect by devices. Besides, calculation results can assist in further exploring the potential of HTS samples or applications and provide guiding predictions when the experimental conditions are temporarily unattainable. At present, there are several typical finite element method (FEM) models derived from Maxwell equations for the calculation of the electromagnetic characteristics of HTS models: A-V formulation[176], T-ϕ formulation [177], T-A formulation [178], minimum electromagnetic entropy production (MEMEP) method [179], H-formulation et al [180], [181]. In A-V formulation, the magnetic vector potential A, which is preferred for electromagnetic computations in commercial FEM software packages, is used for the calculation and V is the electric potential [182]. T-A formulation focuses on the rapid calculation of 2D models where the current vector potential T is calculated only within the superconducting region, while the magnetic vector potential A is calculated throughout the entire computation domain. Due to the high aspect ratio of HTS tapes, modelling the entire surface requires extensive simulation time. The T-A formula employs a unique method to resolve this issue by treating the tape as extremely thin [178]. This geometric simplification reduces the surface area of the HTS tape to a thin slice. The MEMEP method develops a general variational formalism to calculate the electromagnetic properties of superconductors described by any E(J) relation under varying magnetic fields. It holds advantages in rapid calculations related to HTS tapes, especially the AC losses of coils with a large number of turns [179], [183]. H-formulation is the most widely used in the calculation of HTS models where the single dependent variable of magnetic field intensity H is used to calculate macroscopic current and field distributions in HTS materials. It accurately represents the flux-pinning effects observed in HTS materials. This is crucial for accurately modelling the behaviour of HTS materials, particularly in situations where magnetic fields change over time.

As previously noted, mechanical strength is pivotal for the reliability and performance of trapped field HTS magnets due to the Lorentz forces that result from the interaction

of large induced currents in HTS materials and the magnetic field. The methodology for mechanical analysis is relatively mature, utilizing the results of electromagnetic models as input for mechanical equilibrium equations to discern the distribution of stress-strain.

3.3.1 H-Formulation for HTS-Stacked Ring Magnet.

Considering the magnetization condition, unique 3D geometry, computation accuracy and later mechanical coupled model, the numerical study towards the HTS-stacked ring magnet and the hybrid HTS-stacked ring magnets are conducted based on the H-formulation. Generally, the H-formulation employs the FEM models to resolve Faraday's equation:

$$\varepsilon = -\frac{d\Phi}{dt} \tag{3.1}$$

where ε is the electromotive force (EMF) and Φ is the magnetic flux.

Since a time-varying magnetic field always accompanies a spatially varying (also possibly time-varying), non-conservative electric field, the actual numerical calculation uses Maxwell-Faraday's equation:

$$\nabla \times E = -\frac{\partial B}{\partial t} \tag{3.2}$$

Where ∇ is the curl operator and $E\ (r,\ t)$ is the electric field and $B\ (r,\ t)$ is the magnetic flux density.

Using the relationship between magnetic flux density B and magnetic field H, equation (3.2) can be written as:

$$\nabla \times E = -\mu_0 \mu_r \frac{\partial H}{\partial t} \tag{3.3}$$

Where μ_0 and μ_r are the vacuum permeability and relative permeability respectively.

Then according to Ampere's law (3.4) and Ohm's law (3.5),

$$J = \nabla \times H \tag{3.4}$$

$$E = J \cdot \rho \tag{3.5}$$

the equation (3.3) can be written as

$$\nabla \times (\rho \, \nabla \times H) = -\mu_0 \mu_r \frac{\partial H}{\partial t} \tag{3.6}$$

where ρ is the nonlinear resistivity of HTS materials which is utilized to depict the distinctive electrical properties of superconductors. It is deduced from the *E-J* power law. Given the high aspect ratio of HTS tape materials, the critical current of the HTS tapes is influenced not only by the external magnetic field but also by the angle between the tape's normal direction and the direction of the external magnetic field. Besides, in this thesis, the (hybrid) HTS-stacked ring magnets are magnetized with stable temperature and the ramping rates for the externally applied field are very slow. Therefore, the influence of temperature change on the critical current is ignored and the *E-J* power law for HTS tape material can be written as:

$$\rho = \frac{E_0}{J_c(\theta, B)} \times \left(\frac{J}{J_c(\theta, B)} \right)^{n-1} \tag{3.7}$$

where E_0 is the critical current criterion equal to 100 µV/m and n is the power law exponent which is normally set as 21. *J* is the induced current density and $J_c(\theta, B)$ is the critical current of the HTS tapes affected by the angle and magnitude of the external and self-induced magnetic field. The $J_c(\theta, B)$ data of HTS tapes can be interpolated into the model as shown in Fig. 3.9.
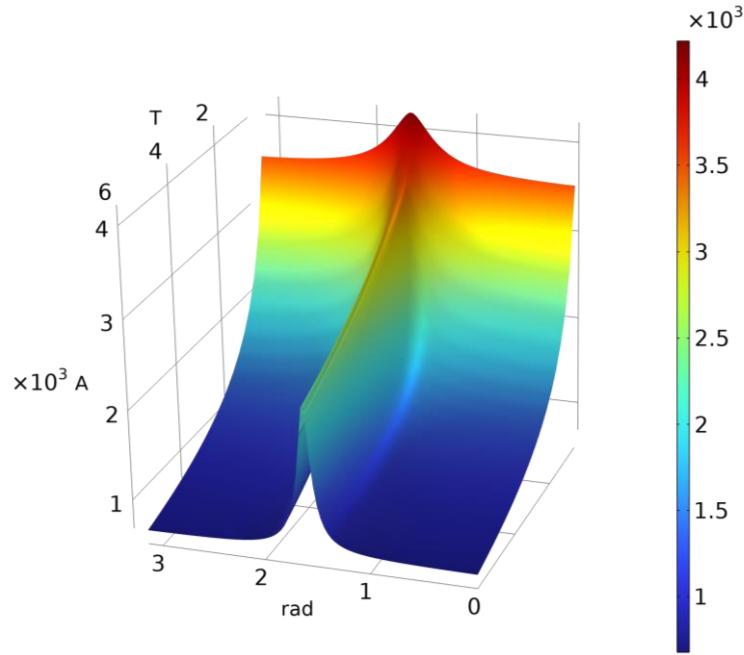
Figure 3.9: Magnetic field-dependent critical current of the HTS tapes used in the study

The modelling of HTS bulk materials adopts a simulation methodology akin to that of the HTS-stacked ring magnet, as detailed in the preceding section. However, determining the critical current for HTS bulk materials presents more challenges compared to HTS tapes, especially when accounting for the influence of applied fields and when operating at a temperature of 25 K. In this thesis, the critical current density of HTS bulks is deduced based on the trapped field observed in the HTS bulk under liquid nitrogen conditions (77 K).

The correlation between the trapped field of a cylindrical HTS bulk and its critical current density is articulated as follows [184]:

$$B_{trap} = ak\mu_0 J_{cbt}(0.8\ T,\ 77\ K) \tag{3.8}$$

$$k = \frac{t}{2a} ln\left(\frac{a}{t} + \sqrt{1 + \left(\frac{a}{t}\right)^2}\right) \tag{3.9}$$

Where B_{trap} is 0.8 T, a and t are the diameter and thickness of the bulk.

The field dependence of critical current density $J_{cbt}(B)$ at 25 K is calculated with the Eq. (3.10) named Kim model [185] and Eq. (3.11) [184]:

$$J_{cbt}(B) = \frac{J_{cbt}(0)}{\left(1 + \frac{|B|}{B_0}\right)} \tag{3.10}$$

$$J_{cbt}(T) = J_{cbt}(0)\left(1 - \left(\frac{T}{T_c}\right)^2\right)^{1.5} \tag{3.11}$$

Where $B_0 = 1.3$ and $T_c = 92$ K.

For the air and other non-conductive areas, the resistivity can be set as 1 Ω·m which is much higher than the resistance of superconducting regions. Therefore, the current flow can only occur in the superconducting areas. In this case, it facilitates to definition of the material properties by setting the resistances of different calculation domains differently.

Both 2D and 3D models are established using the software COMSOL Multiphysics in this study. To conduct the H-formulation in COMSOL, there are two general methods to realize it. One is to use the embedded "Magnetic Field Formulation(mfh)" interface [186], which has the default equations prepared, and another one is to formulate relevant equations according to specific requirements with the "General Form Partial Differential Equation (PDE)" interface. The latter is chosen for the simulation in this thesis because it offers a higher degree of freedom and is more conducive to conducting an in-depth analysis of the magnetization phenomena addressed in this thesis. For H-formulation, the difference between 3D and 2D model calculations is not significant, involving only the addition of variables related to the z-axis. Hence, the general form PDE for the 3D calculation model is given as:

$$e_a \frac{\partial^2 u}{\partial t^2} + d_a \frac{\partial u}{\partial t} + \nabla \cdot \Gamma = f \tag{3.12}$$

$$u = [H_X, H_Y, H_Z] \tag{3.13}$$

$$\nabla = [\frac{\partial}{\partial x}, \frac{\partial}{\partial y}, \frac{\partial}{\partial z}] \tag{3.14}$$

Where e_a is set as 0, since there isn't a second-order derivative term in the H-formulation. The other parameters are set as:

$$d_a = \begin{bmatrix} \mu_0\mu_r & 0 & 0 \\ 0 & \mu_0\mu_r & 0 \\ 0 & 0 & \mu_0\mu_r \end{bmatrix} \tag{3.15}$$

$$\Gamma=\begin{bmatrix} 0 & E_z & -E_y \\ -E_z & 0 & E_x \\ E_y & -E_x & 0 \end{bmatrix} \tag{3.16}$$

$$f=\begin{bmatrix} 0 \\ 0 \\ 0 \end{bmatrix} \tag{3.17}$$

The externally applied field can be given by setting the Dirichlet boundary conditions of the whole calculation domain to calculate the magnetization of the HTS materials [187], [188].

3.3.2 Mechanical Calculation of the (Hybrid) HTS-Stacked Ring Magnet.

The HTS-stacked ring magnet is fixed inside a brass holder using a blend of paraffin wax and aluminium nitride powder for impregnation. A brass cover stabilizes the sample's top. During and post-magnetization, substantial Lorentz forces act on the HTS tapes, posing a risk of deformation or damage. The impregnation and holder, with its cover, alter the stress distribution and intensity in the magnet compared to those without reinforcement. Direct observation or measurement of these variations is difficult with current tools. Hence, numerical modelling becomes essential for examining the magnet's mechanical performance. Using the H-formulation in this thesis for electromagnetic analysis of the ring magnet, the Lorentz forces (equivalent to $J \times B$) affecting the HTS tapes can be derived from the computational findings.

To calculate the stress distribution of the HTS-stacked ring magnet caused by the Lorentz force and other mechanical constraints during field cooling magnetization, the mechanical equilibrium equations based on Newton's second law in direct tensor form can be written as [189], [190]:

$$\nabla \cdot \sigma_S + F_L = g\frac{\partial^2 u}{\partial t^2} \tag{3.11}$$

$$F_L = J \times B = \begin{vmatrix} i & j & k \\ J_x & J_y & J_z \\ B_x & B_y & B_z \end{vmatrix} \tag{3.12}$$

Where $F_L = [F_{Lx}, F_{Ly}, F_{Lz}]$ denotes the Lorentz forces, and σ_S is the Cauchy stress tensor. g and u are the mass density and the displacement. Given the tightly stacked arrangement of the HTS tapes within the sample holder, it is reasonable to treat them as a solid body in the modelling process. Consequently, the initial tension that results from the stretching of the HTS-stacked rings during fabrication is disregarded. In the proposed models, the mechanical parameters of density, Young's modulus, and Poisson's ratio are assigned values of $8890\,\mathrm{kg/m^3}$, $174\,\mathrm{GPa}$, and 0.3, respectively [191], [192]. In this thesis, it is assumed that no relative motion occurs between the stacking HTS tapes, which are tightly conjoined. As a result, the HTS-stacked ring magnet, being composed of stacked tapes, is considered a unified entity, thereby warranting the continued adoption of the homogenized model. This also applies to the HTS stack insert.

The present study considers the HTS tapes to possess the characteristics of metallic plastic materials, and as such, employs the fourth strength theory, commonly referred to as the Von Mises strength theory, as the criterion for analysis. The von Mises stress is calculated as

$$\sigma_v = \frac{\sqrt{(\sigma_x-\sigma_y)^2+(\sigma_y-\sigma_z)^2+(\sigma_z-\sigma_x)^2+6(\tau_{xy}^2+\tau_{yz}^2+\tau_{zx}^2)}}{\sqrt{2}} \tag{3.12}$$

Where σ_v is the von Mises stress or equivalent tensile stress, σ_x, σ_y, σ_z, τ_{xy}, τ_{yz} and τ_{zx} are the 3 normal stresses and 3 shear stresses.

3.3.4 Homogenization of Stacked HTS Tapes

As noted in Section 3.2, the HTS-stacked ring magnet is constructed by stacking 180 pieces of HTS tapes. If each of the tapes is calculated separately, it would be very time-consuming. In FEM calculation, each calculation domain must be properly meshed to guarantee the convergence and accuracy of the results. Given that the thickness of each tape is approximately 0.15 mm and the overall size of the HTS magnet is considerably larger, the number of meshes will increase significantly, thereby greatly increasing the computational load. To address this issue, the concept of the homogenized model was

proposed, which demonstrated high efficiency in calculating the magnetization of stacked thin HTS materials, while also ensuring the accuracy of the results. The essence of the homogenized model is to treat multiple adjacent stacked tapes as a single superconducting domain for calculation as shown in Fig. 3.10. Since the tapes were originally separated from each other, there is also an air between each superconducting domain after homogenization to characterize the difference between the stack and a solid block. Although the superconducting layer only takes around 1% thickness of the HTS coated conductors, the homogenization methodology can still effectively demonstrate the simulation with accuracy as validated in previous studies [39].
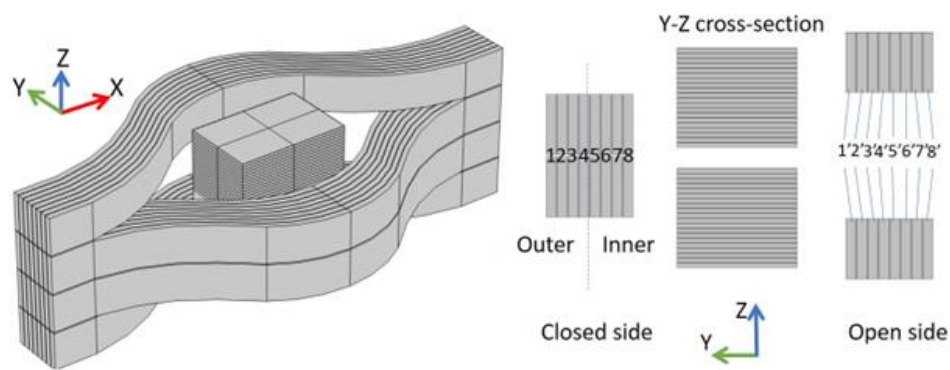
Figure 3.10: Homogenized modelling of (hybrid) HTS-stacked ring magnet

In this thesis, both 2D and 3D homogenized models are established for the HTS-stacked ring magnet, as well as for the HTS stack inset. In these models, every group of 10 HTS rings is treated as a single HTS domain. Given that the non-superconducting layers in the HTS tapes do not affect the slow magnetization process, the concept of engineering critical current is applied in the homogenization [39], [180]. This implies that the cumulative critical current of 10 HTS tapes equals the critical current of one single HTS domain. The coupling of the H-formulation and the homogenized models has been conducted and verified in previous studies. For the mechanical analysis of the HTS-stacked ring magnet, given that the stacked rings are considered a solid entity, the gaps between each homogenized domain are disregarded.

The numerical analysis of the trapped field HTS double-pancake coil doesn't use the homogenized model due to the application of a 2D axisymmetric model, which offers

satisfactory calculation efficiency. The specifics of the modelling will be detailed in Chapter 7.

3.4 Conclusion

This chapter began with a comprehensive presentation of the design and fabrication process of the HTS-stacked ring magnet sample. Special attention was devoted to the aspects of thermal and mechanical enhancement design, where adjustable brass blocks played a significant role.

After the detailed introduction, the focus was shifted to the simulation methodology utilized throughout the study. This methodology comprises three main components. The first is the H-formulation, a powerful tool for analysing the electromagnetic properties inherent to the ring magnet design. The second component is the modelling of HTS bulk materials which considers the variation of magnetic field and temperature. Then it is the mechanical stress-strain analysis, essential for comprehending the mechanical performance of the sample under various force and constraint conditions. Finally, the third aspect involves the use of homogenized models, which help simplify the complex nature of the stacked HTS tapes.

Chapter 4. Magnetization of the HTS-Stacked Ring Magnet

4.1 Introduction

Previous research on the magnetization of HTS-stacked ring magnets primarily emphasized the magnitude and distribution of the trapped field, in addition to alterations in the trapped field under specific conditions. These investigative approaches mirror the methodologies utilized in research concerning traditional HTS bulk materials. However, there exists a distinguishing characteristic that sets the HTS-stacked ring magnet significantly apart from conventional HTS bulk materials. This distinction arises from the unique parallel stacking method utilized in the fabrication of the HTS-stacked ring magnet. In the case of traditional HTS bulk materials, regardless of whether it is a solid cylindrical bulk or a hollow ring-shaped bulk, the magnetization process—either field cooling or zero field cooling—always initiates penetration from the outer region to the inner region. This is due to the conductive nature of the entire HTS bulk material, and the Bean model has a good explanation. Conversely, the circumstances within the HTS-stacked ring magnet are entirely distinct. Even though each HTS tape is firmly attached to its adjacent counterparts and is furnished with a conductive copper coating, the induced current primarily traverses the superconducting layers owing to their significantly lower resistance. Consequently, the HTS tapes act as almost insulating to each other. Besides, the parallel stacking method makes the distribution of the stacked HTS tapes asymmetric. For example, the current in domain 1 and domain 1' (Fig. 3.10) is from one closed-loop HTS tape which means theoretically their total current should be zero. These factors could significantly influence the penetration sequence during magnetization and the characteristics of the trapped field performance. However, these aspects have not been sufficiently emphasized in previous research.

4.2 Field Cooling Process and Experimental Results

This thesis predominantly centres on exploring the magnetization mechanism, trapped field performance, and mechanical properties of the (hybrid) HTS-stacked ring magnet as well as the HTS double-pancake coil with soldered joints. Specifically, it investigates these characteristics under the condition of field cooling magnetization, a technique renowned for its efficacy in attaining a higher trapped field.

4.2.1 Field Cooling Magnetization Setup

In this study, the magnetization temperature is set as 25 K which is much lower than the liquid nitrogen temperature (77 K) and a wide bore magnet is employed for the FC process as shown in Fig. 4.1. The temperature of the sample is monitored in real-time by two Cernox SD temperature sensor. One is at the top of the brass cover and controlled around 25 K through a feedback regulation system. Another is fixed near the centre of the sample and monitors the temperature variation of the central area as well as the central Hall sensor. Cold helium gas evaporated from liquid helium is blown out through the small holes below the sample to cool it down.
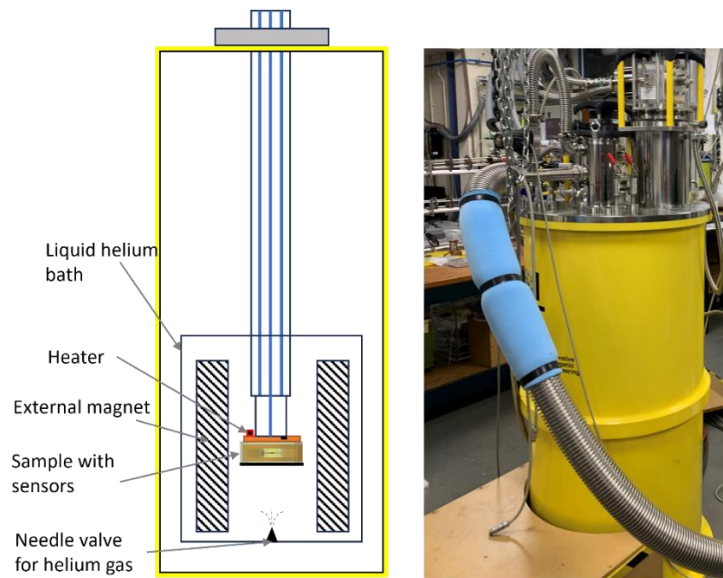
Figure 4.1: 12 T wide-bore magnet used for magnetizing the sample

Chapter 4. Magnetization of the HTS-Stacked Ring Magnet

It is well known that during field cooling magnetization process, significant current can be induced in the HTS material. This can result in considerable temperature rise, potentially leading to a decay in critical current or in extreme cases, a quench. This temperature rise typically occurs due to the rapid generation of induced current coupled with inadequate heat exchange. As noted in Chapter 3, the HTS-stacked ring magnet is impregnated with a mixture of paraffin wax and aluminium nitride powered and attached to brass blocks. Those measures can enhance the heat exchange during magnetization. Regarding the issue of rapidly generated induced current, the most immediate and efficient solution during the field cooling magnetization process is to lower the rate of decrease in the applied magnetic field. In all instances of field cooling magnetization detailed in this thesis, the ramping rate of the applied magnetic field is set at 0.75 T/min. This rate has been determined to be sufficiently low to minimize heat generation within the sample.

4.2.2 Trapped Field Distribution of the HTS-Stacked Ring Magnet
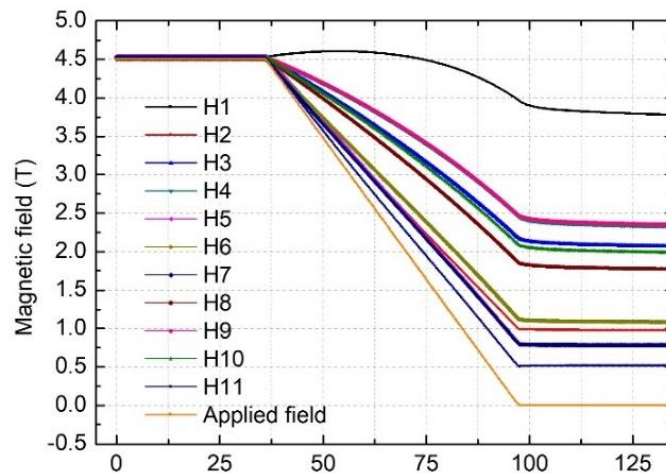
Figure 4.2: Magnetic field at the locations of 11 Hall sensors during and after magnetization

A 4.5 T magnetic field is employed for the FC magnetization of the HTS-stacked ring magnet, devoid of any HTS material inserts. Fig. 4.2 showcases the magnetic field at the locations of 11 Hall sensors. Of these, H1—located at the centre of the sample—achieves the highest trapped field of approximately 3.79 T, observed after a relaxation

period of 25 minutes. Given that the final achieved field is apparently lower than the initially applied field, it can be inferred that the HTS-stacked ring magnet has been fully penetrated. Consequently, the potential for a significantly higher trapped field in this sample is minimal. It should be noted that the magnetic fields measured in the thesis are vertical to the Hall sensors.
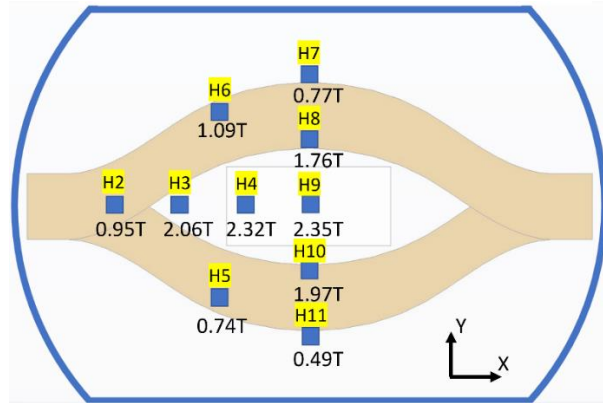
Figure 4.3: Magnetic fields at 5 mm above the sample surface during magnetization

As for the other 10 Hall sensors, which measure the magnetic field 5 mm above the sample surface during magnetization, they are distributed on the concentric circles centred on H9 (illustrated in Fig. 3.7). As shown in Fig. 4.3, while H4 is located to the left of the centre, both H9 and H4 register similar peak values of 2.3 T, while the H8 and H10 only have the fields of 1.76 T and 1.97 T. It preliminarily indicates that the gradient of the trapped field reduction in y axis is much larger than that in the x axis. A similar situation can be observed in the H3, H5, H6, H7 and H11 circle. Among these points, H3 has the highest field and H7 and H11 have the lowest fields. This can be explained by the superposition of magnetic fields. The superposition of the fields generated by both sides in the middle part makes the magnetic field in the middle greater than that on both sides.

In addition, H6 and H7 have higher field values than those at H5 and H11 which means the distribution of the trapped field has a tilted pattern, which is different from HTS bulk materials' centrosymmetric distribution of magnetic fields. This unevenly distributed trapped field can be thought to be caused by the unique ring shape of the HTS-stacked ring magnet. As shown in Fig. 3.9, the HTS tapes at open sides are closer to the up and bottom surfaces, while the closed side stays at the middle area.

The trapped field of H2, measured at 0.95 T, exhibits a precipitous decline from the position of H3. Intriguingly, the interstitial distance from H2 to H3 parallels the distance from H3 to H4 and is congruent with the distance between H4 and H9. This can be attributed to the alteration in the direction of current flow at the edges of the split HTS tapes. As shown in Fig. 4.4, the current begins to turn to the z axis, which is vertical to the x-y plane, to form a current circuit. The current direction in upper layers is opposite to that in lower layers due to the stacking method and this has a reducing effect on the magnetic field as well.
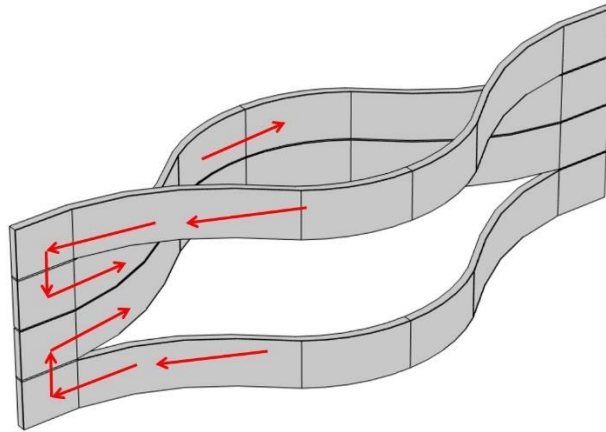
Figure 4.4: Induced current flow in the HTS tapes

Upon analysis, it is observed that a trapped magnetic field of 2.35T can be attained at the central point, positioned 5 mm above the HTS-ring magnet's surface. Distinctively, the field does not display a symmetrical distribution akin to that seen in conventional HTS bulk materials. Over the central hollow region, the magnetic field consistently exhibits a greater magnitude compared to the area above the HTS tape. The asymmetrical design of the ring magnet contributes to a tilted field distribution. Furthermore, owing to the countervailing current directions at the edges of the HTS tapes, the magnetic field experiences a significant reduction in this region.

4.2.3 Central field Ascent During Magnetization

As illustrated in Fig. 4.2, a noteworthy ascent of the central field at the centre of the HTS-stacked ring magnet is observed during the process of field cooling

magnetization. To facilitate a more accurate portrayal and comparison of the curve fluctuations, the axis scale of the central field has been modified in Fig. 4.5. The magnetization demonstrates an initial incline, subsequently followed by a downturn after reaching an apex approximately at 4.6 T, yielding an arc-shaped trend.
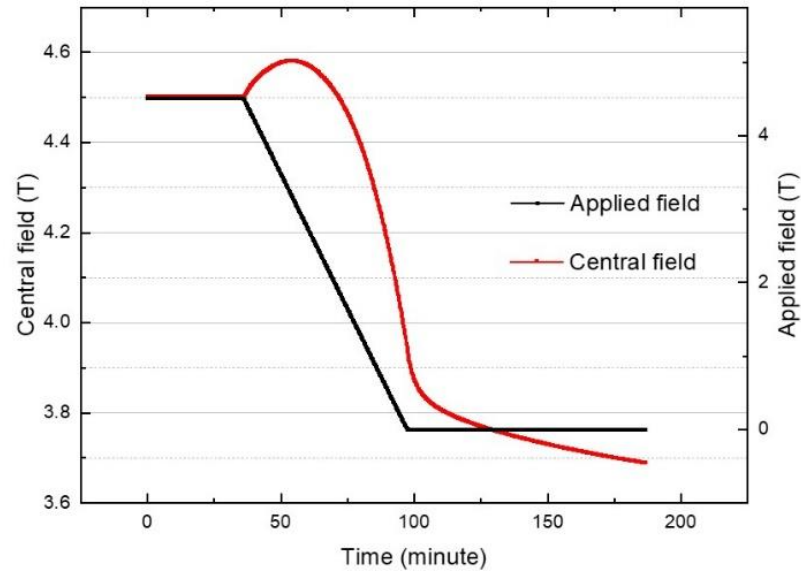
Figure 4.5: The central field and applied field of the HTS-stacked ring magnet during magnetization

This observation indicates that the sum of the central field confined by the HTS-stacked rings and the external field exceeds the initially applied field. This is a unique magnetization phenomenon, hitherto unobserved in the field cooling magnetization of other HTS materials. Within the traditional field cooling magnetization paradigm for HTS bulk materials, the central field can, at its maximum, equal the externally applied field, even when situated between two solid bulk superconductors as shown in Fig. 4.6 [158].
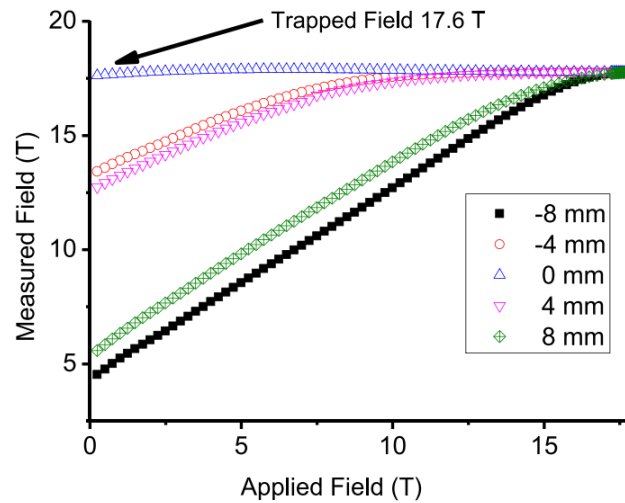
Figure 4.6: Central fields of traditional HTS bulk materials during FC magnetization

The temperature fluctuations documented by the two Lakeshore Cernox SD temperature sensors throughout the experiments are depicted in Fig. 4.7. During magnetization, both temperature sensors exhibit a minor temperature increase, which is caused by the induction of induced current. However, these increments are less than one degree. Such a minimal rise in temperature is unlikely to significantly impact the properties of the Hall sensor. The temperature of the cover is found to be higher than that at the centre, primarily due to the cold helium gas that cools the sample from the bottom, consequently establishing a temperature gradient from the bottom to the top of the sample.
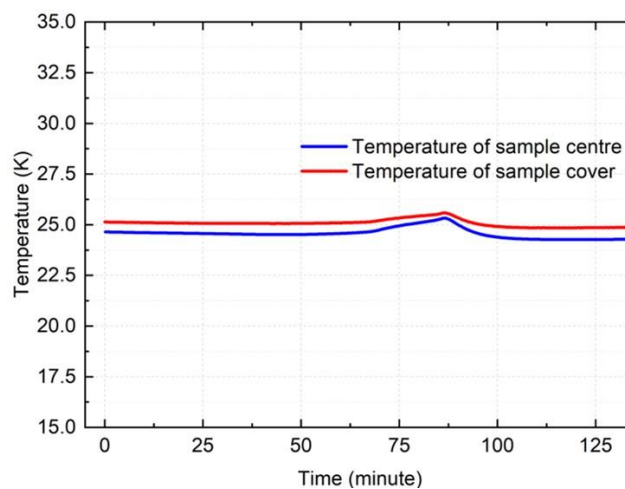
Figure 4.7: Temperature variations during 4.5 T magnetization

It merits attention that in recent years, the HTS lens, constructed from HTS bulk superconductors, has also accomplished a central field surpassing the applied field [193], [194], [195], [196], [197], [198]. However, the HTS lens relies on the diamagnetic shielding effect (Meissner effect) of two closely arranged bulk superconductors to concentrate the magnetic field, necessitating an external field source for its maintenance [195]. Fujishiro et al. unveiled a hybrid trapped field magnet lens concept, constituted of a traditional HTS lens fashioned from HTS bulk material, accompanied by an auxiliary external HTS bulk ring serving as a trapped field magnet, as depicted in Fig. 4.8 [193]. In the pursuit of a more intensely concentrated magnetic field, the internal HTS bulk should remain in a diamagnetic state, while the external HTS bulk undergoes magnetization through the field cooling process. This necessitates that the two differing bulk materials exhibit distinct critical temperatures, or alternatively, the temperatures of two identical bulk materials can be regulated independently.

The HTS-stacked ring magnet discussed within this thesis and the HTS lens both exhibit the potential capacity to attain a central field that exceeds the applied field, but substantial disparities exist between the two. The operational principles underlying the HTS lens have been comprehensively elucidated. Nevertheless, the mechanism facilitating the central field's escalation within the HTS-stacked ring magnet amid standard field cooling processes remains a subject requiring further investigation.
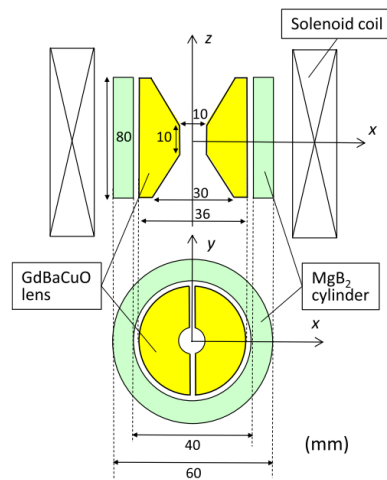
Figure 4.8: Hybrid design of HTS lens with GdBCO and MgB_2 materials

4.3 Investigation of Central field Ascent

As analysed previously, the manifestation of the central field ascension phenomenon during standard field cooling magnetization of the HTS-stacked ring magnet has not been seen. Remarkably, it also marks the initial observation of the central field exceeding the applied field within the ambit of field cooling magnetization studies of HTS materials. This revelation presents two salient inquiries concerning HTS trapped field magnets: primarily, what is the underlying mechanism facilitating this central field ascension phenomenon? Furthermore, despite the observed field ascent during magnetization, the ultimate trapped field remains inferior to the applied field. Could there be potential for a final trapped field that exceeds the initially applied field, given an appropriately engineered design of the HTS-stacked ring magnet?

In this section, the issues will be examined via the utilisation of numerical models. A homogenized field cooling magnetization model based on the H-formulation, as introduced in Chapter 3, will be constructed. The validity of the modelling will be first assured through a comparative analysis between simulation outputs and empirical results. Upon confirmation of the model's validity, the investigation will proceed to examine the induced current and the field penetration attributes of the HTS-stacked ring magnet throughout the magnetization process. Subsequently, a comparative study involving traditional HTS bulk materials and the HTS-stacked ring magnet will be undertaken, particularly with respect to the induced current distribution. This will provide a thorough analysis concerning the unique central field ascension phenomenon observed in the HTS-stacked ring magnet. Lastly, based on the numerical model and corresponding analysis, the feasibility of attaining a higher trapped field than the applied field under standard field cooling magnetization for the HTS-stacked ring magnet will be explored and assessed.

4.3.1 Validation of the Numerical Model.

To affirm the veracity of the simulation model, the field cooling magnetization of the homogenized HTS-stacked ring magnet model is computed with an initial applied field

configured at 4.5 T. Considering the considerably slow ramping down rate of the applied field during experiments (0.75 T/min), coupled with the inclusion of an appropriate thermal conduction design, the actual temperature alteration of the sample is presumed minimal. This assumption allows for the critical current of the HTS tapes to be largely unaffected by the temperature change. Consequently, the simulation model omits consideration of the effects of heat generated by the HTS tapes and the temperature-dependent critical current. Without the implications of heat, the model's ramping down of the applied field can be executed at a significantly faster pace than in real-world experiments without compromising the precision of the calculation. This greatly enhances the efficiency of the calculation. To facilitate a comparison between simulation output and empirical results, it is necessary to normalize the time, as depicted in Fig. 4.9. Evidently, the two curves representing the simulation output and experimental results exhibit the same trend and similar values, with the simulation results faithfully reproducing the central field ascent phenomenon. These findings suffice to demonstrate the validity and accuracy of the numerical modelling.
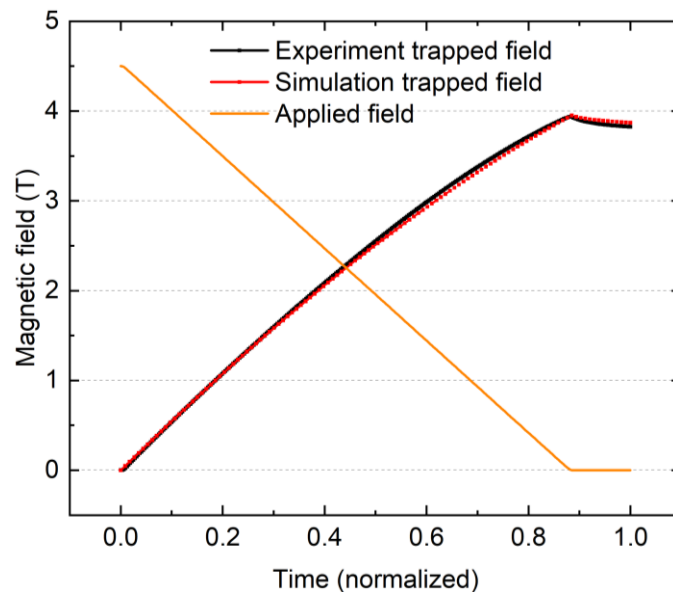
Figure 4.9: Results of the trapped field by simulation

4.3.2 Current Distribution and Field Penetration of HTS-Stacked Ring Magnets.

The magnitude and distribution of the magnetic field in HTS trapped field magnets are fundamentally dictated by the induced current in the HTS materials. Consequently, an analysis of the induced current in the HTS-stacked ring magnet during field cooling magnetization represents the most efficacious approach to investigate the fundamental causes of observed trapped field characteristics, including the ascension of the central field.

In Chapter 3, it is mentioned that for more efficient simulation modelling, each set of 10 HTS tapes is integrated into one HTS domain. Due to the symmetrical design of the HTS-stacked ring magnet, it is anticipated that the magnitude and distribution of the induced current in the corresponding top and bottom layers would be identical. Therefore, to provide a more intuitive investigation into the change in the magnitude of the induced currents within the inner and outer layers, each pair of corresponding top and bottom HTS domains is paired together. As depicted in Fig. 4.10, the corresponding HTS domains were labelled numerically from 1 to 8 for the left-side HTS domains and from 1' to 8' for the right-side domains. The induced current in each pair is recorded as C1 to C8 and C1' to C8', respectively, for comparative analysis. Given the split tape construction of the HTS-stacked ring magnet, meaning each tape forms a closed current loop, the sum of each pair of Cn and Cn' should equate to zero. Thus, Cn equals -Cn' and only Cn is discussed here for the sake of simplifying the investigation.
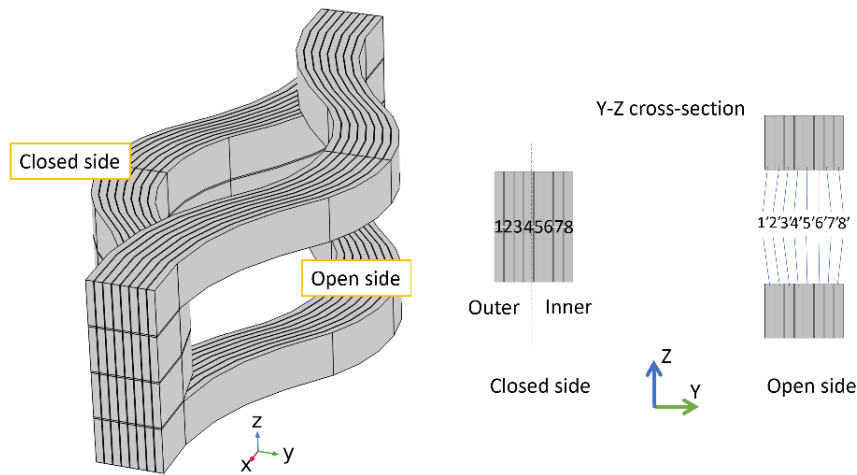
Figure 4.10: Homogenized model of HTS-stacked ring magnet and the relationship of the induced currents among each domain

By analysing Fig. 4.11, it is clear that from 0s to 0.5s (normalized time), C1-C8, C2-C7, C3-C6, and C4-C5 each display nearly identical induced currents. In the initial stage, the outer layers are fist magnetized, so the induced current in C1-C8 increased quickly while the others see a slow current increment. From 0.5s to 0.8s, gaps in the induced current appear in C1-C8 and C2-C7, while for the remaining pairs, the differences are less noticeable. By the final stage of magnetization, the induced current of each pair tends to equalize again. Based on this induced current analysis, it can be inferred that during the field cooling magnetization of the HTS-stacked ring magnet, the induced current is almost symmetrically generated for each side of the magnet (open side and closed side). In other words, the inner rings have almost the same induced current as the outer rings, and this is preliminarily considered to be related to the parallel stacking method used in the HTS-stacked rings. This is a key distinction between the magnetization of traditional HTS bulk materials and the HTS-stacked ring magnet and will be analysed comparatively in the next section.
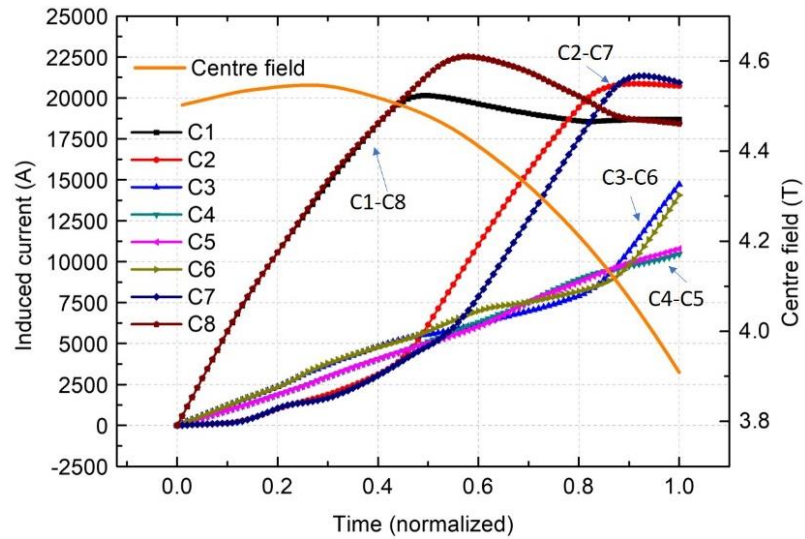
Figure 4.11: Induced currents at each domain of HTS-stacked rings and central field during 4.5 T magnetization.
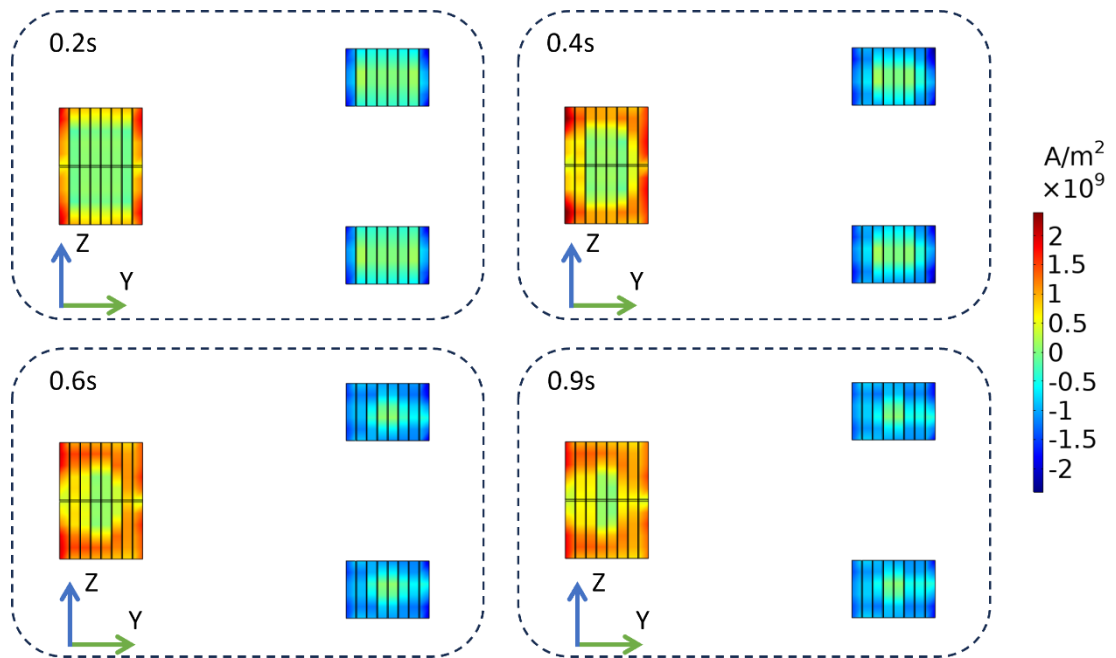
Figure 4.12: The induced current density along the x-axis during 4.5 T magnetization

Fig. 4.12 showcases the evolution of induced current density along the x-axis during magnetization. The y-z plane cross-section, taken from the ring magnet's centre, represents the current states at intervals of 0.2s, 0.4s, 0.6s, and 0.9s. Observations indicate that induced currents transition from outer to inner pairs, consistent with Fig. 4.11 patterns. For instance, at 0.6s, domain 8 has a more expansive current density representation than domain 1, mirroring the divergence between C1 and C8 in Fig.

4.11. By 0.6s and 0.9s, while greater current is evident in the HTS domains, an uneven current density distribution persists. The closed side, particularly domains 8 and 7, displays broader current induction than C1 and C2. On this side, there's less current mid-way between the two layers, contrasting with the open side.

To delve deeper into the current distribution, Fig. 4.13 and Fig. 4.14 respectively show the critical current densities and the critical currents of each HTS domain during magnetization. Fig. 4.13 reveals that domains nearer the HTS-stacked ring magnet's centre have a reduced critical current density, while the central-outer area exhibits a higher current density, indicated by the red area. The critical current magnitude is influenced by the total magnetic field, combining both trapped and applied fields. Between 0.6s to 0.9s, variations in domain 8's critical current distribution are subtle. However, Fig. 4.14 highlights a significant drop in domain 8's critical current. Notably, the induced current in domain 8 closely follows the trend of the critical current, beginning from C8's peak point. This implies that the reduced induced current in the outer domain (C8) seen in Fig. 4.11 results from a drop in the critical current.
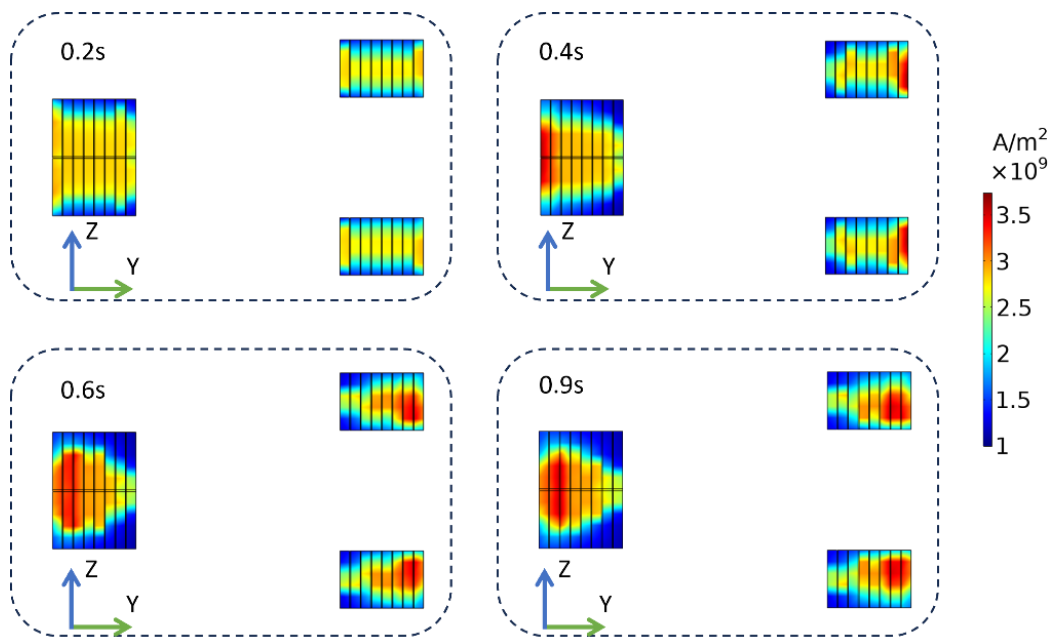
Figure 4.13: The critical current density along the x-axis during 4.5 T magnetization
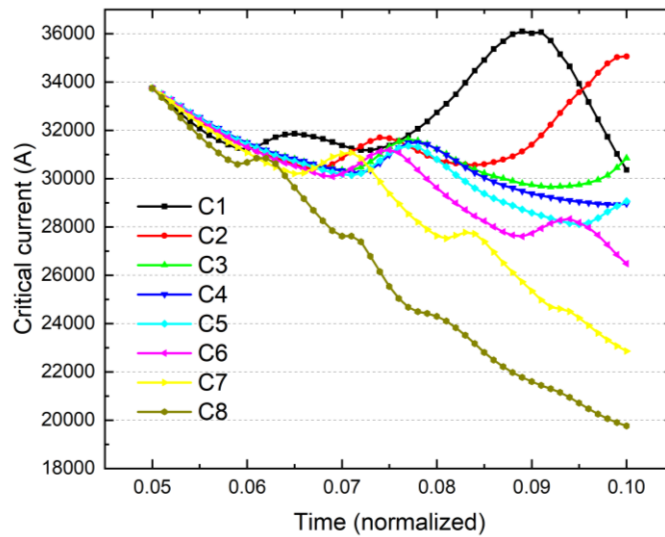
Figure 4.14: Critical currents at each domain of HTS-stacked rings during 4.5 T magnetization.
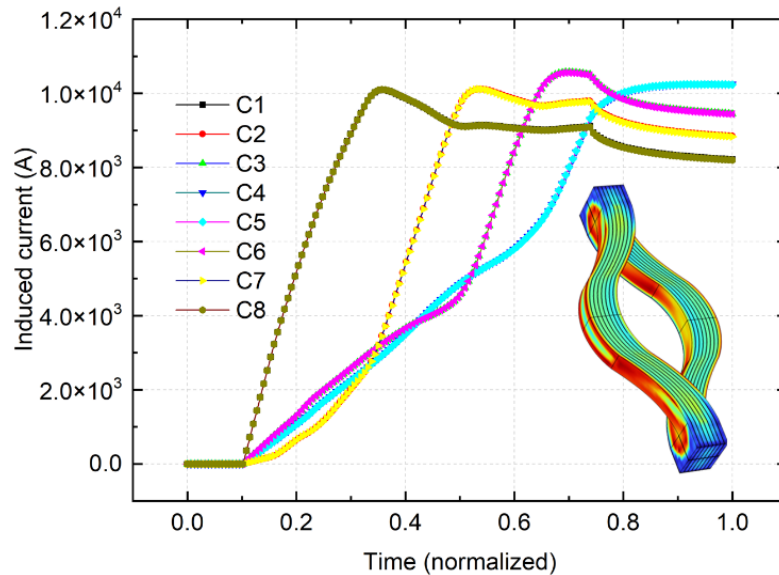
Figure 4.15: Induced current distribution of a single-layer HTS-stacked ring magnet

Referring back to Fig. 4.11, distinct variations within each paired set (C1-C8, C2-7, C3-C6, and C4-C5) are observed during magnetization, even if their overall trajectories align. It's considered that the asymmetry between the open and closed sides, resulting in an uneven trapped field, drives these variations. To confirm this, Fig. 4.15 displays the induced current distribution for a single-layer HTS-stacked ring magnet. Remarkably, each paired set (C1-C8, C2-C7, C3-C6, and C4-C5) exhibits identical induced currents throughout the magnetization. The associated distributions in Fig.

4.16 confirm symmetric magnetization on both sides of the ring magnet. Thus, the observed discrepancies within the pairs stem from stacking two HTS-stacked ring magnets, leading to the noted asymmetrical current distributions.
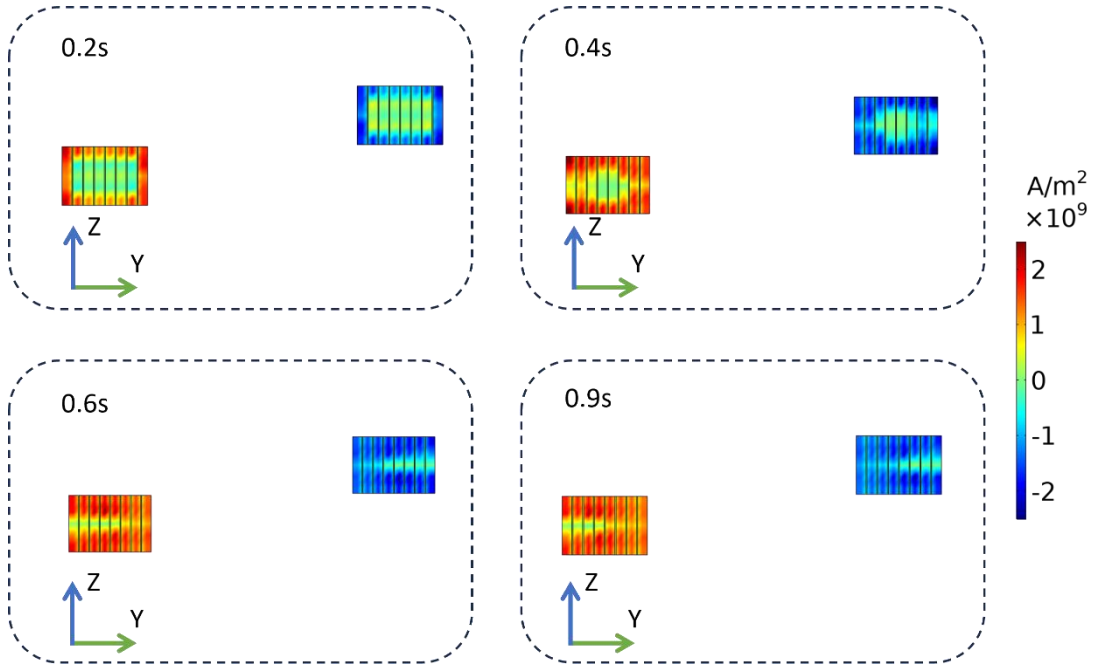
Figure 4.16: The induced current density of a single-layer HTS-stacked ring magnet

4.3.3 Difference of Induced Current in HTS Bulks and HTS Ring Magnets During Field Cooling Magnetization

The prior section highlighted that, by the end of magnetization, the inner and outer domains manifest identical induced currents due to the parallel stacking approach in the HTS-stacked rings. Does this phenomenon explain the central field's rise during typical field cooling magnetization? This section will delve into this question, contrasting the behaviours between traditional trapped field HTS bulk materials and the HTS-stacked ring magnet to discern the root cause of the central field ascent.

To make the comparison, the geometry of the HTS-stacked ring magnet stays unchanged, while the HTS domains are applied to the whole geometry. It means that there are no air gaps between each HTS domain and the ring magnet is considered as a solid HTS bulk superconductor. To facilitate a comparative analysis, the HTS material properties are set as the same as the previous model including the magnetic

field-dependent critical current. The actual volume of HTS domains is slightly increased due to the volume of the air gaps added in. But those effects are very small to the study, so the effects are neglected here. The same field cooling magnetization modelling is conducted to the "solid HTS ring" with 4.5 T applied field and the marking method for each domain and pair also remains consistent.
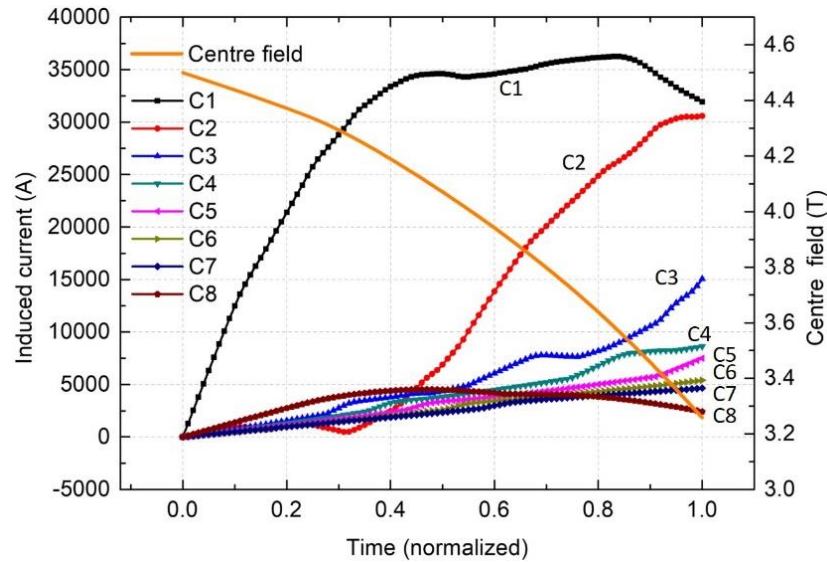
Figure 4.17: Induced currents at each domain of "solid HTS ring" and central field during 4.5 T magnetization.

Fig. 4.17 illustrates the central field during magnetization and the induced current in each HTS domain pair with the same presentation method in Fig. 4.11. As anticipated, the central field diminishes immediately once the external field starts to decrease. Compared with Fig. 4.11, the induced currents in the "solid HTS ring" have similarities with the induced currents in the original HTS-stacked ring magnet model, but there are more differences. The similarity is the induced current C1 also experiences a decrescent before the end of the magnetization which can also be caused by the reduced critical current in that area. Except for this, the patterns of the central field and induced currents within other domains exhibit substantial disparities. Firstly, it is clearly evident that the central field undergoes a continuous decline from the outset until the end of the magnetization process. This phenomenon aligns consistently with the field cooling magnetization that is customarily observed in our studies. Then, at the end of the magnetization, the magnitudes of C1 to C8 decrease in sequence which

means the penetration initiates from the outer domains inward for the magnetization of the "solid HTS ring".

To illustrate the magnetization process more intuitively and to make a comparison with the original HTS-stacked ring magnet, Fig. 4.18 shows the variation of the induced current in the "solid HTS ring". It can be seen clearly that at the start of the magnetization, the current is induced from the outer domains of the "solid HTS ring" and there is nearly no induced current in the inner domains. It follows the rule of the penetration of normal HTS bulk materials' magnetization. As the applied field decreases, more induced current is induced from the outer domains into the inner domains. On the closed side, there is a small blue area that accompanies the entire magnetization process, and gradually moves inward as magnetization progresses. It indicates there is a small reverse current induced inside the closed side, which means there is a small current loop in the closed side. A similar situation can also be seen on the open side, where the inner domains have a reverse current. This phenomenon arises due to the absence of any air gaps between individual domains, enabling the induced current to traverse unimpededly across the entire geometry. Besides, due to the centre hollow space, the open side and closed side are subjected to separated magnetization and can generate local toroidal current respectively. Building on this basis, the existence of an unbalanced trapped field instigates localized magnetization.
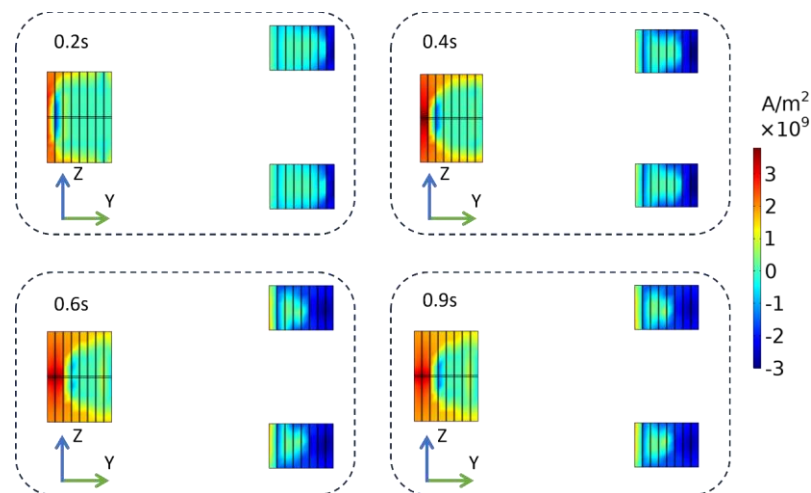
Figure 4.18: The induced current density of the "solid HTS ring" during 4.5 T magnetization

Based on the above analysis, it can be found that under the same field cooling magnetization conditions, the presence or absence of air gaps significantly influences the spatial distribution of the induced current and the central field during magnetization. Building upon this understanding, a comparative analysis of these two models is undertaken, scrutinizing their respective impacts on the overall trapped field. Such an investigation would engender a deeper comprehension of the field trapping characteristics inherent to the HTS-stacked ring magnet, and a deeper understanding of the central field ascent phenomenon.

Fig. 4.19 illustrates the trapped flux distribution of the original HTS-stacked ring magnet model and the "solid ring magnet" model after 4.5 T field cooling magnetization in the y-z plane. To uphold the congruity and hence the comparability of the findings, the methodology and parameters employed for the placement of flux streamlines within the two models are consistently maintained. The method of positioning adheres to a Magnitude Controlled protocol, with the "Minimum distance" and "Maximum distance" set as 0.0025 and 0.05 respectively. The designation for the "First starting point" is configured to be the "Automatic setting". It can be observed that the flux density at the central area of the HTS-stacked ring magnet notably exceeds that associated with the "solid ring magnet" which reaffirms the difference in the central magnetic fields between the two configurations under equivalent magnetization conditions. Contrastingly, the flux density inherent in the HTS domains of the "solid HTS ring" evidently surpasses the flux density at the corresponding positions within the HTS-stacked ring magnet. The induced current in the inner HTS domains plays a pivotal role in affecting the different flux line distributions. The current within these inner domains engenders a magnetic field that is commensurate in strength to that generated by the outer domains. Consequently, the stacked HTS tapes function as a magnetic shield, expelling the flux line from its own body. This can be interpreted as the HTS tapes pushing more flux lines from the magnet's body area towards the central space, thereby amplifying the central flux density. This attribute is posited to hold considerable potential for applications involving trapped fields, given that in most scenarios, only the magnetic field within the central region is functionally utilizable.
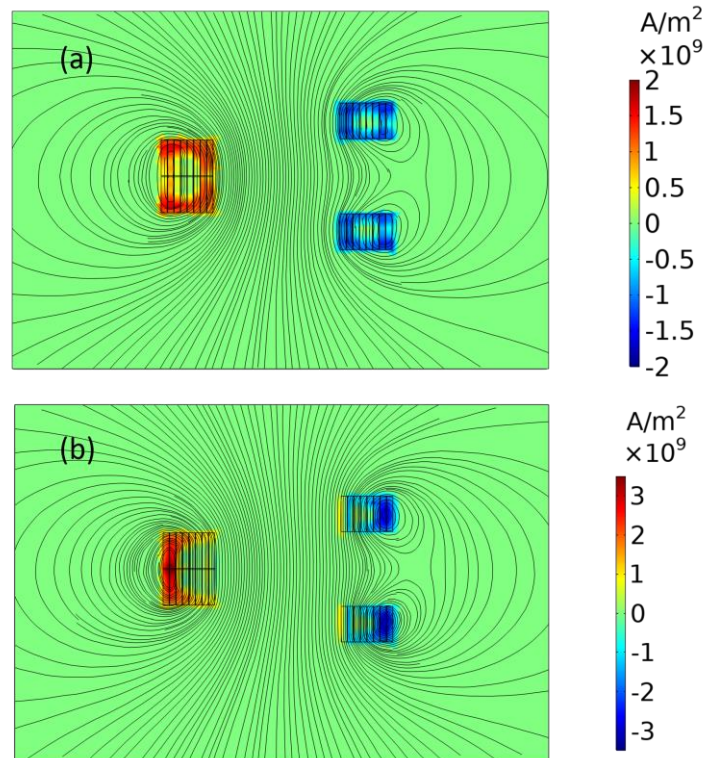
Figure 4.19: Trapped flux distribution of HTS-stacked ring magnet (a) and "solid HTS ring"(b)

4.3.4 Potential of Achieving a Higher Trapped Field Than the Applied Field

The analysis in the previous section indicates that the unique induced current distribution in the HTS-stacked ring magnet is affecting the magnitude of the central trapped field. More specifically, the induced current in the inner tapes equalling that in the outer tapes can make the central trapped ascend during the field cooling magnetization. However, although a central field ascent is observed, it drops after peaking and the final trapped field at the end of magnetization is still lower than the applied field. After figuring out the reason for the field ascent, a thought consequently emerged: is it possible to realize a final trapped magnetic field that exceeds the externally applied magnetic field, a situation similar to the HTS lens without the need for staged magnetization? This section investigates the possibility of achieving a final

trapped field higher than the applied field by the HTS-stacked ring magnet configuration under the field cooling magnetization process.

Given that the construction of the HTS-stacked ring magnet is based on the cumulative layering of sectioned HTS tapes, one important factor intrinsically intertwined with this methodology is the number of these tapes. Upon the introduction of additional tapes, there ensues a consequential increment in both the width and the length of the ring magnet. The elongation is attributable to the requirement for extended tapes with increased central cuts. Such a configuration is indispensable to guarantee that the tapes can be sufficiently stretched to facilitate a congruous stacking process. However, within the confines of this thesis, the size of the comprehensive HTS-stacked ring magnet sample is inherently limited by the dimensions of the bore of the external magnet. Consequently, the direct investigation concerning the effects of increasing the number of tapes is infeasible. Therefore, the examination conducted in this section is underpinned by the application of a numerical modelling tool.
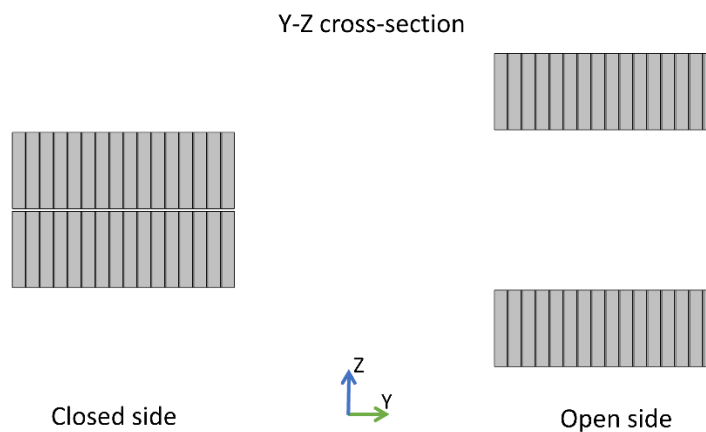
Figure 4.20: The Y-Z cross-section of the HTS-stacked ring magnet with doubled number of tapes

To facilitate the comparison between the trapped field of the HTS-stacked ring magnet before and after increasing the number of tapes, the central distances between the closed side and open side stay the same and the width of the tape is still 12 mm as shown in Fig. 4.20. The other parameters including the external applied field and the field decay rate are also unchanged for the same field cooling magnetization process. The number of tapes is doubled for both the upper and lower layers of the ring magnet.

Fig. 4.21 illustrates the central magnetic field within the double-turn HTS-stacked ring magnet during a 4.5 T magnetization process. Notably, the central field commences its escalation concomitantly with the decrement of the externally applied field. The central field reaches its highest value at 5.2 T when the applied field measures around 1 T, thereby implying that the trapped field at this moment is 4.2 T. Subsequent to its peak, the central field declines to approximately 5.13 T as the applied field goes to zero. After the relaxation process, a residual 4.95 T remains at the centre, representing the actual trapped field. This final trapped field surpasses the applied field by an approximate margin of 0.4 T, a phenomenon unseen in the field cooling magnetization process of conventional HTS bulks or stacks. This thereby affirms, via numerical computation, that a final trapped field exceeding the initial applied field is attainable by field cooling magnetization of the HTS-stacked ring magnet with proper designs.
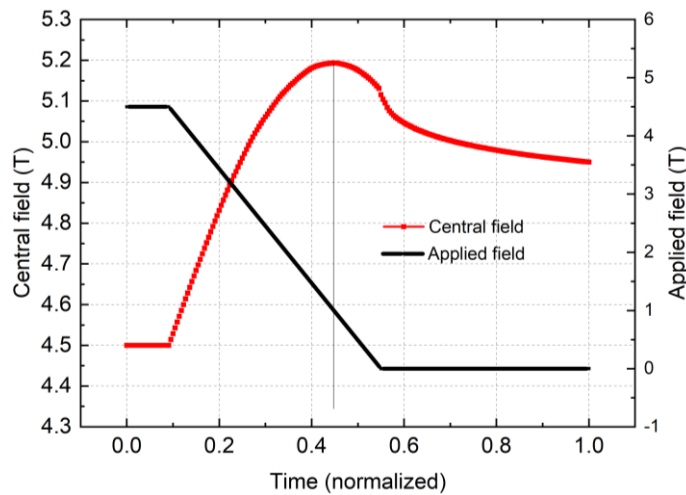
Figure 4.21: Central field of the double-turn HTS-stacked ring magnets with and without HTS stack inserts.

Fig. 4.22 presents the x-axis induced current in the cross-section of the double-turn model at the end of relaxation. While the pattern of the induced current distribution echoes that of the model of the original size, the doubling of the tape number has amplified the influence of induced current within the inner domains. This intensification is evident as a great number of flux lines are propelled towards the centre region, which consequently results in an increased trapped field within the central area.
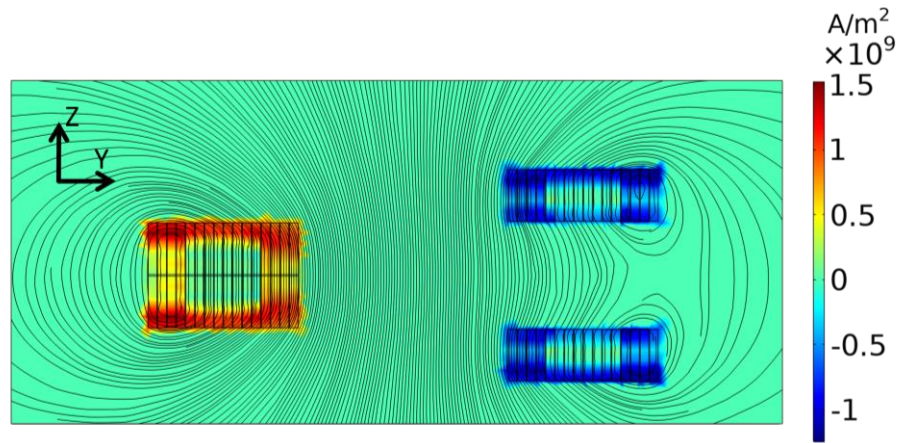
Figure 4.22: Induced current and trapped flux of the double-turn HTS-stacked ring magnet after 4.5 T magnetization

4.3.5 Analysis of Trapping Capability Based on Magnetic Flux

The fundamental principle underlying magnetic field trapping is the initiation of induced currents and their associated magnetic flux, while magnetic field (flux density) is more widely used for measuring the capability of the trapped field. In this section, an investigation based on the trapped magnetic flux field distribution is conducted for a more comprehensive understanding of the field ascent phenomenon as well as the HTS-stacked ring magnet. The HTS-stacked ring magnet in this thesis has an asymmetric geometry in the y-z plane which complicates the analysis of magnetic flux and magnetic field distribution. Thereby in this section, it is assumed the HTS-stacked ring magnet has an infinite length so that the gap on the open side can be reduced to match that of the closed side. Based on the assumption, 2D homogenised models are built as shown in Fig. 4.23. Following the parallel stacking method, the induced current within the stacked HTS tapes follows the equation $Cn+Cn'=0$. As a point of comparison, a model with the current restriction of $C1+C2+\ldots+C8=C1'+C2'+\ldots+C8'$, which behaves like normal HTS bulk material, is also calculated.
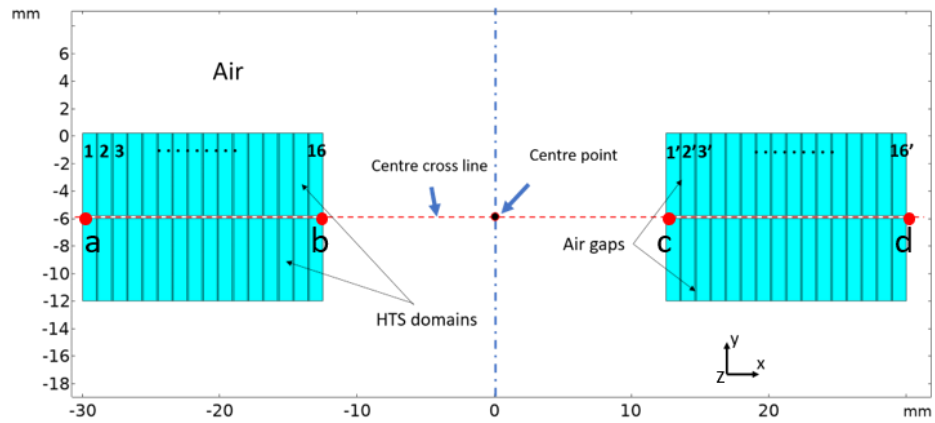
Figure 4.23: 2D HTS-stacked ring models with infinite length.

Fig. 4.24 and Fig. 4.25 respectively depict the central field profiles of the two models during a 4.5 T field cooling magnetization process. The central field of the stacked HTS tapes continuously ascends throughout magnetization, in contrast to the steadily declining central field of the HTS bulk material, which begins to diminish at the onset of magnetization. At the end of magnetization, the central trapped field approximates 5.2 T, surpassing the initial 4.5 T, whereas the HTS bulk material model traps less than 4.2 T. These observations reaffirm the practicability of achieving a trapped field that outstrips the applied field.
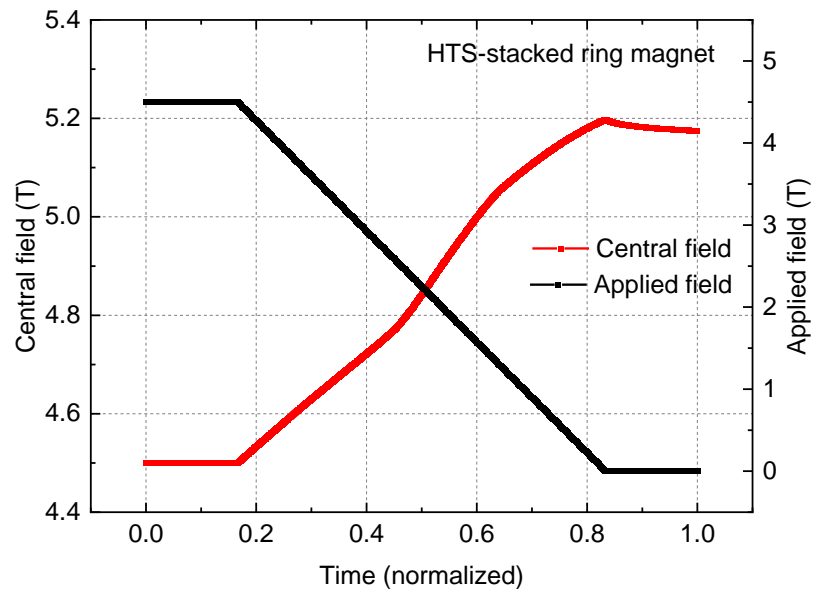
Figure 4.24: Central field of the 2D model of the HTS-stacked rings
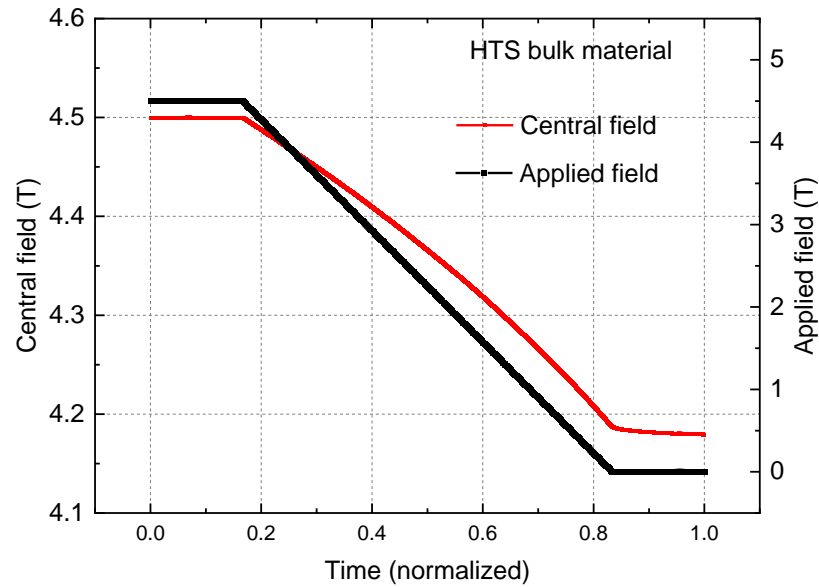
Figure 4.25: Central field of the 2D model of the HTS bulk material

In addition to the central field, Fig. 4.26 delineates the distribution of trapped fields (By) along the central cross-lines for both models, with the dashed area marking the positions of the HTS domains. A conspicuous leap in the central region is observed on the black line, signifying the trapped field of stacked HTS tapes. This field, manifested as a concave shape, is notably higher in the central area. Meanwhile, the field average within the HTS tape area is much lower, falling below 2 T. In contrast, the red line, representing the trapped field of the HTS bulk material, exhibits a substantially uniform distribution, where the trapped field within the HTS area approximates the initially applied field. This dichotomy highlights a distinct phenomenon - the segregated and stacked HTS tapes appear to repel more flux lines towards the central area, while conventional HTS bulk materials can retain more flux within themselves. It should be noted that the HTS materials are not fully penetrated in this scenario. With higher applied fields which are strong enough to fully penetrate the HTS-stacked ring magnets, the final trapped field can be further increased, but not able to exceed the initial applied field.
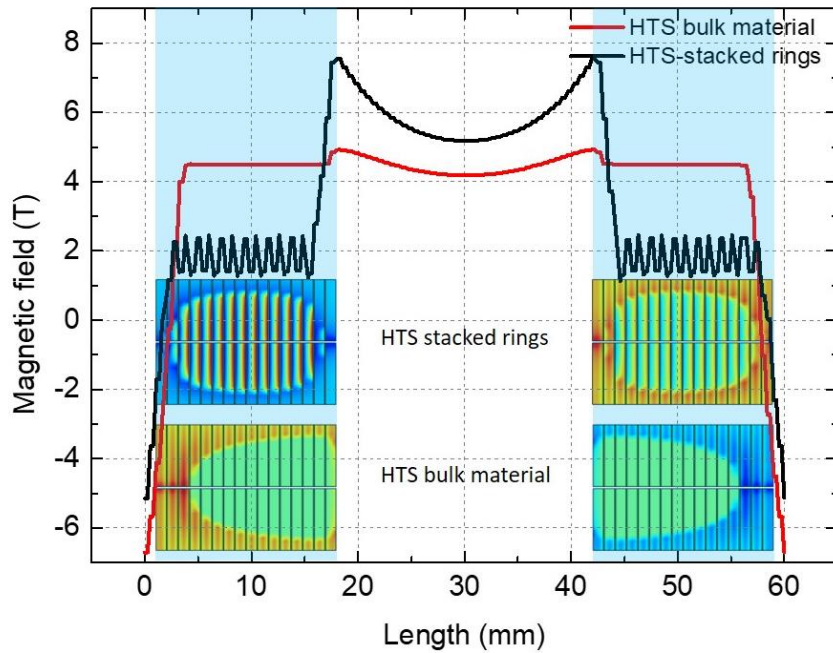
Figure 4.26: Distributions of trapped fields at the centre cross line.

In Fig. 4.27, the induced current in both models is depicted. Void of any asymmetric geometric interference, it becomes evident that the stacked HTS tapes induce currents that establish a distinct periphery around the HTS tapes. In stark contrast, the HTS bulk material demonstrates a heightened resistance to the induction of currents, complicating their penetration into the bulk material's interior.
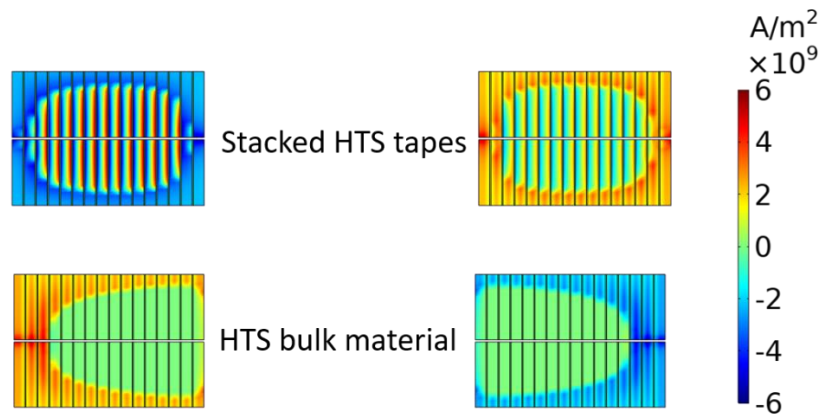
Figure 4.27: Induced currents of the 2D models

Benefiting from the symmetrical geometric distribution of the 2D models, it is more conducive to calculate and compare the flux based on a uniform measurement metric. Fig. 4.28 depicts the change in y-axis magnetic flux across the centre cross line, which

covers the width of the model (from point a to point d as shown in Fig. 4.22). Since they are 2D models, the magnitude of magnetic flux along the centre cross line is derived through the integration of the magnetic field density (By) over the width. It can be expressed by the following formula:

$$\Phi_z = \int_{-\frac{width}{2}}^{\frac{width}{2}} B_z \, dr \tag{4.1}$$

The normal unit of total magnetic flux (Φ_z) is Wb, but since it is a 2D model, Wb/m is applied here meaning the flux in the 1-meter depth of the z axis. In Fig. 4.28, initially, both models have the same magnetic flux which is given by the external field. Then, the flux of the stacked HTS tapes decreases more quickly, resulting in a lower trapped flux along the centre cross line. The flux on the centre cross line of the stacked HTS tapes is 4.5% lower than that of the HTS bulk material model. This indicates that even though the stacked HTS tapes can achieve a higher centre trapped field, it does not necessarily mean a higher total trapped flux in the entire centre area.
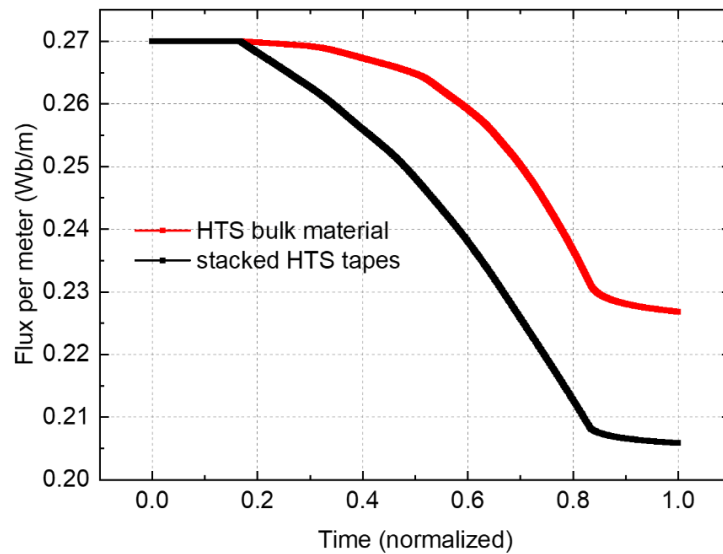
Figure 4.28: Magnetic flux through the centre cross line (point a to point d) during magnetization.

In contrast, Fig. 4.29 displays the flux along the inner central cross line (point b to point c) for both models. The flux along the inner central cross line in the case of the stacked HTS tapes manifests a progressive growth trend from the beginning of

magnetization. Conversely, the flux of the HTS bulk material displays relative stability, with a subtle decline noticeable over time.
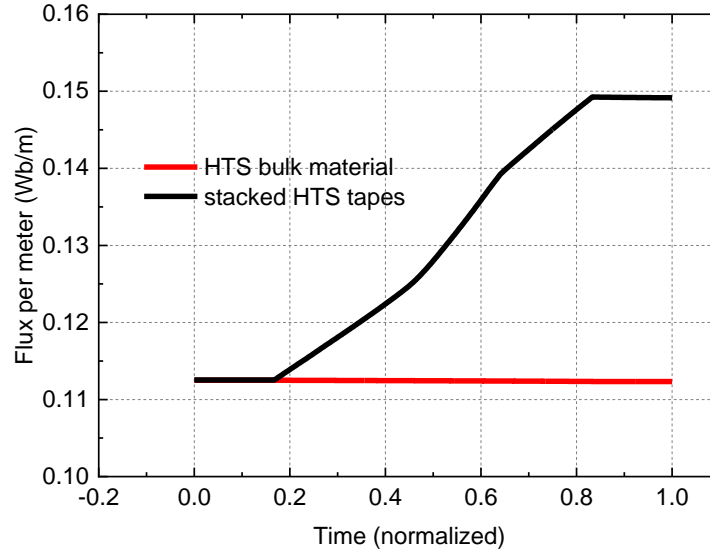
Figure 4.29: Magnetic flux through the centre cross line (point b to point c) during magnetization.

The final magnetic energy E_m of the two models are calculated based on the equation as follows:

$$E_m = \frac{1}{2} \int H \cdot B \, dv \tag{4.2}$$

Where v is the space for the magnetic field, which is the entire domain of the model. Since they are 2D models, the default depth (z axis) is set at 1 meter, so the unit for the magnetic energy is J/m. The final magnetic energy of the stacked HTS tapes is 15661 J/m, while that of the HTS bulk material is 16056 J/m, which does not show a big difference.

In conjunction with the above analysis, it can be inferred that under equivalent field cooling magnetization conditions, the stacked HTS tapes or HTS-stacked ring magnets do not necessarily trap more magnetic flux or magnetic energy. However, they do have the capacity to concentrate a greater amount of magnetic flux into the central hollow region. This leads to a central trapped magnetic field that surpasses that of traditional HTS bulk materials and may even exceed the initial applied magnetic field.

4.4 Conclusion

This chapter delved into the magnetization mechanism of the HTS-stacked ring magnet via experiments and numerical modelling, yielding several key insights:

Central field ascent phenomenon: During field cooling with a 4.5 T field at 25 K, an initial central field rise, followed by a decrease to a final trapped field of 3.79 T, was noticed. Such a rise is unprecedented in traditional trapped field HTS magnets. Observed temperature shifts ruled out heating as a factor influencing this field value.

Surface trapped field distribution: Post-magnetization, the trapped field 5 mm above the sample displayed an asymmetry, attributed to the HTS-stacked ring magnet's asymmetric configuration.

Magnetization mechanism: A 3D homogenized model, validated with experimental data, revealed that the HTS-stacked ring magnet simultaneously induces currents in both inner and outer layers, diverging from traditional HTS bulk behaviour.

Comparative investigation between the HTS bulk materials and HTS-stacked ring magnets: The central field ascent in the HTS-stacked ring magnet is traced to an enhanced induced current in its inner layers. Unlike HTS-stacked ring magnets, HTS bulk materials are penetrated from their exterior to their core.

Prospects for enhanced trapped field: Simulations, informed by the central field ascent rationale, indicate that increasing the tape number can enable the HTS-stacked ring magnet to trap a central field exceeding the applied one. Compared to HTS bulk materials, the HTS-stacked ring magnet can produce a more intensified central field, though the bulk material retains more magnetic flux. However, in terms of total trapped flux, the two are comparable.

Chapter 5. Hybrid HTS-Stacked Ring Magnet with HTS Inserts

5.1 Introduction

The HTS-stacked ring magnet discussed in the preceding chapter demonstrates considerable field trapping capabilities, achieving a central trapped field of 3.79 T. Nonetheless, when contrasted with conventional HTS bulk materials and stacks, the field trapped by the HTS-stacked ring magnet is substantially lower. Moreover, the presence of an internal void within the HTS-stacked ring magnet reduces the total quantity of HTS material employed per unit volume. Consequently, despite its considerable diameter, the magnet's field trapping efficiency is compromised due to the reduced usage of HTS material per volume. This suggests that the design of the HTS-stacked ring magnet, while advantageous in certain respects, has inherent limitations that impact its overall performance and efficiency. Further research and optimization could explore ways to address these issues and improve the magnet's trapped field capabilities.

The concept of amalgamating the benefits of HTS-stacked ring magnets and HTS bulks or stacks emerges as a natural progression to maximize the field trapping capabilities. This integration aims to yield more extensive trapped field distributions compared to those produced by HTS bulks and stacks, while also achieving a higher trapped field than that generated by the HTS-stacked ring magnet. This approach represents a compelling compromise that capitalizes on the strengths of both configurations. It seeks to harness the expansive field distributions of HTS-stacked ring magnets, in conjunction with the higher trapped fields found in HTS bulks and stacks. The resultant design may offer the potential to surpass the performance of either individual design, or as such, is a promising avenue for further exploration in the pursuit of superior field trapping capabilities.

Chapter 5. Hybrid HTS-Stacked Ring Magnet with HTS Inserts

As discussed in Chapter 2, in potential applications of trapped fields, there is typically a requirement for both higher trapped fields and a robust design. Consequently, a discernible gap exists between the findings of previous studies [38], [39], [174], [175] and the research presented in this chapter. This study aims to bridge this gap by developing a robust design that could potentially achieve higher trapped fields, thereby aligning more closely with practical application requirements. This chapter commences with experimental observations and building upon the sample from the previous chapter, compares the difference in trapped fields between hybrid and non-hybrid HTS-stacked ring magnets. Subsequently, the trapped fields and magnetization mechanisms are investigated through simulations, with a particular focus on the electromagnetic interactions between the HTS-stacked ring magnet and the inserted HTS materials during the magnetization process. Two types of HTS materials, HTS bulks and HTS stacks, are utilized as inserts for the hybrid magnet, enabling a comprehensive study of the field cooling magnetization of hybrid magnets.

5.2 Hybrid HTS-Stacked Ring Magnet Samples

In this chapter, two variants of hybrid HTS-stacked ring magnets are fabricated and examined. One model is hybridized with HTS stacks, while the other employs HTS bulks. HTS stacks, typically constructed by slicing second-generation (2G) HTS tapes into identical, smaller pieces, and then stacking them together, exhibit greater mechanical robustness compared to HTS bulk materials, owing to the protective effects of substrate layers, buffer layers, and stabilizer layers. However, the volume of HTS materials in the HTS tapes is significantly less, resulting in a comparatively lower engineering current density than that observed in HTS bulks.

5.2.1 Hybrid HTS-Stacked Ring Magnet with HTS Stacks

The hybrid HTS-stacked ring magnet with HTS stacks under study is predicated upon the design examined in Chapter 4. This HTS-stacked ring magnet showcased a central field ascent during the field cooling magnetization process. For this study, HTS stacks

crafted from 12 mm S-Innovations tapes were utilized, each furnished with a 10-15 µm PbSn coating on both sides, as displayed in Fig. 5.1.

Figure 5.1: A piece of HTS tape with PbSn coating

Each stack is composed of 100 cut tapes, each measuring 20 mm in length and 12 mm in width, a size compatible with the central space of the brass sample holder. These tape pieces were then stacked together, enveloped in Kapton tape, and secured with a custom pressure mould. As seen in Fig. 5.2, the mould is equipped with four springs that apply pressure to the HTS stacks. To minimize inter-layer air pockets and enhance thermal conductivity, the HTS stacks and the pressure mould were placed in an oven to solder the HTS tapes together. The temperature schedule for the heat treatment is outlined in Fig. 5.3. The heating temperature was calibrated to 210°C—sufficient to melt the PbSn soldering layers, yet not overly high to risk degradation of the HTS tape. Each completed HTS stack possesses an approximate thickness of 11 mm.

Figure 5.2: The pressure mould for fabrication of HTS stacks
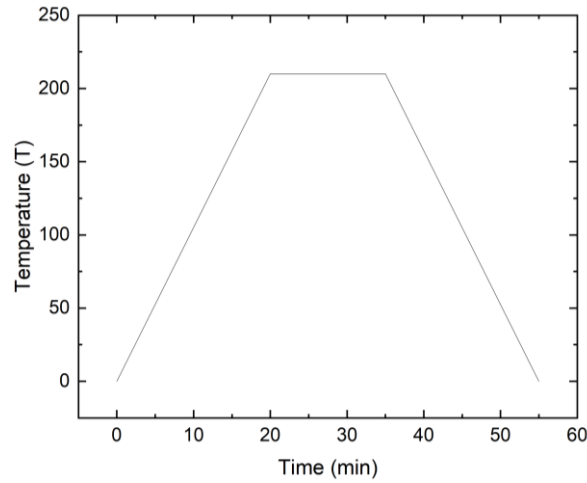
Figure 5.3: Temperature schedule for heating treatment

The soldered HTS stacks are depicted in Fig. 5.4. Following soldering, they were positioned within the brass sample holder. A Hall sensor, utilized to measure the central field, was affixed between the two HTS stacks. All other components, including the brass blocks, Cernox SD sensors and other Hall sensors, remained consistent with their arrangements in Chapter 4. To conclude the preparation process, both the HTS-stacked ring magnet and the HTS stacks were impregnated with a mixture of paraffin wax and aluminium nitride powder.

Figure 5.4: Soldered HTS stacks

5.2.2 Hybrid HTS-Stacked Ring Magnet with HTS Bulks.

While HTS stacks have showcased exceptional field trapping performance, HTS bulks, specifically YBCO and GdBCO, are more commonly utilized to achieve robust and powerful trapped fields. Therefore, a hybrid HTS-stacked ring magnet sample with HTS bulks, targeting a higher trapped field, is fabricated and examined. For this investigation, two YBCO HTS bulks supplied by ATZ GmbH are used. These bulks possess dimensions of 16 mm in diameter and 12 mm in thickness. Their performance was tested through FC magnetization at 77 K without any reinforcement process, with a single HTS bulk trapping a field of 0.8 T. Given that the shape of the HTS inserts transitioned from a cuboid to a cylinder, the sample holder required a corresponding adjustment. For this sample, a brass sample holder featuring a hollow central bolt, which can hold the HTS bulk inserts, was employed as depicted in Fig. 5.5. In this hybrid sample, the HTS-stacked ring magnet was fabricated using two layers of HTS rings composed of 12 mm Superpower M4 AP tapes. Each layer consists of 100 HTS rings, yielding a total of 200 HTS rings, as illustrated in Fig. 5.5. The tapes exhibited a critical current of 520 A at 77 K. The same Hall sensor (Lakeshore HGT-2101) from the previous samples, is placed between the two HTS bulks.
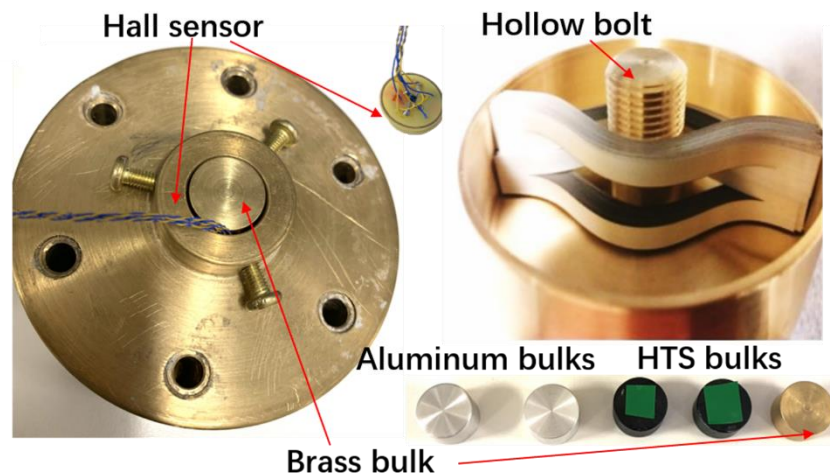
Figure 5.5: Hybrid HTS-stacked ring magnet with HTS bulks

5.3. Magnetization of Hybrid HTS-Stacked Ring Magnet with HTS Stack Inserts

The hybrid HTS-stacked ring magnet, integrated with HTS stacks, was subjected to field cooling magnetization with applied fields of 5 T and 8.5 T, respectively. These processes utilized the same Royce wide bore magnet, with the temperature set at 25 K. The ramping rate of the applied fields is controlled at 0.075 T/min. Maintaining a consistent configuration for the magnetization of the hybrid sample enhances the comparability with prior studies on the HTS-stacked ring magnet.

5.3.1. 6.2 T Trapped Field by The Hybrid HTS-Stacked Ring Magnet with HTS Stack Inserts
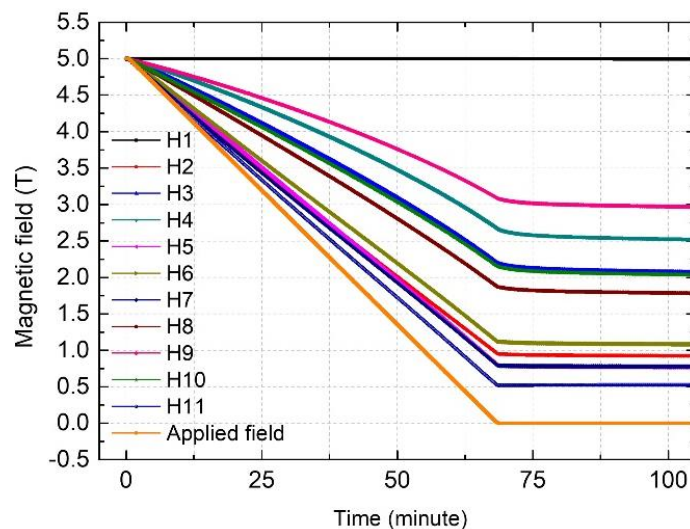
Figure 5.6: Field values during 5 T FC magnetization of the hybrid HTS-stacked ring magnet with HTS stacks

The field changes, as recorded by the Hall sensors during the 5 T magnetization, are illustrated in Fig. 5.6. The magnetic field at the sample's centre remained consistent throughout the magnetization with a 5 T applied field, and no central field ascent is observed during magnetization. In the field cooling magnetization process, if the trapped field aligns with the initial applied field, it typically signifies that the HTS

78

material hasn't been fully penetrated. This implies that the HTS material has only undergone partial magnetization. The unchanging central field of the hybrid sample hints that it might not have achieved full penetration, suggesting there is room for trapping a greater field with an increased external field. The final trapped fields from Hall sensor 2 to Hall sensor 11 are presented in Fig. 5.7. When contrasted with the HTS-stacked ring magnet (as seen in Fig. 4.2), the trapped fields around the outer perimeter don't show significant growth, but those closer to the inner circle, especially H9, exhibit a heightened trapped field. Specifically, the field at H9 rose from 2.35 T to 2.95 T.
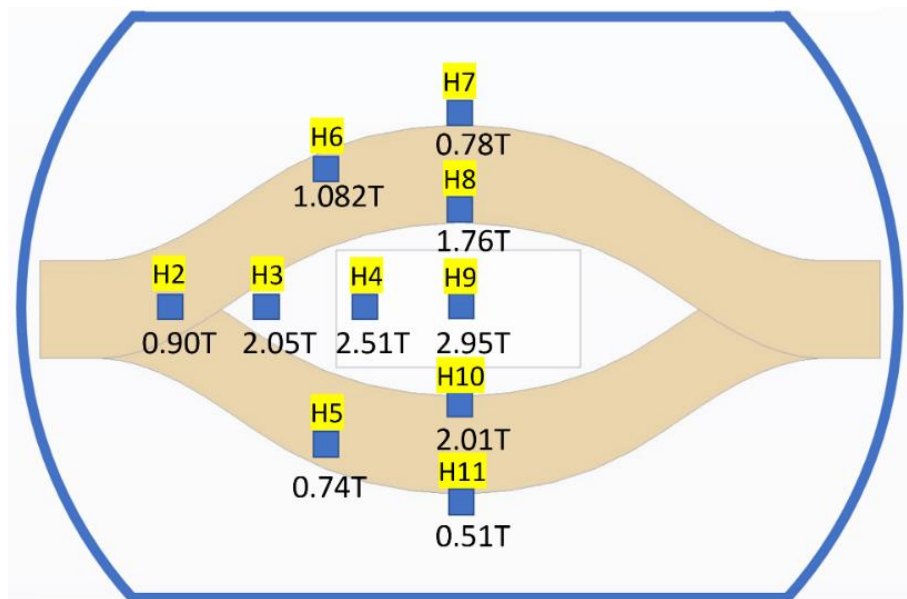
Figure 5.7: The final trapped fields from Hall sensor 2 to Hall sensor 11 after 5 T magnetization

Because the 5 T applied field was unable to completely penetrate the hybrid sample, the magnitude of the applied magnetic field for magnetization was increased to 8.5 T. It's important to mention that before the 8.5 T magnetization, the sample was heated to a stable 100 K to ensure the HTS materials were completely quenched. The corresponding magnetic field readings from the 11 Hall sensors are depicted in Fig. 5.8.
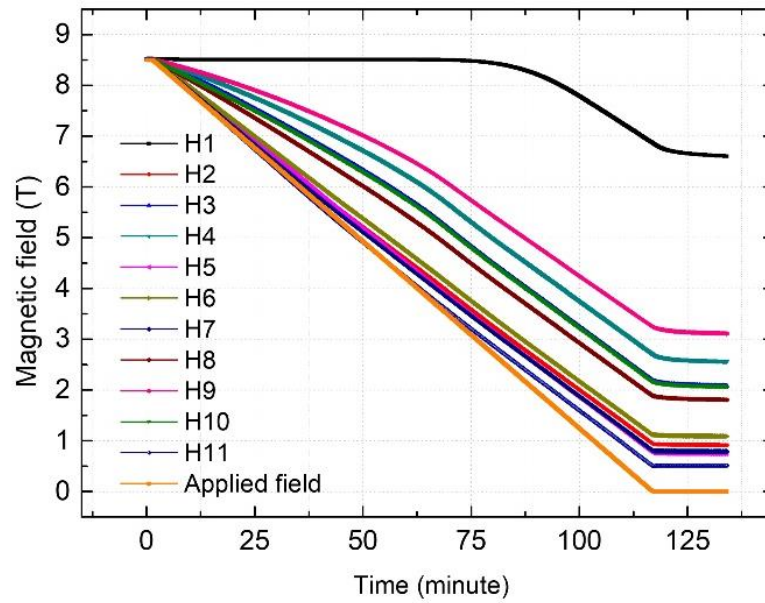
Figure 5.8: Field values during 8.5 T FC magnetization of the hybrid HTS-stacked ring magnet

When subjected to the increased applied field, the hybrid sample starts to show signs of complete penetration. This is evidenced by a decline in the central magnetic field before the termination of the magnetization process as shown in Fig. 5.8. It indicates that the sample has achieved the highest trapped field, so magnetizations with higher applied fields were not conducted. The final magnetic field trapped at the centre amounted to 6.6 T. By checking the curve of the central field throughout the entire procedure, it can be sure again that there is no ascending trend for the central field of the hybrid HTS-stacked ring magnet during field cooling magnetization.
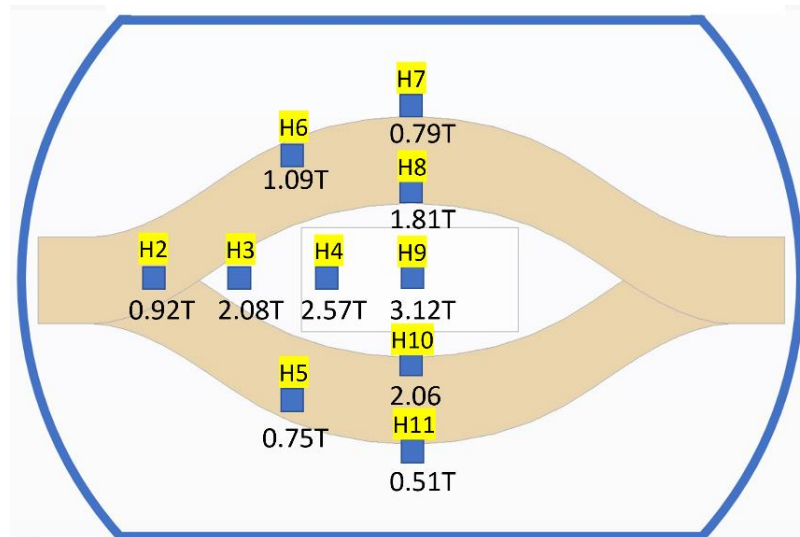
Figure 5.9: The final trapped fields from Hall sensor 2 to Hall sensor 11 after 8.5 T magnetization

As illustrated in Fig. 5.9, following magnetization with an escalated applied field, the magnetic fields at the outer circle exhibit negligible alterations when compared with the results of 5 T magnetization, whilst the central trapped field increases from 2.95 T to 3.12 T. This consolidates the notion that the HTS stacks inserted in the centre impart marginal influence on the field dispersion in the hybrid HTS-stacked ring magnet's outer region, primarily bolstering the magnitude of the centrally trapped field. Moreover, even when compared with findings from Chapter 4, the enhancement of the trapped field in the sample's outer region remains minimal.

5.3.2 Temperature Variation of The Hybrid HTS Ring Magnet with HTS Stacks

Fig. 5.10 displays the temperatures recorded by the Cernox sensors during the 5T magnetization process. Both the sample centre and the sample cover exhibit a minor temperature increase, consistent with previous experiments. The temperatures start to rise towards the end of magnetization and peak when the applied field reaches zero. The temperature fluctuations for this process remain under 1 K, similar to the magnetization of the HTS-stacked ring magnet, which can hardly affect the performance of the centre Hall sensor.
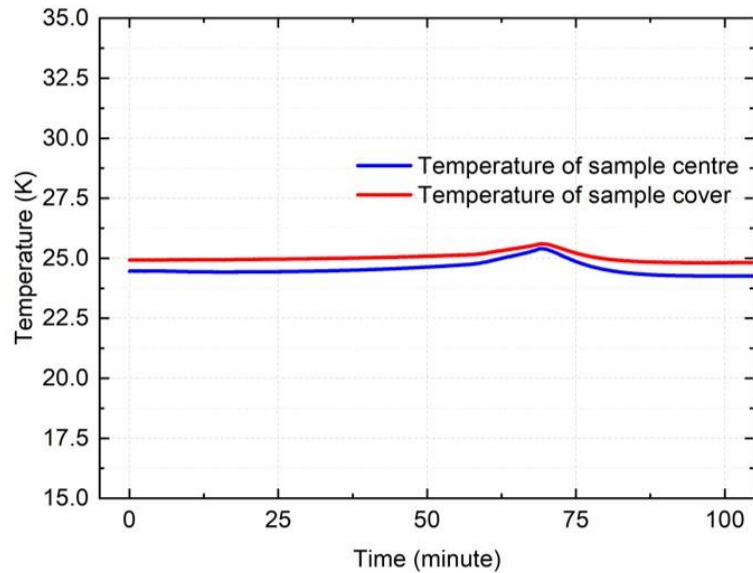
Figure 5.10: Temperatures recorded by the Cernox sensors during the 5T magnetization

The temperatures at the cover and the centre during 8.5T magnetization are shown in Fig. 5.11. The temperature changes exhibit a trend of initial rise, followed by stabilization, and finally, a return to the initial set value. During the temperature stabilization phase, there is a corresponding decrease in the central magnetic field. This suggests that at this point, the superconducting material of the magnet is nearing complete penetration, with the induced current in the superconducting material no longer increasing. Other metallic parts may still be generating a small amount of heat until the applied magnetic field is entirely nullified. It's important to note that as the sample's temperature was set at 25 K, the amount of cold helium gas under the bottom of the sample would adjust automatically based on the temperature. Hence, these temperature changes can only serve for qualitative analysis and cannot be used for quantitative analysis of the magnitude and changes of the induced current in the sample.
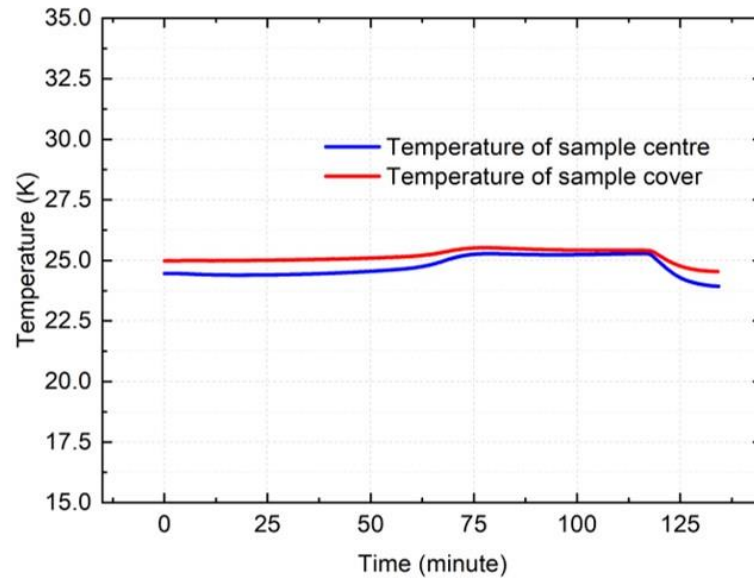
Figure 5.11: Temperatures recorded by the Cernox sensors during the 8.5T magnetization

5.3.3 Disappearance of Central field Ascent with HTS Stack Inserts

In Chapter 4, when the HTS-stacked ring magnet underwent magnetization under a 4.5 T applied field, there was a noticeable increase in the central field, accompanied by a subtle temperature change. Given the marginal extent of this temperature fluctuation, it was inferred that the heating of the Hall sensor wasn't responsible for the central field rise. In this chapter, similar temperature shifts are observed during the magnetization of the hybrid HTS-stacked ring magnet. Yet, contrary to the earlier observations, the central fields here do not display any upward shift. This leads to an unequivocal conclusion that the central field ascent in the HTS-stacked ring magnet sample is not an outcome of the central Hall sensor getting heated. Furthermore, once the HTS stacks are integrated into the centre of the HTS-stacked ring magnet, the trajectory of the central field remains unchanged, regardless of the degree of penetration achieved by the hybrid sample. Thus, it can be concluded that the HTS stack inserts can eliminate the phenomenon of the central field rising.

5.4 Magnetization Characteristics of Hybrid HTS-Stacked Ring Magnet with HTS Stacks

5.4.1 Verification of the Numerical Modelling

Compared with the modelling of the HTS-stacked ring magnet, there are additional two HTS stacks in the hybrid HTS-stacked ring magnet required to be considered. Since the HTS stacks are also fabricated with HTS tape materials, homogenized modelling is also used for calculating the HTS stacks. As shown in Fig. 5.12, there are 20 separated HTS domains in each HTS stack. An air gap is between each domain and one domain represents 5 short HTS tapes. The data of the field-dependent critical current ($J_c = (\theta, B)$) of the S-innovation tapes is acquired from the measurement examined by Wimbush, et al [199], [200]. It should be noted that due to the cutting, heating, and pressing of the HTS tapes for the stacks, the actual critical current might be diminished. Therefore, a lift factor of 0.78 is used for calculations.
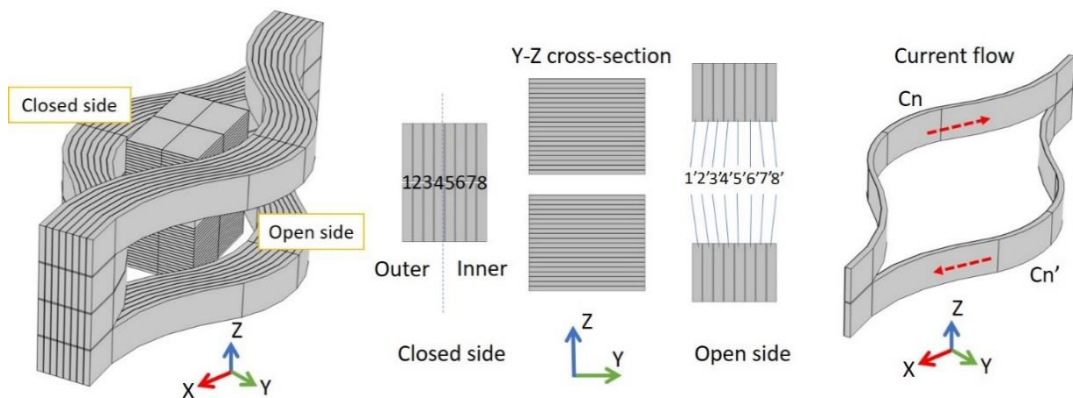
Figure 5.12: Diagram of hybrid HTS-stacked ring magnet and current flow
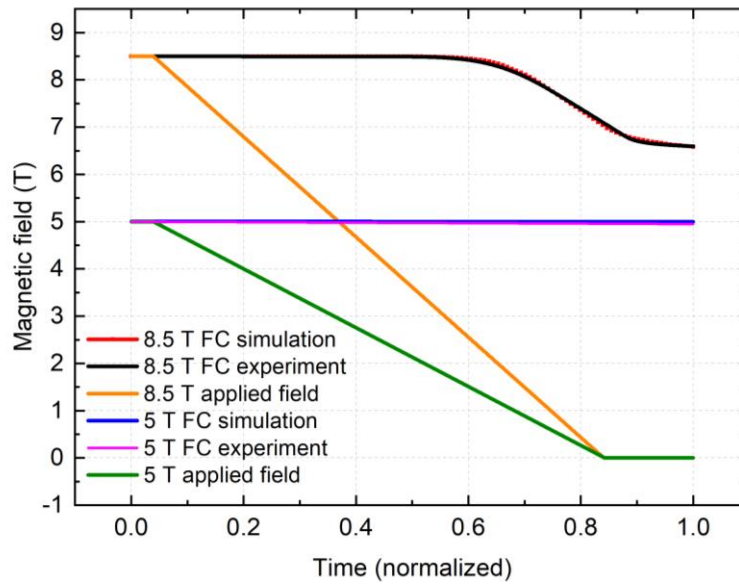
Figure 5.13: Central fields of the hybrid HTS-stacked ring magnet with HTS stack inserts during the 5T and 8.5T magnetizations

After the calculation, the central fields of the hybrid HTS-stacked ring magnet with HTS stack inserts during the 5 T and 8.5 T magnetizations are presented in Fig. 5.13. The simulation results for both magnetization levels align closely with the experimental results. This consistency strengthens the credibility of the numerical model. Building on the methods detailed in Chapter 4, this numerical approach will be further employed in subsequent sections of this chapter. The aim is to elucidate the underlying factors leading to the observed difference in central field trends and to gain a deeper understanding of the magnetization properties of the hybrid HTS-stacked ring magnet.

5.4.2 Comparative Analysis Between the Magnetizations of Hybrid and Non-Hybrid HTS-Stacked Ring Magnets Under 4.5 T Applied Field.

As mentioned above, with the presence of the HTS stacks, the field in the centre ceases to rise during 5 T and 8.5 T magnetizations. To figure out the reason, the study begins with the induced current in the HTS-stacked rings of the hybrid HTS-stacked ring magnet. In the study of HTS material magnetizations, the situation of the induced current can also be considered as the field penetration.

To carry out a comparative study with the previous HTS-stacked ring magnet magnetization, the modelling of the hybrid HTS-stacked ring magnet with a 4.5 T applied field is first conducted.
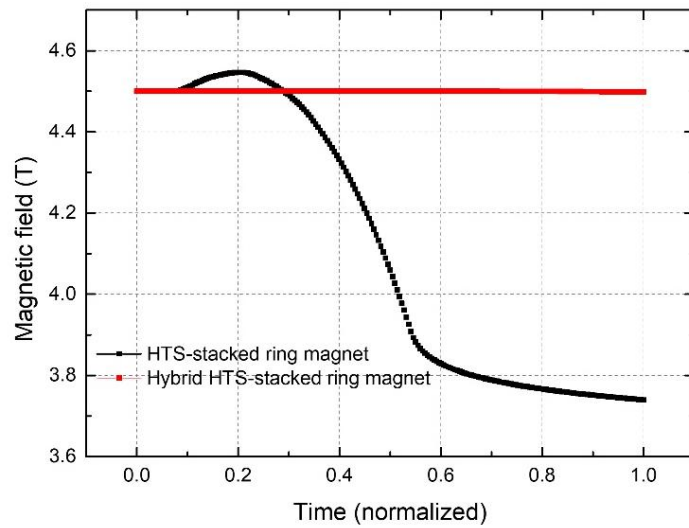
Figure 5.14: Simulation results of central fields of the hybrid HTS-stacked ring magnet and the HTS-stacked ring magnet

The central fields of the hybrid HTS-stacked ring magnet and the HTS-stacked ring magnet are shown in Fig. 5.14. The central field of the hybrid one exhibits a stable value, which is within expectations. Next is to investigate the induced current in the hybrid HTS-stacked ring magnet. To measure the induced current in the inserted HTS stacks, each HTS stack is divided symmetrically into four parts as shown in Fig. 5.15. Since there is a circulating current in each of the tapes of the HTS stacks, the induced current in the HTS stacks is calculated by surface integration of the induced current density in half of the cross-section which is represented by the yellow section in Fig. 5.15.
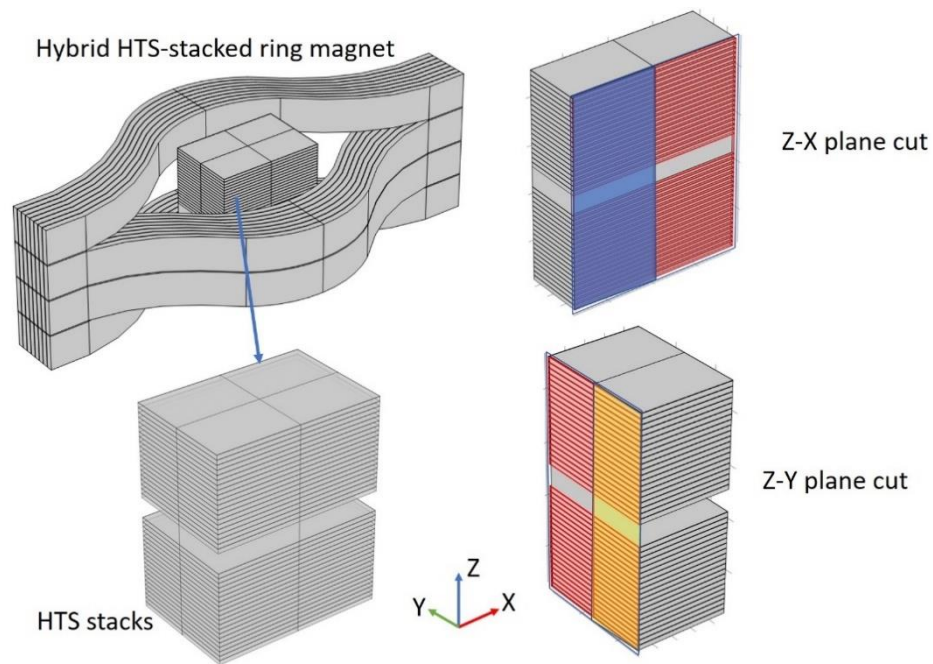
Figure 5.15: Diagram of the cross-sections of the HTS stacks

The total induced current in the hybrid HTS-stacked ring magnet can be divided into 2 parts. One is the induced current in the HTS-stacked rings and another is the induced current in the HTS stacks. For the HTS-stacked ring magnet, there is only induced current in the HTS-stacked rings. The total induced current in the HTS-stacked rings is calculated by surface integration of the induced current density in the green area as shown in Fig. 5.16.
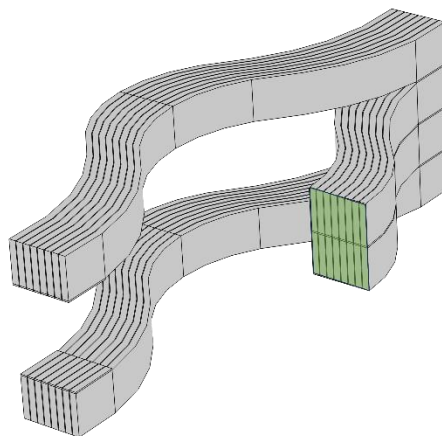
Figure 5.16: The cross-section of HTS-stacked rings for current calculations

The total induced currents for both models are illustrated in Fig. 5.17. The total current of the hybrid HTS-stacked ring magnet equals the sum of the red curve and the blue curve, while the black curve represents the total induced current in the HTS-stacked ring magnet. In the case of a hybrid design, the total induced current within the HTS-stacked rings (red) is slightly reduced, and there is induced current shared in the HTS stacks (black) during the magnetization. The sum of the induced current in the hybrid design is evidently higher than that in the non-hybrid, which is consistent with the trapped fields by the two designs.
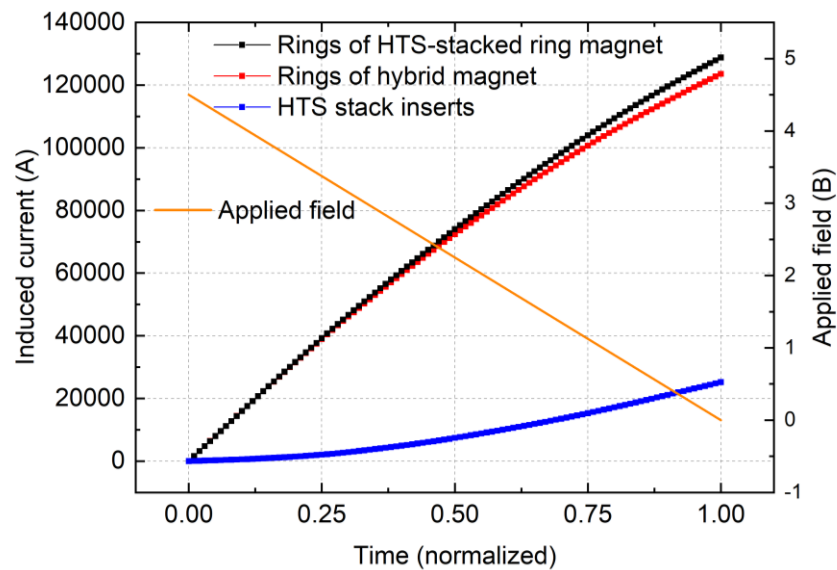
Figure 5.17: Total induced current in the HTS-stacked rings and the induced current in the HTS stacks.

The induced current distributions at the end of the magnetizations of the two models are shown in Fig. 5.18. The distribution and magnitude of the induced currents in the HTS-stacked rings of the two models exhibit considerable similarity, which indicates the magnetization characteristics of the HTS-stacked rings remain largely unaffected after inserting the HTS stacks. Due to the asymmetric geometry of HTS-stacked rings, the HTS stacks are penetrated (magnetized) asymmetrically in the z-y plane, but it still follows the penetration law of ordinary HTS materials, i.e., the penetration occurs from the outside to the inside and the integration of the current density of each half of the HTS stacks should be equal.
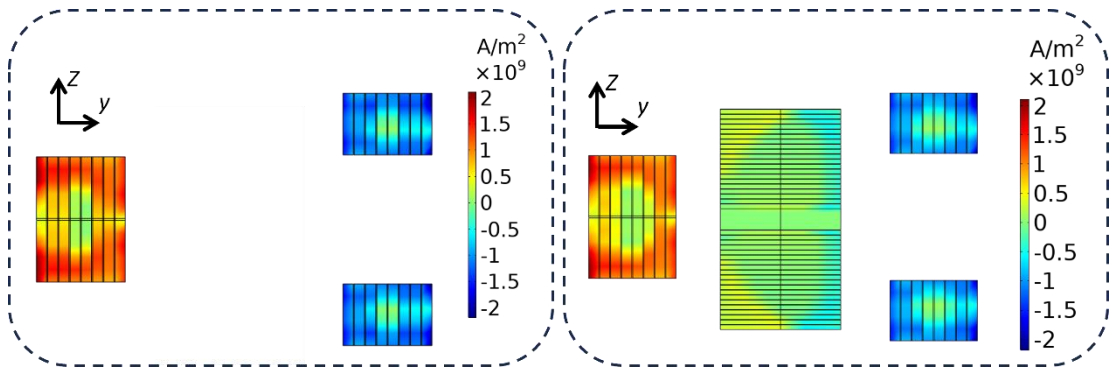
Figure 5.18: Induced current in the HTS-stacked ring magnet (left) and the hybrid HTS-stacked ring magnet (right) after 4.5 T magnetization

Fig. 5.19 illustrates the induced currents within each HTS domain for both models during 4.5 T magnetizations. The conventions used to designate the currents in the HTS domains of the two designs remain in alignment with the definitions provided in Chapter 4. At the outset of magnetization, the generation and evolution of induced currents in corresponding regions between the two models exhibit close resemblance. However, as magnetization continues, there is a discernible decrease in the induced currents in the innermost domains of the hybrid design, specifically in domains C7 and C8. These domains predominantly influence the central field, and this decrement is attributed to the incorporation of HTS stack inserts. This attenuation could potentially stem from a diminished critical current of the HTS-stacked rings as a result of an enhanced trapped field, a phenomenon that will be explored in subsequent sections. Drawing from the induced current analyses, it's plausible to posit that the concurrent influences of diminished current in the inner HTS-stacked rings and current distribution within the HTS stacks collectively determine the trajectory of the central field in the hybrid HTS-stacked ring magnet.
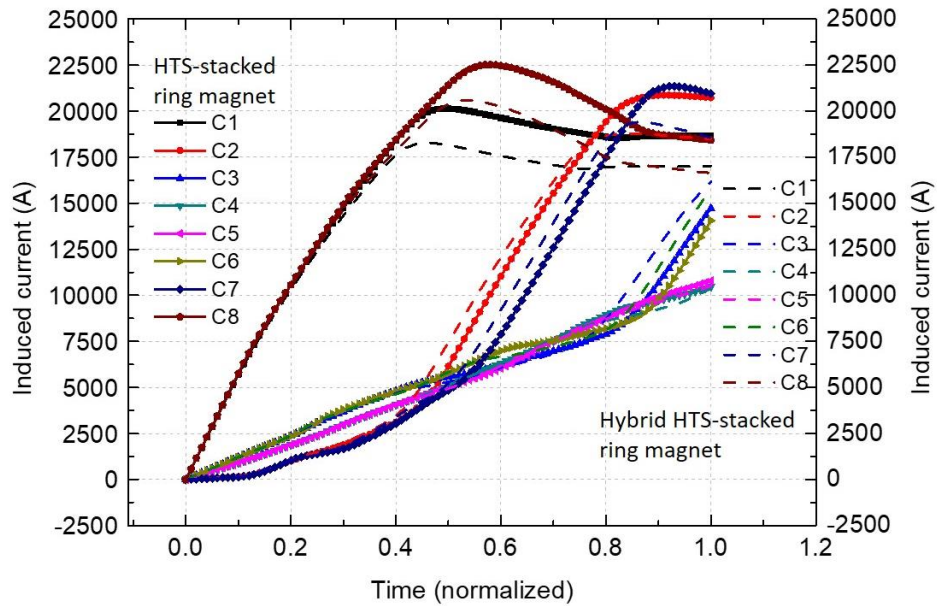
Figure 5.19: Induced current in each domain of HTS-stacked rings

5.4.3 Inverse Magnetization Characteristics of the Inserted HTS Stacks.

In Chapter 4, findings indicate that the ultimately trapped field of a well-designed HTS-stacked ring magnet can surpass the initially applied field. The subsequent analysis elucidates that this phenomenon results from the distinct parallel stacking method for the HTS-stacked ring magnet. This method ensures that the induced currents in the inner domains closely mirror those in the outer domains, leading to the expulsion of magnetic flux from the HTS materials and concentrated magnetic field in the centre space. According to the study in the last section, the existence of HTS stack inserts that share the induced current in the HTS-stacked rings can suppress the central field ascent and achieve higher trapped fields. Nonetheless, under a 4.5 T applied field, the HTS-stacked ring magnet achieves full penetration, but its trapped field caps at 3.79 T. This raises the imperative for additional investigations to discern the behaviour of an optimally designed HTS-stacked ring magnet with HTS stack inserts and to further explore its magnetization characteristics. To state it plainly, the question at hand is how the central field would be affected if the hybrid HTS-stacked ring magnet had twice the number of turns in the HTS-stacked rings.
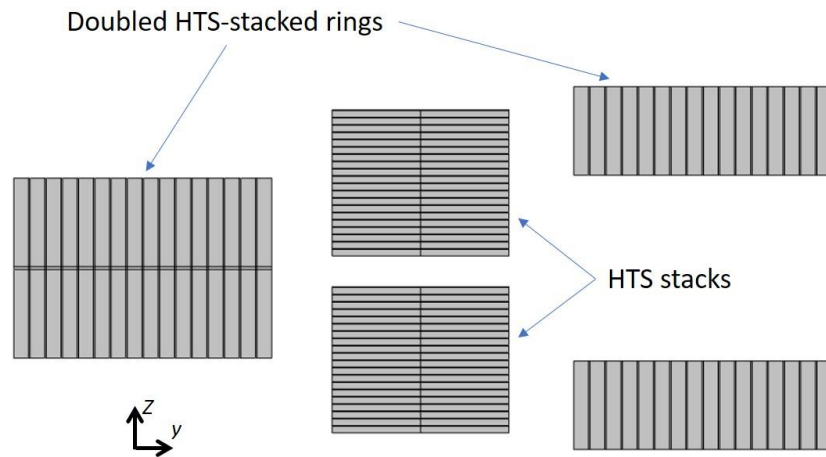
Figure 5.20: Hybrid HTS-stacked ring magnet with increased HTS-stacked rings

As shown in Fig. 5.20, the size of the central HTS stacks remains the same, while the number of the surrounding HTS-stacked rings is doubled. For a comparative investigation, the applied field remains at 4.5 T for the magnetization of the double-turn hybrid HTS-stacked ring magnet.

Fig. 5.21 presents a comparison between the central fields of the double-turn hybrid HTS-stacked ring magnet and the previously studied double-turn HTS-stacked ring magnet. While the central field of the HTS-stacked ring magnet exhibits a pronounced rise, resulting in a final trapped field exceeding the applied field, the hybrid HTS-stacked ring magnet's central field, denoted by the red curve, consistently remains at 4.5 T. This suggests that the incorporation of additional HTS stacks at the centre might result in reduced trapped fields under specific conditions. This is an interesting finding since it challenges the conventional belief that the more HTS material present, the greater the trapped field that can be achieved through field cooling magnetization. Indeed, this discovery upends traditional assumptions and underscores the complexity of interactions within hybrid HTS structures. It's essential to consider not just the quantity but also the arrangement and interaction of the HTS materials when aiming for optimal magnetization outcomes.
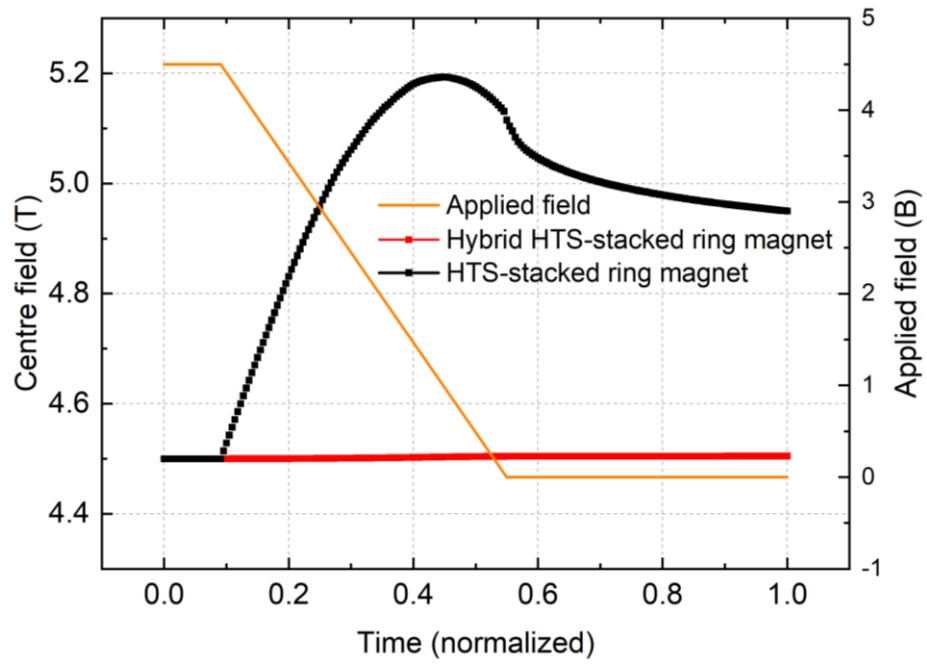
Figure 5.21: Comparison between the central fields of the double-turn hybrid HTS-stacked ring magnet and HTS-stacked ring magnet
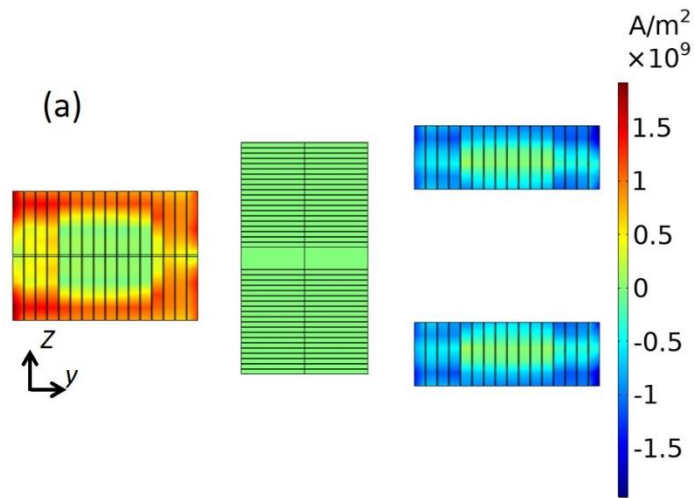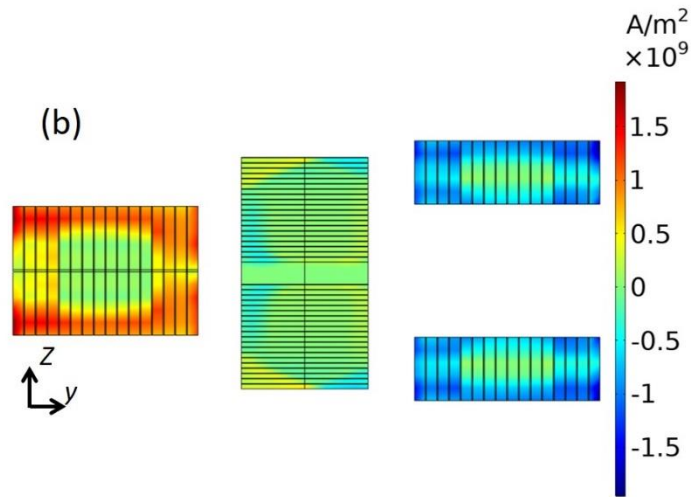
Figure 5.22: Induced current density of the double-turn HTS magnet. (a) HTS-stacked ring magnet and (b) hybrid HTS-stacked ring magnet.

The induced current distributions (field penetration) at the end of the magnetization are shown in Fig. 5.22. The same as the HTS-stacked ring magnet, the hybrid HTS-stacked ring magnet is far from fully penetrated and the current is mainly induced in the innermost and outermost domains at the end of magnetization. Given the marked similarity in the distribution of induced currents between the models, it's intriguing to observe that the central trapped field in the hybrid configuration is lower than its non-hybrid counterpart. The induced current within the HTS stacks may play a role in mitigating the trapped field. To delve deeper into this intriguing observation, the induced currents in both the hybrid HTS-stacked ring magnet and the standard HTS-stacked ring magnet during magnetization have been computed and presented in Fig. 5.23 and the direction of the current is standardized to be positive in the counter-clockwise direction on the x-y plane. While the induced currents in the HTS-stacked rings of both models depict a similar pattern, the direction of the current in the stack is contrary to that in the HTS-stacked ring. This computational evidence suggests that the incorporated HTS stacks play a pivotal role in mitigating the augmentation of the trapped field in this magnetization situation.
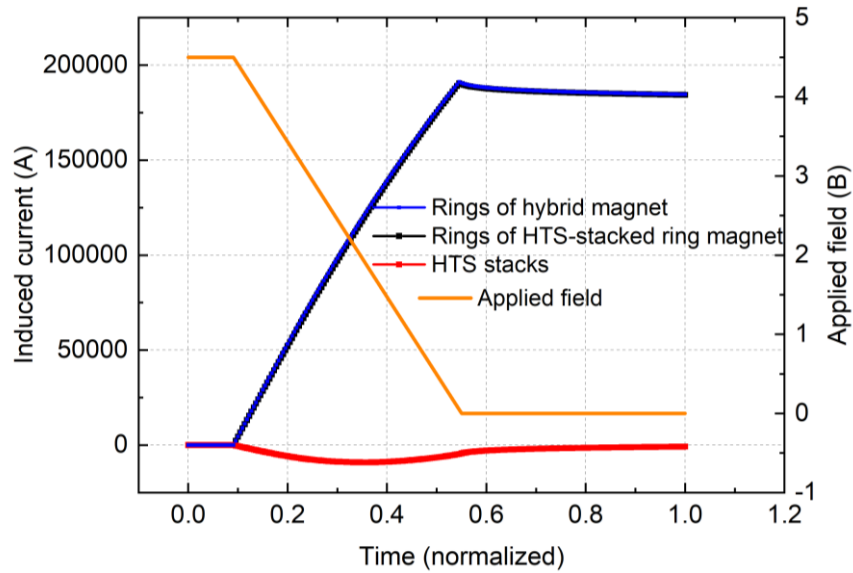
Figure 5.23: The total induced current within ring domains and HTS stack domains

To ascertain the reason behind the reversed induced current in the HTS stacks, a thorough examination of the induced current's variation and distribution during magnetization is undertaken. On the z-y plane cross-section, the induced current densities within the HTS stacks over multiple time points are depicted in Fig. 5.24. To streamline the analysis, the upper stack is segmented into areas A and B, showcasing the induced current density in the x-axis direction (J_x).
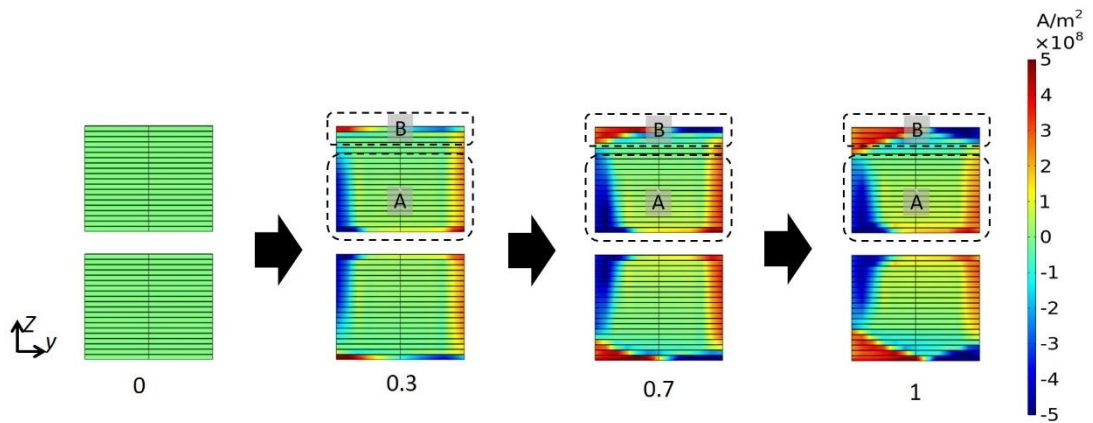
Figure 5.24: Penetration of the z−y cross-section of the HTS stacks during magnetization.

Initially, a conspicuous observation is the asymmetric induction of J_x in both areas A and B. Within area A, the magnitude of negative J_x on the right side (represented in blue) consistently exceeds its positive counterpart (in red). Conversely, by the culmination of the magnetization process in area B, the magnitude of positive J_x marginally surpasses the negative J_x. Such uneven current distributions stem from the non-uniform trapped field engendered by the HTS-stacked rings, as delineated in Fig. 5.25. This non-uniformity is especially prevalent near the closed side of the HTS-stacked rings, predominantly at its centre.
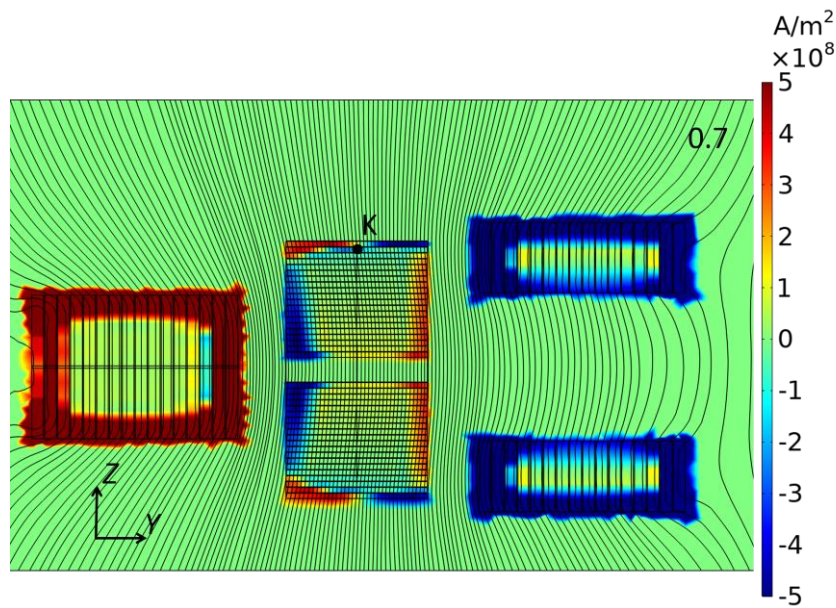
Figure 5.25: Non-uniform trapped field trapped by the HTS-stacked rings

Beyond the asymmetries within areas A and B, it's discernible that the magnetized domain in area A exceeds that of area B. This implies that the induced current in area A primarily shapes the magnetization characteristics of the HTS stacks. Compared to the induced current in the HTS-stacked rings shown in Fig. 5.23, it's evident that the current distribution directions in area A are opposite to those in the HTS-stacked rings. This inversion suggests that throughout the entirety of the magnetization phase, the induced current within area A serves to attenuate the central trapped field of the hybrid HTS-stacked ring magnet. In contrast, area B perennially augments the trapped field.

Given that the magnetization of the HTS stacks results from the cumulative magnetic field produced by both the externally applied field and the trapped field from the HTS-

stacked ring magnet, attention is directed to Fig. 5.26, which showcases the compounded field (without the HTS stacks) at the centre of area B (designated as point K). Here, a minuscule ascent in the field is observed during magnetization, which then steadily declines until magnetization's termination. This magnetic field variation aligns the magnetization direction of area B with that of the HTS-stacked ring magnet.

It's imperative to underscore that this scenario delineates conditions absent of HTS stack insertion. Once the HTS stacks are integrated, the induced current within area A will affect the field at point K, complicating the magnetization. However, Fig. 5.23 provides valuable understanding regarding the distinct magnetizations observed in areas A and B.
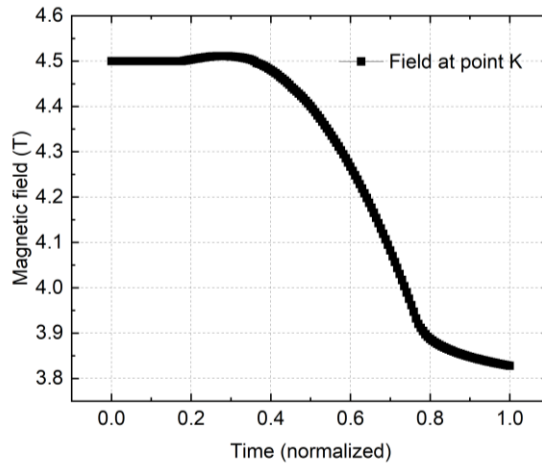
Figure 5.26: Magnetic field at the centre of area B (designated as point K)
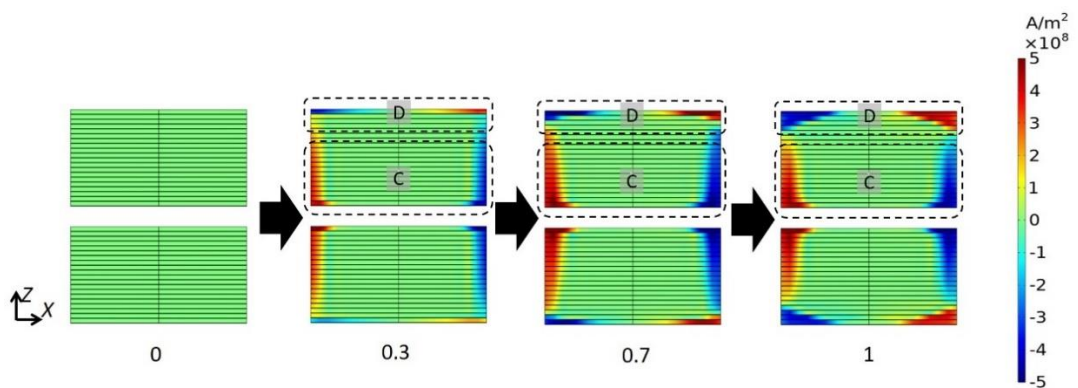
Figure 5.27: Penetration of the z−x cross-section of the HTS stacks during magnetization.

Distinct from the z-y plane cross-section, the induced current density in the z-x plane cross-section is distributed symmetrically, as depicted in Fig. 5.27. This is attributed to the symmetric geometry of the HTS-stacked ring magnet in the z-y plane. The same temporal points are chosen to display the induced current density in the y-axis direction (J_y). This illustration offers a clearer perspective on how a singular HTS stack can manifest diametrically opposite magnetization directions in its upper and lower sections. As magnetization progresses, the induced current in area D amplifies at a quicker rate than that in area C. By the end of the magnetization process, the induced currents on both sides of the stack (left and right) tend to equilibrate. This pattern is consistent with the trajectory of the total induced current in the HTS stacks, as represented in Fig. 5.22.

5.4.4 Suppression or Enhancement Effects of the HTS Stack Inserts on Trapped Field.

The above study reveals that adding HTS stacks can not only enhance the final trapped field but also suppress the final trapped field in some situations. While this may seem contradictory at first, a discernible pattern does emerge. Owing to the distinctive geometry of the HTS-stacked rings, establishing an exact mathematical formulaic relationship proves challenging. Nevertheless, the preceding analysis allows us to discern several general patterns.

Firstly, when both the HTS-stacked ring magnet and the hybrid HTS-stacked ring magnet are fully penetrated with field cooling magnetization, the hybrid variant with a greater volume usage of HTS materials can achieve a superior trapped field. For instance, as observed in the experiments detailed in this chapter, while the HTS-stacked ring magnet can only attain a trapped field of 3.69 T, the introduction of additional HTS stacks can enhance this value to 6.2 T.

Secondly, in scenarios where the HTS-stacked ring magnet is fully penetrated, leading to a central field ascent but culminating in a trapped field lower than the applied field, the introduction of HTS stacks can stabilize the central field throughout the magnetization process. This stabilization ensures it matches the applied field, although

the applied field might not completely penetrate the hybrid variant. Furthermore, with a heightened applied field, the trapped field of the hybrid HTS-stacked ring magnet can be augmented.

Thirdly, in instances where the HTS-stacked ring magnet yields a trapped field exceeding the applied field, the incorporation of HTS stacks will result in a reduction of the trapped field, aligning it to match the applied field.

5.5 A 7.35 T Trapped Field Achieved by the Hybrid HTS-Stacked Ring Magnet with HTS Bulk Inserts

Compared with HTS stacks, HTS bulk materials have the advantage of much higher critical current density, but their mechanical strengths are very limited due to their ceramic-like properties. In this section, the magnetization characteristics of the hybrid HTS-stacked ring magnet with HTS bulk inserts will be investigated. As introduced previously, the hybrid HTS-stacked ring magnet sample with two HTS bulks has a hollow bolt which can hold the cylindrical HTS bulks and a Hall sensor is fixed between the two HTS bulks. The diagram of the design is shown in Fig. 5.28. In this design, the HTS bulks were not impregnated by wax. There were two aluminium prepared for replacing the HTS bulks by which the magnetization of the HTS-stacked ring magnet without HTS bulks can be measured for comparison purposes.
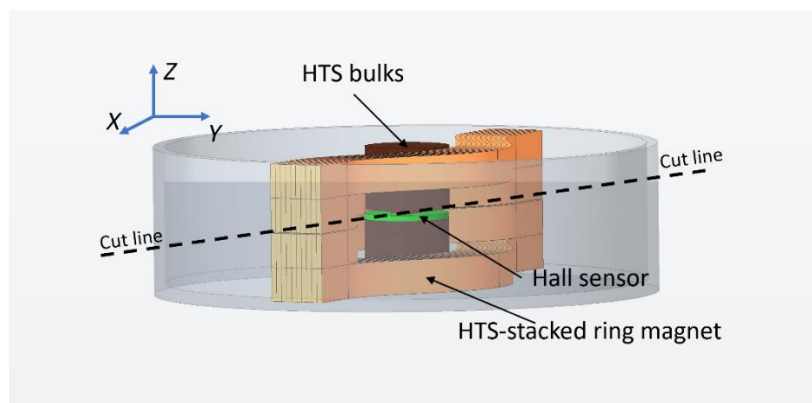
Figure 5.28: Diagram of the hybrid HTS-stacked ring magnet with HTS bulks

The magnetizations of the two configurations were conducted with the same Royce wide bore magnet under the same temperature of 25 K. Field cooling magnetization with 0.075 T/min was adopted. After the measurement of the hybrid HTS-stacked ring magnet, the HTS bulks were then replaced by two aluminium bulks to quantify how the HTS bulks increased the trapped field for the HTS-stacked ring magnet.

As depicted in Fig. 5.29, the HTS-stacked ring magnet, when magnetized with a 6 T applied field, trapped a field of 3.5 T at its centre. This demonstrates that the non-hybrid sample had been fully penetrated, making it challenging to achieve significant further improvement.
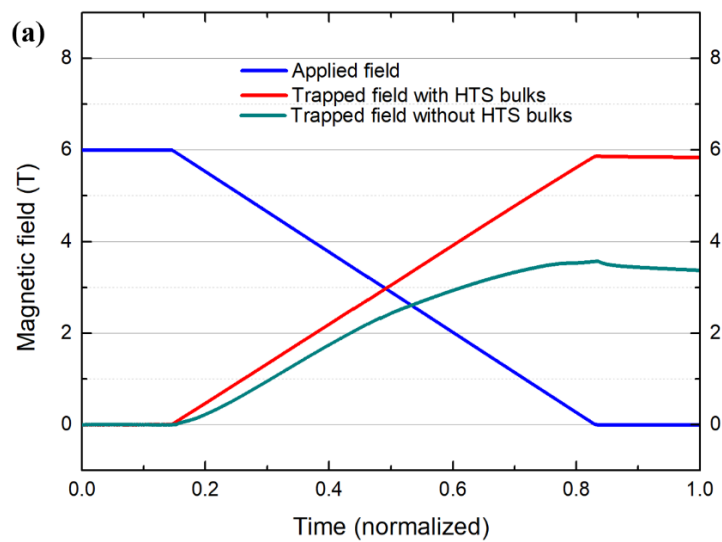
Figure 5.29: Trapped fields of HTS-stacked ring magnet with and without HTS bulks with 6 T magnetization

Given this result, the sample was then warmed and removed from the wide bore magnet. Subsequently, two HTS bulks were inserted into the hollow bolt, thereby creating a hybrid HTS-stacked ring magnet. When this hybrid sample was magnetized under identical conditions with a 6 T applied field, it achieved a trapped field of 5.9 T, as presented in Fig. 5.29. Such an outcome suggests that the central field remained relatively stable during magnetization. Furthermore, it implies that the hybrid HTS-stacked ring magnet might not have been fully penetrated, indicating the potential for achieving a superior trapped field.

In pursuit of this potential, the applied field was increased to 8 T after cooling the hybrid sample to 100 K. The results of this field cooling magnetization are shown in Fig. 5.30. With the augmented applied field, the trapped field rose to 7.3 T. Notably, this is higher than the trapped field achieved by the preceding hybrid sample with HTS stacks, which stood at 6.6 T. Such findings are consistent with expectations regarding the pronounced enhancement of trapped fields attributable to the HTS bulks.
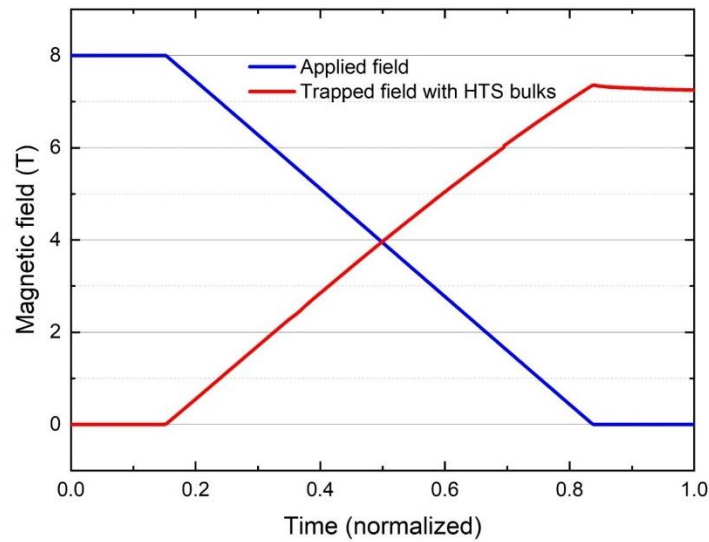
Figure 5.30: Trapped fields of HTS-stacked ring magnet with and without HTS bulks with 8 T magnetization

After achieving a trapped field of 7.35 T – which, despite being lower than the applied 8 T field, indicated signs of complete penetration – the applied field was subsequently increased to 10 T. During this magnetization process, one of the HTS bulks succumbed to the Lorentz force, resulting in a crack forming in its centre. This event also led to damage to the Hall sensor, as depicted in Fig. 5.31. In contrast, the HTS tapes used for the HTS-stacked rings remained undamaged. It's worth noting that the HTS bulks were not subjected to any mechanical reinforcement or impregnation. The primary consideration in this experiment was the sample size.
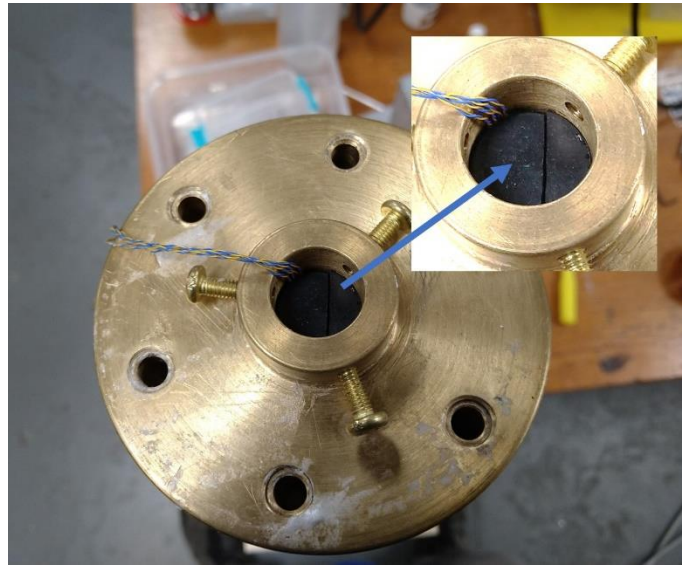
Figure 5.31: Damaged HTS bulks under 10 T magnetization

A straightforward method for reinforcing these bulks involves fitting them with stainless-steel rings using an interference fit, which augments the pre-tightening force [158]. Adopting this method necessitates either enlarging the hollow bolt's hole or reducing the HTS material's diameter. Choosing the former option would increase both the size of the HTS-stacked ring magnet and the diameter of the sample holder. However, this expansion is limited by the dimensions of the Royce wide bore magnet. Opting for the latter would mean the already diminutive HTS bulks would need to be further reduced, negatively impacting the trapped magnetic field. This is because the trapped magnetic field of bulk material is typically directly proportional to its diameter [115].

Based on these experiments, the measurement confirmed a trapped field record of 7.35 T for the hybrid HTS-stacked ring magnet, measuring 90 mm in length and 60 mm in width. While the aim of this study was not to break records for trapped fields, its focus was primarily on assessing the feasibility of the hybrid methodology and exploring its magnetization.

5.6 Investigation of the Magnetization Mechanism of the Hybrid HTS-Stacked Ring Magnet with HTS Bulks

The field cooling magnetization measurements reveal a marked enhancement in the trapped field of the HTS-stacked ring magnet upon the insertion of HTS bulks. While these measurements provide initial insights, a comprehensive understanding of the electromagnetic interaction between the HTS-stacked rings and HTS bulks during magnetization necessitates detailed numerical studies and analysis. Using the calculation methodology outlined in Chapter 3, this section delves into the intricacies of the hybrid HTS-stacked ring magnet integrated with HTS bulks. Building on the analysis from the previous section, which focused on the hybrid HTS-stacked ring magnet with HTS stacks, attention is now directed towards magnets with HTS bulks. Central to this investigation is the electromagnetic relationship between the bulk and the HTS-stacked rings, especially in instances of complete penetration or magnetization. The discussion begins with model validation, transitions to assess the magnetic field distribution on the hybrid magnet's surface, and concludes with an in-depth exploration of the magnet's unique two-step magnetization mechanism.

5.6.1 Validation of The Modelling of the Hybrid HTS-Stacked Ring Magnet with HTS Bulks

Fig. 5.32 presents a comparison between the trapped field measurements at 8 T and corresponding simulations, both of which align closely when normalized for time. Notably, simulating the entire magnetization process on a real-time scale (120 minutes in total) is infeasible. This discrepancy partly accounts for the slightly elevated simulation results compared to the hall sensor measurements, arising from the absence of long-time flux creep in the simulation.
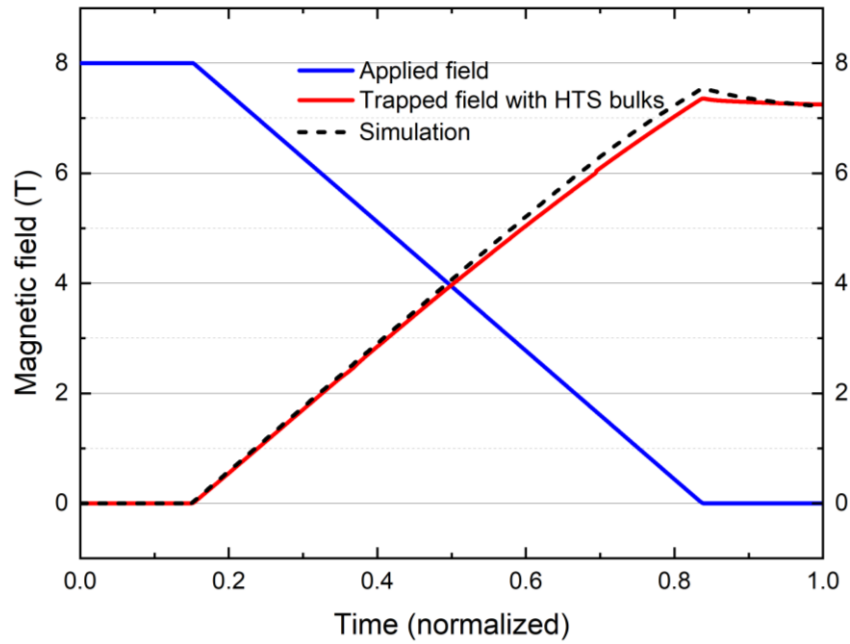
Figure 5.32: Simulation and experiment results of 8 T magnetization of HTS-stacked ring magnet with HTS bulks

5.6.2 Profile of the Trapped Field at 5 mm Above the Hybrid HTS-Stacked Ring Magnet.

As previously discussed, traditional HTS bulks and HTS stacks can achieve trapped fields up to 17 T with appropriate reinforcement, magnetization processes, and thermal control. However, both face limitations due to geometric size. Additionally, HTS bulks have inherent weak mechanical strength, further hindering their practical applications. The hybrid HTS-stacked ring magnet, measuring 90 mm in length and 60 mm in width, achieved a trapped field of 7.35 T. This showcases its advantages in terms of size and field trapping capability, with significant potential for further improvement.

Based on the simulation, the trapped field distribution along the centre cut line (as shown in Fig. 5.28) of the hybrid HTS-stacked ring magnet and non-hybrid HTS-stacked ring magnet are illustrated in Fig. 5.33. It is clear that the HTS-stacked ring magnet and the HTS bulk both contribute to the 7.35 T trapped field but the trapped field area created by the hybrid HTS-stacked ring magnet is much wider than the stand-alone HTS bulks.
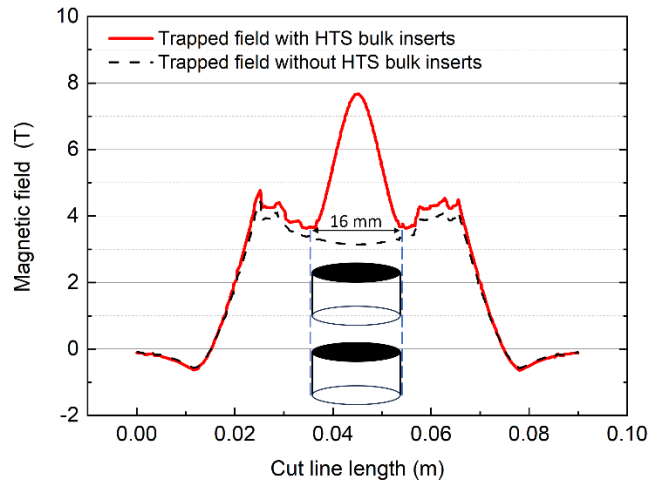
Figure 5.33: Trapped field distribution along the centre cut line of the hybrid HTS-stacked ring magnet with HTS bulks.

The trapped field distribution 2 mm above the surface of the hybrid HTS-stacked ring magnet is illustrated in Fig. 5.34. The cone shape profile of the trapped field of the hybrid design is similar to that of the cylindrical HTS bulks, which indicates the hybrid HTS-stacked ring magnet possesses similar field trapping performance but with much larger sizes. The magnetic flux in this area is calculated by integrating the magnetic flux density and this area and it achieves 5.12 mWb.
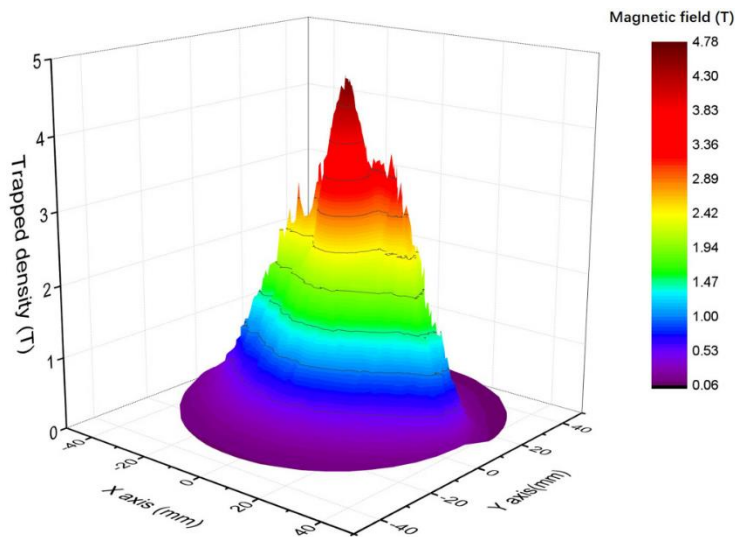
Figure 5.34: Field distribution at 2 mm above the surface of the hybrid HTS-stacked ring magnet.

5.6.3 Two Stage Magnetization Mechanism of Hybrid HTS Ring Magnets

Contrary to the investigations in the preceding sections, this part emphasizes situations involving full penetration. To grasp the electromagnetic dynamics between the two primary HTS components, the HTS-stacked rings and HTS bulks, an analysis of the induced current distribution during magnetization is conducted.
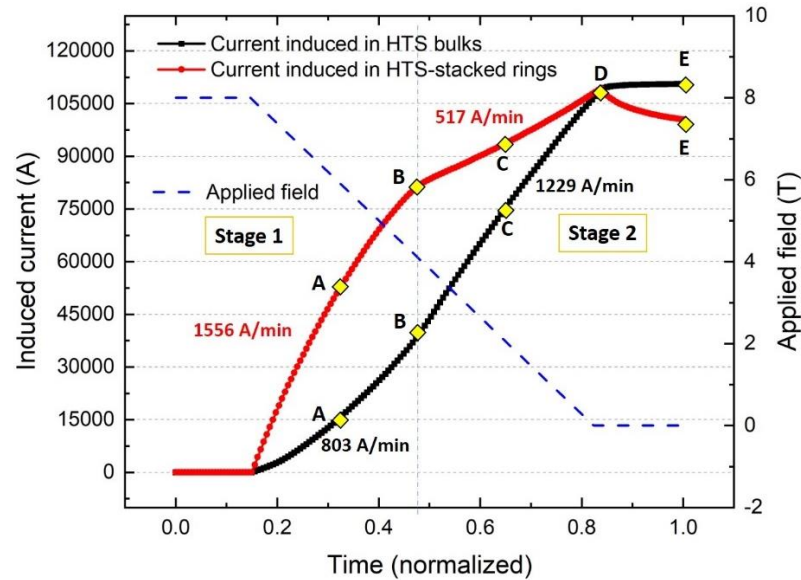
Figure 5.35: Induced current in the cross-sections of the hybrid HTS-stacked ring magnet

Fig. 5.35 delineates the total induced current within the hybrid HTS-stacked ring magnet during an 8 T field cooling magnetization. The HTS-stacked ring's total induced current is represented by the red line (derived from surface integration of the induced current density in section α of Fig. 5.36), while the black line depicts the induced current within the HTS bulks (surface integration of section β in Fig. 5.36).
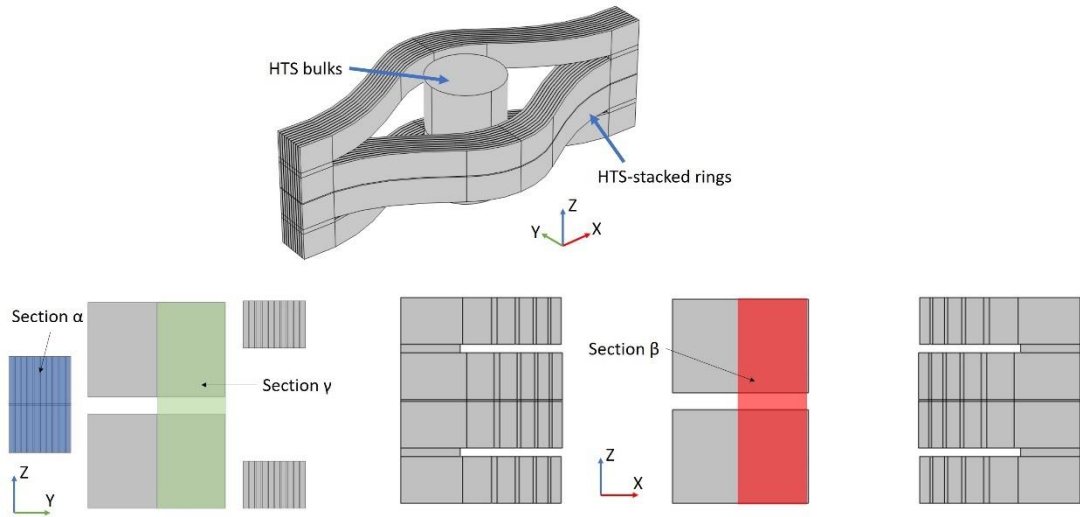
Figure 5.36: Diagram of cross-sections of hybrid HTS-stacked ring magnet

A notable observation is the alteration in magnetization speed at point B, coinciding with a reduction in the applied field to around 4 T. Consequently, this hybrid magnet's field cooling magnetization procedure can be divided into two distinct stages. The average current increase rate is used to characterize the magnetization speed or penetration speed. The duration of the entire magnetization process is calculated based on the initial applied magnetic field and the field ramping down rate. For instance, when the magnetic field drops from 8 T to 4 T, given that the actual ramping down rate in the experiment is 0.075T/min, it takes a total of 53 minutes.

During stage 1, where the applied field ramps down from 8 T to 4 T, the HTS-stacked rings and the HTS bulks experience average current increase rates of 1556 A/min and 803 A/min, respectively. In the subsequent stage, as the applied field descends from 4 T to 0 T, the HTS-stacked rings' magnetization decelerates, resulting in a diminished current growth rate from 1556 A/min to 517 A/min. Conversely, the HTS bulks exhibit an acceleration in magnetization, evidenced by an escalated average current growth rate from 803 A/min to 1229 A/min.
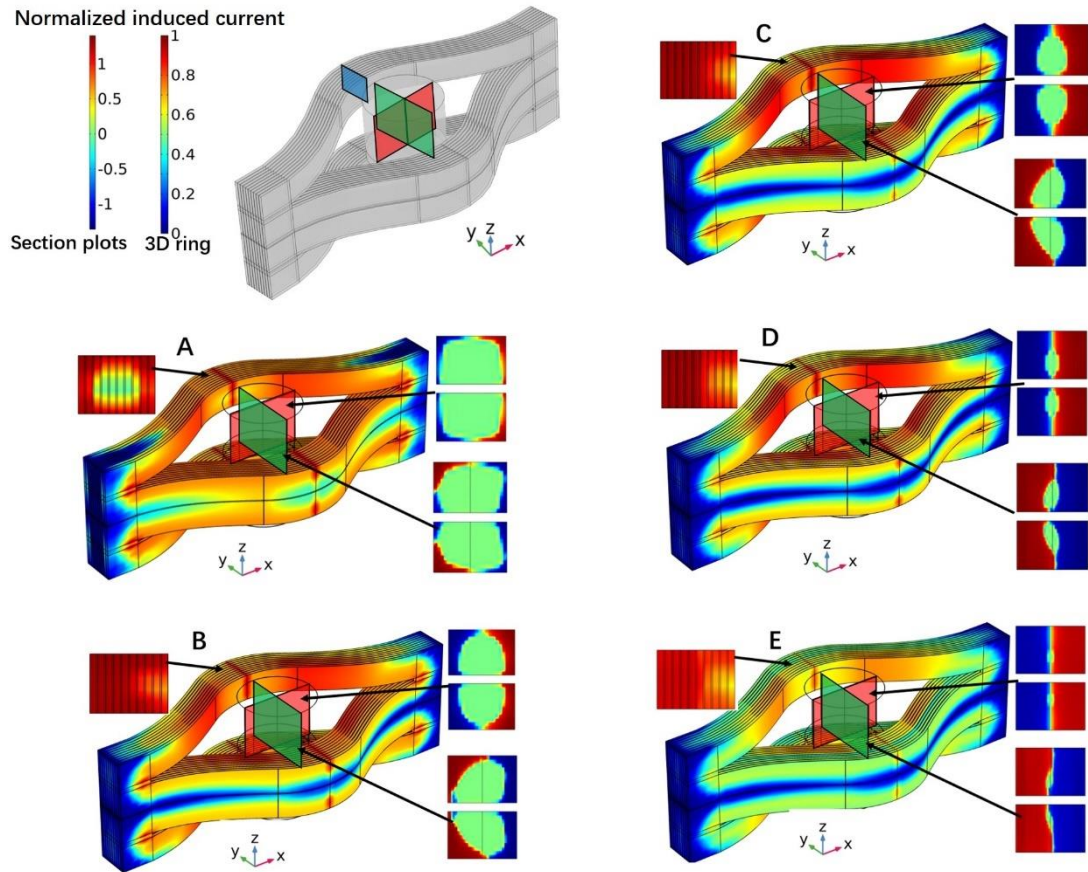
Figure 5.37: Plots of the spacial current distribution profiles when the applied field is ramped down to 6 (A), 4 (B), 2 (C), 0 T (D), and after flux creep (E).

Given the linear reduction in the applied field, the observed alteration in the magnetization rate during field cooling aroused curiosity. To address this anomaly, the current penetration throughout the magnetization was subjected to a simulation. Fig. 5.37 visualizes the normalized current distribution within both the HTS-stacked rings and the HTS bulk across five magnetization time steps: A, B, C, D, and E.

At time step A, both the HTS-stacked rings and HTS bulks commence penetration. However, virgin regions, denoted by zones with zero current, persist at the magnets' core. The crucial transition from the first to the second phase transpires at time step B. Here, the HTS-stacked rings achieve full penetration, evident from the absence of virgin regions in the current distribution cross-section depicted in Fig. 5.37. This state of full penetration in the HTS-stacked rings remains consistent through time steps B, C, and D, with the only fluctuation being in the critical current density.

Post time step B, even as the HTS-stacked rings' magnetization pace decelerates, they continue to witness an escalation in their induced current. In an alternative model with a fixed critical current (1×10^9 A/m) for the HTS-stacked rings, a stark difference is observed after stage 1. As indicated in Fig. 5.38, the induced current in the HTS-stacked rings plateaus, with the rate of current increase transitioning sharply from 1519 A/min to zero. Concurrently, the HTS bulks witness a surge in induced current, compensating for the stagnation in the HTS-stacked rings and significantly influencing the final trapped field.
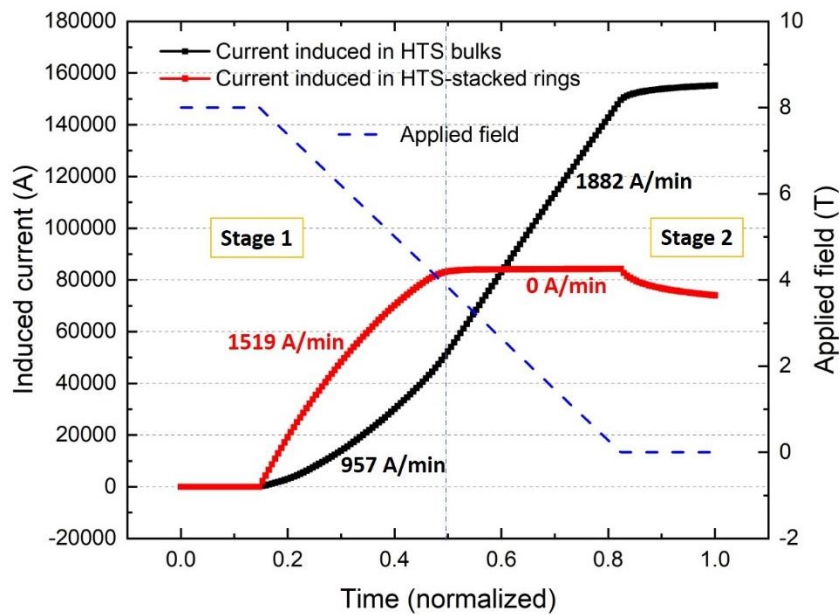
Figure 5.38: Induced current in the cross-sections of the hybrid HTS-stacked ring magnet with a fixed critical current

The inference drawn is that the deceleration of magnetization observed in the HTS-stacked rings during the second phase results from the eradication of the unpenetrated region within these rings. Put differently, the slowing down of magnetization transpires once the critical current region in the HTS ring is completely penetrated. This reduced rate is attributed to the increment of critical current within the HTS-stacked rings during the second phase, concomitant with the dwindling applied field, which impacts the field-dependent J_c values. The intensified magnetization of the HTS bulks during the second phase compensates for the HTS-stacked rings' reduced magnetization rate.

Between time steps D and E, relaxation and flux creep lead to a reduction in the induced current within the HTS-stacked rings, resulting in a decline in the trapped field they contribute. Intriguingly, this decline can be interpreted as an enhanced magnetization for the HTS bulks, leading to a rise in their induced current.

5.7 Conclusion

In this chapter, the intricacies of the hybrid HTS-stacked ring magnet, comprising both HTS stacks and HTS bulks, are investigated in detail. The primary findings of this investigation can be consolidated as:

Performance Augmentation through Hybridization: Introduction of HTS stacks or HTS bulks into the design manifestly elevates the trapped field of the hybrid samples.

Magnetization characteristics of the Hybrid with HTS Stacks: With the same temperature rises, the introduction of HTS stacks curtails the central field ascent observed in the magnetization of the sole HTS-stacked ring magnet. Numerical insights reveal that reduced current, particularly in the inner turns of the HTS-stacked rings and current sharing within the HTS stacks, drive this phenomenon. Remarkably, a reverse-induced current emerges, somewhat diminishing the trapped field of the hybrid in comparison to its non-hybrid counterpart.

Attributes of the Hybrid with HTS Bulks: A substantial trapped field of 7.35 T is achieved. The trapped field distribution profile of the hybrid design distinctly exceeds that of conventional HTS bulks or stacks. The hybrid design displays a distinct two-stage magnetization mechanism in situations of complete penetration. The two stages are distinctly demarcated by the full penetration of the HTS-stacked rings. Post this point, the current growth rate in the HTS-stacked rings diminishes, while the HTS bulks exhibit an enhanced rate of current increase.

Asymmetric Magnetization: Owing to the geometric asymmetry inherent in the design of the HTS-stacked ring magnet, both the HTS stacks and HTS bulks experience asymmetrical magnetization.

Chapter 5. Hybrid HTS-Stacked Ring Magnet with HTS Inserts

Conclusively, these insights offer pivotal guidance for future design considerations and practical applications of hybrid HTS-stacked ring magnets.

Chapter 6. Mechanical Analysis of the Hybrid HTS-Stacked Ring Magnet

6.1 Introduction

As discussed in Chapter 2, the Lorentz force, which acts upon HTS trapped field magnets both during and after magnetization, can induce substantial mechanical stresses. Such stresses are especially problematic for traditional ceramic HTS bulk samples, given their characteristic fabrication process and inherently low tensile strength [190], [201]. In light of these challenges, there have been a lot of research efforts specifically targeting the elucidation of the mechanical behaviour and intricacies of stress distribution inherent to these HTS bulks. Such scholarly pursuits predominantly aim to refine and fortify the reinforcement methodologies and concurrently amplify their field trapping capability. Stainless steel rings and carbon-fibre wrapping are widely employed for trapped field magnets [49], [115], [158]. More recent innovations propose fortifying the mechanical robustness of HTS bulk materials by introducing minuscule holes into the HTS bulks and then filling them with Stycast or a blend of copper and solder [32].

With the progressive enhancement of simulation tools, deeper insights have been gleaned regarding the mechanical stresses that cylindrical and annular HTS bulk samples endure. Samples reinforced with rings during their magnetization phase have notably piqued interest. They have prominently featured in relevant research studies [202], [203]. Alongside these explorations, significant attention has been devoted to investigating fracture phenomena inherent to HTS bulks, especially crack failures induced by the Lorentz force. For instance, the extended finite element method (XFEM) was employed to study the fracture behaviour of the HTS bulk superconductors under substantial electromagnetic force. Further, the Stress Intensity Factor (SIF) of various cracks under the influence of this electromagnetic force was exhaustively examined

[204]. Jing, on the other hand, introduced a sophisticated theoretical modelling framework. This framework, which integrates the electromagnetic H-formulation with the phase-field fracture model, is adept at simulating crack initiation and progression within bulk superconductors during magnetization [205]. Within this structure, variables like thermal stress, magnetic field, current density, the stress/strain field, and diverse magnetization processes are accounted for, offering a comprehensive analysis of the mechanical behaviour of HTS bulk materials.

The HTS-stacked ring magnet represents an innovative frontier in the realm of trapped field magnets. Its mechanical properties, albeit nascent in academic exploration, are pivotal to understanding its potential and limitations. To date, comprehensive mechanical analyses specific to this magnet are conspicuously absent from the literature. Nevertheless, the design of the HTS-stacked ring magnet stands out as a versatile alternative, distinctly juxtaposed with the conventional HTS trapped field magnets. A paramount differentiation emerges when comparing the construction methodologies of the HTS-stacked ring magnet with that of HTS stacks and bulks. Whereas HTS stacks typically rely on shorter segments of HTS tapes and HTS bulks necessitate intricate reinforcement measures, the HTS-stacked ring magnet benefits from the use of extended commercial 2G HTS tapes, thus offering enhanced scalability and reliability.

Despite the advancements in design, HTS-stacked ring magnets remain susceptible to the ramifications of the Lorentz force. Empirical investigations have underscored the intrinsic susceptibilities of the HTS-stacked ring magnet, particularly when exposed to intensified magnetic fields. Specific instances have demonstrated the dangers of reinforcement or impregnation. As shown in Fig. 6.1, under the applied magnetic fields as potent as 20 T, the HTS-stacked ring magnet sample without proper impregnation and reinforcement exhibited the catastrophic breakdown of the HTS tape, which culminated in a total failure of the specimen.

Figure 6.1: Damaged HTS-stacked ring magnet after FC magnetization

The academic community has extensively studied HTS tapes, cables, and coils [206], [207], [208], [209], [210], [211]. However, the mechanical dynamics of these innovative HTS-stacked ring magnets, despite their significance, have not been as comprehensively explored.

In this chapter, the primary focus is an exploration of the mechanical complexities of HTS-stacked ring magnets, specifically examining both configurations: those with and without central HTS inserts. Considering the analogous force dynamics faced by HTS bulks and HTS stacks in the hybrid design, the emphasis will naturally be on the HTS stack.

Initially, the investigation establishes numerical models based on H-formulations and mechanical equilibrium equations. To ensure the credibility of these models, their accuracy is rigorously verified by comparison with experimental data. Following this, the discussion delves into the distribution patterns of the Lorentz force and von Mises stress within the HTS-stacked rings, with a particular focus on underscoring the influence of different fixation techniques. Subsequently, this paves the way for identifying a unique deformation trend that is evident in the HTS-stacked ring magnet.

Moreover, an in-depth analysis is conducted on the dynamics of the Lorentz force as they impact the HTS stack inserts during magnetization. Alongside this, there's an investigation into the resulting stress distribution. The insights derived from this chapter not only illuminate the force dynamics and stress focal points related to both HTS-stacked ring magnets and the central HTS stacks but also set the stage for potential innovations in their design and fine-tuning. Consequently, this knowledge is pivotal in steering the design and optimization of HTS-stacked ring magnets towards diverse applications.

6.2 Model Establishment for (Hybrid) HTS-Stacked Ring Magnet Mechanical Simulation.

In this analysis, the mechanical behaviour and stress-strain characteristics of the hybrid HTS-stacked ring magnet with HTS stacks, as discussed in Chapter 4 and Chapter 5, are examined. For the non-hybrid HTS-stacked ring magnet, the mechanical evaluation is grounded on a 4.5 T field cooling magnetization. Conversely, for the hybrid design, the assessment is performed under the 8.5 T magnetization condition. The electromagnetic simulation verification for these two models was accomplished in Chapters 4 and 5, hence it will not be reiterated here. Relying on the methodology for Lorentz force calculation discussed in Chapter 3, the Lorentz force density distributions for both models post 4.5 T and 8.5 T magnetizations are presented in Fig. 6.2 and Fig. 6.3. The force distribution of the HTS stacks is shown in Fig. 6.4. These figures respectively illustrate the Lorentz force densities along the x, y, and z axes (denoted as F_x, F_y, and F_z). Such visual representations facilitate an immediate understanding of the force dynamics within the (hybrid) HTS-stacked ring magnet after magnetization. A noteworthy observation is the reverse directionality of F_x and F_z at the end of the HTS-stacked rings on identical tapes, which merits scrutiny. Despite the introduction of HTS stacks and an elevation of the applied field to 8.5 T, the Lorentz force exerted on the HTS-stacked rings doesn't manifest a marked increase. It's imperative to recognize that, regardless of their diminutive size, the HTS stacks endure substantial forces. The derived Lorentz force densities serve as the "Body load"

input within the "Solid Mechanics" framework for subsequent stress-strain computations.
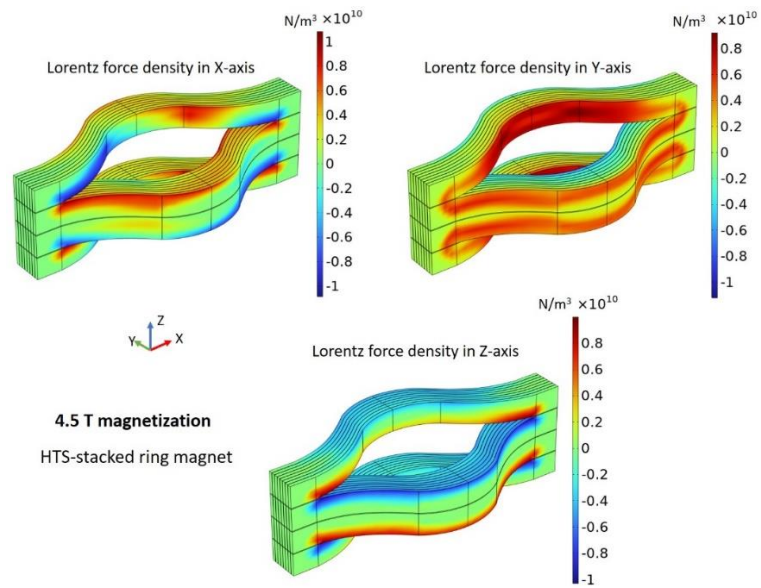
Figure 6.2: Lorentz force distribution of HTS-stacked ring magnet after 4.5 T magnetization
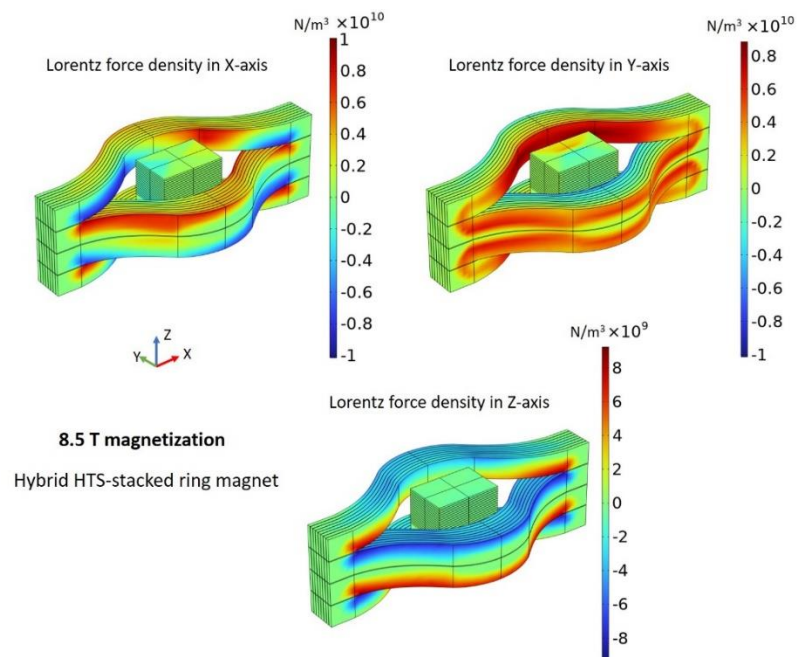
Figure 6.3: Lorentz force distribution of the hybrid HTS-stacked ring magnet after 8.5 T magnetization
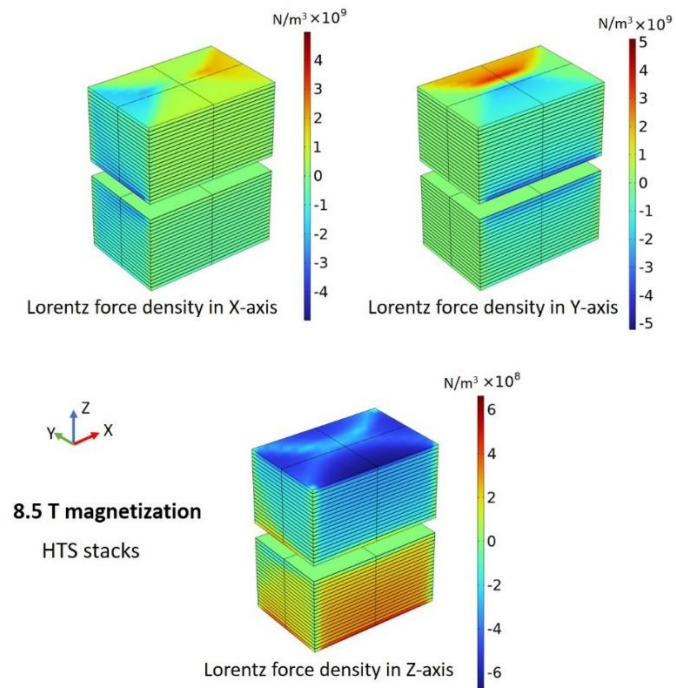
Figure 6.4: Lorentz force distribution of the HTS stacks after 8.5 T magnetization

Previous failures observed in the HTS-stacked ring samples (refer to Fig. 6.1) coupled with insights from the Lorentz force density distribution patterns have led to the identification of five critical edges on the HTS-stacked rings for a more granular stress distribution analysis. Fig. 6.5 provides a visual representation where Lines 1 through 4 correspond to the outer edges at the extremities of the HTS-stacked rings. In contrast, Line 5 demarcates the edge of the tape located centrally within the HTS-stacked ring magnet.
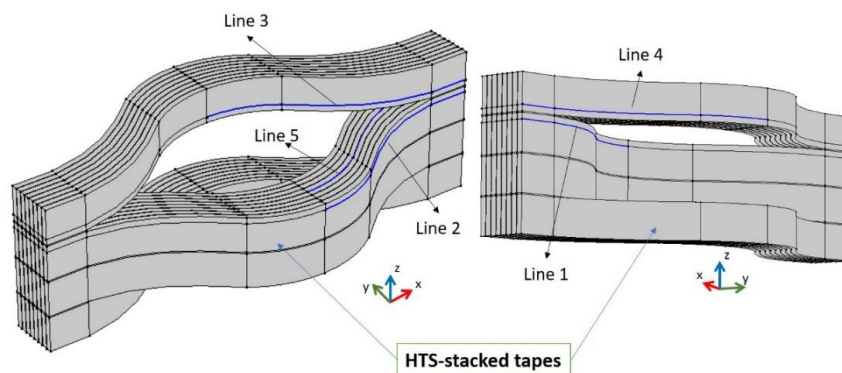
Figure 6.5: Scheme of the 5 lines for stress analysis

Chapter 6. Mechanical Analysis of the Hybrid HTS-Stacked Ring Magnet

To facilitate a precise computation of the stress endured by the HTS-stacked ring magnet—secured and impregnated with a composite of paraffin wax and aluminium nitride powder—a detailed 3D model has been built. This model, grounded in the exact geometric parameters of the holder design, can be referenced in Fig. 6.6. An important caveat is the fixed position of the cover's top to the support of the Royce wide-bore magnet during real-world testing. Coupled with the omission of gravity in the simulations, this model serves as a robust reflection of the force dynamics intrinsic to the sample. A comprehensive breakdown of the mechanical attributes of components such as the brass holder, cover, stainless-steel bolts, and paraffin wax-aluminium nitride powder impregnation is available in Table 6.1.
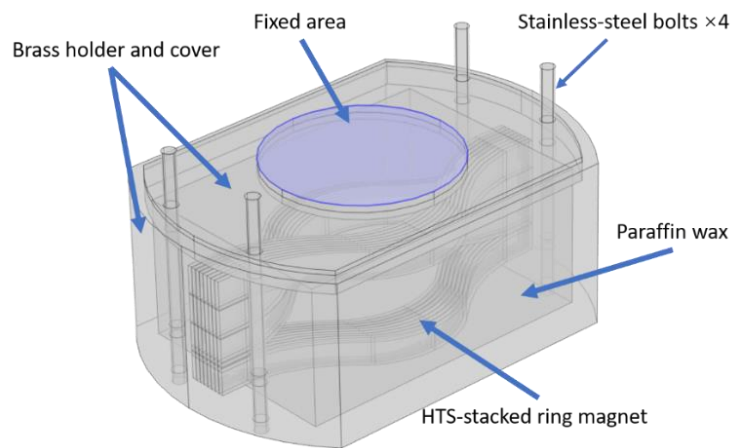
Figure 6.6: 3D HTS-stacked ring magnet model with sample holder and wax impregnation

Table 6.1

	Young's modulus	Poisson's ratio	Density
Paraffin wax with AlN powder	0.24 GPa	0.4 [212]	960 kg/m^3
Brass	137 GPa	0.34	8960 kg/m^3
Stainless steel	200 GPa	0.2	7800 kg/m^3

6.3 Stress and Strain of the HTS-Stacked Ring Magnet

This section examines the stress distribution and potential deformation characteristics of the HTS-stacked ring magnet post a 4.5 T field cooling magnetization, which resulted in trapping a 3.79 T field. While maintaining a consistent applied Lorentz force, emphasis is placed on understanding the influence of fixation methodologies and impregnation on the stress and deformation dynamics of the sample. The insights derived from this analysis are pivotal in guiding subsequent efforts for the optimization and reinforcement of the HTS-stacked ring magnet.

6.3.1 Two Sides of the HTS-Stacked Ring Magnet Fixed

The mechanical properties of HTS-stacked ring magnets significantly differ from those of HTS bulk materials, primarily due to their enhanced elasticity. Such a characteristic makes the physical constraints, imparted by various fixing methods, pivotal in determining their performance.

At a fundamental level, to preserve the ring shape of the HTS-stacked ring magnet, one must ensure an open central space while anchoring both tape ends. Such a fixation approach has been the preferred strategy in several HTS-stacked ring magnet studies [174], [175]. In these studies, owing to the limited number of tapes used and the relatively moderate applied fields, the HTS tapes often retain their shape due to inherent tension.

However, the scenario changes with increased applied fields, such as the magnitudes explored in this thesis. Elevated fields equate to intensified Lorentz forces. To explore the implications of these heightened forces, numerical modelling delves into a mechanical analysis premised on an HTS-stacked ring magnet undergoing a field cooling process, while both ends remain fixed as shown in Fig. 6.7.
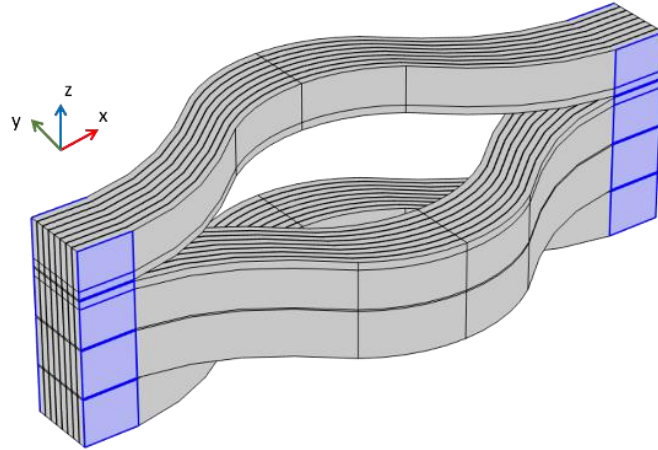
Figure 6.7: The two sides of the HTS-stacked ring magnets set as fixed

Fig. 6.8 presents the deformation observed post-magnetization of the HTS-stacked ring magnet using a 4.5 T field. As the magnet ends are anchored, they remain undeformed. In contrast, significant deformation is evident in the open side area of the HTS-stacked ring magnet. The primary force exerted on the HTS-stacked ring magnet instigates an outward expansion, aiming to enlarge the central space. Concurrently, forces directed at the open side work to compress the HTS tapes toward the centre.

For a better understanding of this dynamic, Fig.6.9 shows the streamlines of trapped flux and the induced current along the x-axis. Based on the established criteria for evaluating the Lorentz force, one can deduce that the HTS tapes at the open side undergo a force pushing them inward. In general, the collective force acting on the HTS-stacked ring magnet promotes an expansive, outward movement.
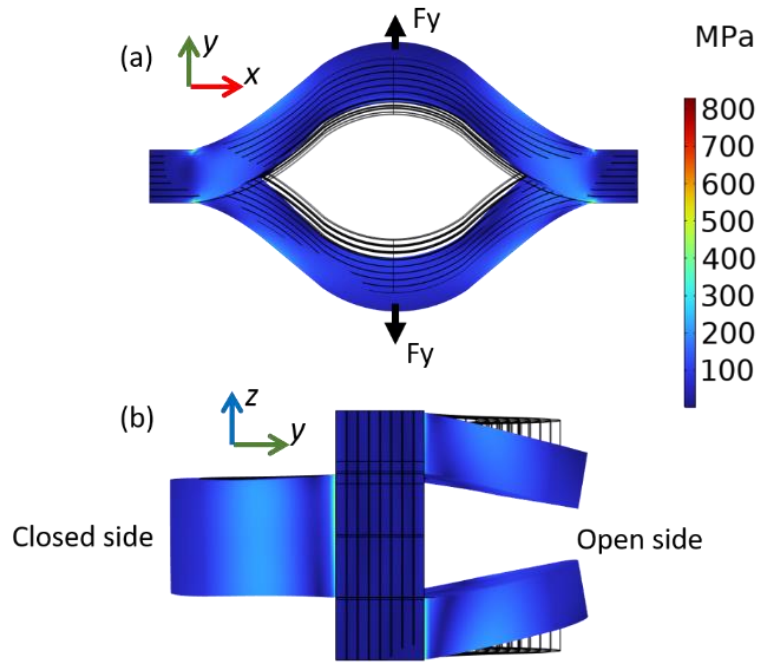
Figure 6.8: Deformation trend of the ring magnet under Lorentz force
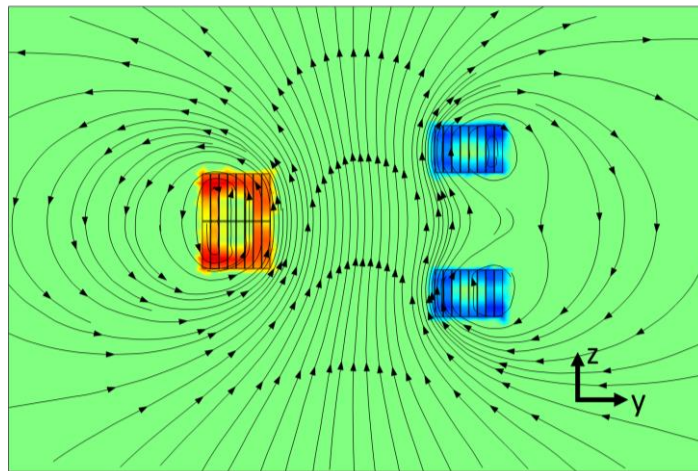
Figure 6.9: Induced current and trapped magnetic flux

Fig. 6.10 provides a visual representation of the von Mises stress distributions throughout the HTS-stacked ring magnet, focusing particularly on the stress observed along Lines 1 to Line 4. A notable observation is the abrupt spike in stress at the terminations of the splits. Notably, Lines 1 and Line 3 see the highest stress levels, reaching around 800 Mpa. Such elevated stress can lead to mechanical fractures and

failures as discussed in reference [211]. Fig. 6.11 shows the corresponding 3D von Mises stress distribution of the HTS-stacked ring magnet. The observed failure, represented in Fig. 6.1, manifests as a tear at the split terminations of the HTS tapes, corroborating the analytical findings discussed herein.
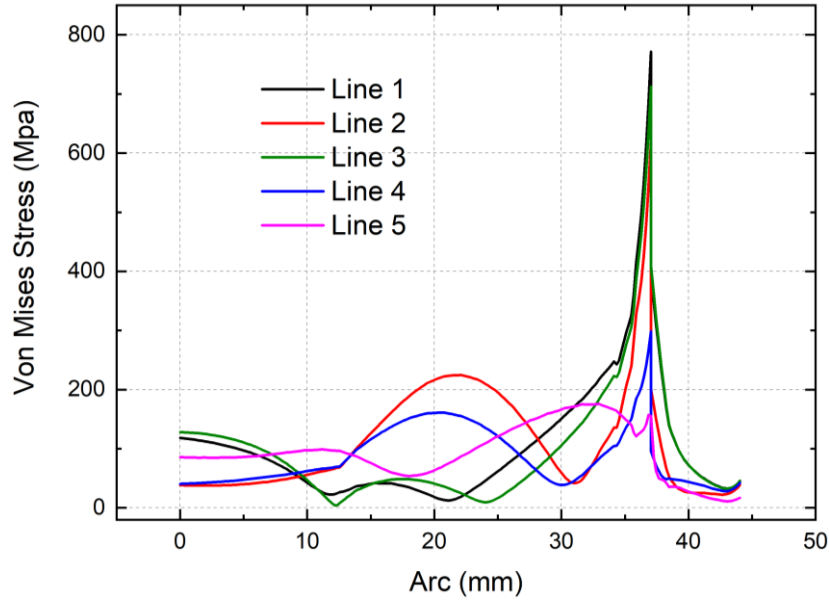
Figure 6.10: Von Mises stress distribution in Line 1 to Line5 with two sides fixed
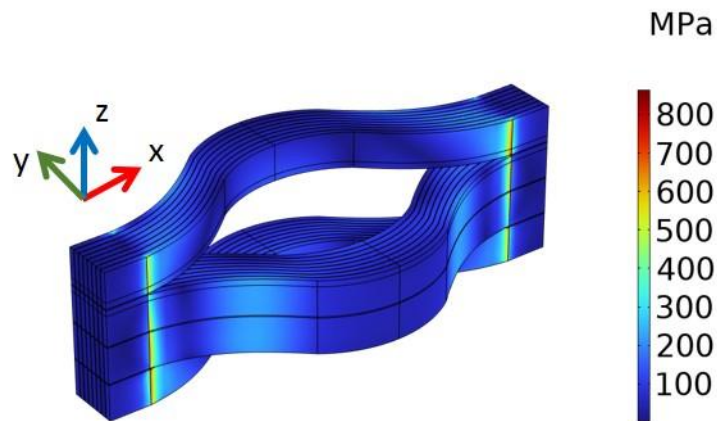
Figure 6.11: 3D Von Mises stress distribution of the HTS-stacked ring magnet with two sides fixed

In a quest to comprehend the origins of these stress surges, the z-axis Lorentz force has been quantified and is also illustrated in Fig. 6.12. A defining feature at the splits' ends is the presence of opposing Lorentz force loads: F_{z1} and F_{z2}. These forces,

positioned on either side of the tape, exert a pulling effect, potentially ripping the HTS tape along the z-axis. This tearing action, coupled with the force F_y, which instigates the outward expansion of the HTS-stacked ring magnet, culminates in a pronounced stress concentration in this region. Additionally, an external force, designated as F_{z3}, emerges from the interaction between the magnetic field and current directions, as depicted in Fig. 6.9. This force exerts an inward push on the open sides, driving the HTS tapes there to converge towards the magnet's middle. The visual representation of the effects induced by this force is also shown in Fig. 6.12
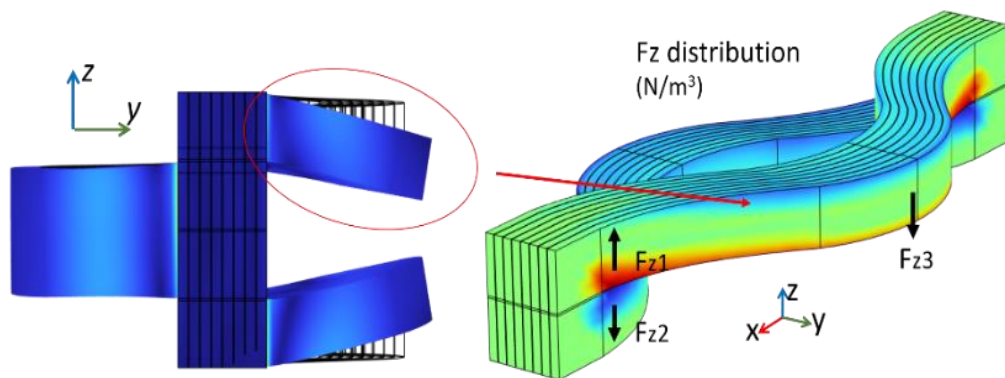
Figure. 6.12: Z-axis Lorentz force load and after magnetization

6.3.2 Stress Behaviour with Wax Impregnation and Brass Holder Fixation

In the actual experiment, the sample was impregnated with a blend of paraffin wax and aluminium nitride powder. For support, a brass sample holder was utilized. Additionally, a brass cover was securely affixed atop the sample and rigidly anchored to an external support. Despite potential vulnerabilities highlighted by earlier calculations, the HTS-stacked ring magnet remained undamaged through numerous tests. This resilience can be largely attributed to the protective measures of impregnation and the use of a brass sample holder. In the subsequent sections, a detailed analysis will delve into the pivotal roles played by these preventive measures in safeguarding the HTS materials.

The 3D model's geometry mirrors the actual dimensions of the (hybrid) HTS-stacked ring magnet, ensuring calculation validity. This accuracy is crucial, as the stress distribution is influenced by geometry. Relevant mechanical parameters are detailed in Table 6.1. Given that the quantity of aluminium nitride powder is significantly lower than that of paraffin wax, the analysis predominantly considers the mechanical properties of the paraffin wax.

Fig. 6.13 showcases the von Mises stress distribution after undergoing a 4.5 T field cooling magnetization process, this time accounting for impregnation and fixation effects. In comparison to the HTS-ring magnet model with just the two sides fixed, the peak stress is dramatically reduced, decreasing by more than 75%. Yet, stress still predominantly manifests at the split ends. Fig. 6.14 delves into the stress distribution across Lines 1 to 5. Here, Line 5 bears the brunt of the maximum stress. Contrarily, in Fig. 6.10, Line 1 is the primary stress recipient, with Line 5 being the least affected. The introduction of paraffin wax and the brass holder markedly modifies both the stress magnitude and its distribution.
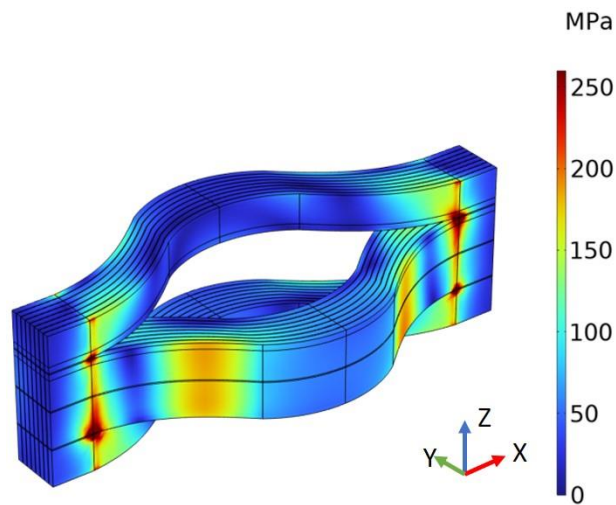
Figure 6.13: Von Mises stress in the HTS-stacked ring magnet with brass holder and wax impregnation

The change in stress on Line 5 suggests that the inner layers of the HTS-stacked ring magnet are more susceptible to stress concentration. As the paraffin wax and brass holder can limit the outward expansion and deformation of the HTS tapes, some of the tensile stress observed in the prior model has been transformed into compressive stress.

This compressive stress seems to be predominantly housed within the middle layers. Through this comparison, the importance of impregnation and external restraints in the engineering of HTS-stacked ring magnets becomes much clearer.
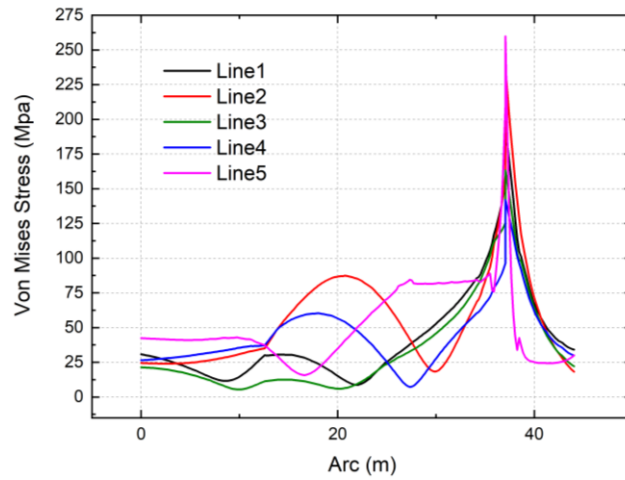
Figure 6.14: Von Mises stress distribution along Line 1 to Line5 magnet with brass holder and wax impregnation

The observed resilience of the HTS-stacked ring magnet sample during magnetization and subsequent tests is noteworthy, indicating its maintained structural integrity post the 4.5 T magnetization. However, a pivotal consideration is the sample's temperature, held consistently at 25 K. This temperature could considerably alter the mechanical attributes of the entire sample, with the paraffin wax being particularly sensitive. Given the unavailability of data regarding the Young's modulus of the paraffin wax when combined with aluminium nitride powder at this temperature, it's plausible to assume its actual Young's modulus might surpass the designated 0.24 Gpa. To comprehensively understand the influence of potential variations in the wax impregnation's properties on the stress endured by the HTS-stacked ring magnet, further calculations were executed. In these evaluations, Young's modulus of the paraffin wax and aluminium nitride powder mixture was adjusted to values of 0.5 Gpa, 1 Gpa, 1.5 Gpa, and 2 Gpa for comparative analysis.

Fig. 6.15 presents the calculated outcomes, delineating a discernible inverse relationship between the peak stress and Young's modulus of the paraffin wax. In the specific range of 0.5 GPa to 2 GPa for Young's modulus, the apex of stress is predominantly located in Line 2. When Young's modulus is set to 2 GPa, the highest

stress concentration remains at a mere 80 MPa. This is a substantial reduction of 185 MPa compared to the stress pinnacle identified with the wax impregnation's modulus fixed at 0.24 GPa. Intriguingly, an incremental surge in Young's modulus leads to a relative increment in the stress in Line 5, though the absolute differential remains relatively modest. Consequently, these findings suggest that the inherent stress within the HTS-stacked ring magnet could be effectively reduced through the adoption of materials characterized by a superior Young's modulus. Nevertheless, pronounced stress concentrations at the terminal ends of the splits continue to be an area of concern.
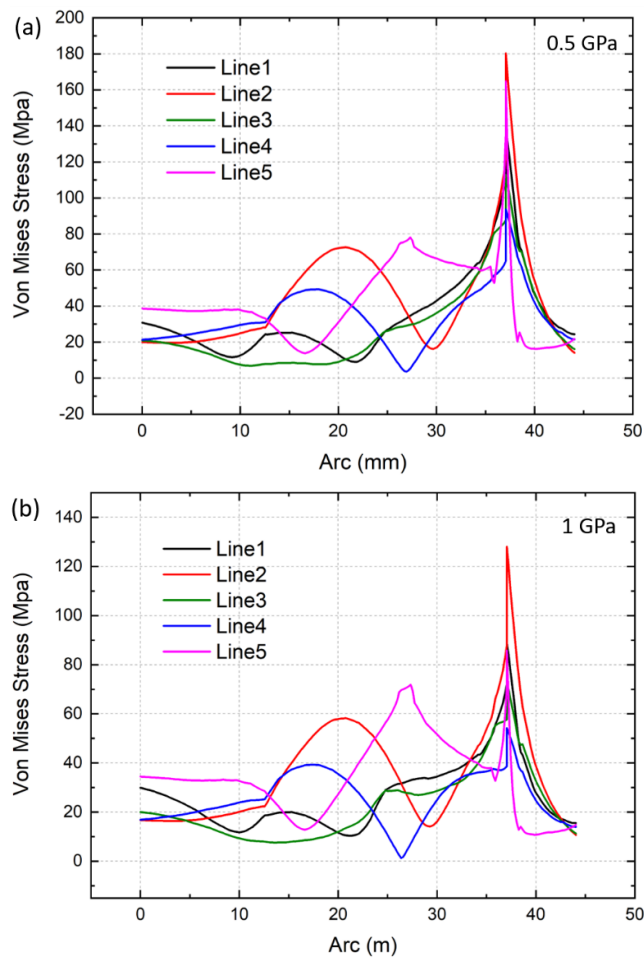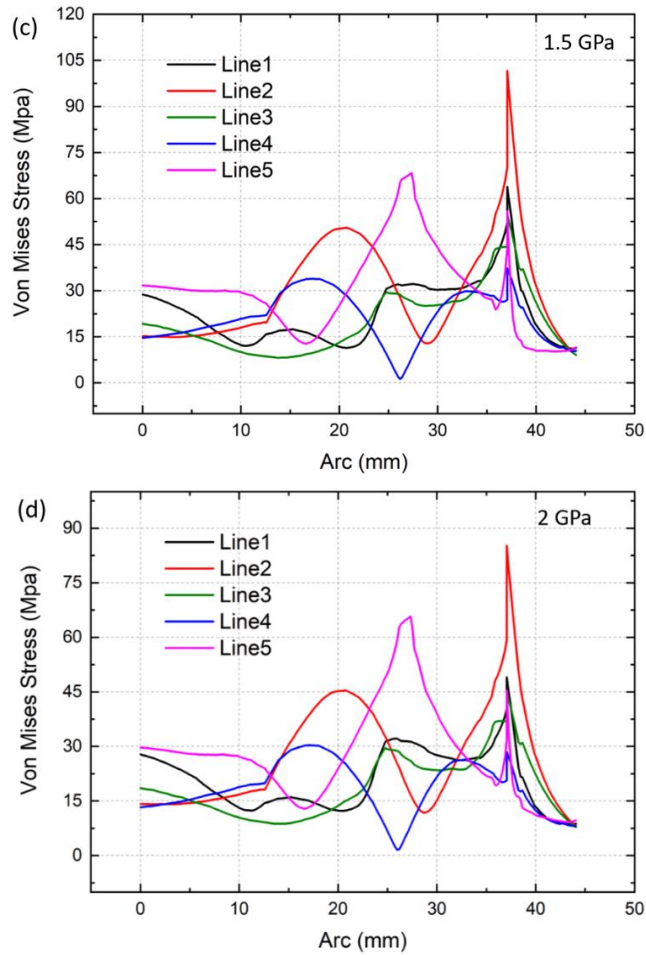
Figure 6.15: Von Mises stress distribution along Line 1 to Line 5 with different Young's modulus of impregnation wax. (a) 0.5 GPa; (b) 1 GPa; (c) 1.5 GPa; (d) 2 Gpa

6.3.3 All Boundaries of the HTS-Stacked Ring Magnet Fixed

Based on the conducted investigation, it becomes evident that the mechanical attributes, primarily Young's modulus, of impregnation materials play a pivotal role in dictating the peak stress within the HTS-stacked ring magnet. Recognizing this interplay, further exploration of the stress distribution was undertaken. In this extended analysis, the boundaries of the HTS-stacked rings in the numerical model are considered to be firmly fixed. This condition simulates a scenario wherein the sample is optimally secured within its holder, supported by a rigid impregnation.

Fig. 6.16 visually represents the von Mises stress distribution across the HTS-stacked ring magnet post a 4.5 T field cooling magnetization. Remarkably, the apex stress

witnesses a sharp decline, plummeting by approximately 90 percent. From Fig. 6.17, it's evident that despite the heightened stress near the split terminations, the risk of HTS tape rupture due to Lorentz force is effectively mitigated. Fig. 6.16 reveals that by fixing the boundaries, the inner layers of the HTS-stacked rings endure greater stress than the outer layers. Delving deeper, it's noted that the stress distribution within the central layers (as characterized by Line 5) is dominated by a pronounced stress concentration. This phenomenon resonates with prior research conclusions, suggesting that the tensile stress present in a model with both ends fixed is partially metamorphosed into compressive stress.
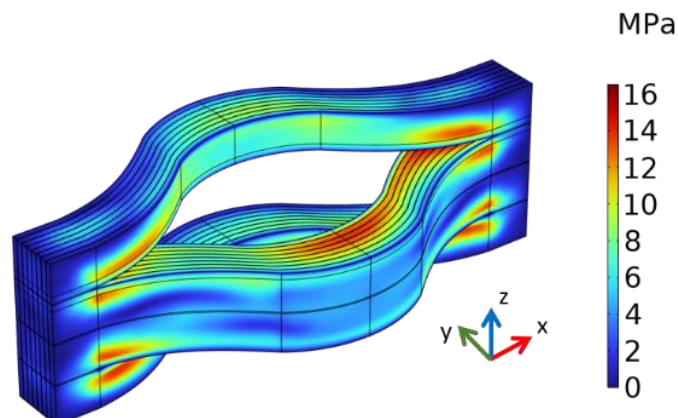
Figure 6.16: Von Mises stress in the HTS-stacked ring magnet with boundaries fixed
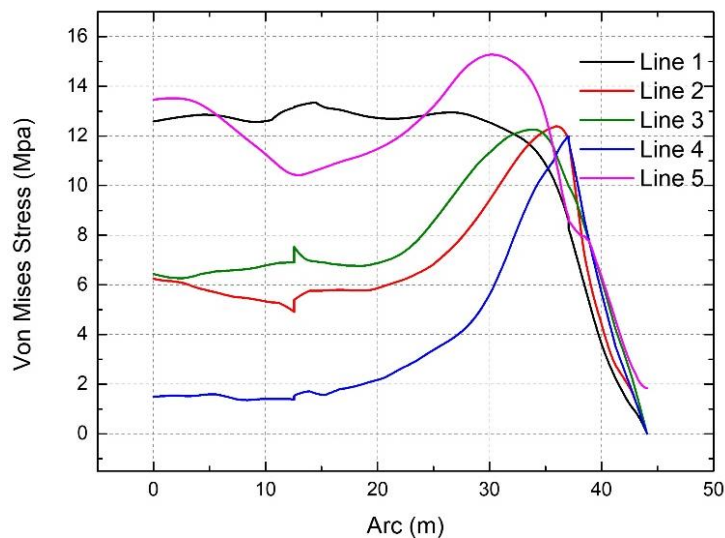
Fig 6.17: Von Mises stress distribution along Line 1 to Line5 with all boundaries fixed

Chapter 6. Mechanical Analysis of the Hybrid HTS-Stacked Ring Magnet

The outcomes derived from the investigations not only shed light on the mechanical behaviour of the HTS-stacked rings under varying conditions but also pave the way for innovative structural optimization strategies for the HTS-stacked ring magnet design. These insights are indispensable for enhancing the operational robustness and longevity of such HTS trapped field magnets. By selecting materials with greater rigidity and optimizing the supporting structures, the HTS stacked ring magnet holds the potential for attaining significantly elevated trapped fields under more extreme applied fields and at reduced temperatures.

6.4 Stress of The HTS Ring Magnets after Inserting HTS Stacks

To optimize the trapped field and more efficiently use the space within the HTS-stacked ring magnet, two additional HTS stacks were incorporated into the sample's centre. The sample then underwent magnetization with an 8.5 T applied field, as previously described. In this configuration, the HTS stack inserts would partly share the total induced current, trapping a certain field magnitude. This could influence the stress dynamics within the external HTS-stacked ring magnets. Concurrently, these HTS stacks would experience the Lorentz force, thereby presenting a potential risk of mechanical failure.

In Fig. 6.18, the von Mises stress distributions for Lines 1 to Line 5 are depicted for the hybrid model, with Young's modulus of the paraffin wax established at 0.24 GPa. In comparison with Fig. 6.15, the enhanced central trapped field resulting from the HTS stacks insertion does not dramatically alter the stress distribution trend. Notably, peak stresses in these lines only show a nominal decline. It is worth noting that the magnitude of the Lorentz force acting on the HTS tapes is influenced by both the induced current and the magnetic field present within these tapes. While the insertion of the HTS stacks bolsters the central trapped field, the magnetic field around the outer region of the HTS-stacked ring magnet may not experience a proportionate increase. This is primarily because the augmented central trapped field is predominantly attributed to the integrated stacks. Moreover, a heightened trapped field has the

potential to curtail the critical current of the HTS tapes, leading in turn to a reduction in the induced current within the HTS-stacked ring magnet.
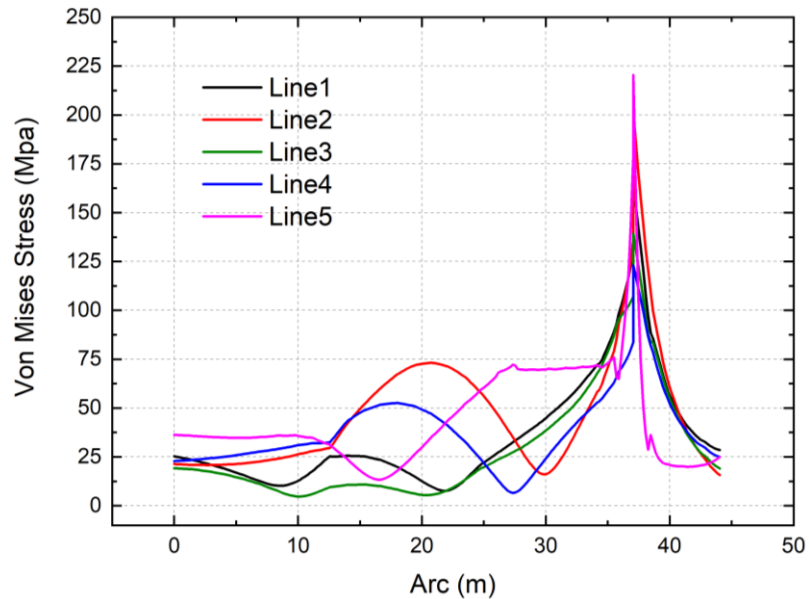
Figure 6.18: Von Mises stress distribution along Line 1 to Line 5 after inserting HTS stacks with Young's modulus of paraffin wax configured at 0.24 GPa

In the investigation of stress distribution across Lines 1 through 5, where the boundaries of the HTS-stacked ring magnet are fixed, the influence of the inserted HTS stacks appears negligible. As delineated in Fig. 6.19, the impact on the stress within the HTS ring magnet is minimal, with the peak stress on Line 5 showing only a slight reduction. This suggests that advanced impregnation techniques and materials, which provide more rigid support to the HTS-stacked ring magnet, could further diminish the effects of the HTS inserts on the stress dynamics of the HTS-stacked ring magnet.
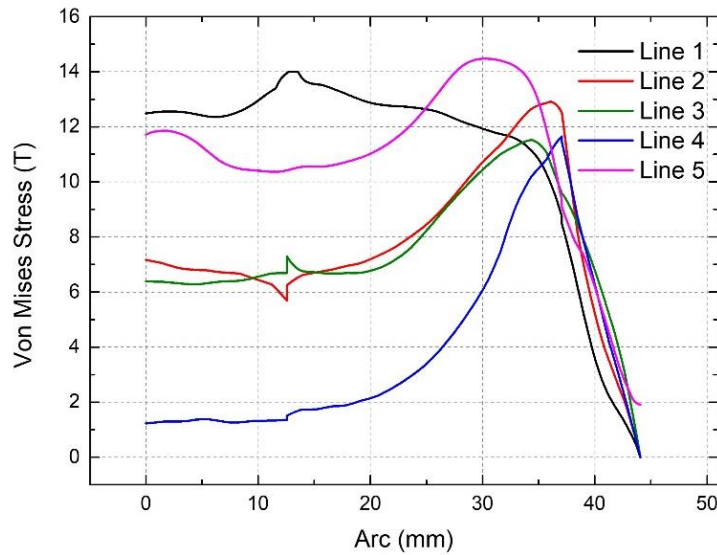
Figure 6.19: Von Mises stress distribution along Line 1 to Line 5 after inserting HTS stacks with the boundaries fixed

6.5 Force and Stress of HTS Stack Inserts

As discussed in Chapter 5, the HTS inserts in the hybrid design undergo asymmetric magnetization due to the non-uniform geometry of the HTS-stacked ring magnet. As illustrated in Fig. 6.8 and Fig. 6.11, the induced current on the y-z plane cross-section presents a left-to-right asymmetry, with this imbalance evolving throughout the magnetization process.

6.5.1 Unbalanced Lorentz Force of HTS Stack Inserts

Fig. 6.20 illustrates the Lorentz forces experienced by the two HTS stacks in x axis, y axis and z axis during magnetization. Throughout the magnetization process, the total Lorentz forces in the x and z axes remain approximately negligible. However, in the y-axis direction, the Lorentz force initially demonstrates a positive increase, subsequently undergoes a directional reversal, and ultimately manifests a negative force upon the completion of magnetization.
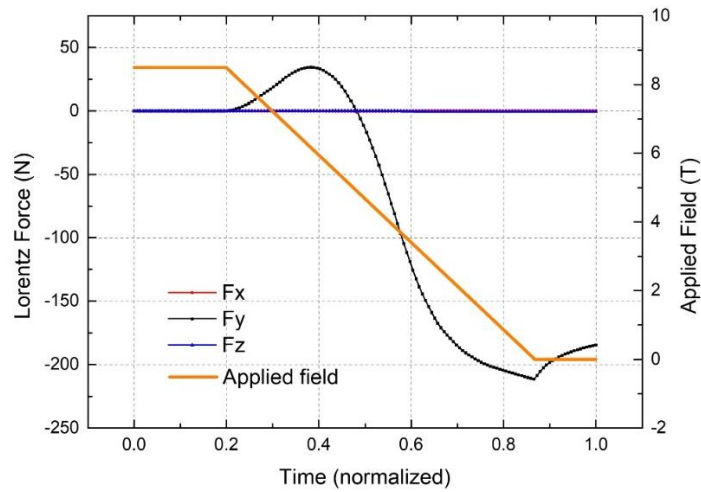
Figure 6.20: Lorentz force experienced during the magnetization of the HTS stacks

To discern the underlying causes of force fluctuations along the y axis, Fig. 6.21 presents the distribution of the y-axis Lorentz force on the z-y plane cross-section of the inserted HTS stacks. Notably, during phases when $F_y > 0$, positive Lorentz forces are prominently localized at the central-left corners of each stack, as delineated within the red circle. These regions substantially contribute to a positive directional force in F_y. However, as magnetization ensues, the aforementioned regions (highlighted in red) wane, giving way to areas marked in blue, indicative of negative Lorentz forces.
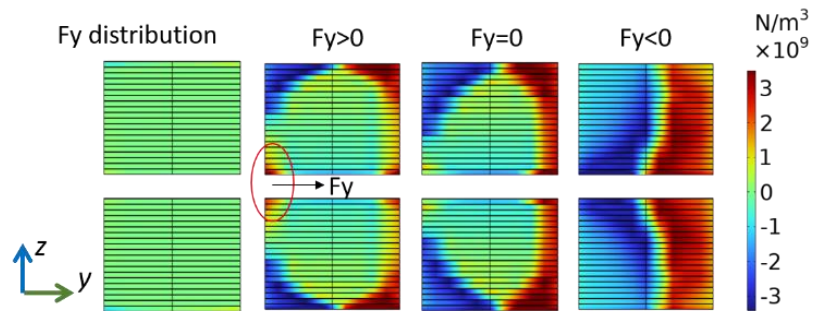
Figure 6.21: Y-axis Lorentz force load distribution in the z-y cross-section of HTS stacks

The shift in force distribution can be attributed to the asymmetric magnetic field produced by the HTS-stacked rings and the ensuing asymmetric magnetization within the HTS stacks. As delineated in Fig. 6.22, the presence of transverse magnetic flux components, namely $-B_y$ and $+B_y$, near the closed side, results in the transverse magnetization of the HTS stacks, predominantly in the early phases of magnetization.

This lateral magnetization yields a negative J_x at the central-left corners of the HTS stacks, as illustrated in Fig. 6.23. The combination of $-J_x$ and $+B_z$ leads to a transverse force that propels the HTS stacks in the direction of the open side of the HTS-stacked rings. This phenomenon elucidates the initially positive F_y observed during the magnetization process.
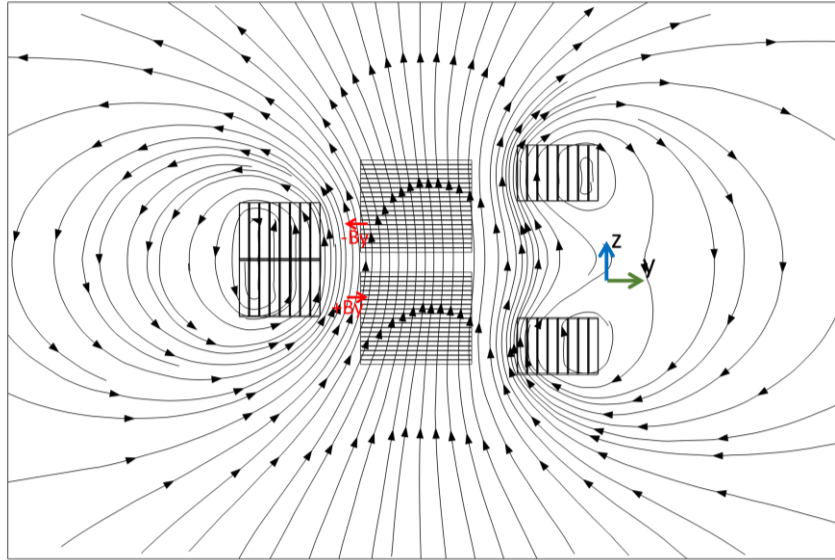
Figure 6.22: Asymmetric magnetic flux (-By, +By) generated by HTS-stacked rings affecting the HTS stack inserts

As elucidated in Chapter 5, the full magnetization of the hybrid HTS-stacked ring magnet undergoes a two-stage process. Initially, once the HTS-stacked rings achieve full penetration, the contribution of the HTS stack inserts to the trapped field becomes more pronounced, persisting until magnetization concludes. In the subsequent phase, there's a rise in the trapped flux within the HTS stacks. Consequently, the attraction force between the closed side of the HTS-stacked rings and the HTS stacks amplifies. This phenomenon can be attributed to the closed side of the HTS-stacked rings inducing a stronger B_z on the left side of the HTS stacks, as illustrated in Fig. 6.22. This heightened magnetic interaction is postulated to be the underpinning for the amplified negative y-axis Lorentz force observed in the HTS stacks as magnetization culminates.
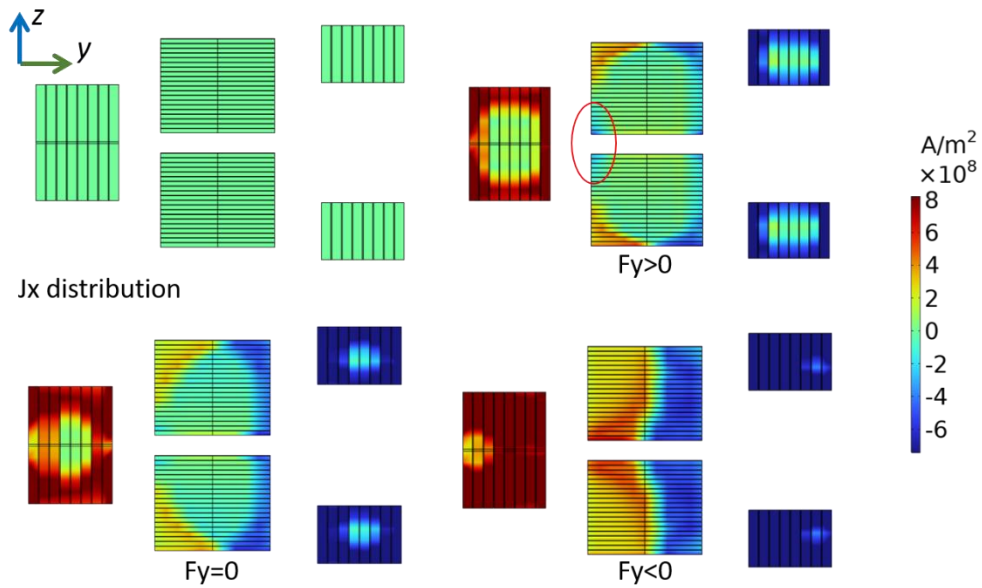
Figure 6.23: X-axis induced current distribution during magnetization

6.5.2 Stress of HTS Stack Inserts

During the magnetization tests, the HTS stacks were not reinforced, hence boundary constraints were not incorporated into the stress calculations. Moreover, given the modest magnitude of the unbalanced y-axis force, it was deemed inconsequential for the stress computation.

Fig. 6.24 presents the von Mises stress distributions post-magnetization, across the z-y, z-x, and x-y cross-sections. Notably, the stress is distributed asymmetrically across both the z-y and z-x planes. The most pronounced stress, approximately 7.5 MPa, is localized at the top and bottom regions, which undergo greater penetration during magnetization. The x-y cross-sectional stress distribution at the top and bottom layers shows an asymmetry along the y axis, a consequence of the uneven y-axis Lorentz force. Given the robustness of standard commercial HTS tapes, this is unlikely to markedly impair their efficacy. In this setup, customary reinforcement methods employed for HTS bulk materials are superfluous.
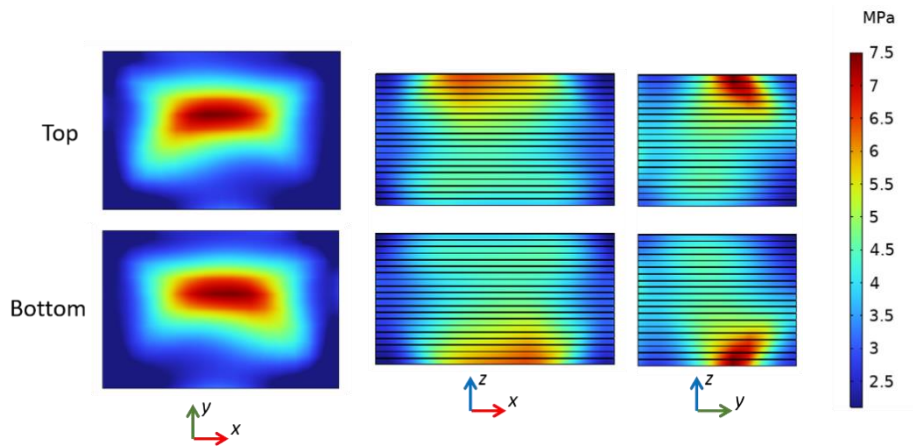
Figure 6.24: Stress distribution in the cross-sections of HTS stacks

6.6 Conclusion

In this chapter, a detailed analysis was conducted on the Lorentz force and stress distribution within the HTS-stacked ring magnet, considering configurations both with and without HTS stack inserts during field cooling magnetization. Key insights include:

Stress vulnerability: Without proper fixation techniques, the HTS-stacked rings encounter notable stress concentrations at the split ends. This leaves them susceptible to damage from the Lorentz force.

Impregnation and reinforcement benefits: Incorporating methods such as paraffin wax impregnation and a rigid brass holder can significantly diminish stress concentrations.

Stress after hybridizing: By introducing HTS stacks into the core space of the HTS-stacked rings, the trapped field is enhanced. Concurrently, there is a slight reduction in the von Mises stress within these rings, but this alteration is so subtle that it's essentially inconsequential.

Asymmetry in forces: Due to the intrinsic trapped field asymmetry in the HTS-stacked rings, centrally placed HTS stacks undergo an imbalanced Lorentz force in the y-axis during the field cooling magnetization process.

Stress distribution peaks of HTS stacks: The ultimate stress distributions within the HTS stack cross-sections are notably asymmetric. Peaks manifest predominantly near the top and bottom sections.

Stress resilience of HTS stacks: Even devoid of specialized reinforcement for the HTS stacks, the stress remains comfortably below the threshold of common commercial HTS tape.

Overall, this chapter's insights provide a rich tapestry of knowledge on the mechanical intricacies of HTS-stacked ring magnets, paving the way for informed design and application choices in the future.

Chapter 7. Magnetization of the HTS Double-Pancake Coil with Joints

7.1 Introduction

HTS double-pancake coils, compared to HTS-stacked ring magnets, have a more regular shape and result in more symmetrically distributed fields. The coils wound with commercial HTS tapes, are capable of generating strong magnetic fields upon high current injection. Despite their capabilities, HTS magnets often require external power sources via a pair of current leads, due to joint resistance and flux creep. This introduces a heat load from the current leads, which limits the transport current and hampers operations at high currents, particularly for conduction-cooled magnets. Additionally, reliance on an external power supply compromises magnetic field stability, a critical concern for MRI/NMR magnets. Certain applications or devices necessitate a compact form factor, in which case, the substantial size of the power supply system can compromise the functionality of the HTS coils.

Recent advances in flux pumps, capable of injecting flux into a superconducting coil or circuit without electrical contact, have showcased the ability to generate direct current (DC) using AC power supplies or travelling wave flux. Two prominent types have emerged: HTS transformer-rectifier flux pumps and HTS travelling wave flux pumps [213], [214], [215], [216], [217].

HTS transformer-rectifier flux pumps use "switches" to facilitate flux pumping into the HTS coils or circuits. Among these switches include thermal switch [218], MOSFET switch [219], overcurrent switch [220], et al. Recently, a self-rectifying flux pump, employing an overcurrent switch, exceeded 2 kA [221]. This design employs an asymmetric current waveform for its primary winding, simplifying its system and avoiding dissipative components in the cryogenic setting as illustrated in Fig. 7.1. This

pump also showcased the potential for through-wall excitation of high current HTS magnets.
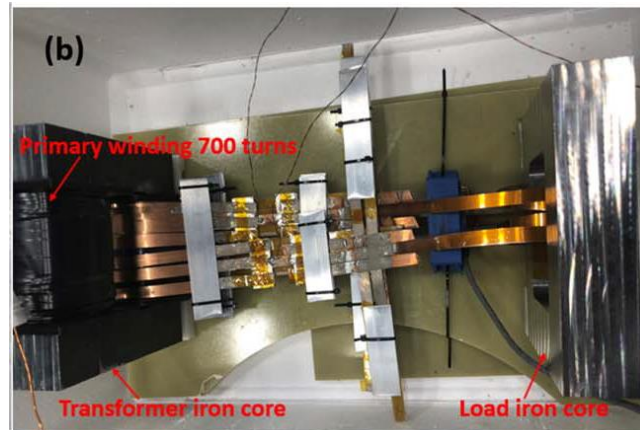
Figure 7.1: The whole circuit of a high current transformer–rectifier flux pump

HTS travelling wave flux pumps, leveraging a waving magnetic field, fall into three categories: the HTS dynamo [222], the linear-pulse field HTS flux pump [223], [224], and the linear-motor type HTS flux pump [225], [226]. All use a unipolar travelling magnetic wave, perpendicular to a YBCO stator tape, to induce DC. The HTS dynamo uses rotating discs with unipolar magnets. With the HTS coil tape perpendicular to the magnetic field, Hamilton's squirrel-cage design, using eight parallel 12 mm HTS tapes, achieved a 700 A output as shown in Fig. 7.2 [227], [228].

The compact linear-motor type flux pump combines AC and DC windings with a magnetic circuit, producing a DC-biased AC wave, charging the HTS coils as shown in Fig. 7.3. Without rotating discs, it's more efficient than traditional HTS dynamos. A 2022 design with 12 parallel HTS stators reached 1610 A [229].
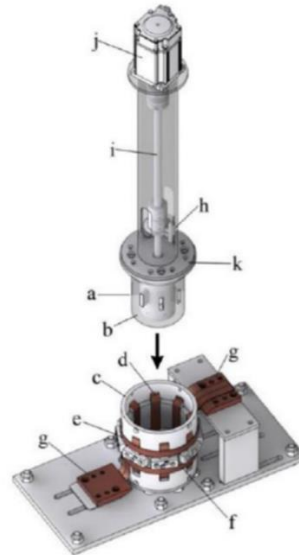
Figure 7.2: A dynamo with squirrel-cage design
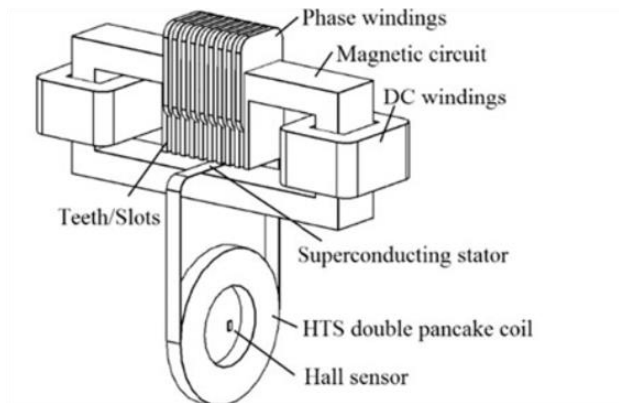
Figure 7.3: Scheme of linear-motor type flux pump design

However, while the above HTS flux pumps have demonstrated kA level current injection, they were normally under the condition of low inductance of the load HTS coils and the kA level current was the sum of the current in each parallel tapes or coils. This implies a limitation in the number of coil turns and, consequently, the magnetic field generated by the flux pump.

The recent advances in soldering technology for HTS tapes have made it possible to keep the resistance of joints low, which allows for slow current dissipation [230], [231]. This important development may make it feasible to inject large currents into HTS coils using field cooling magnetization, a method used for magnetizing the HTS-stacked ring magnet as discussed in Chapter 4. Compared to the direct power supply

charging and flux pumps, magnetization can generate a strong magnetic field in both HTS bulks and stacked tapes without charging or transformer devices. It was noted that with an appropriate design, especially by increasing the number of turns, the HTS-stacked ring magnet could potentially trap a field higher than the applied one. However, this increases the length of the HTS-stacked ring magnet, making magnetization more challenging due to the limited size of the magnet bore. On the other hand, the HTS double-pancake coils do not face this issue. Because of their circular shape, increasing the number of turns only results in a small change in size, allowing for easy insertion into the magnet bore for magnetization. Since the HTS double-pancake coils are also made with commercial HTS tapes, they have great potential to achieve a widely distributed and strong magnetic field through field cooling magnetization, possibly even higher than the initially applied field.

In this chapter, an HTS double-pancake coil sample with terminals soldered through a bridge tape is fabricated and investigated. The resistance of the joints at 77 K was measured before the magnetization experiment. The completed sample is then magnetized using a field cooling process in liquid helium. A quench test is conducted by employing a heater to raise the temperature of the sample with a trapped field. The results of the magnetization and quench tests are then compared with the outcomes calculated by FEM modelling. Additionally, the decay rate of the trapped field is investigated through measurements and curve fitting, based on the calculation of current dissipation in a coil. This study delineates the characteristics of HTS double-pancake coil magnetization and assesses the viability of utilizing HTS double-pancake coils as trapped field magnets. The findings will serve as a crucial reference for the design and application of closed-loop HTS double-pancake coils with joints.

7.2 Fabrication of the HTS Double-Pancake Coil and the Joints

For the fabrication of the double pancake coils, a specialized winding machine, designed within the laboratory, was employed, as shown in Fig. 7.4. The chosen material for the coils was the Fujikura 12 mm FESC-SCH tapes, consistent with the material selection for the preceding HTS-stacked ring magnet. Kapton tapes were used

for insulation, as delineated in Fig. 7.5. An illustrative representation of the wound HTS double-pancake coil without soldering joints can be observed in Fig. 7.6. This specific design encompasses 80 turns for each layer, culminating in a composite of 160 turns. Structurally, the coil has an inner diameter of 50 mm and an outer diameter measuring 78 mm.
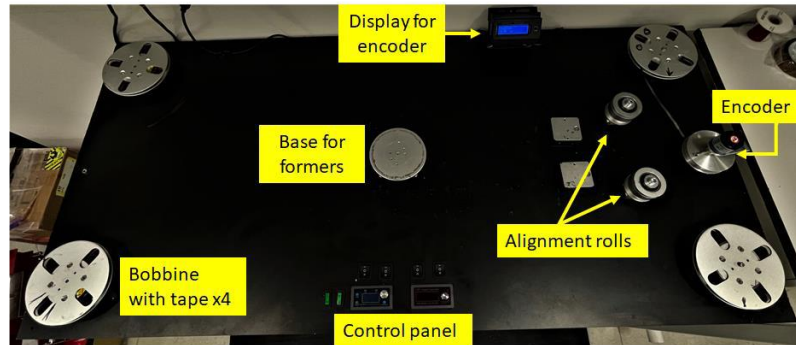
Figure 7.4: Winding machine for HTS double-pancake coils
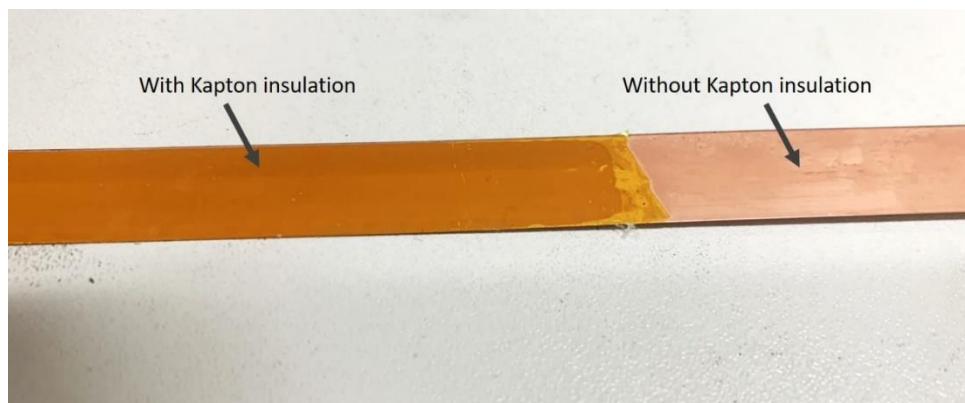
Figure 7.5: The HTS tape insulated with Kapton tapes
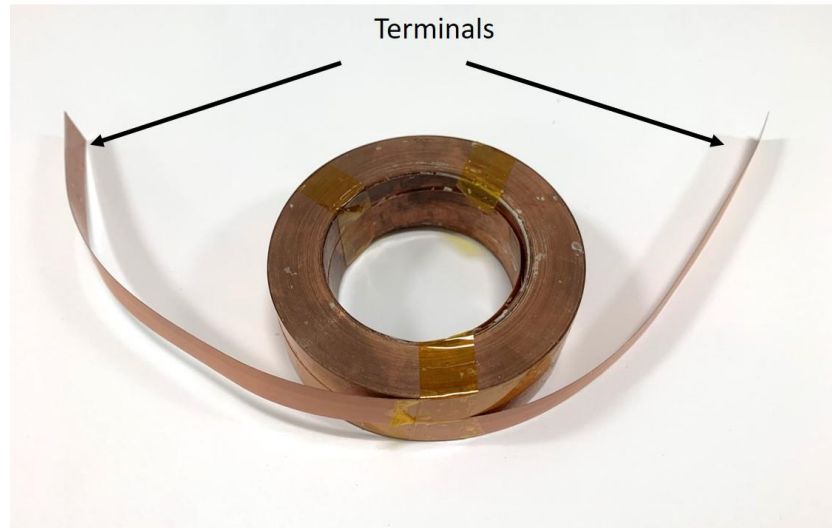
Figure 7.6: HTS double-pancake coil before soldering

For the double-pancake coil's terminal connections, a bridge-type soldering joint is employed, as depicted in Fig. 7.7 and Fig. 7.8. This design ensures that the current bypasses the Hastelloy layers, minimizing joint resistance and simplifying the winding of the terminals back to the coil. The identical Fujikura tape was used for the bridge to ensure performance consistency. Neither the terminals of the HTS coil designated for soldering nor the bridge tape were insulated. Each terminal was soldered individually to the bridge tape, leading to two distinct soldering joints. For joint formation, the non-insulated HTS tapes were initially treated with MG Chemicals 835 rosin flux for PbSn coating. Subsequently, they were immersed in a heated soldering pot containing molten PbSn and then removed, resulting in a solder layer on their surfaces.
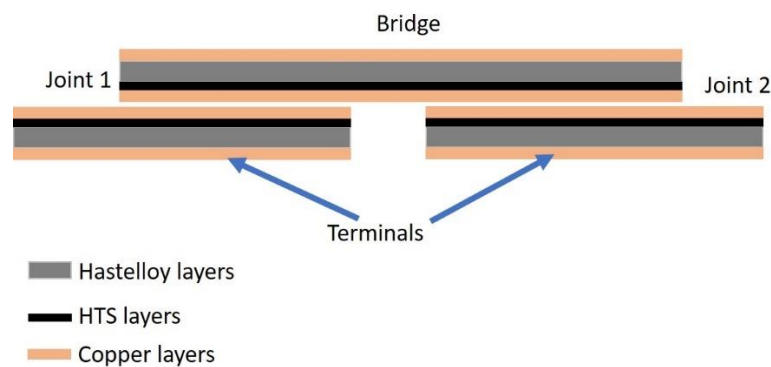
Figure 7.7 Bridge-type soldering joint
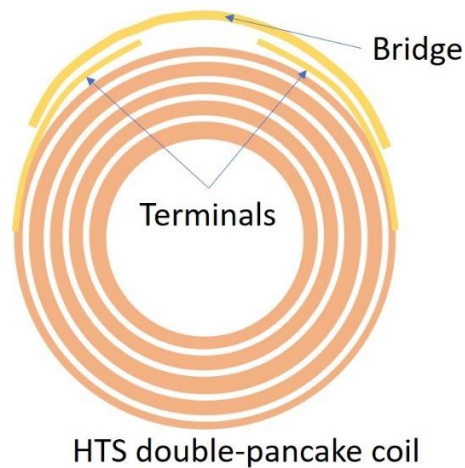
Figure 7.8: Scheme of connecting the terminals of the coil

The soldering phase follows the coating process. For this research, a heating and pressing technique was employed for joint creation, using an apparatus depicted in Fig. 7.9. This soldering machine consists of two stainless steel plates with embedded heaters. A display monitors the plates' surface temperatures, and the upper plate is hydraulically connected to a jack, allowing adjustable pressure control between the plates.

Figure 7.9: Heating and pressing machine for soldering joints

In preparation for soldering, the tinned tapes were treated with rosin flux to enhance the soldering quality. One terminal of the coil was overlapped with one side of the bridge and was secured in place using Kapton tapes to prevent any relative movement.

The plates of the soldering machine were then brought close together, and the tapes for soldering were carefully positioned between them. The temperature of the plates was set to 220°C, just above the melting point of PbSn. When this temperature was achieved, the upper plate pressed down on the tapes. The heaters were then immediately deactivated, and a fan was used to rapidly cool down the plates and tapes. Once the temperature dropped below 60°C, ensuring the solidification of the soldering material, the plates were separated, and the joint could be removed. This procedure was repeated for the second joint.

It is worth noting that the HTS double-pancake coil was designed to maintain a ring shape. This means the soldered terminals, along with the bridge, had to be wound back after the soldering process. Consequently, the lengths of both the joints and the bridge were carefully considered before initiating the soldering process.

The two soldered bridge-type joints are shown in Fig. 7.10 and each of the joints has a length of around 20 cm trying to reduce the resistance. The soldered terminals and bridges were then flipped and wound back to form the coil. To test the capability of the trapped field through magnetization, a brass sample holder was machined for the finished HTS double-pancake coil as shown in Fig. 7.11.

Figure 7.10: The soldered bridge-type joints
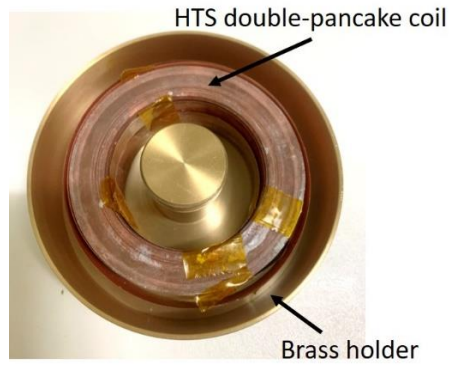
Figure 7.11 Finished HTS double-pancake coil

The double-pancake coil was impregnated with a mixture of paraffin wax and aluminium nitride powder, enhancing thermal conduction and mechanical resilience. This mixture was previously employed in the HTS-stacked ring magnet.

Fig. 7.12 illustrates the setup for trapped field measurements. A cryogenic Hall sensor (LHP-NP), calibrated for precision, was centrally positioned on the HTS double-pancake coil. To track temperature variations during testing, a Lakeshore Cernox sensor was integrated within the wax impregnation. For heating purposes, a 40 Ω polyimide heater was affixed to the sample holder's base, interfacing with a Lakeshore 336 temperature controller. Additionally, a connector ensured the sample's secure attachment to the external magnet's support during evaluations.
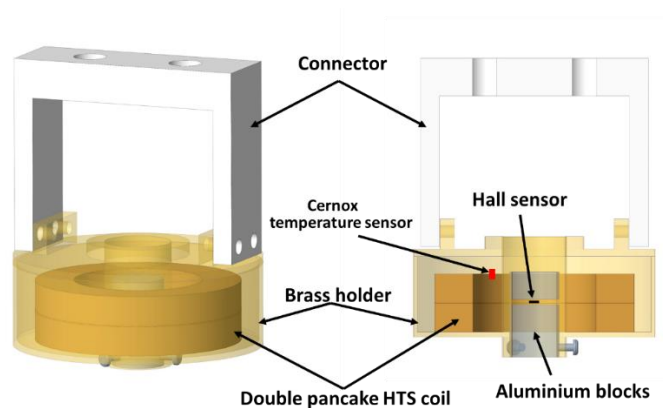
Figure 7.12: Scheme of the sample for trapped field measurements

7.3 Measurements of the HTS Double-Pancake Coil.

The resistance due to soldering HTS tapes together is inevitable since current needs to flow through non-superconducting layers. The joint resistance was measured before the magnetization process under liquid nitrogen temperature in our lab. The magnetization and trapped field measurements were conducted in LNCMI, Grenoble, France, using a high field magnet with a 100 mm bore. It can provide a stable magnetic field and a slow enough field ramping rate, but the sample temperature is at 4.2 K and it is not adjustable since it uses liquid helium as the coolant.

7.3.1 Measurement of the Resistance Of The Joints

Fig. 7.13 illustrates the resistance measurement scheme of two joints connecting the two terminals and the bridge. For this measurement, the joints are immersed in liquid nitrogen, while the remainder of the coil remains at room temperature. As the joints are cooled below their critical temperature, they transition into the superconducting state. Conversely, the double-pancake coil remains in its normal conducting state. This ensures that the electrical current bypasses the coil and flows exclusively through the joints.

To measure the resistance, a DC power supply is connected across the joints, and the resultant voltage drop is recorded using a National Instruments (NI) data acquisition card. The exact procedure for this measurement is detailed in Fig. 7.14.
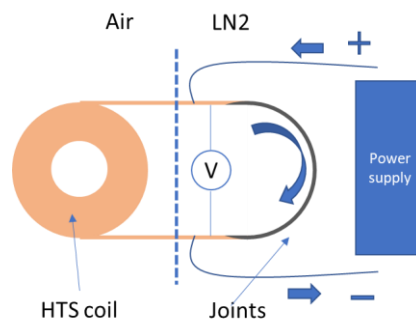
Figure 7.13: Resistance measurement scheme
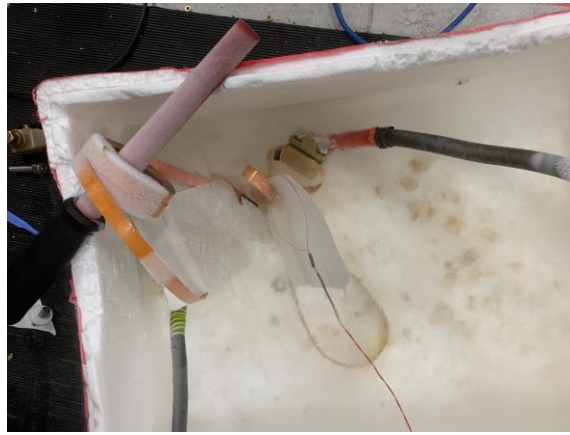
Figure 7.14: Procedure of resistance measurement

The input current was incrementally ramped from zero, with pauses at 50 A, 100 A, and 150 A to ensure stable data collection. The corresponding current and voltage measurements are presented in Fig. 7.15. Utilizing Ohm's law, the resistance of the two joints is calculated and graphically represented in Fig. 7.16.

A linear correlation is observed between the increasing current and the voltage, while the resistance remains relatively stable. From the results, it can be inferred that the resistance of the two joints, when at a temperature of 77 K, is approximately 12 nΩ.
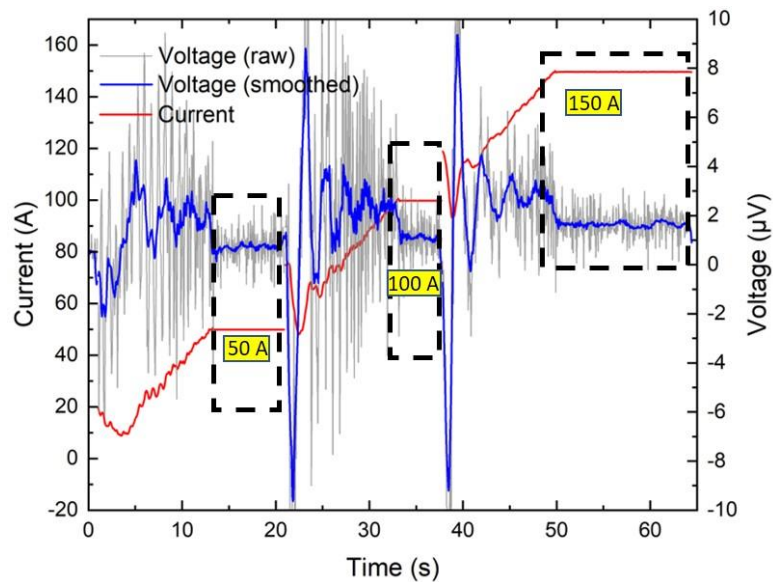
Figure 7.15: Current and voltage of the joints
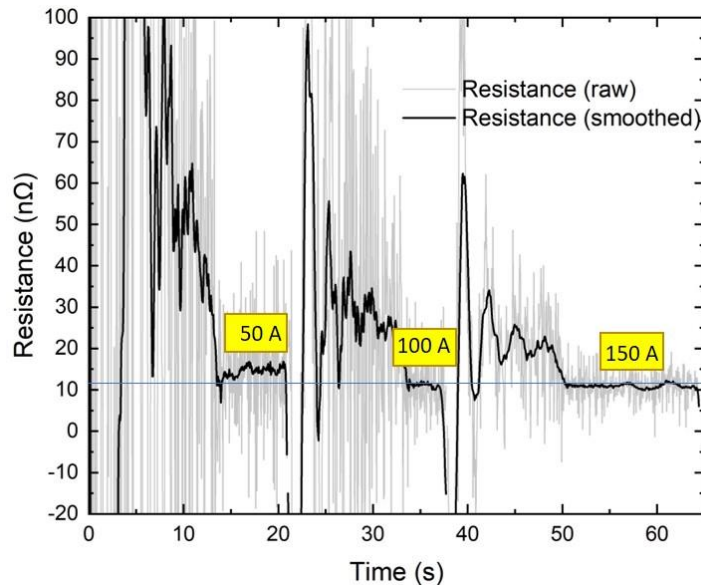
Figure 7.16: Resistance of the joints

7.3.2 Achieving Higher Trapped Fields Than Applied Fields by Field Cooling Magnetization

In Chapter 4, the potential of the HTS-stacked ring magnet to surpass the applied field in terms of trapped field is discussed, given that the number of turns and the geometry are well designed. The HTS double-pancake coil bears a resemblance to the HTS-stacked ring magnet in that both are fabricated using HTS tape materials. However, a distinct feature of the HTS double-pancake coil is the equal current carried by each tape. Notably, an increase in the number of turns of the coil results in only a marginal expansion of its diameter. This property facilitates the addition of more turns without significantly altering the coil's size, ensuring its compatibility with the bore of the high-field magnet.

The HTS double-pancake coil sample was taken to LNCMI for the field cooling magnetization measurement. Fig. 7.17 depicts the high-field magnet utilized for the measurements, which is primarily constructed from copper conductors. Due to the use of copper, the magnet's volume is substantial, with its main body situated behind the stairs. For a more lucid understanding of the measurement setup, a schematic is

147

provided in Fig. 7.18. Liquid nitrogen is needed for pre-cooling the cryostat and liquid helium is used to keep the sample at 4.2K.

Figure 7.17: High field magnet for HTS double-pancake coil magnetization
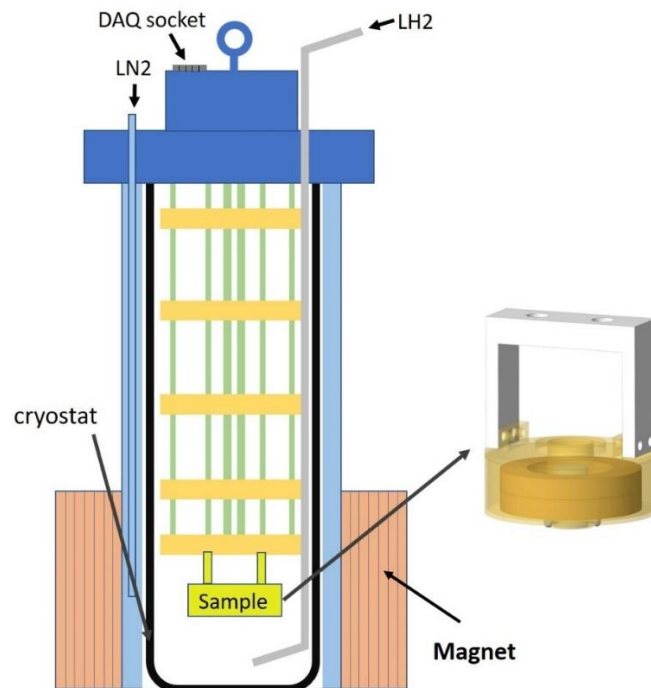
Figure 7.18: Scheme of the magnet and measurement

The sample underwent a field cooling magnetization process with initially applied fields set separately at 1.07 T and 4.5 T. Between these two magnetization measurements, the sample underwent a natural heating process for 12 hours with the heater inactivated. Before the 4.5 T magnetization, the HTS coil's temperature was approximated to 120 K, ensuring that the HTS materials had been quenched. The field ramping rate was set at 20 G/s for the field cooling magnetization to avert potential temperature increases during the field's ramp-down phase.

The central and trapped fields observed during and after the two magnetization processes are depicted in Fig. 7.19 and Fig. 7.20. The central field commences its upward trajectory as the applied field starts its decrement and continues to rise until the applied field is zero. Following the end of the external field's decrement, there's a gradual decline in the central field, caused by the combined effects of flux relaxation and the resistive attributes of the joints. In Fig. 7.20 it becomes apparent that the trapped field exceeds the initial applied field and exhibits an impressively slow decay rate.
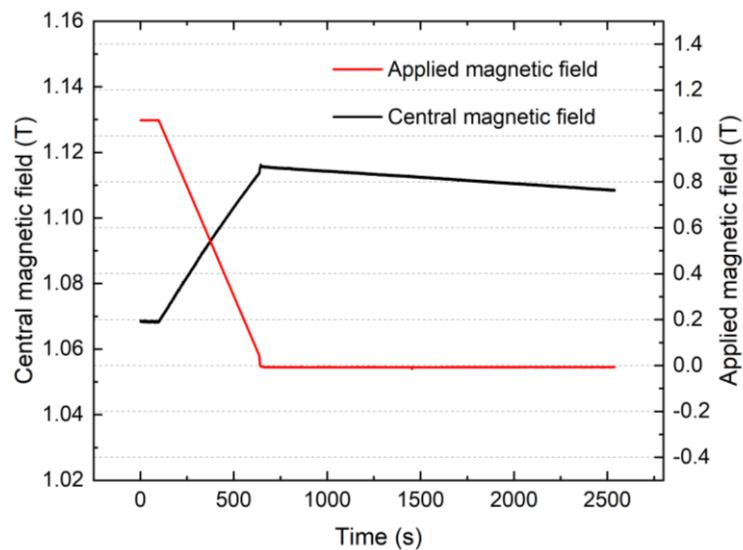
Figure 7.19: Central field of the HTS double-pancake coil during 1.07 T magnetization
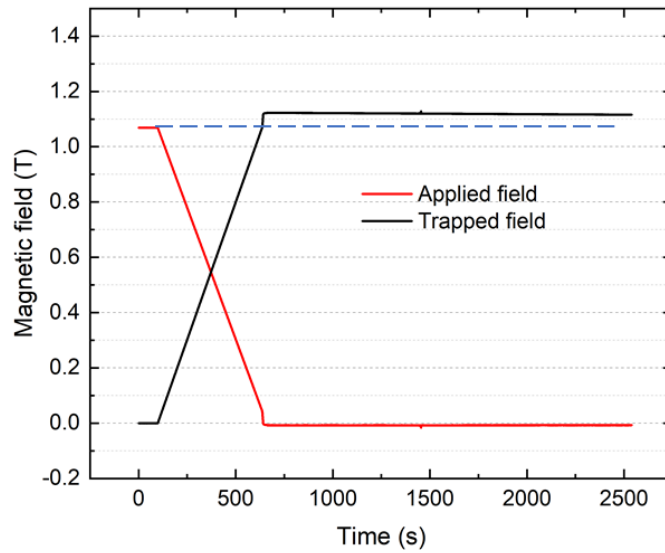
Figure 7.20: Trapped field of the HTS double-pancake coil during 1.07 T magnetization

Fig. 7.21 represents the trapped field during the 4.5 T magnetization. Initially, the central field shows the same upward trend in the magnetization's initial stages. It attains its peak at approximately 4.6 T before it witnesses a consistent decline. Once the applied field is reduced to zero, the central field sees a steady decrease, a phenomenon contributed by the current dissipation resulting from the resistance of the joints. An intriguing observation is the similarity of the central field's curve during the 4.5 T field cooling magnetization with that of the double-turn HTS-stacked ring magnet model analysed in Chapter 4. These two curves underscore the veracity of the prediction made in Chapter 4 concerning a trapped field higher than the applied field can be achieved by HTS-stacked ring magnets.
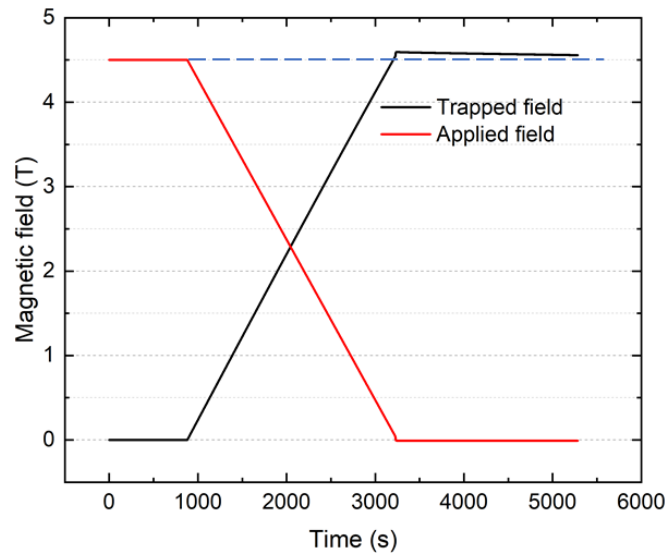
Figure 7.21: Trapped field of the HTS double-pancake coil during 4.5 T magnetization
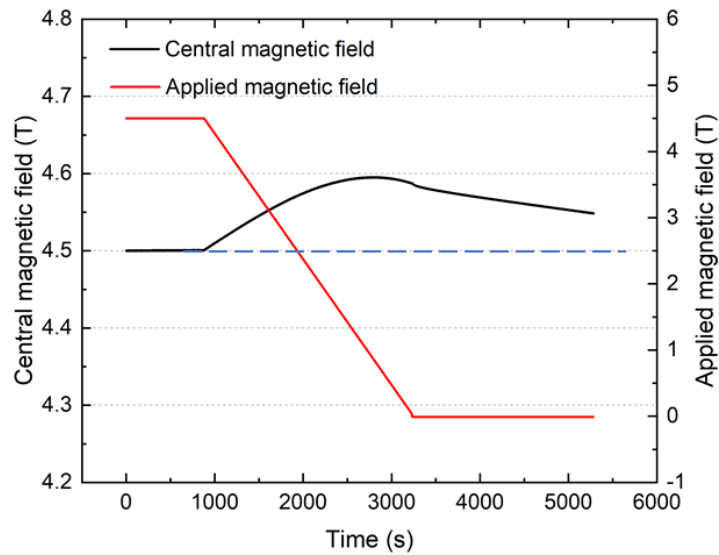
Figure 7.22: Central field of the HTS double-pancake coil during 4.5 T magnetization

Fig. 7.22 shows more intuitively that the central trapped field surpasses the initial applied field. With the applied field decreased to zero, the central trapped field was 4.59 T—a differential of approximately 0.1 T relative to the initially applied field. A temporal progression of 30 minutes (equivalent to 1800 seconds) witnesses the central field's decay to 4.55 T, a value which still exceeds the originally applied 4.5 T.

151

7.3.3 Quench Test of the HTS Double-Pancake Coil

As previously mentioned, a polyimide heater was affixed to the bottom of the brass sample holder, as shown in Fig. 7.23. After the 4.5 T magnetization process, the heater, which was interfaced with a Lakeshore 336 temperature controller, was activated. The temperature was pre-set to 100 K with the power setting adjusted to "medium". The temperature trajectory recorded by the Cernox sensor is presented in Fig. 7.24.

Figure 7.23: The polyimide heater

Upon the initiation of the temperature increase, the central trapped field exhibited a gentle decrement. Yet, a notable anomaly occurred when the temperature approached approximately 13 K: the trapped field suddenly plummeted to zero within a span of less than one second, concurrent with a rapid temperature surge. This was followed by the temperature reaching its peak before subsequently declining.
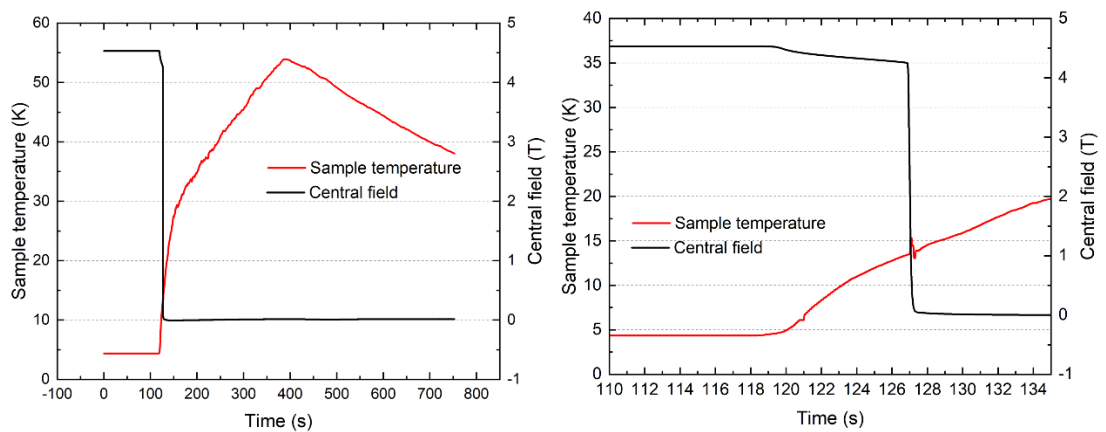
Figure 2.24: Temperature variations during the heating process

The initial slow decline in the trapped field, alongside the escalating temperature, is thought to be an outcome of the reduction in the critical current. Conversely, the abrupt quench observed in the HTS coil, coupled with the quick temperature rise, is considered to be triggered by overheating at certain vulnerable segments on the HTS coil. The induced current experienced swift dissipation due to a simultaneous rise in resistance and temperature, which further diminished the critical current.

It is important to underscore that at the time of the quench, a residual amount of liquid helium remained in the cryostat, and the thermal conduction had hysteresis. Consequently, the immediate temperature spike could potentially surpass the recorded data. Furthermore, a comparable heating procedure was implemented for the HTS-stacked ring magnet measurement. Notably, no such abrupt quench was observed across multiple heating cycles in previous experiments. This lends credence to the hypothesis that the sudden quench predominantly originates from the coil's soldering joints.

7.3.4 Magnetization and Field Decay After Quench Test

After the HTS coil was quenched by the heater, another field cooling process was conducted again with an applied field of 10 T and other parameters were kept the same. Fig. 7.25 shows the central field and the applied field during the magnetization. There was a pause at the initial phase of the applied field ramping down to halt the surge of temperature rise. In the residual process, there is no other manual interference even though there is still temperature fluctuation. The central field remarkedly decreases simultaneously with the applied field. There is a stable differential of about 1.9 T between the applied field and the central field which should be the trapped field by the HTS coil. After the applied field decreases to zero, the central field decays quickly as shown in Fig. 7.26. It indicates that the resistance of the coil is much higher than before.
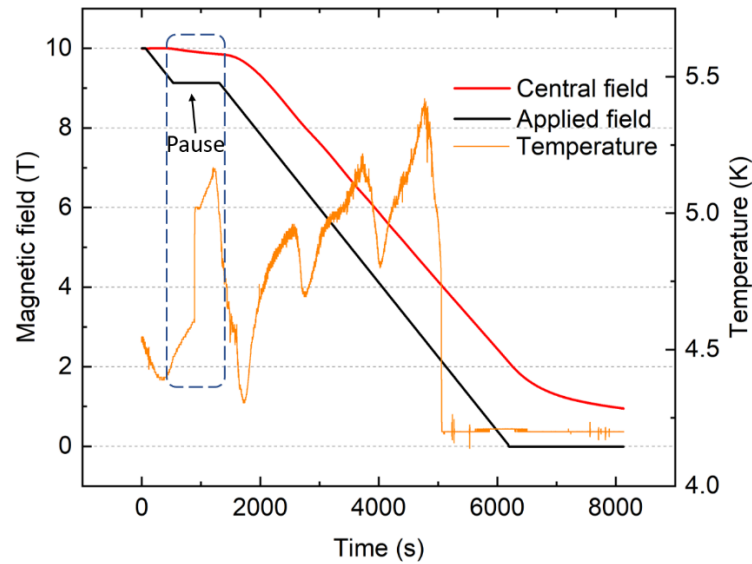
Figure 7.25: Central field and temperature during 10 T magnetization

A comparison is made between the trapped field decay rates following 1.07 T and 10 T magnetizations to assess the impact of manual heating quench and resistance changes on the decay rate. As illustrated in Fig. 7.27, the decay rate after the 10 T magnetization is much faster than that of the 1.07 T magnetization. Both trapped fields initiate their decay from 1.115 T. At 650 seconds, the trapped field after the 1.07 T magnetization retains a value of 1.112 T, while that following the 10 T magnetization reduces to 0.956 T. In this context, the predominant factor influencing the decay rate appears to be the resistance of the joints. The data suggests that the resistance of the joints has increased significantly and that the heating quench process might have compromised the integrity and quality of the soldered joints. The following investigation will further discuss the change of joint resistance after the quench test.
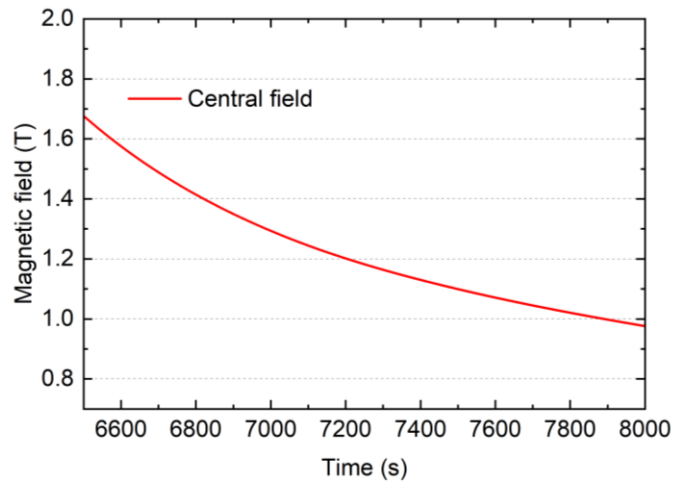
Figure 7.26: Central field decay after 10 T magnetization
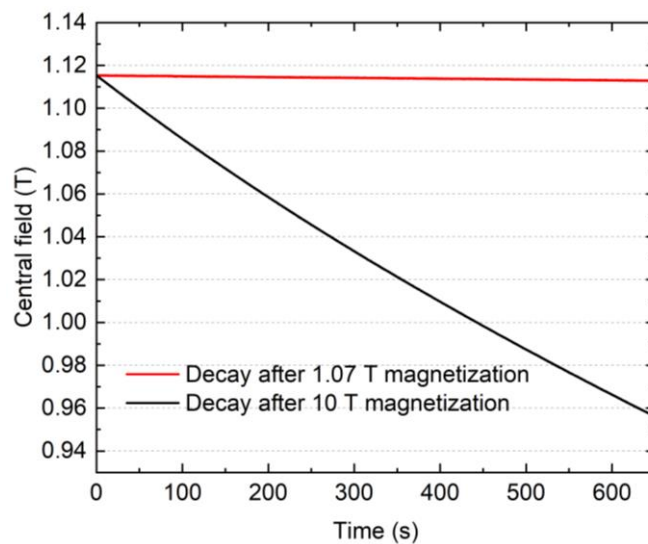
Figure 7.27: Central field decay after 1.07 T and 10 T magnetization

7.4 Post-Experiment Inspection on the HTS Double-Pancake Coil and Joints

To comprehensively ascertain the extent of damage to the joints and provide insights for future HTS trapped field coil fabrication, the soldered joints were cut from the coil and re-evaluated in our laboratory using liquid nitrogen. Fig. 7.28 displays the application of a 4-point measurement to assess the joints. Voltage taps at positions A, B, and C were employed to independently test the resistance of each joint. By placing the voltage taps at positions A and C, the total voltage drop across both joints was

recorded, as depicted in Fig. 7.29. The rapid and consistent increase in voltage indicates a substantial rise in resistance for the joints, approximating a value of 5.3 μΩ.
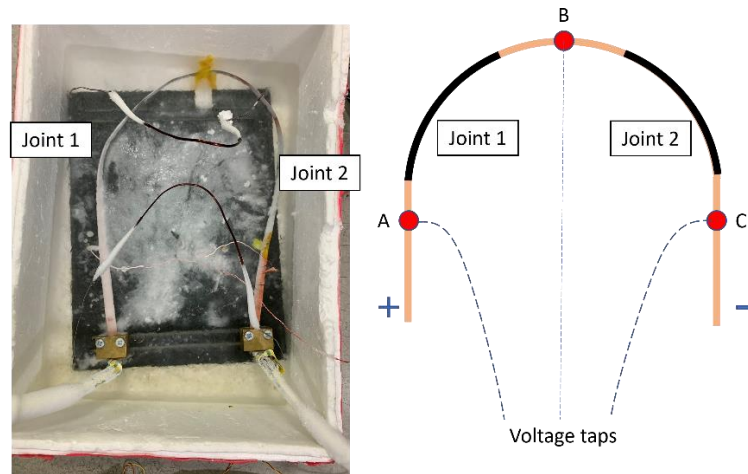
Figure 7.28: Resistance measurement after quench test

Subsequently, the voltage taps were adjusted to positions A and B, with a 100 A current serving as the benchmark for the assessment. The resulting current and voltage plots are illustrated in Fig. 7.30. From these observations, the resistance of joint 1 is calculated to be approximately 5.3 μΩ. This confirms that joint 1 sustained damage, which in turn impacted the trapped field and field decay characteristics of the HTS coil. An evaluation of joint 2 revealed a resistance value close to 4 nΩ (Fig. 7.31), suggesting that this joint remains largely unaltered from its initial soldered state.
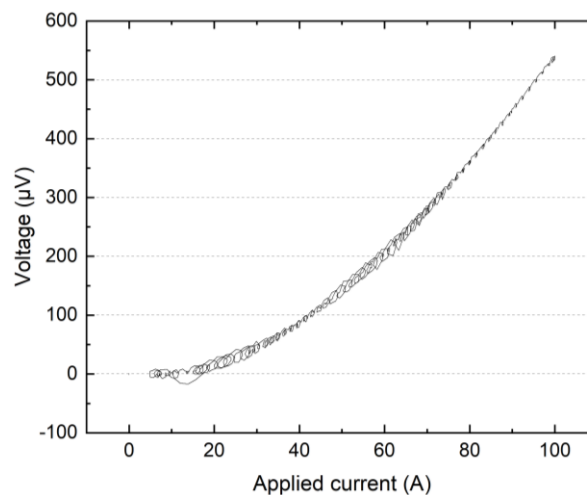
Figure 7.29: Resistance of the 2 joints after quench test
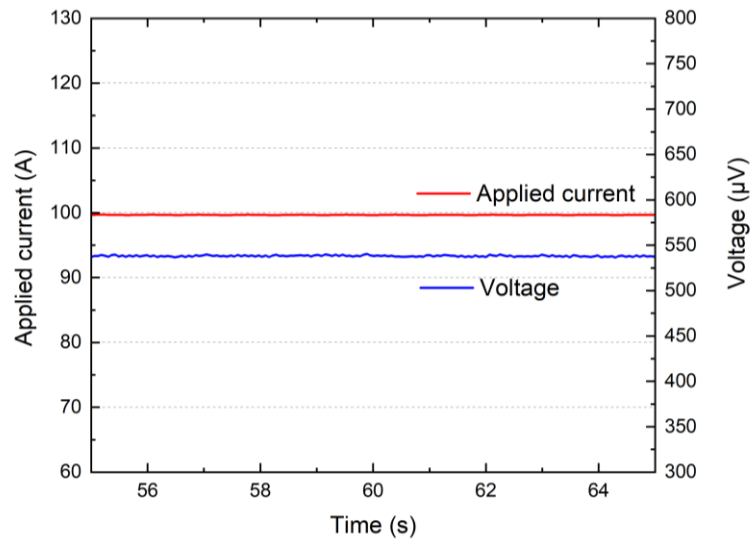
Figure 7.30: Resistance of joint 1 after quench test
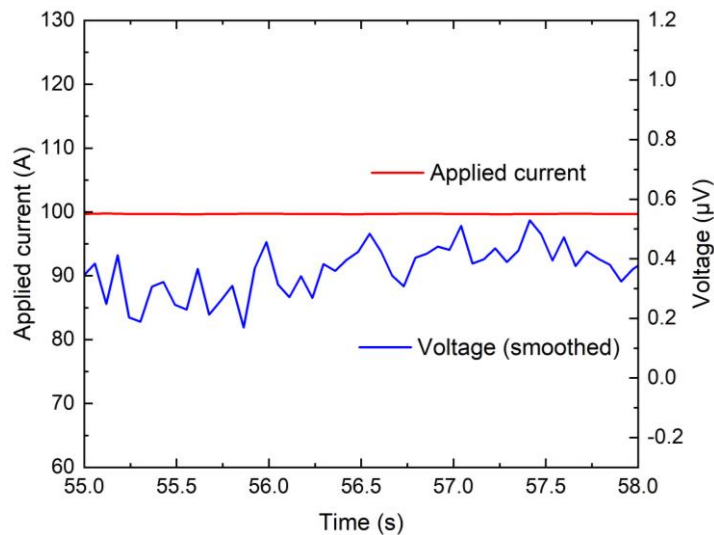
Figure 7.31: Resistance of joint 2 after quench test

During the finalization process of the HTS double-pancake coil sample, the joints' critical current was not evaluated, primarily to mitigate potential risks of thermal degradation or burning. Subsequent investigations focused on the critical current of joint 2, with the current-voltage relationship depicted in Fig. 7.31. Observations indicate that joint 2 has a critical current of approximately 300 A, which falls short of the tape's standard critical current, typically measured around 550 A. This data suggests degradation in the tape joint, likely stemming from the heating and pressing of the soldering process. Elevated temperatures could lead to oxygen coming out of

the ReBCO materials, consequently diminishing the performance of the HTS tapes. Additionally, excessive pressure during soldering may result in mechanical damage to the tapes. Optimizing the soldering process is essential to concurrently achieve reduced resistance and enhanced critical current in the joints for future studies.
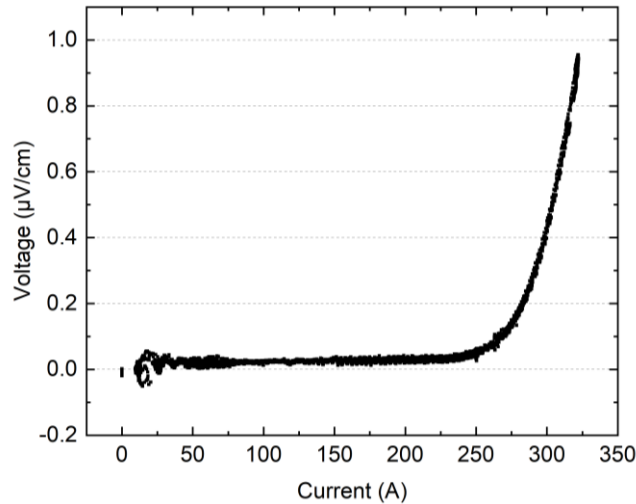
Figure 7.32: Critical measurement of joint 2 after 10 T magnetization

7.5 Investigation of the HTS Double-Pancake Coil Magnetization

In Chapter 4, the potential of the HTS-stacked ring magnet to exceed the applied magnetic field in terms of the trapped field was predicted, and the underlying mechanism was elucidated through numerical simulation. In contrast, the HTS double-pancake coil demonstrated the possibility of achieving a trapped field higher than the applied field through experimental measurement in this chapter. Despite the commonality of both structures being fabricated from HTS tapes, the architecture of current flow in the two configurations is markedly different. In the HTS-stacked ring magnet, each turn has its current loop, leading to varying current levels across different turns. Conversely, the HTS double-pancake coil is wound from a single tape, resulting in uniform current distribution across all turns. This section will engage in a numerical analysis of the magnetization and field decay behaviours exhibited by the HTS coil and will explore the mechanisms enabling it to trap a field surpassing the applied field.

7.5.1 Field Decay Rate Calculation

When the external field is completely removed, the closed-loop HTS double-pancake coil can be seen as an *RL* circuit that is short-circuited, so the current can be calculated according to:

$$\frac{di}{dt} + \frac{R}{L}i = 0 \tag{7.1}$$

Where i is the current, R is the resistance, and L is the inductance.

The solution to this equation is

$$i(t) = i_0 e^{\left(\frac{Rt}{L}\right)} \tag{7.2}$$

Where i_0 is the initial current at $t=0$

Since the magnitude of the trapped field is linear to the current in the coil, the field decay is also linear to the current dissipation. The central field can be calculated based on Eq. 7.3

$$F_c = A_0 e^{\left(\frac{Rt}{L}\right)} \tag{7.3}$$

Where F_c is the central trapped field of the HTS coil and A_0 is the initial field during field decay.

The inductance of the HTS double-pancake coil is consistent, registering at 550 μH as measured by an LCR meter. According to Eq. 7.3, the decay of the central trapped field follows an exponential curve. Data fitting can therefore be conducted using software tools such as Origin to calculate the resistance. Fig. 7.33 presents the fitting curve representing the field decay over 10 hours based on the prior 4.5 T magnetization. As indicated by the fit, the central field decayed to 4.4 T—a 3.9% reduction—after 3 hours from its initial value of 4.58 T. After 10 hours, the field reached 4.03 T, corresponding to a decay rate of 12%. Given that the inductance is already known, the resistance is calculated to be 2 nΩ. This is substantially lower than the previously measured 12 nΩ resistance of the joints in liquid nitrogen, a discrepancy attributed to the reduced resistance of the PbSn soldering material at the liquid helium temperature. It is posited that with greater inductance or optimized joint resistance, the HTS coil's

trapped field could be sustained for a longer duration. This would be advantageous in applications such as short-distance aviation HTS motors, where a high field and controllable slow decay rate are desirable.
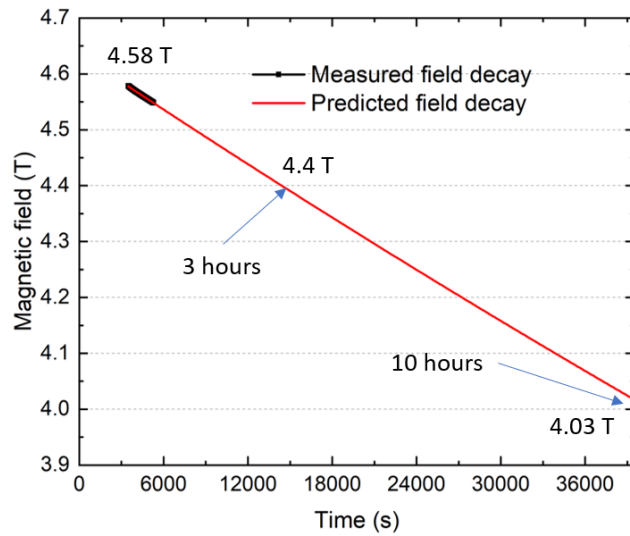
Figure 7.33: The fitting curve of the field decay after 4.5 T magnetization

Employing the same fitting methodology, the decay curve following the 10 T magnetization with the damaged joint has also been derived and is depicted in Fig. 7.34. This curve suggests that the trapped field will deplete to zero within approximately 6.7 hours.
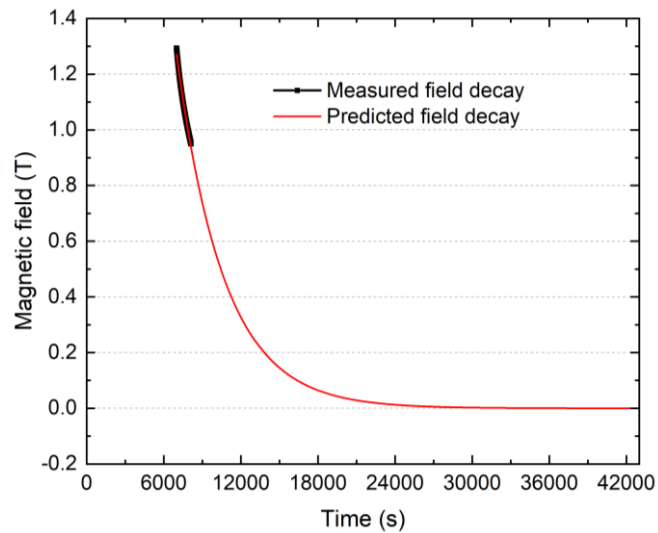
Figure 7.34: The fitting curve of the field decay after 10 T magnetization

7.5.2 FEM Modelling of The HTS Double-Pancake Coil Magnetization

To further investigate the magnetization properties of the HTS double-pancake coil and dig out the reason for trapping a higher field than the applied field, numerical models will be established for analysis. Different from the HTS-stacked ring magnets which feature an asymmetrical geometry, HTS double-pancake coils are perfectly symmetrical. Therefore, in this section, a 2D axisymmetric model is utilized for the numerical simulation. The equations and parameters for the modelling are the same as those employed in Chapter 4 because the same HTS materials were chosen for the HTS double-pancake coil. Since 2D axisymmetric models are used for the coil, homogenized modelling is not necessary and is not used.

As shown in Fig. 7.35, only half of the double-pancake coil (upper coil) is calculated and is mirrored against the symmetrical boundary, so that the whole double-pancake coil can be calculated. Since the induced currents in each turn are the same, current constraints are used to realize this situation. Besides, even though the resistance of joints can have a slight effect on the trapped field, this influence is neglectable for the simulation of the magnetization process, because the field decay is significantly determined by time and the 4.5 T magnetization was processed within about 30 minutes. In addition, it is not practical for the simulation model to demonstrate the half-hour current dissipation. Therefore, the HTS coil model does not consider the resistance in the coil. The same methodology for the field cooling magnetization simulation as employed in Chapter 4 is used in this Chapter.
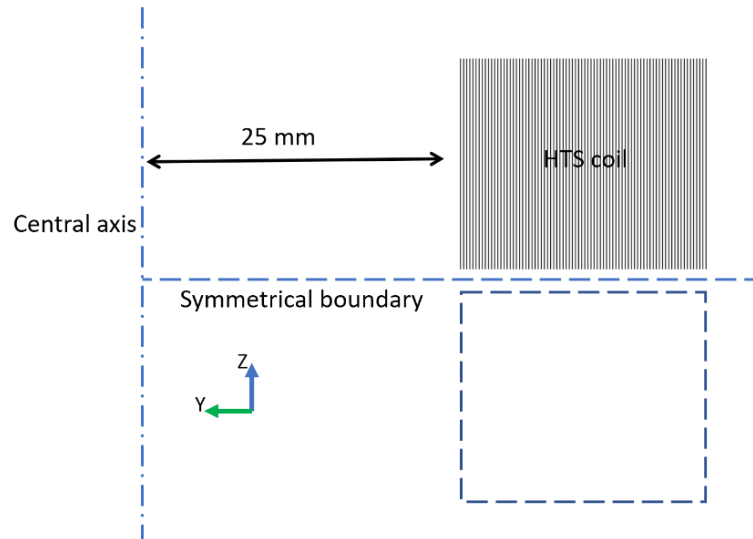
Figure 7.35: 2D axisymmetric model of HTS double-pancake coil
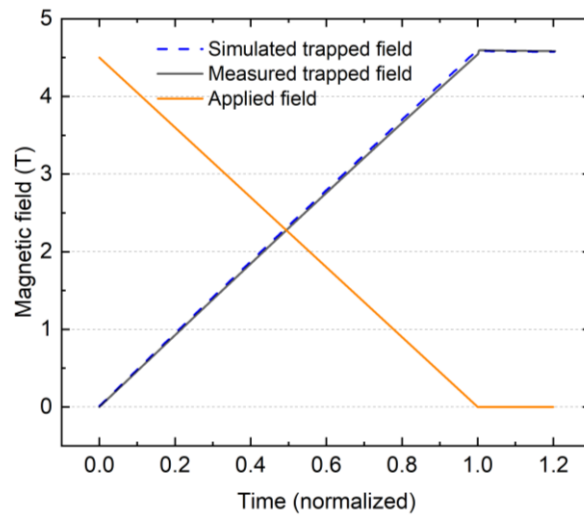
Figure 7.36: Results of simulation and experiment results of trapped fields of HTS double-pancake coil

Fig. 7.36 depicts the trapped fields resulting from the 4.5 T magnetization as determined both through simulation and experimental measurement. Given that the simulation model is constrained by time limitations and not applicable to the actual time of the experiment, normalized time is employed to facilitate comparison. A good congruence between the simulated and empirically measured trapped fields is evident, thereby affirming the validity of the simulation model.

7.5.3 The Mechanism of Achieving Higher Trapped Fields Than Applied Fields by HTS Coils

To figure out the reason for the HTS coil easily trapping a higher field than the applied field, a comparative study is carried out based on the verified simulation model. As mentioned previously, HTS bulk materials are not capable of achieving a trapped field higher than the applied field, so a calculation of the HTS bulk material with the same geometry and double-pancake-coil-structure is conducted as shown in Fig. 7.37. The only difference between this model and the HTS coil model is that this bulk material model doesn't have current constraints for each HTS domain, which means it acts like a stack of multiple concentric bulk material rings and their induced currents are independent of each other.
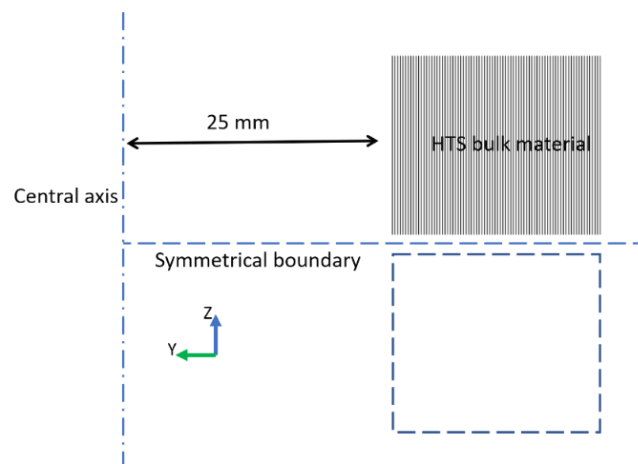
Figure 7.37: 2D axisymmetric model of HTS bulk material with a double-pancake structure

The central trapped field of the HTS bulk model under the same 4.5 T magnetization is shown in Fig. 7.38. The trapped field is lower than the applied field which follows the rule of the magnetization of HTS bulk materials.

To investigate the reason why the HTS coil can trap a higher central field, the induced current density distributions after magnetizations of both models are depicted in Fig. 7.39. Their current density distributions see marked differences. For comparison, their outer turns are zoomed in and divided into A, B, and C three parts for inspection. It can be seen that there is both negative and positive current density in the outer turn of the HTS coil, while in the bulk material, there are only positive components. The

negative induced current density in the HTS coil occurs near the middle of the double-pancake coil. The cause of the negative current density can be considered as the reversed magnetization which coincides with the rising trapped field. During field cooling magnetization, the external field is gradually reduced which will induce the positive current. However, the unique central field ascent by the HTS coil can lead to a reversed magnetization and it affects most in the middle area of the double-pancake coil.
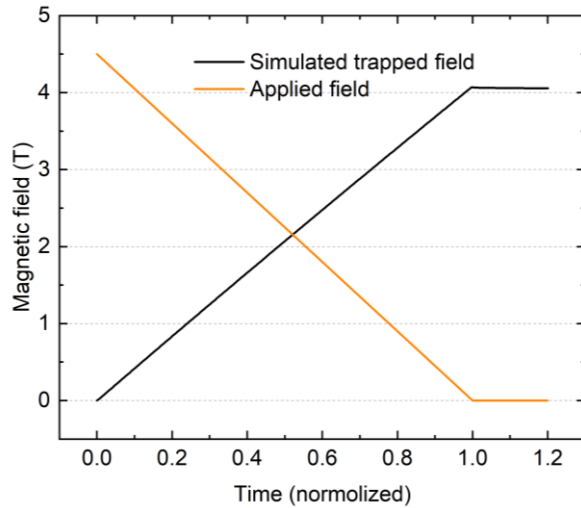
Figure 7.38: The trapped field of HTS bulk material with a double-pancake structure
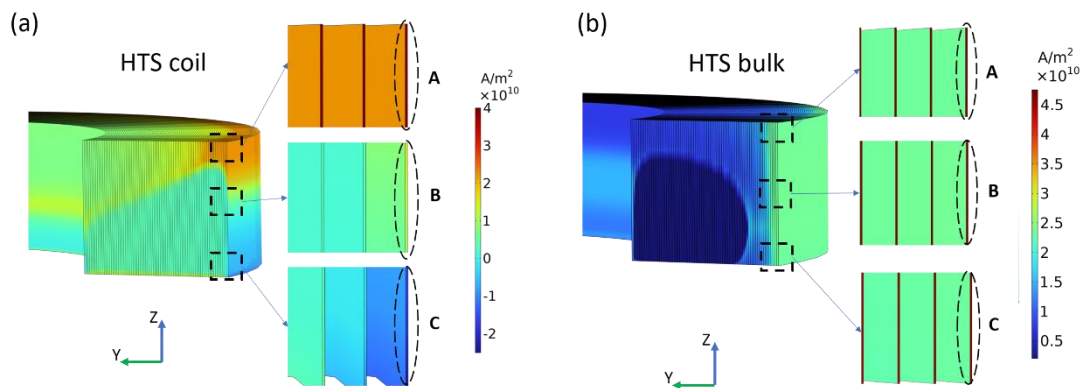
Figure 7.39: Induced current distribution in coil model (left) and bulk model (right)

Fig. 7.40 illustrates the trapped flux line distributions of the two models. Focusing on the flux density in the HTS areas, it can be noticed that more flux lines are crossing the HTS bulk which means the HTS bulk material can keep more flux lines inside the material itself. The HTS coil pushes the flux lines out of itself so that the flux line in

the central air area can be denser, and a higher trapped field can be seen in the central space of the HTS coil. It can also be understood by different magnitude distributions of induced currents. A higher induced current appears at the outer area of the HTS bulk material generating a higher magnetic field, while the HTS coil has the same induced current in each turn.
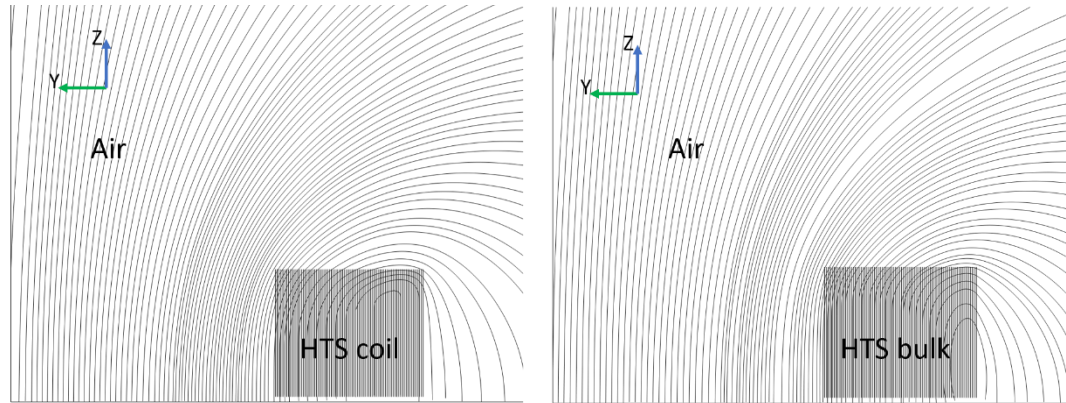
Figure 7.40: Trapped flux distribution in coil model (left) and bulk model (right)

Fig. 7.41 shows the scheme of the central line for the trapped field distributions of both the models under study. The trapped fields on the z-axis (B_z) spanning from point P to Q are represented in Fig. 7.42. At the central area, the trapped field exhibited by the HTS coil surpasses that of the HTS bulk material. Notably, there's a rapid drop in the trapped field within the area inside the HTS coil. In contrast, the HTS bulk displays an almost consistent field throughout its volume. In comparison to the tape-double HTS-stacked ring magnet (refer to Fig. 4.25), the trapped field within the HTS coil demonstrates a linear descent, whereas the field in the HTS-stacked ring magnet diminishes by half. Given that every turn of the coil conducts an identical current, coupled with the implications of Faraday's law, this linear decline in the field inside the HTS coil stands out as a distinctive feature of the HTS double-pancake coil configuration.

In summary, the HTS double-pancake coil can generate a trapped field at its centre that exceeds the applied field. This can be visualized as a compression of flux lines towards the central space, squeezing from within the coil's body. The uniform induced current across each turn facilitates this phenomenon, similar to the behaviour observed in the HTS-stacked ring magnet. Such an enhanced field trapping capability implies

that less external field is required to magnetize the HTS coils, paving the way for greater efficiency and reduced energy consumption in related applications.
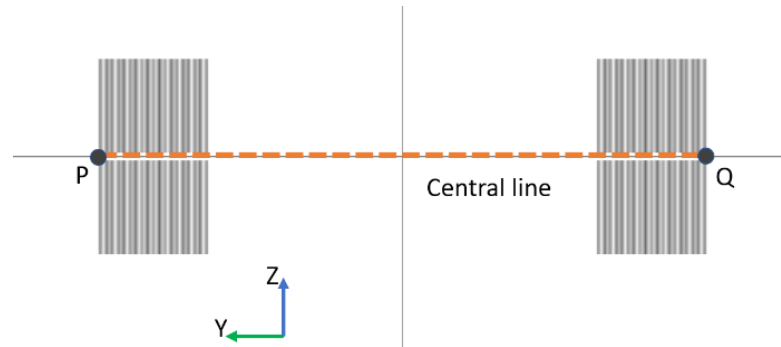
Figure 7.41: Scheme of the central line of the HTS double-pancake coil
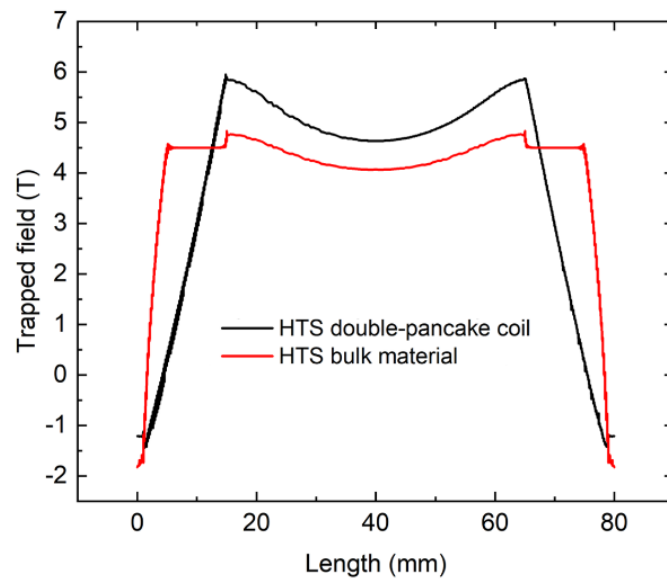
Figure 7.42: Trapped field distributions of the coil model and the bulk model

7.6 Conclusion

In this chapter, the fabrication and analysis of an HTS double-pancake coil are discussed. The coil was uniquely wound using a custom-built winding machine with 12 mm Fujikura FESC-SCH tapes. The major insights and findings include:

Chapter 7. Magnetization of the HTS Double-Pancake Coil with Joints

Joint Fabrication: A bridge-type soldering method was employed, optimized for reduced joint resistance and ease of winding. Initial measurements revealed a joint resistance of 12 nΩ.

Magnetization of the HTS Coil Sample: The coil, after undergoing a field cooling magnetization process under liquid helium, exhibited the remarkable ability to achieve trapped fields that surpassed the applied external fields for both 1.07 T and 4.5 T.

Quench Concerns: A sudden quench and temperature spike were observed during the coil heating process. Post-quench evaluations indicated a compromised performance, with elevated resistance and diminished trapped field capability. Further resistance measurements post-quench revealed a significant increase in resistance in one of the joints.

Simulation Analysis: With 2D axisymmetric models, insights were gained into the current distribution and factors enabling the coil to trap a higher field than the applied field. Comparative analyses showed the HTS coil's ability to centralize more flux due to the uniformly constrained current in each turn. In contrast, the HTS bulk material was found to retain a greater amount of flux within itself.

This chapter underscores the potential and challenges associated with HTS double-pancake coils and suggests references for further research and optimizations.

Chapter 8. Thesis Conclusions and Future Work

8.1 Conclusions

Compact HTS trapped field magnets are a promising technology that has a great impact on advanced industrial equipment, transportation electrification and medical devices. While traditional HTS bulks and stacks achieved trapped fields over 17 T, they face geometric and durability constraints. Advancements in 2G commercial HTS tape fabrication spotlight their potential for broader, consistent trapped fields. The emergence of HTS-stacked ring magnets, created by stretching and stacking HTS tapes, offers a promising alternative. With refined quality control and extended dimensions of these tapes, the potential size of HTS-stacked ring magnets could be virtually limitless. Despite these advances, key areas need further exploration. The magnetization, trapped field enhancements, and the mechanics of HTS-stacked ring magnets at lower temperatures require deeper study. Modern soldering techniques for HTS tapes now enable low-resistance joints. This development opens the possibility of fabricating HTS double-pancake coils with soldered joints, ensuring a closed-loop current post-magnetization. Such an approach is anticipated to provide more uniform trapped field profiles, attributed to the consistent geometry of double-pancake coils.

Addressing these concerns, this thesis delves into the magnetization characteristics and mechanical behaviour of HTS-stacked ring magnets, aiming to offer insights for optimal design and application strategies. Moreover, the research explores the feasibility and unique magnetization attributes of employing HTS double-pancake coils as trapped field magnets. Both (hybrid) HTS-stacked ring magnet specimens and HTS double-pancake coils with joints were fabricated, followed by rigorous magnetization experiments to study the trapped fields. Numerical methodologies were harnessed to provide a more profound understanding of the underlying mechanisms and analyses. Broadly, the contributions of this thesis span across four principal

domains of knowledge, with each domain elucidated comprehensively in the subsequent sections.

Unique magnetization behaviour and mechanism of the HTS-stacked ring magnet

The study in this thesis first investigates the HTS-stacked ring magnet's magnetization process using experiments and numerical modelling. A notable central field ascent phenomenon was observed during field cooling at 25 K with a 4.5 T field, where the central field initially rose before settling at 3.79 T, distinguishing it from typical HTS trapped field magnets. The magnet also demonstrated an asymmetrical trapped field distribution attributed to its unique design. Differing from traditional HTS bulk materials, the 3D modelling highlighted that the HTS-stacked ring magnet induces currents in both its inner and outer layers simultaneously. Based on this study, further numerical investigation showed the HTS-stacked ring magnet has the potential for trapping a central field higher than the applied field when the number of HTS tapes is doubled.

Enhanced trapped fields of hybrid HTS-stacked ring magnets

The extensive study of hybrid HTS-stacked ring magnets, which intricately combine both HTS stacks and HTS bulks, reveals findings that can reshape our approach to magnet design and application. The introduction of either HTS stacks or bulks into the magnetic equation substantially elevates the trapped field capacities. The hybrid designs presented a moderated central field ascent, influenced by internal current dynamics. These dynamics, highlighted by numerical models, show reduced currents in inner turns and shared currents in the HTS stacks. An intriguing consequence of this was the emergence of a counter-induced current, subtly reducing the trapped field of the hybrid design compared to non-hybrid counterparts in certain situations.

In contrast, the hybrid design with HTS bulks achieved a trapped field of 7.35 T. Their performance, in terms of field distribution, overshadows that of standalone HTS bulks or stacks. This hybrid design unveils a two-stage magnetization process FC magnetization, marked by the full penetration of the HTS-stacked rings. Intriguingly, regardless of the specific hybrid composition, geometric asymmetry remains a

consistent theme, causing both the HTS stacks and bulks to undergo uneven magnetization.

Mechanical behaviours of (hybrid) HTS-stacked ring magnets

The study also investigates the mechanical intricacies of the HTS-stacked ring magnet, spotlighting the effects of the Lorentz force and stress distribution. Without specific fixation, the HTS-stacked rings suffer from pronounced stress concentration at split ends, a vulnerability to the Lorentz force. However, this vulnerability diminishes with paraffin wax impregnation and brass holders.

The study further reveals that the integration of HTS stacks into the magnet's core amplifies the trapped field, yet with a barely perceptible impact on internal stress levels. This highlights the inherent robustness of these rings. Moreover, asymmetries are evident throughout, from uneven Lorentz forces in centrally placed HTS stacks due to the intrinsic trapped field distribution, to stress peaks at the top and bottom sections of the stacks. Yet, even under these conditions, the stacks demonstrate remarkable resilience, staying well within commercial HTS tape safety thresholds.

Conclusively, this deep dive into the mechanical behaviour of HTS-stacked ring magnets furnishes invaluable insights, crucial for optimizing design and ensuring durability.

Magnetization of HTS double-pancake coil with a higher trapped field than the applied field

Finally, the study of this thesis delves into the creation and evaluation of an HTS double-pancake coil, crafted using a custom winding machine with 12 mm Fujikura FESC-SCH tapes. A bridge-type soldering approach ensured minimized joint resistance, measured as 12 nΩ at 77 K. Remarkably, the coil's trapped fields exceeded externally applied levels, demonstrating its capability of achieving a trapped field higher than the applied field. Yet, challenges arose, notably a concerning quench event during heating that flagged potential vulnerabilities. Subsequent post-quench measurements revealed elevated resistance in one joint and diminished trapping capabilities.

Simulations via 2D axisymmetric models offered insights into the coil's unique current distribution and its capacity to surpass externally applied fields. Comparative studies highlighted the coil's advantage for flux concentration due to consistent current constraints, while the HTS bulk material showcased superior internal flux trapping.

In essence, this study unveils the potential and complexities of HTS double-pancake coils, laying groundwork for future explorations and enhancements.

8.2 Future Work

This section provides recommendations for potential avenues of future research and advancements based on the insights and conclusions drawn from the present study.

Balanced Field Distribution in HTS-Stacked Ring Magnet

The current hybrid HTS-stacked ring magnet exhibits an uneven trapped field due to its asymmetric design. For applications requiring symmetrical trapped fields, a potential solution might involve integrating two HTS-stacked ring magnets with opposing stretching directions. While theoretically, this design can offset the unbalanced field, it does introduce complexities in the magnet's structure. For one magnet to fit inside the other, intricate size and geometrical considerations are crucial. Moreover, given the typically constrained bores of globally available magnets suitable for FC magnetization at cryogenic temperatures, designing a balanced HTS-stacked ring magnet presents its own set of challenges.

Charging Mechanisms for Larger HTS-Stacked Ring Magnets

As the dimensions of the HTS-stacked ring magnet surpass those of the bores of conventional external magnets, traditional FC or ZFC magnetization techniques become infeasible. For applications like body-scan MRI machines which require larger diameters, new magnetization methods are vital. Present MRI devices that utilize LTS coils mainly rely on persistent current switches for energization. Given that the HTS-stacked ring magnet comprises separated HTS tapes, conventional charging methods become ineffective. The prevalent flux pumps, which often rely on coil charging, might not be suitable, either. Thus, developing a unique charging methodology for

large-sized HTS-stacked ring magnets is important, especially since there are currently no proposed methods addressing this need.

Improving Joint Reliability in HTS Double-Pancake Coils

Chapter 7 highlights a joint failure that occurred post-magnetization. Such damages, besides being permanent, can lead to sudden quenches, releasing significant heat and potentially affecting the coil. For optimal trapped field performance, enhancing joint reliability is imperative. There is a need to refine the soldering techniques to ensure joint durability while maintaining low resistance. Aspects such as pressure and temperature control during the soldering process must be fine-tuned to eliminate joint vulnerabilities. Furthermore, protective designs for these joints, which can redirect currents during adverse conditions, might prove beneficial. Such designs could minimize Joule heat at the joint, and when coupled with optimized thermal conductivity, can effectively dissipate heat, reducing potential harm to the joints.

References

[1]   Y. Lvovsky and P. Jarvis, "Superconducting systems for MRI-present solutions and new trends," *IEEE Transactions on Applied Superconductivity*, vol. 15, no. 2 PART II, pp. 1317–1325, 2005, doi: 10.1109/TASC.2005.849580.

[2]   Y. Iwasa, J. Bascuñán, S. Hahn, M. Tomita, and W. Yao, "High-temperature superconducting magnets for NMR and MRI: R&D activities at the MIT Francis Bitter Magnet Laboratory," *IEEE Transactions on Applied Superconductivity*, vol. 20, no. 3, pp. 718–721, Jun. 2010, doi: 10.1109/TASC.2010.2040073.

[3]   J. Ling *et al.*, "Towards liquid-helium-free, persistent-mode MgB2 MRI magnets: FBML experience," *Supercond Sci Technol*, vol. 30, no. 5, p. 053001, Mar. 2017, doi: 10.1088/1361-6668/AA5FED.

[4]   N. Bulut and D. J. Scalapino, "Analysis of NMR data in the superconducting state of YBa2Cu3O7," *Phys Rev Lett*, vol. 68, no. 5, p. 706, Feb. 1992, doi: 10.1103/PhysRevLett.68.706.

[5]   H. Maeda and Y. Yanagisawa, "Recent Developments in High-Temperature Superconducting Magnet Technology (Review)," *IEEE Transactions on Applied Superconductivity*, vol. 24, no. 3, Jun. 2014, doi: 10.1109/TASC.2013.2287707.

[6]   R. K. Birdwhistell and E. M. Schubert1, "Utilizing the Evans method with a superconducting NMR spectrometer in the undergraduate laboratory," *Journol of Chemical Education*, vol. 69, no. 1, p. 62, 1992, doi: 10.1021/ED069P62.1.

[7]   Z. Deng *et al.*, "A High-Temperature Superconducting Maglev-Evacuated Tube Transport (HTS Maglev-ETT) Test System," *IEEE Transactions on Applied Superconductivity*, vol. 27, no. 6, Sep. 2017, doi: 10.1109/TASC.2017.2716842.

[8]   M. Ono, S. Koga, and H. Ohtsuki, "Japan's superconducting Maglev train," *IEEE Instrum Meas Mag*, vol. 5, no. 1, pp. 9–15, Mar. 2002, doi: 10.1109/5289.988732.

References

[9]   S. Kusada *et al.*, "The project overview of the HTS magnet for superconducting Maglev," *IEEE Transactions on Applied Superconductivity*, vol. 17, no. 2, pp. 2111–2116, Jun. 2007, doi: 10.1109/TASC.2007.899691.

[10]   S. Kusada *et al.*, "The project overview of the HTS magnet for superconducting Maglev," *IEEE Transactions on Applied Superconductivity*, vol. 17, no. 2, pp. 2111–2116, Jun. 2007, doi: 10.1109/TASC.2007.899691.

[11]   F. Grilli *et al.*, "Superconducting motors for aircraft propulsion: the Advanced Superconducting Motor Experimental Demonstrator project," *J Phys Conf Ser*, vol. 1590, no. 1, p. 012051, Jul. 2020, doi: 10.1088/1742-6596/1590/1/012051.

[12]   P. J. Masson and C. A. Luongo, "High power density superconducting motor for all-electric aircraft propulsion," *IEEE Transactions on Applied Superconductivity*, vol. 15, no. 2 PART II, pp. 2226–2229, Jun. 2005, doi: 10.1109/TASC.2005.849618.

[13]   Y. Terao, A. Seta, H. Ohsaki, H. Oyori, and N. Morioka, "Lightweight Design of Fully Superconducting Motors for Electrical Aircraft Propulsion Systems," *IEEE Transactions on Applied Superconductivity*, vol. 29, no. 5, Aug. 2019, doi: 10.1109/TASC.2019.2902323.

[14]   L. Tomkow, I. M. Harca, K. Machaj, A. Smara, T. Reis, and B. A. Glowacki, "Experimental system for testing a superconducting motor at temperatures close to 15 K," *Cryogenics (Guildf)*, vol. 112, p. 103206, Dec. 2020, doi: 10.1016/J.CRYOGENICS.2020.103206.

[15]   K. S. Haran *et al.*, "High power density superconducting rotating machines—development status and technology roadmap," *Supercond Sci Technol*, vol. 30, no. 12, p. 123002, Nov. 2017, doi: 10.1088/1361-6668/AA833E.

[16]   T. A. Coombs, "Development of 1 MW-class HTS motor for podded ship propulsion system Development of 1 MW-class HTS motor for podded ship propulsion system," 2010, doi: 10.1088/1742-6596/234/3/032060.

References

[17] M. Frank *et al.*, "High-temperature superconducting rotating machines for ship applications," *IEEE Transactions on Applied Superconductivity*, vol. 16, no. 2, pp. 1465–1468, 2006, doi: 10.1109/TASC.2005.864263.

[18] A. Barzkar and M. Ghassemi, "Electric power systems in more and all electric aircraft: A review," *IEEE Access*, vol. 8, pp. 169314–169332, 2020, doi: 10.1109/ACCESS.2020.3024168.

[19] C. Friedrich and P. A. Robertson, "Hybrid-electric propulsion for aircraft," *J Aircr*, vol. 52, no. 1, pp. 176–189, Jan. 2015, doi: 10.2514/1.C032660/ASSET/IMAGES/LARGE/FIGURE18.JPEG.

[20] S. Sahoo, X. Zhao, and K. Kyprianidis, "A Review of Concepts, Benefits, and Challenges for Future Electrical Propulsion-Based Aircraft," *Aerospace 2020, Vol. 7, Page 44*, vol. 7, no. 4, p. 44, Apr. 2020, doi: 10.3390/AEROSPACE7040044.

[21] X. Zhang, C. L. Bowman, T. C. O'Connell, and K. S. Haran, "Large electric machines for aircraft electric propulsion," *IET Electr Power Appl*, vol. 12, no. 6, pp. 767–779, Jul. 2018, doi: 10.1049/IET-EPA.2017.0639.

[22] H. Padamsee, "The science and technology of superconducting cavities for accelerators," *Supercond Sci Technol*, vol. 14, no. 4, p. R28, Apr. 2001, doi: 10.1088/0953-2048/14/4/202.

[23] L. Rossi and L. Bottura, "Superconducting Magnets for Particle Accelerators," *https://doi.org/10.1142/S1793626812300034*, vol. 41, no. 5, pp. 595–608, Jan. 2013, doi: 10.1142/S1793626812300034.

[24] A. Devred *et al.*, "Challenges and status of ITER conductor production," *Supercond Sci Technol*, vol. 27, no. 4, p. 044001, Mar. 2014, doi: 10.1088/0953-2048/27/4/044001.

[25] L. Rossi and L. Bottura, "Superconducting Magnets for Particle Accelerators," *https://doi.org/10.1142/S1793626812300034*, vol. 41, no. 5, pp. 595–608, Jan. 2013, doi: 10.1142/S1793626812300034.

References

[26] K. A. Müller and J. G. Bednorz, "The Discovery of a Class of High-Temperature Superconductors," *Science (1979)*, vol. 237, no. 4819, pp. 1133–1139, Sep. 1987, doi: 10.1126/SCIENCE.237.4819.1133.

[27] G. Blatter, M. V. Feigel'Man, V. B. Geshkenbein, A. I. Larkin, and V. M. Vinokur, "Vortices in high-temperature superconductors," *Rev Mod Phys*, vol. 66, no. 4, p. 1125, Oct. 1994, doi: 10.1103/RevModPhys.66.1125.

[28] J. R. Hull and M. Murakami, "Applications of bulk high-temperature superconductors," *Proceedings of the IEEE*, vol. 92, no. 10, pp. 1705–1717, 2004, doi: 10.1109/JPROC.2004.833796.

[29] Z. Xu *et al.*, "An overview of rotating machine systems with high-temperature bulk superconductors," *Supercond Sci Technol*, vol. 25, no. 10, p. 103001, Aug. 2012, doi: 10.1088/0953-2048/25/10/103001.

[30] F. N. Werfel *et al.*, "Large-scale HTS bulks for magnetic application," *Physica C Supercond*, vol. 484, pp. 6–11, Jan. 2013, doi: 10.1016/J.PHYSC.2012.03.007.

[31] W. Zhai, Y. Shi, J. H. Durrell, A. R. Dennis, and D. A. Cardwell, "The influence of Y-211 content on the growth rate and Y-211 distribution in Y-Ba-Cu-O single grains fabricated by top seeded melt growth," *Cryst Growth Des*, vol. 14, no. 12, pp. 6367–6375, 2014, doi: 10.1021/cg501135q.

[32] K. Y. Huang *et al.*, "Improved trapped field performance of single grain Y-Ba-Cu-O bulk superconductors containing artificial holes," *Journal of the American Ceramic Society*, vol. 104, no. 12, pp. 6309–6318, Dec. 2021, doi: 10.1111/jace.18017.

[33] M. Suyama, S. Pyon, Y. Iijima, S. Awaji, and T. Tamegai, "Trapping a magnetic field of 17.89 T in stacked coated conductors by suppression of flux jumps," *Supercond Sci Technol*, vol. 35, no. 2, 2022, doi: 10.1088/1361-6668/ac4560.

[34] A. Baskys, A. Patel, S. C. Hopkins, V. Kalitka, A. Molodyk, and B. A. Glowacki, "Self-supporting stacks of commercial superconducting tape trapping fields up to 1.6 T using pulsed field magnetization," *IEEE*

References

Transactions on Applied Superconductivity, vol. 25, no. 3, pp. 1–4, 2015, doi: 10.1109/TASC.2014.2360871.

[35]   A. Patel *et al.*, "A trapped field of 17.7 T in a stack of high temperature superconducting tape," *Supercond Sci Technol*, vol. 31, no. 9, 2018, doi: 10.1088/1361-6668/aad34c.

[36]   V. M. R. Zermeño and F. Grilli, "3D modeling and simulation of 2G HTS stacks and coils," *Supercond Sci Technol*, vol. 27, no. 4, 2014, doi: 10.1088/0953-2048/27/4/044025.

[37]   A. Patel, A. Baskys, S. C. Hopkins, V. Kalitka, A. Molodyk, and B. A. Glowacki, "Pulsed-field magnetization of superconducting tape stacks for motor applications," *IEEE Transactions on Applied Superconductivity*, vol. 25, no. 3, 2015, doi: 10.1109/TASC.2015.2389142.

[38]   J. Sheng, M. Zhang, Y. Wang, X. Li, and J. Patel, "A new ring-shape high-temperature superconducting trapped-field magnet," 2017.

[39]   M. Z. Ali, J. Zheng, F. Huber, Z. Zhang, W. Yuan, and M. Zhang, "4.6 T generated by a higherature superconducting ring magnet," *Supercond Sci Technol*, vol. 33, no. 4, 2020, doi: 10.1088/1361-6668/ab794a.

[40]   S. Jinhong, B. Wang, B. Shen, and J. Sheng, "Numerical Study on Ring-shape Superconducting Trapped Field Magnet Based on Circuit Model," *IEEE Transactions on Applied Superconductivity*, vol. 01, no. August 2017, pp. 1–1, 2021, doi: 10.1109/tasc.2021.3089126.

[41]   H. G. Lee *et al.*, "Design and fabrication of permanent mode magnet by using coated conductor," *Physica C: Superconductivity and its Applications*, vol. 445–448, no. 1–2, pp. 1099–1102, Oct. 2006, doi: 10.1016/J.PHYSC.2006.05.044.

[42]   D. van Delft and P. Kes, "The discovery of superconductivity," 2010, doi: 10.1063/1.3490499.

References

[43]   T. Nakamura *et al.*, "Development of a superconducting bulk magnet for NMR and MRI," *Journal of Magnetic Resonance*, vol. 259, pp. 68–75, 2015, doi: 10.1016/j.jmr.2015.07.012.

[44]   R. Hott, "Application Fields of High-Temperature Superconductors," *High Temperature Superconductivity 2*, no. September 2003, pp. 35–48, 2004, doi: 10.1007/978-3-662-07764-1_2.

[45]   S. Asai, "Application of high magnetic fields in inorganic materials processing," *Model Simul Mat Sci Eng*, vol. 12, no. 2, 2004, doi: 10.1088/0965-0393/12/2/R01.

[46]   H. Maeda, J. Shimoyama, Y. Yanagisawa, Y. Ishii, and M. Tomita, "The MIRAI Program and the New Super - High Field NMR Initiative and its Relevance to the Development of Superconducting Joints in Japan," vol. 8223, no. c, pp. 1–10, 2019, doi: 10.1109/TASC.2019.2905360.

[47]   J. G. Bednorz and K. A. Müller, "Possible high Tc superconductivity in the Ba-La-Cu-O system," *Zeitschrift für Physik B Condensed Matter*, vol. 64, no. 2, pp. 189–193, Jun. 1986, doi: 10.1007/BF01303701/METRICS.

[48]   M. K. Wu *et al.*, "Superconductivity at 93 K in a new mixed-phase Y-Ba-Cu-O compound system at ambient pressure," *Phys Rev Lett*, vol. 58, no. 9, p. 908, Mar. 1987, doi: 10.1103/PhysRevLett.58.908.

[49]   M. Tomita and M. Murakami, "High-temperature superconductor bulk magnets that can trap magnetic fields of over 17 tesla at 29 K," *Nature 2003 421:6922*, vol. 421, no. 6922, pp. 517–520, Jan. 2003, doi: 10.1038/nature01350.

[50]   C. A. Luongo *et al.*, "Next generation more-electric aircraft: a potential application for hts superconductors," *IEEE Transactions on Applied Superconductivity*, vol. 19, no. 3, pp. 1055–1068, 2009, doi: 10.1109/TASC.2009.2019021.

[51]   P. J. Masson and C. A. Luongo, "HTS machines for applications in all-electric aircraft," *2007 IEEE Power Engineering Society General Meeting, PES*, pp. 1–6, 2007, doi: 10.1109/PES.2007.385622.

References

[52] A. Colle, T. Lubin, S. Ayat, O. Gosselin, and J. Leveque, "Test of a Flux Modulation Superconducting Machine for Aircraft," *J Phys Conf Ser*, vol. 1590, no. 1, 2020, doi: 10.1088/1742-6596/1590/1/012052.

[53] W. Meissner and R. Ochsenfeld, "Ein neuer Effekt bei Eintritt der Supraleitf higkeit," *Naturwissenschaften*, vol. 21, no. 44, pp. 787–788, Nov. 1933, doi: 10.1007/BF01504252.

[54] J. Auer and H. Ullmaier, "Magnetic Behavior of Type-II Superconductors with Small Ginzburg-Landau Parameters," *Phys Rev B*, vol. 7, no. 1, p. 136, Jan. 1973, doi: 10.1103/PhysRevB.7.136.

[55] E. Babaev and M. Speight, "Semi-Meissner state and neither type-I nor type-II superconductivity in multicomponent superconductors," *Phys Rev B Condens Matter Mater Phys*, vol. 72, no. 18, p. 180502, Nov. 2005, doi: 10.1103/PHYSREVB.72.180502/FIGURES/1/MEDIUM.

[56] M. Strongin, A. Paskin, D. G. Schweitzer, O. F. Kammerer, and P. P. Craig, "Surface Superconductivity in Type I and Type II Superconductors," *Phys Rev Lett*, vol. 12, no. 16, p. 442, Apr. 1964, doi: 10.1103/PhysRevLett.12.442.

[57] H. A. Boorse, D. B. Cook, and M. W. Zemansky, "Superconductivity of Lead," *Physical Review*, vol. 78, no. 5, p. 635, Jun. 1950, doi: 10.1103/PhysRev.78.635.

[58] D. K. Finnemore, T. F. Stromberg, and C. A. Swenson, "Superconducting Properties of High-Purity Niobium," *Physical Review*, vol. 149, no. 1, p. 231, Sep. 1966, doi: 10.1103/PhysRev.149.231.

[59] J. G. Daunt and J. W. Cobble, "Superconductivity of Technetium," *Physical Review*, vol. 92, no. 2, p. 507, Oct. 1953, doi: 10.1103/PhysRev.92.507.

[60] E. Maxwell, "Isotope Effect in the Superconductivity of Mercury," *Physical Review*, vol. 78, no. 4, p. 477, May 1950, doi: 10.1103/PhysRev.78.477.

[61] I. Giaever and H. R. Zeller, "Superconductivity of Small Tin Particles Measured by Tunneling," *Phys Rev Lett*, vol. 20, no. 26, p. 1504, Jun. 1968, doi: 10.1103/PhysRevLett.20.1504.

References

[62] T. E. Faber and A. B. Pippard, "The penetration depth and high-frequency resistance of superconducting aluminium," *Proc R Soc Lond A Math Phys Sci*, vol. 231, no. 1186, pp. 336–353, Sep. 1955, doi: 10.1098/RSPA.1955.0178.

[63] L. Cooley, P. Lee, and D. Larbalestier, "Flux-pinning mechanism of proximity-coupled planar defects in conventional superconductors: Evidence that magnetic pinning is the dominant pinning mechanism in niobium-titanium alloy," *Phys Rev B*, vol. 53, no. 10, p. 6638, Mar. 1996, doi: 10.1103/PhysRevB.53.6638.

[64] R. M. Bozorth, A. J. Williams, and D. D. Davis, "Critical field for Superconductivity in Niobium-Tin," *Phys Rev Lett*, vol. 5, no. 4, p. 148, Aug. 1960, doi: 10.1103/PhysRevLett.5.148.

[65] R. McDermott, S. K. Lee, B. Ten Haken, A. H. Trabesinger, A. Pines, and J. Clarke, "Microtesla MRI with a superconducting quantum interference device," *Proceedings of the National Academy of Sciences*, vol. 101, no. 21, pp. 7857–7861, May 2004, doi: 10.1073/PNAS.0402382101.

[66] G. Morrow, "Progress in MRI magnets," *IEEE Transactions on Applied Superconductivity*, vol. 10, no. 1, pp. 744–751, 2000, doi: 10.1109/77.828339.

[67] T. C. Cosmus and M. Parizh, "Advances in whole-body MRI magnets," *IEEE Transactions on Applied Superconductivity*, vol. 21, no. 3 PART 2, pp. 2104–2109, Jun. 2011, doi: 10.1109/TASC.2010.2084981.

[68] J. Cheng *et al.*, "Fabrication of NbTi superconducting joints for 400-MHz NMR application," *IEEE Transactions on Applied Superconductivity*, vol. 22, no. 2, Apr. 2012, doi: 10.1109/TASC.2012.2185795.

[69] "Luvata | Superconductors." Accessed: Oct. 02, 2023. [Online]. Available: https://www.luvata.com/products/superconductors

[70] S. Rogers *et al.*, "Electro-mechanical properties of REBCO coated conductors from various industrial manufacturers at 77 K, self-field and 4.2 K, 19 T," *Supercond Sci Technol*, vol. 28, no. 4, p. 045011, Feb. 2015, doi: 10.1088/0953-2048/28/4/045011.

References

[71]   C. Senatore, C. Barth, M. Bonura, M. Kulich, and G. Mondonico, "Field and temperature scaling of the critical current density in commercial REBCO coated conductors," *Supercond Sci Technol*, vol. 29, no. 1, p. 014002, Dec. 2015, doi: 10.1088/0953-2048/29/1/014002.

[72]   M. Iwakuma *et al.*, "Development of REBCO superconducting power transformers in Japan," *Physica C Supercond*, vol. 469, no. 15–20, pp. 1726–1732, Oct. 2009, doi: 10.1016/J.PHYSC.2009.05.246.

[73]   M. Zhang, W. Yuan, J. Kvitkovic, and S. Pamidi, "Total AC loss study of 2G HTS coils for fully HTS machine applications," *Supercond Sci Technol*, vol. 28, no. 11, p. 115011, doi: 10.1088/0953-2048/28/11/115011.

[74]   Y. Gao *et al.*, "Design and study of a 2G HTS synchronous motor with brushless HTS flux pump exciters," *IEEE Transactions on Applied Superconductivity*, vol. 29, no. 5, pp. 1–5, 2019, doi: 10.1109/TASC.2019.2898505.

[75]   I. A. C. and M. L. Z. I V Kulikov , M Y Chernykh , T S Krylova, D S Yashkin, "Superconducting joint fabrication for HTS second generation Superconducting joint fabrication for HTS second generation GdBCO / YBCO tapes," 2020.

[76]   H. Hosono and K. Kuroki, "Iron-based superconductors: Current status of materials and pairing mechanism," *Physica C: Superconductivity and its Applications*, vol. 514, pp. 399–422, Jul. 2015, doi: 10.1016/J.PHYSC.2015.02.020.

[77]   R. M. Fernandes, A. V. Chubukov, and J. Schmalian, "What drives nematic order in iron-based superconductors?," *Nature Physics 2014 10:2*, vol. 10, no. 2, pp. 97–104, Jan. 2014, doi: 10.1038/nphys2877.

[78]   H. Hosono, A. Yamamoto, H. Hiramatsu, and Y. Ma, "Recent advances in iron-based superconductors toward applications," *Materials Today*, vol. 21, no. 3, pp. 278–302, Apr. 2018, doi: 10.1016/J.MATTOD.2017.09.006.

[79]   P. M. Aswathy, J. B. Anooja, P. M. Sarun, and U. Syamaprasad, "An overview on iron based superconductors," *Supercond Sci Technol*, vol. 23, no. 7, p. 073001, Jun. 2010, doi: 10.1088/0953-2048/23/7/073001.

References

[80] A. Goyal, M. P. Paranthaman, and U. Schoop, "The RABiTS Approach: Using Rolling-Assisted Biaxially Textured Substrates for High-Performance YBCO Superconductors," *MRS Bull*, vol. 29, no. 8, pp. 552–561, 2004, doi: 10.1557/MRS2004.161.

[81] Y. Shi *et al.*, "Batch-processed GdBCO–Ag bulk superconductors fabricated using generic seeds with high trapped fields," *Physica C: Superconductivity and its Applications*, vol. 470, no. 17–18, pp. 685–688, Sep. 2010, doi: 10.1016/J.PHYSC.2010.06.013.

[82] Y. H. Shi, A. R. Dennis, and D. A. Cardwell, "A new seeding technique for the reliable fabrication of large, SmBCO single grains containing silver using top seeded melt growth," *Supercond Sci Technol*, vol. 28, no. 3, p. 035014, Feb. 2015, doi: 10.1088/0953-2048/28/3/035014.

[83] X. Yao, M. Kambara, T. Umeda, and Y. S. Y. Shiohara, "95 K NdBCO Single Crystal Grown in Air   by Controlling Liquid Composition," *Jpn J Appl Phys*, vol. 36, no. 4A, p. L400, Apr. 1997, doi: 10.1143/JJAP.36.L400.

[84] S. M. Khalil, "Enhancement of superconducting and mechanical properties in BSCCO with Pb additions," *Journal of Physics and Chemistry of Solids*, vol. 62, no. 3, pp. 457–466, Mar. 2001, doi: 10.1016/S0022-3697(00)00088-3.

[85] K. R. Marken, H. Miao, M. Meinesz, B. Czabaj, and S. Hong, "BSCCO-2212 conductor development at Oxford superconducting technology," *IEEE Transactions on Applied Superconductivity*, vol. 13, no. 2 III, pp. 3335–3338, Jun. 2003, doi: 10.1109/TASC.2003.812307.

[86] H. Sözeri, N. Ghazanfari, H. Özkan, and A. Kilic, "Enhancement in the high-Tc phase of BSCCO superconductors by Nb addition," *Supercond Sci Technol*, vol. 20, no. 6, p. 522, May 2007, doi: 10.1088/0953-2048/20/6/007.

[87] K. H. Sandhage, G. N. Riley, and W. L. Carter, "Critical issues in the OPIT processing of high-Jc BSCCO superconductors," *JOM*, vol. 43, no. 3, pp. 21–25, Mar. 1991, doi: 10.1007/BF03220158/METRICS.

References

[88] CAN Superconductors, "CAN Superconductors," https://www.can-superconductors.com/hts-bulks-and-materials/rebco-melt-textured-bulks/. Accessed: Oct. 02, 2023. [Online]. Available: https://www.can-superconductors.com/

[89] Y. Kamihara, T. Watanabe, M. Hirano, and H. Hosono, "Iron-based layered superconductor LaOFeAs with Tc = 26 K," *J Am Chem Soc*, vol. 130, no. 11, pp. 3296–3297, Mar. 2008, doi: 10.1021/JA800073M/SUPPL_FILE/JA800073M-FILE003.CIF.

[90] H. Hosono, A. Yamamoto, H. Hiramatsu, and Y. Ma, "Recent advances in iron-based superconductors toward applications," *Materials Today*, vol. 21, no. 3, pp. 278–302, Apr. 2018, doi: 10.1016/J.MATTOD.2017.09.006.

[91] P. Zhang *et al.*, "Observation of topological superconductivity on the surface of an iron-based superconductor," *Science (1979)*, vol. 360, no. 6385, pp. 182–186, Apr. 2018, doi: 10.1126/SCIENCE.AAN4596/SUPPL_FILE/AAN4596_ZHANG_SM_DATA_S1.ZIP.

[92] Z. A. Ren and Z. X. Zhao, "Research and Prospects of Iron-Based Superconductors," *Advanced Materials*, vol. 21, no. 45, pp. 4584–4592, Dec. 2009, doi: 10.1002/ADMA.200901049.

[93] M. Strongin, A. Paskin, D. G. Schweitzer, O. F. Kammerer, and P. P. Craig, "Surface Superconductivity in Type I and Type II Superconductors," *Phys Rev Lett*, vol. 12, no. 16, p. 442, Apr. 1964, doi: 10.1103/PhysRevLett.12.442.

[94] U. ESSMANN and H. TRAUBLE, "The direct observation of individual flux lines in type II superconductors," *Physics Letters*, vol. 24A, no. 10, pp. 526–527, 1967, Accessed: Oct. 02, 2023. [Online]. Available: http://chair.itp.ac.ru/biblio/papers/ClassicPapersSeminar/EssmannTrauble1967.pdf

[95] J. Lowell and J. B. Sousa, "Mixed-state thermal conductivity of type II superconductors," *J Low Temp Phys*, vol. 3, no. 1, pp. 65–87, Jul. 1970, doi: 10.1007/BF00628399/METRICS.

References

[96]   A. M. Campbell and J. E. Evetts, "Flux vortices and transport currents in type II superconductors," *Adv Phys*, vol. 21, no. 90, pp. 199–428, Jan. 1972, doi: 10.1080/00018737200101288.

[97]   P. Nozières and W. F. Vinen, "The motion of flux lines in type II superconductors," *The Philosophical Magazine: A Journal of Theoretical Experimental and Applied Physics*, vol. 14, no. 130, pp. 667–688, 1966, doi: 10.1080/14786436608211964.

[98]   B. Rosenstein and D. Li, "Ginzburg-Landau theory of type II superconductors in magnetic field," *Rev Mod Phys*, vol. 82, no. 1, pp. 109–168, Jan. 2010, doi: 10.1103/REVMODPHYS.82.109/FIGURES/15/MEDIUM.

[99]   J. Bardeen, L. N. Cooper, and J. R. Schrieffer, "Microscopic Theory of Superconductivity," *Physical Review*, vol. 106, no. 1, p. 162, Apr. 1957, doi: 10.1103/PhysRev.106.162.

[100] M. V. Miloević and R. Geurts, "The Ginzburg–Landau theory in application," *Physica C Supercond*, vol. 470, no. 19, pp. 791–795, Oct. 2010, doi: 10.1016/J.PHYSC.2010.02.056.

[101] M. Cyrot, "Ginzburg-Landau theory for superconductors," *Reports on Progress in Physics*, vol. 36, no. 2, p. 103, Feb. 1973, doi: 10.1088/0034-4885/36/2/001.

[102] A. A. Abrikosov, "The magnetic properties of superconducting alloys," *Journal of Physics and Chemistry of Solids*, vol. 2, no. 3, pp. 199–208, Jan. 1957, doi: 10.1016/0022-3697(57)90083-5.

[103] F. S. Wells, A. V. Pan, X. R. Wang, S. A. Fedoseev, and H. Hilgenkamp, "Analysis of low-field isotropic vortex glass containing vortex groups in YBa2Cu3O7−x thin films visualized by scanning SQUID microscopy," *Scientific Reports 2015 5:1*, vol. 5, no. 1, pp. 1–5, Mar. 2015, doi: 10.1038/srep08677.

[104] C. P. Bean, "Magnetization of High-Field Superconductors."

[105] E. M. Gyorgy, R. B. Van Dover, K. A. Jackson, L. F. Schneemeyer, and J. V. Waszczak, "Anisotropic critical currents in Ba2YCu3O7 analyzed using an

References

extended Bean model," *Appl Phys Lett*, vol. 55, no. 3, pp. 283–285, Jul. 1989, doi: 10.1063/1.102387.

[106] T. Matsushita, "Flux pinning in superconducting 123 materials," *Supercond Sci Technol*, vol. 13, no. 6, p. 730, Jun. 2000, doi: 10.1088/0953-2048/13/6/320.

[107] D. Dew-Hughes, "Flux pinning mechanisms in type II superconductors," *Philosophical Magazine*, vol. 30, no. 2, pp. 293–305, 1974, doi: 10.1080/14786439808206556.

[108] E. J. Kramer, "Scaling laws for flux pinning in hard superconductors," *J Appl Phys*, vol. 44, no. 3, pp. 1360–1370, Mar. 1973, doi: 10.1063/1.1662353.

[109] E. Mezzetti *et al.*, "Control of the critical current density in YBa2Cu3O7−δ films by means of intergrain and intragrain correlated defects," *Phys Rev B*, vol. 60, no. 10, p. 7623, Sep. 1999, doi: 10.1103/PhysRevB.60.7623.

[110] V. Selvamanickam *et al.*, "Recent progress in second-generation HTS conductor scale-up at superPower," *IEEE Transactions on Applied Superconductivity*, vol. 17, no. 2, pp. 3231–3234, Jun. 2007, doi: 10.1109/TASC.2007.899360.

[111] M. V. Feigelman, V. B. Geshkenbein, and V. M. Vinokur, "Flux creep and current relaxation in high-Tc superconductors," *Phys Rev B*, vol. 43, no. 7, pp. 6263–6265, 1991, doi: 10.1103/PhysRevB.43.6263.

[112] D. Zhou *et al.*, "Exploiting flux jumps for pulsed field magnetisation," *Supercond Sci Technol*, vol. 31, no. 10, p. 105005, Aug. 2018, doi: 10.1088/1361-6668/AAD786.

[113] M. Ainslie and H. Fujishiro, "Fundamentals of bulk superconducting materials," in *Numerical Modelling of Bulk Superconductor Magnetisation*, IOP Publishing, 2019, pp. 1-1-1–22. doi: 10.1088/978-0-7503-1332-2ch1.

[114] Y. Zhang, D. Zhou, T. Ida, M. Miki, and M. Izumi, "Melt-growth bulk superconductors and application to an axial-gap-type rotating machine," *Supercond Sci Technol*, vol. 29, no. 4, p. 0, 2016, doi: 10.1088/0953-2048/29/4/044005.

References

[115] M. Murakami, "High-temperature superconductor in bulk magnets that can trap magnetic in fields of over 17 Tesla at 29 K," vol. 106, no. 2002, pp. 1–4, 2009, [Online]. Available: http://www.nature.com/nature/journal/v421/n6922/pdf/nature01350.pdf

[116] K. Iida, N. H. Babu, Y. Shi, and D. A. Cardwell, "Seeded infiltration and growth of large, single domain Y–Ba–Cu–O bulk superconductors with very high critical current densities," *Supercond Sci Technol*, vol. 18, no. 11, p. 1421, Sep. 2005, doi: 10.1088/0953-2048/18/11/002.

[117] D. A. Cardwell *et al.*, "Top-seeded melt growth of Y-Ba-Cu-O superconductor with multiseeding," *Supercond Sci Technol*, vol. 13, no. 2, p. 195, Feb. 2000, doi: 10.1088/0953-2048/13/2/314.

[118] F. N. Werfel *et al.*, "Large-scale HTS bulks for magnetic application," *Physica C: Superconductivity and its Applications*, vol. 484, pp. 6–11, Jan. 2013, doi: 10.1016/j.physc.2012.03.007.

[119] J. R. Hull and M. Murakami, "Applications of bulk high-temperature superconductors," in *Proceedings of the IEEE*, Institute of Electrical and Electronics Engineers Inc., 2004, pp. 1705–1717. doi: 10.1109/JPROC.2004.833796.

[120] H. W. Neumüller, G. Klaus, and W. Nick, "Status and prospects of HTS synchronous machines," *Industrial Ceramics*, vol. 27, no. 1, pp. 41–49, 2007, doi: 10.4028/www.scientific.net/ast.47.228.

[121] E. H. Ailam, D. Netter, J. Lévêque, B. Douine, P. J. Masson, and A. Rezzoug, "Design and testing of a superconducting rotating machine," *IEEE Transactions on Applied Superconductivity*, vol. 17, no. 1, pp. 27–32, 2007, doi: 10.1109/TASC.2006.887544.

[122] R. Dorget *et al.*, "Design of a 500 kW partially superconducting flux modulation machine for aircraft propulsion," *J Phys Conf Ser*, vol. 1975, no. 1, 2021, doi: 10.1088/1742-6596/1975/1/012033.

References

[123] F. Weng, M. Zhang, T. Lan, Y. Wang, and W. Yuan, "Fully superconducting machine for electric aircraft propulsion: study of AC loss for HTS stator," *Supercond Sci Technol*, vol. 33, no. 10, p. 104002, 2020, doi: 10.1088/1361-6668/ab9687.

[124] M. Watasaki *et al.*, "Stability model of bulk HTS field pole of a synchronous rotating machine under," 2021.

[125] M. I. and H. H. 1 B Felder1, M Miki1, K Tsuzuki1, "Optimization of a condensed-neon cooling system for a HTS synchronous motor with Gd-bulk HTS field-pole magnets Optimization of a condensed-neon cooling system for a HTS synchronous motor with Gd-bulk HTS field-pole magnets," 2010, doi: 10.1088/1742-6596/234/3/032009.

[126] H. Liao *et al.*, "Dynamic levitation performance of Gd-Ba-Cu-O and Y-Ba-Cu-O bulk superconductors under a varying external magnetic field," *Supercond Sci Technol*, vol. 31, no. 3, p. 035010, Feb. 2018, doi: 10.1088/1361-6668/aaa82a.

[127] H. Salamati and P. Kameli, "The effect of Bi-2212 phase on the weak link behavior of Bi-2223 superconductors," *Physica C Supercond*, vol. 403, no. 1–2, pp. 60–66, Mar. 2004, doi: 10.1016/J.PHYSC.2003.11.009.

[128] J. Jiang *et al.*, "Doubled critical current density in Bi-2212 round wires by reduction of the residual bubble density," *Supercond Sci Technol*, vol. 24, no. 8, p. 082001, Jun. 2011, doi: 10.1088/0953-2048/24/8/082001.

[129] J. Jiang *et al.*, "High-performance Bi-2212 round wires made with recent powders," *IEEE Transactions on Applied Superconductivity*, vol. 29, no. 5, 2019, doi: 10.1109/TASC.2019.2895197.

[130] C. Buzea and T. Yamashita, "Review of the superconducting properties of MgB2," *Supercond Sci Technol*, vol. 14, no. 11, p. R115, Nov. 2001, doi: 10.1088/0953-2048/14/11/201.

[131] J. M. Rowell, "The widely variable resistivity of MgB2 samples," *Supercond Sci Technol*, vol. 16, no. 6, p. R17, Apr. 2003, doi: 10.1088/0953-2048/16/6/201.

References

[132] M. W. Rupich *et al.*, "The development of second generation HTS wire at American superconductor," *IEEE Trans. Appl. Supercond.*, vol. 17, no. 2, pp. 3379–3382, Jun. 2007, doi: 10.1109/tasc.2007.899076.

[133] T. Masuda *et al.*, "Fabrication and installation results for albany HTS cable," *IEEE Trans. Appl. Supercond.*, vol. 17, no. 2, pp. 1648–1651, Jun. 2007, doi: 10.1109/tasc.2007.898122.

[134] M. W. Rupich, D. T. Verebelyi, W. Zhang, T. Kodenkandath, and X. Li, "Metalorganic deposition of YBCO films for second-generation high-temperature superconductor wires," *MRS Bull.*, vol. 29, no. 8, pp. 572–578, 2004, doi: 10.1557/mrs2004.163.

[135] A. P. Malozemoff *et al.*, "Progress in high temperature superconductor coated conductors and their applications," *Supercond Sci Technol*, vol. 21, no. 3, p. 034005, Feb. 2008, doi: 10.1088/0953-2048/21/3/034005.

[136] O. A. Shyshkin, Y. G. Kazarinov, M. Tallouli, T. Famakinwa, and S. Yamaguchi, "Inverse Problem Solution Algorithms for Current Density Distribution Calculation in Different HTS Tape Configurations Basing on Minimum Self-Magnetic Field Measurements," *IEEE Transactions on Applied Superconductivity*, vol. 26, no. 3, Apr. 2016, doi: 10.1109/TASC.2016.2521169.

[137] S. Rogers *et al.*, "Electro-mechanical properties of REBCO coated conductors from various industrial manufacturers at 77 K, self-field and 4.2 K, 19 T," *Supercond Sci Technol*, vol. 28, no. 4, p. 045011, Feb. 2015, doi: 10.1088/0953-2048/28/4/045011.

[138] M. Takayasu, L. Chiesa, P. D. Noyes, and J. V. Minervini, "Investigation of HTS Twisted Stacked-Tape Cable (TSTC) Conductor for High-Field, High-Current Fusion Magnets," *IEEE Transactions on Applied Superconductivity*, vol. 27, no. 4, Jun. 2017, doi: 10.1109/TASC.2017.2652328.

[139] Y. Iwasa, "HTS and NMR/MRI magnets: Unique features, opportunities, and challenges," *Physica C: Superconductivity and its Applications*, vol. 445–448, no. 1–2, pp. 1088–1094, Oct. 2006, doi: 10.1016/J.PHYSC.2006.05.040.

References

[140] D. W. Hazelton *et al.*, "Recent developments in 2G HTS coil technology," *IEEE Transactions on Applied Superconductivity*, vol. 19, no. 3, pp. 2218–2222, Jun. 2009, doi: 10.1109/TASC.2009.2018791.

[141] J. H. Kim *et al.*, "Investigation of the over current characteristics of HTS tapes considering the application for HTS power devices," *IEEE Transactions on Applied Superconductivity*, vol. 18, no. 2, pp. 1139–1142, Jun. 2008, doi: 10.1109/TASC.2008.922521.

[142] S. Samoilenkov *et al.*, "Customised 2G HTS wire for applications," *Supercond Sci Technol*, vol. 29, no. 2, p. 024001, Dec. 2015, doi: 10.1088/0953-2048/29/2/024001.

[143] F. Dong *et al.*, "R&D of No-Insulation HTS Magnets Using 2G Wires in a Prototype for Maglev Applications," *IEEE Transactions on Applied Superconductivity*, vol. 29, no. 5, Aug. 2019, doi: 10.1109/TASC.2019.2904643.

[144] S. J. Lee, M. Park, I. K. Yu, Y. Won, Y. Kwak, and C. Lee, "Recent Status and Progress on HTS Cables for AC and DC Power Transmission in Korea," *IEEE Transactions on Applied Superconductivity*, vol. 28, no. 4, Jun. 2018, doi: 10.1109/TASC.2018.2820721.

[145] S. J. Lee and H. S. Yang, "Recent progress and design of three-phase coaxial HTS power cable in Korea," *IEEE Transactions on Applied Superconductivity*, vol. 29, no. 5, Aug. 2019, doi: 10.1109/TASC.2019.2908616.

[146] L. Cavallucci *et al.*, "Roebel cables from REBCO coated conductors: a one-century-old concept for the superconductivity of the future," *Supercond Sci Technol*, vol. 27, no. 9, p. 093001, Aug. 2014, doi: 10.1088/0953-2048/27/9/093001.

[147] W. H. Fietz, M. J. Wolf, A. Preuss, R. Heller, and K. P. Weiss, "High-Current HTS Cables: Status and Actual Development," *IEEE Transactions on Applied Superconductivity*, vol. 26, no. 4, Jun. 2016, doi: 10.1109/TASC.2016.2517319.

References

[148] M. Vojenčiak *et al.*, "Magnetization ac loss reduction in HTS CORC® cables made of striated coated conductors," *Supercond Sci Technol*, vol. 28, no. 10, p. 104006, Sep. 2015, doi: 10.1088/0953-2048/28/10/104006.

[149] M. Majoros, M. D. Sumption, E. W. Collings, and D. C. Van Der Laan, "Magnetization losses in superconducting YBCO conductor-on-round-core (CORC) cables," *Supercond Sci Technol*, vol. 27, no. 12, p. 125008, Nov. 2014, doi: 10.1088/0953-2048/27/12/125008.

[150] N. H. Sung, Y. J. Jo, B. K. Cho, P. A. Joy, A. Kumar, and S. K. Date, "The relationship between field-cooled and zero-field-cooled susceptibilities of some ordered magnetic systems," *Journal of Physics: Condensed Matter*, vol. 10, no. 48, p. 11049, Dec. 1998, doi: 10.1088/0953-8984/10/48/024.

[151] T. Ida *et al.*, "Magnetization properties for Gd–Ba–Cu–O bulk superconductors with a couple of pulsed-field vortex-type coils," *Physica C Supercond*, vol. 412–414, no. SPEC. ISS., pp. 638–645, Oct. 2004, doi: 10.1016/J.PHYSC.2003.12.082.

[152] T. Ida, Z. Li, M. Miki, M. Watasaki, and M. Izumi, "Waveform Control Pulse Magnetization for HTS Bulk with Flux Jump," *IEEE Transactions on Applied Superconductivity*, vol. 28, no. 4, Jun. 2018, doi: 10.1109/TASC.2018.2816099.

[153] H. Matsuzaki *et al.*, "An axial gap-type HTS bulk synchronous motor excited by pulsed-field magnetization with vortex-type armature copper windings," *IEEE Transactions on Applied Superconductivity*, vol. 15, no. 2 PART II, pp. 2222–2225, Jun. 2005, doi: 10.1109/TASC.2005.849617.

[154] N. Sakai, A. Mase, H. Ikuta, S. J. Seo, U. Mizutani, and M. Murakami, "Mechanical properties of Sm-Ba-Cu-O/Ag bulk superconductors," *Supercond Sci Technol*, vol. 13, no. 6, p. 770, Jun. 2000, doi: 10.1088/0953-2048/13/6/328.

[155] T. Miyamoto, J. Katagiri, K. Nagashima, and M. Murakami, "Effect of Ag addition on the mechanical properties of bulk superconductors," *IEEE Transactions on Applied Superconductivity*, vol. 9, no. 2 PART 2, pp. 2066–2069, 1999, doi: 10.1109/77.784872.

References

[156] G. Fuchs *et al.*, "Trapped magnetic fields larger than 14 T in bulk YBa2Cu3O7−x," *Appl Phys Lett*, vol. 76, no. 15, pp. 2107–2109, Apr. 2000, doi: 10.1063/1.126278.

[157] M. Tomita and M. Murakami, "Improvement of the mechanical properties of bulk superconductors with resin impregnation," *Supercond Sci Technol*, vol. 13, no. 6, p. 722, Jun. 2000, doi: 10.1088/0953-2048/13/6/318.

[158] J. H. Durrell *et al.*, "A trapped field of 17.6 T in melt-processed, bulk Gd-Ba-Cu-O reinforced with shrink-fit steel," *Supercond Sci Technol*, vol. 27, no. 8, 2014, doi: 10.1088/0953-2048/27/8/082001.

[159] A. Patel *et al.*, "A trapped field of 17.7 T in a stack of high temperature superconducting tape," *Supercond Sci Technol*, vol. 31, no. 9, Jul. 2018, doi: 10.1088/1361-6668/aad34c.

[160] K. Yuan Huang *et al.*, "The effect of stabilizer on the trapped field of stacks of superconducting tape magnetized by a pulsed field," *Supercond Sci Technol*, vol. 28, no. 8, p. 085009, Jul. 2015, doi: 10.1088/0953-2048/28/8/085009.

[161] J. Cheng *et al.*, "Fabrication of NbTi superconducting joints for 400-MHz NMR application," *IEEE Transactions on Applied Superconductivity*, vol. 22, no. 2, Apr. 2012, doi: 10.1109/TASC.2012.2185795.

[162] Y. Park, M. Lee, H. Ann, Y. H. Choi, and H. Lee, "A superconducting joint for GdBa2Cu3O7−δ-coated conductors," *NPG Asia Materials 2014 6:5*, vol. 6, no. 5, pp. e98–e98, May 2014, doi: 10.1038/am.2014.18.

[163] Y. Wang *et al.*, "Superconducting joint of REBCO wires for MRI magnet," *J Phys Conf Ser*, vol. 1054, no. 1, p. 012038, Jul. 2018, doi: 10.1088/1742-6596/1054/1/012038.

[164] S. Matsumoto *et al.*, "Estimation of Joint Resistance in REBCO Single-Turn Loop under Magnetic Fields," *IEEE Transactions on Applied Superconductivity*, vol. 29, no. 5, Aug. 2019, doi: 10.1109/TASC.2019.2903392.

[165] G. Nishijima *et al.*, "Transport property of REBCO superconducting joints in magnetic fields at various temperatures," *IEEE Transactions on Applied*

References

Superconductivity, vol. 29, no. 5, Aug. 2019, doi: 10.1109/TASC.2019.2907713.

[166] S. Ito, H. Hashizume, N. Yanagi, and H. Tamura, "Bridge-type mechanical lap joint of HTS STARS conductors using an integrated joint piece," *Fusion Engineering and Design*, vol. 146, pp. 590–593, Sep. 2019, doi: 10.1016/J.FUSENGDES.2019.01.030.

[167] H. Hashizume, S. Ito, N. Yanagi, H. Tamura, and A. Sagara, "Development of remountable joints and heat removable techniques for high-temperature superconducting magnets," *Nuclear Fusion*, vol. 58, no. 2, p. 026014, Dec. 2017, doi: 10.1088/1741-4326/AA874F.

[168] S. Ito, H. T. Fujii, R. Hayasaka, Y. S. Sato, and H. Hashizume, "Comparison of heat assisted lap joints of high-temperature superconducting tapes with inserted indium foils," *IEEE Transactions on Applied Superconductivity*, vol. 29, no. 5, Aug. 2019, doi: 10.1109/TASC.2019.2892050.

[169] X. Jin *et al.*, "Microstructural analysis of superconducting joint fabricated Using CJMB between Gd123-Coated Conductors," *IEEE Transactions on Applied Superconductivity*, vol. 29, no. 5, Aug. 2019, doi: 10.1109/TASC.2019.2909203.

[170] H. S. Shin, M. A. Diaz, Z. M. Bautista, and S. Awaji, "Joint Resistance Characteristics in Ultrasonic Weld REBCO CC Tapes at Various Temperatures and Magnetic Fields," *IEEE Transactions on Applied Superconductivity*, vol. 28, no. 4, Jun. 2018, doi: 10.1109/TASC.2017.2788085.

[171] X. Jin *et al.*, "Superconducting joint between multi-filamentary Bi2Sr2Ca2Cu3O10+δ tapes based on incongruent melting for NMR and MRI applications," *Supercond Sci Technol*, vol. 32, no. 3, p. 035011, Feb. 2019, doi: 10.1088/1361-6668/AAFC44.

[172] S. Lee *et al.*, "Characteristics of an HTS pancake coil in persistent current mode using wind-and-flip winding method," *IEEE Transactions on Applied Superconductivity*, vol. 23, no. 3, 2013, doi: 10.1109/TASC.2013.2238577.

References

[173] G. A. Levin *et al.*, "Persistent current in coils made out of second generation high temperature superconductor wire.," *Appl Phys Lett*, vol. 93, no. 6, p. 16, Aug. 2008, doi: 10.1063/1.2969798/322980.

[174] J. Shi, X. Li, and J. Sheng, "Compensation Effect of Superconducting Hybrid Trapped Field Magnet," *IEEE Transactions on Applied Superconductivity*, vol. 32, no. 4, pp. 1–5, 2022, doi: 10.1109/TASC.2022.3142705.

[175] J. Sheng *et al.*, "A New Concept of a Hybrid Trapped Field Magnet," *IEEE Transactions on Applied Superconductivity*, vol. 29, no. 5, pp. 1–5, 2019, doi: 10.1109/TASC.2019.2903269.

[176] D. J. Gameiro Carvalho *et al.*, "Superconducting magnetic bearings with bulks and 2G HTS stacks: comparison between simulations using H and A-V formulations with measurements," *Supercond Sci Technol*, vol. 31, no. 2, p. 025006, Jan. 2018, doi: 10.1088/1361-6668/AA9DC1.

[177] N. Amemiya, S. I. Murasawa, N. Banno, and K. Miyamoto, "Numerical modelings of superconducting wires for AC loss calculations," *Physica C Supercond*, vol. 310, no. 1–4, pp. 16–29, Dec. 1998, doi: 10.1016/S0921-4534(98)00427-4.

[178] H. Zhang, M. Zhang, and W. Yuan, "An efficient 3D finite element method model based on the T–A formulation for superconducting coated conductors," *Supercond Sci Technol*, vol. 30, no. 2, p. 024005, Dec. 2016, doi: 10.1088/1361-6668/30/2/024005.

[179] E. Pardo, J. Šouc, and L. Frolek, "Electromagnetic modelling of superconductors with a smooth current–voltage relation: variational principle and coils from a few turns to large magnets," *Supercond Sci Technol*, vol. 28, no. 4, p. 044003, Feb. 2015, doi: 10.1088/0953-2048/28/4/044003.

[180] Z. Hong, A. M. Campbell, and T. A. Coombs, "Numerical solution of critical state in superconductivity by finite element software," *Supercond Sci Technol*, vol. 19, no. 12, p. 1246, Oct. 2006, doi: 10.1088/0953-2048/19/12/004.

References

[181] M. Zhang and T. A. Coombs, "3D modeling of high-Tc superconductors by finite element software," *Supercond Sci Technol*, vol. 25, no. 1, p. 015009, Dec. 2011, doi: 10.1088/0953-2048/25/1/015009.

[182] F. Grilli, "Numerical modeling of HTS applications," *IEEE Transactions on Applied Superconductivity*, vol. 26, no. 3, Apr. 2016, doi: 10.1109/TASC.2016.2520083.

[183] S. Li, J. Kováč, and E. Pardo, "Coupling loss at the end connections of REBCO stacks: 2D modelling and measurement," *Supercond Sci Technol*, vol. 33, no. 7, p. 075014, Jun. 2020, doi: 10.1088/1361-6668/AB9027.

[184] M. D. Ainslie and H. Fujishiro, "Modelling of bulk superconductor magnetization," *Supercond Sci Technol*, vol. 28, no. 5, p. 053002, Mar. 2015, doi: 10.1088/0953-2048/28/5/053002.

[185] Y. B. Kim, C. F. Hempstead, and A. R. Strnad, "Critical Persistent Currents in Hard Superconductors," *Phys Rev Lett*, vol. 9, no. 7, p. 306, Oct. 1962, doi: 10.1103/PhysRevLett.9.306.

[186] H. Liao, J. Zheng, H. Huang, and Z. Deng, "Simulation and Experiment Research on the Dynamic Levitation Force of Bulk Superconductors under a Varying External Magnetic Field," *IEEE Transactions on Applied Superconductivity*, vol. 29, no. 3, 2019, doi: 10.1109/TASC.2018.2880174.

[187] H. Liao, A. R. Dennis, W. Yuan, and M. Zhang, "Magnetization characteristics of HTS-stacked ring magnets with and without HTS stack inserts," *J Appl Phys*, vol. 134, no. 8, p. 83902, Aug. 2023, doi: 10.1063/5.0165643/2908004.

[188] H. Liao, W. Yuan, Z. Zhang, and M. Zhang, "Magnetization mechanism of a hybrid high temperature superconducting trapped field magnet," *J Appl Phys*, vol. 133, no. 2, p. 23902, Jan. 2023, doi: 10.1063/5.0133219/2869153.

[189] L. Wang, H. W. Wu, and H. D. Yong, "Mechanical stress in high-temperature superconducting ring-shaped bulk during the pulsed-field magnetization," *Sci China Technol Sci*, vol. 66, no. 2, pp. 574–585, Feb. 2023, doi: 10.1007/S11431-022-2116-3/METRICS.

References

[190] M. D. Ainslie *et al.*, "Numerical modelling of mechanical stresses in bulk superconductor magnets with and without mechanical reinforcement," *Supercond Sci Technol*, vol. 32, no. 3, p. 034002, Feb. 2019, doi: 10.1088/1361-6668/AAF851.

[191] P. Gao, W.-K. Chan, and X. Wang, "Width-bending characteristic of REBCO HTS tape and flat-tape Rutherford-type cabling," *Supercond Sci Technol*, vol. 34, no. 12, p. 125020, Nov. 2021, doi: 10.1088/1361-6668/AC30EB.

[192] S. Rogers *et al.*, "Electro-mechanical properties of REBCO coated conductors from various industrial manufacturers at 77 K, self-field and 4.2 K, 19 T," *Supercond Sci Technol*, vol. 28, no. 4, p. 045011, Feb. 2015, doi: 10.1088/0953-2048/28/4/045011.

[193] K. Takahashi, H. Fujishiro, and M. D. Ainslie, "A new concept of a hybrid trapped field magnet lens," *Supercond Sci Technol*, vol. 31, no. 4, 2018, doi: 10.1088/1361-6668/aaae94.

[194] S. Namba, H. Fujishiro, T. Hirano, T. Naito, and M. D. Ainslie, "Optimized performance of an all-REBaCuO hybrid trapped field magnet lens (HTFML) with liquid nitrogen cooling," *Physica C: Superconductivity and its Applications*, vol. 575, no. May, p. 1353690, 2020, doi: 10.1016/j.physc.2020.1353690.

[195] Z. Y. Zhang, S. Matsumoto, R. Teranishi, and T. Kiyoshi, "Improving the properties of GdBCO magnetic lenses by adopting a new design and resin impregnation," *Supercond Sci Technol*, vol. 26, no. 4, p. 045001, Feb. 2013, doi: 10.1088/0953-2048/26/4/045001.

[196] T. Kiyoshi, S. Choi, S. Matsumoto, T. Asano, and D. Uglietti, "Magnetic flux concentrator using Gd-Ba-Cu-O bulk superconductors," *IEEE Transactions on Applied Superconductivity*, vol. 19, no. 3, pp. 2174–2177, Jun. 2009, doi: 10.1109/TASC.2009.2018440.

[197] S. Choi *et al.*, "Magnetic lens effect using Gd-Ba-Cu-O bulk superconductor in very high magnetic field," *J Appl Phys*, vol. 111, no. 7, pp. 7–728, Apr. 2012, doi: 10.1063/1.3678301/391188.

References

[198] Z. Y. Zhang, S. Matsumoto, R. Teranishi, and T. Kiyoshi, "Magnetic field, temperature and mechanical crack performance of a GdBCO magnetic lens," *Supercond Sci Technol*, vol. 25, no. 11, p. 115012, Sep. 2012, doi: 10.1088/0953-2048/25/11/115012.

[199] N. M. Strickland, C. Hoffmann, and S. C. Wimbush, "A 1 kA-class cryogen-free critical current characterization system for superconducting coated conductors," *Review of Scientific Instruments*, vol. 85, no. 11, p. 113907, Nov. 2014, doi: 10.1063/1.4902139/356465.

[200] S. C. Wimbush and N. M. Strickland, "A Public Database of High-Temperature Superconductor Critical Current Data," *IEEE Transactions on Applied Superconductivity*, vol. 27, no. 4, Jun. 2017, doi: 10.1109/TASC.2016.2628700.

[201] M. D. Ainslie *et al.*, "Numerical modelling of mechanical stresses in bulk superconductor magnets with and without mechanical reinforcement," 2019.

[202] H. Mochizuki, H. Fujishiro, T. Naito, Y. Itoh, Y. Yanagi, and T. Nakamura, "Trapped Field Characteristics and Fracture Behavior of REBaCuO Bulk Ring during Pulsed Field Magnetization," *IEEE Transactions on Applied Superconductivity*, vol. 26, no. 4, Jun. 2016, doi: 10.1109/TASC.2015.2513415.

[203] H. Fujishiro *et al.*, "Simulation studies of mechanical stresses in REBaCuO superconducting ring bulks with infinite and finite height reinforced by metal ring during field-cooled magnetization," *Supercond Sci Technol*, vol. 30, no. 8, p. 085008, Jul. 2017, doi: 10.1088/1361-6668/AA76A2.

[204] H. Chen, H. Yong, and Y. Zhou, "XFEM analysis of the fracture behavior of bulk superconductor in high magnetic field," *J Appl Phys*, vol. 125, no. 10, p. 103901, Mar. 2019, doi: 10.1063/1.5063893/1074476.

[205] Z. Jing, "Numerical modelling and simulations on the mechanical failure of bulk superconductors during magnetization: based on the phase-field method," *Supercond Sci Technol*, vol. 33, no. 7, p. 075009, Jun. 2020, doi: 10.1088/1361-6668/AB92E6.

References

[206] P. Gao, W.-K. Chan, and X. Wang, "Width-bending characteristic of REBCO HTS tape and flat-tape Rutherford-type cabling," *Supercond Sci Technol*, vol. 34, no. 12, p. 125020, Nov. 2021, doi: 10.1088/1361-6668/AC30EB.

[207] S. Rogers *et al.*, "Electro-mechanical properties of REBCO coated conductors from various industrial manufacturers at 77 K, self-field and 4.2 K, 19 T," *Supercond Sci Technol*, vol. 28, no. 4, p. 045011, Feb. 2015, doi: 10.1088/0953-2048/28/4/045011.

[208] R. Hu *et al.*, "Numerical Study on Mechanical Properties of Conductors on Round Core Cables," *IEEE Transactions on Applied Superconductivity*, vol. 31, no. 5, Aug. 2021, doi: 10.1109/TASC.2021.3062608.

[209] C. Guo *et al.*, "Enhancement of electro-mechanical behaviors in RE–Ba–Cu–O composite superconducting tapes with laser slit edges," *Supercond Sci Technol*, vol. 35, no. 11, p. 115009, Oct. 2022, doi: 10.1088/1361-6668/AC96D5.

[210] D. P. Boso, M. Breschi, A. Musso, E. Pilastro, and P. L. Ribani, "Numerical Investigation on the Thermo-Mechanical Behavior of HTS Tapes and Experimental Testing on Their Critical Current," *IEEE Transactions on Applied Superconductivity*, vol. 30, no. 4, Jun. 2020, doi: 10.1109/TASC.2020.2968040.

[211] H. Milanchian, T. Salmi, A. Halbach, and R. Kouhia, "HTS Tape Mechanical Behavior Sensitivity on Material Properties and Thickness of Material Layers," *IEEE Transactions on Applied Superconductivity*, vol. 33, no. 5, Aug. 2023, doi: 10.1109/TASC.2023.3251293.

[212] L. Valentini, S. Bittolo Bon, M. A. Lopez-Manchado, L. Mussolin, and N. Pugno, "Development of conductive paraffin/graphene films laminated on fluoroelastomers with high strain recovery and anti-corrosive properties," *Compos Sci Technol*, vol. 149, pp. 254–261, Sep. 2017, doi: 10.1016/J.COMPSCITECH.2017.06.023.

[213] T. A. Coombs, "Superconducting flux pumps," *J Appl Phys*, vol. 125, no. 23, 2019, doi: 10.1063/1.5098384.

References

[214] W. Wang, J. Wei, C. Yang, C. Wu, and H. Li, "Review of high temperature superconducting flux pumps," *Superconductivity*, vol. 3, no. July, p. 100022, 2022, doi: 10.1016/j.supcon.2022.100022.

[215] T. A. Coombs, J. Geng, L. Fu, and K. Matsuda, "An overview of flux pumps for HTS coils," *IEEE Transactions on Applied Superconductivity*, vol. 27, no. 4, 2017, doi: 10.1109/TASC.2016.2645130.

[216] J. Geng and T. A. Coombs, "Mechanism of a high- Tc superconducting flux pump: Using alternating magnetic field to trigger flux flow," *Appl Phys Lett*, vol. 107, no. 14, 2015, doi: 10.1063/1.4932950.

[217] H. Li, W. Wang, Y. Gao, H. Ye, Y. Zhang, and J. Wei, "Design, Fabrication, and Testing of a YBCO Racetrack Coil for an HTS Synchronous Motor With HTS Flux Pump," *2020 IEEE International Conference on Applied Superconductivity and Electromagnetic Devices, ASEMD 2020*, vol. 30, no. 4, pp. 5–9, 2020, doi: 10.1109/ASEMD49065.2020.9276334.

[218] W. Wang, J. Wei, C. Yang, C. Wu, and H. Li, "Review of high temperature superconducting flux pumps," *Superconductivity*, vol. 3, p. 100022, Sep. 2022, doi: 10.1016/J.SUPCON.2022.100022.

[219] M. P. Oomen *et al.*, "HTS flux pump for cryogen-free HTS magnets," *IEEE Transactions on Applied Superconductivity*, vol. 15, no. 2 PART II, pp. 1465–1468, Jun. 2005, doi: 10.1109/TASC.2005.849129.

[220] J. Geng and T. A. Coombs, "An HTS flux pump operated by directly driving a superconductor into flux flow region in the E–J curve," *Supercond Sci Technol*, vol. 29, no. 9, p. 095004, Jul. 2016, doi: 10.1088/0953-2048/29/9/095004.

[221] J. Geng, C. W. Bumby, and R. A. Badcock, "Maximising the current output from a self-switching kA-class rectifier flux pump," *Supercond Sci Technol*, vol. 33, no. 4, p. 045005, Feb. 2020, doi: 10.1088/1361-6668/AB6957.

[222] C. Hoffmann, D. Pooke, and A. D. Caplin, "Flux pump for HTS magnets," *IEEE Transactions on Applied Superconductivity*, vol. 21, no. 3 PART 2, pp. 1628–1631, Jun. 2011, doi: 10.1109/TASC.2010.2093115.

References

[223] L. Fu, K. Matsuda, M. Baghdadi, and T. Coombs, "Linear Flux Pump Device Applied to High Temperature Superconducting (HTS) Magnets," *IEEE Transactions on Applied Superconductivity*, vol. 25, no. 3, Jun. 2015, doi: 10.1109/TASC.2015.2406294.

[224] Z. Bai, G. Yan, C. Wu, S. Ding, and C. Chen, "A novel high temperature superconducting magnetic flux pump for MRI magnets," *Cryogenics (Guildf)*, vol. 50, no. 10, pp. 688–692, Oct. 2010, doi: 10.1016/J.CRYOGENICS.2010.06.021.

[225] Y. Zhang *et al.*, "Compact Linear-Motor Type Flux Pumps with Different Wavelengths for High-Temperature Superconducting Magnets," *IEEE Transactions on Applied Superconductivity*, vol. 30, no. 4, Jun. 2020, doi: 10.1109/TASC.2020.2981296.

[226] Z. Yang *et al.*, "The Performance Test of an Updated Linear-Motor Flux Pump With Single-Sided DC Winding," *IEEE Transactions on Applied Superconductivity*, vol. 32, no. 6, Sep. 2022, doi: 10.1109/TASC.2022.3157658.

[227] J. Jiang *et al.*, "High-performance Bi-2212 round wires made with recent powders," *IEEE Transactions on Applied Superconductivity*, vol. 29, no. 5, 2019, doi: 10.1109/TASC.2019.2895197.

[228] K. Hamilton, A. E. Pantoja, J. G. Storey, Z. Jiang, R. A. Badcock, and C. W. Bumby, "Design and Performance of a 'squirrel-Cage' Dynamo-Type HTS Flux Pump," *IEEE Transactions on Applied Superconductivity*, vol. 28, no. 4, Jun. 2018, doi: 10.1109/TASC.2018.2805161.

[229] W. Wang *et al.*, "A Kilo-Amp Linear-Motor Type Flux Pump," *IEEE Transactions on Applied Superconductivity*, vol. 32, no. 6, Sep. 2022, doi: 10.1109/TASC.2022.3168532.

[230] S. Ito, N. Yusa, N. Yanagi, H. Tamura, A. Sagara, and H. Hashizume, "Mechanical and Electrical Characteristics of a Bridge-Type Mechanical Lap Joint of HTS STARS Conductors," *IEEE Transactions on Applied Superconductivity*, vol. 26, no. 2, pp. 1–10, 2016, doi: 10.1109/TASC.2016.2517197.

References

[231] S. Ito, Y. Seino, N. Yanagi, Y. Terazaki, and A. Sagara, "Bridge-Type Mechanical Lap Joint of a 100 kA-Class HTS Conductor having Stacks of GdBCO Tapes ∗)," vol. 9, pp. 1–5, 2014.

References